TECHNISCHE UNIVERSITÄT WIEN

DISSERTATION

Defect Chemistry and Electrochemical Properties of Lithium-Ion Battery Cathode Materials

ausgeführt zum Zwecke der Erlangung des akademischen Grades eines Doktors der Naturwissenschaften unter der Leitung von

Univ.-Prof. Dipl.-Phys. Dr. Jürgen Fleig
E164 - Institute of Chemical Technologies and Analytics

eingereicht an der Technischen Universität Wien
Fakultät für Technische Chemie

von

Andreas Bumberger, MSc.
Mat-Nr.: 11937131

Wien, 19. September 2023

Andreas Bumberger

Eidesstattliche Erklärung:

Ich erkläre an Eides statt, dass die vorliegende Arbeit nach den anerkannten Grundsätzen für wissenschaftliche Abhandlungen von mir selbstständig erstellt wurde. Alle verwendeten Hilfsmittel, insbesondere die zugrunde gelegte Literatur, sind in dieser Arbeit genannt und aufgelistet. Die aus den Quellen wörtlich entnommenen Stellen sind als solche kenntlich gemacht. Das Thema dieser Arbeit wurde von mir bisher weder im In- noch Ausland einer Beurteilerin/einem Beurteiler zur Begutachtung in irgendeiner Form als Prüfungsarbeit vorgelegt. Diese Arbeit stimmt mit der von den Begutachterinnen/Begutachtern beurteilten Arbeit überein.

Ich nehme zur Kenntnis, dass die vorgelegte Arbeit mit geeigneten und dem derzeitigen Stand der Technik entsprechenden Mitteln (Plagiat-Erkennungssoftware) elektronisch-technisch überprüft wird. Dies stellt einerseits sicher, dass bei der Erstellung der vorgelegten Arbeit die hohen Qualitätsvorgaben im Rahmen der geltenden Regeln zur Sicherung guter wissenschaftlicher Praxis "Code of Conduct" an der TU Wien eingehalten wurden. Zum anderen werden durch einen Abgleich mit anderen studentischen Abschlussarbeiten Verletzungen meines persönlichen Urheberrechts vermieden.

Andreas Bumberger

Abstract

Lithium-ion batteries (LIBs) have emerged as one of the key technologies of the 21st century and are currently revolutionizing the automotive industry. On an electrochemical level, energy storage in LIBs is accomplished by lithium insertion materials, which represent an essential class of mixed ionic and electronic conductors (MIECs). During every charge-discharge cycle, a LIB electrode material evolves across a wide range of thermodynamic states, each being defined by a specific electrode potential, Li content, and a corresponding set of electrochemical properties. Thus, an accurate understanding of the overall electrode kinetics requires knowledge of the composition-dependent electrochemical material parameters, which consist of the interfacial charge-transfer resistance, the ionic and electronic conductivity, the chemical capacitance, and the chemical diffusion coefficient. However, complete sets of these properties are rarely reported as a function of state-of-charge (SOC). Moreover, the interpretation of these properties from a defect chemical point of view is not very common. This thesis addresses these shortcomings and lays the groundwork for a better defect chemical understanding of LIB cathode materials and their associated electrochemical properties.

To provide a starting point for the extraction of these material properties from electrochemical measurements, we first revisit the impedance of MIECs based on the one-dimensional transmission line model proposed by Jamnik and Maier, aiming to improve the intuitive understanding of all MIEC impedance spectra and provide a practical approach for the derivation of tailored equivalent circuits for any specific experimental situation. MIEC devices and measurement setups are classified as symmetrical (setups for the characterization of bulk properties), asymmetrical (solid-oxide fuel cell (SOFC) electrodes), and antisymmetrical (battery electrodes) with respect to the ion and electron blocking behavior of the two contacts. For certain boundary conditions, the transmission line is consistent with classical Warburg elements and the intuitively constructed Randles' circuit, but it also provides an extension of these circuits for MIECs with similar ionic and electronic conductivities. Furthermore, we demonstrate how blocking the surface exchange reaction transforms an SOFC electrode into a battery electrode, and how a finite side-reaction resistance can be included in the impedance model of a non-ideal battery.

As a first application example, the impedance of sputtered Li_{1-} CoO_2 thin films is analyzed to extract the fundamental electrochemical properties as a function of SOC. Within the accessible SOC range, the charge-transfer resistance and ionic conductivity vary by more

than one order of magnitude. The chemical capacitance determined from impedance spectra agrees excellently with the differential capacity from charge/discharge curves, and, in the dilute regime, even matches the absolute values predicted by defect thermodynamics. The evolution of the chemical lithium diffusivity along the charge curve is deconvoluted into the separate contributions of ionic conductivity and chemical capacitance. Finally, we apply the principles of defect chemistry to evaluate the observed trends in terms of lithium activity and point defect concentrations. The consistency of impedance measurements, cycling data, and thermodynamic theory highlights the key role of the chemical capacitance as a powerful material descriptor and emphasizes the relevance of defect chemical concepts for all lithium insertion electrode materials.

In the next step, we report a comprehensive impedance study of sputter-deposited epitaxial Li_{2-} Mn_2O_4 thin films as a function of SOC for almost the entire tetrahedral-site regime (1

1 9) and provide a complete set of electrochemical properties, consisting of the charge-transfer resistance, ionic conductivity, volume-specific chemical capacitance, and chemical diffusivity. The obtained properties vary by up to three orders of magnitude and provide essential insights into the point defect concentration dependences of the overall electrode potential. We introduce a defect chemical model based on simple concentration dependences of the Li chemical potential, considering the tetrahedral and octahedral lattice site restrictions defined by the spinel crystal structure. The proposed model is in excellent qualitative and quantitative agreement with the experimental data, excluding the two-phase regime around 4.15 V versus Li^+/Li, and is applicable to the defect chemical analysis of all spinel-type cathode materials.

Finally, we consider the complex interplay of lithium and oxygen nonstoichiometry. The level of oxygen deficiency in high-voltage spinels of the composition $LiNi_{0.5}Mn_{1.5}O_{4-}$ (LNMO) significantly influences the thermodynamic and kinetic properties of the material, ultimately affecting the cell performance of the corresponding lithium-ion batteries. This study presents a comprehensive defect chemical analysis of LNMO thin films with oxygen vacancy concentrations of 2.4% and 0.53%, focusing particularly on the oxygen vacancy regime around 4 V versus Li^+/Li. A set of electrochemical properties is extracted from impedance measurements as a function of SOC for the full tetrahedral-site regime (3.8 to 4.9 V versus Li^+/Li). A defect chemical model (Brouwer diagram) is derived, providing a coherent explanation for all important trends of the electrochemical properties and charge curve. Highly resolved chemical capacitance measurements allow a refining of the defect model for the oxygen vacancy regime, showing that a high level of oxygen deficiency not only impacts the amount of redox active $Mn^{3+/4+}$, but also promotes the trapping of electrons in proximity to an oxygen vacancy. The resulting stabilization of Mn^{3+} thereby mitigates the voltage reduction in the oxygen vacancy regime.

Kurzfassung

Lithium-Ionen-Batterien (LIB) haben sich als eine der Schlüsseltechnologien des 21. Jahrhunderts etabliert und spielen aktuell eine zentrale Rolle in der rapide voranschreitenden Transformation der Autoindustrie. Auf elektrochemischer Ebene wird die Energiespeicherung in LIB durch Li-Interkalationsmaterialien bewerkstelligt, die eine wichtige Klasse ionisch-elektronischer Gemischtleiter (MIECs) darstellen. Beim Laden/Entladen der Batterie durchläuft ein solches Elektrodenmaterial ein breites Kontinuum thermodynamischer Zustände, die jeweils durch ein bestimmtes Elektrodenpotential, einen bestimmten Lithiumgehalt, und die entsprechenden elektrochemischen Materialeigenschaften gekennzeichnet sind. Um die Gesamtkinetik einer LIB-Elektrode genau zu verstehen, werden daher diese elektrochemischen Eigenschaften (Ladungstransferwiderstand, ionische und elektronische Leitfähigkeit, chemische Kapazität und chemischer Diffusionskoeffizient) in Abhängigkeit des Lithiumgehalts benötigt. Solche vollständigen Datensätze wurden bisher allerdings nur selten gemessen, und auch ihre defektchemische Interpretation ist nicht sehr verbreitet. In der vorliegenden Arbeit werden diese Defizite adressiert und der Grundstein für ein defektchemisches Verständnis von LIB-Kathodenmaterialien und ihren elektrochemischen Eigenschaften gelegt.

Um einen Ausgangspunkt für die Bestimmung der Materialeigenschaften aus elektrochemischen Messungen zu schaffen, wird das Impedanzverhalten von MIECs basierend auf dem eindimensionalen Transmission-Line-Modell von Jamnik und Maier betrachtet. Die präsentierten Sichtweisen erleichtern das intuitive Verständnis aller MIEC-Impedanzspektren und bieten einen Ansatz zur Herleitung maßgeschneiderter Ersatzschaltbilder für verschiedenste Messsituationen. MIEC-Bauteile und -Messsituationen werden entsprechend der Art der Kontaktmaterialien als symmetrisch (Charakterisierung von Bulk-Eigenschaften), asymmetrisch (Festoxid-Brennstoffzellen (SOFCs)) oder antisymmetrisch (Batterien) klassifiziert. Je nach Randbedingung mündet die Transmission-Line in klassische Warburg-Elemente und ist damit auch mit dem in der Batterieforschung weitverbreiteten Randles' Circuit konsistent. Das Transmission-Line-Modell erlaubt zudem eine Erweiterung der Warburg-Elemente für MIECs mit ähnlicher ionischer und elektronischer Leitfähigkeit. Darüber hinaus wird gezeigt, dass ein Blockieren der Sauerstoffaustauschreaktion an der Oberfläche einer SOFC-Elektrode diese in eine Batterie-Elektrode verwandelt, und dass Nebenreaktionen in einer nicht-idealen Batterie mithilfe der Transmission-Line im Ersatzschaltbild berücksichtigt werden können.

Als erstes Anwendungsbeispiel wird das Impedanzverhalten gesputterter Li_{1-} CoO_2 Dünnschichten untersucht und daraus die elementaren Materialeigenschaften in Abhängigkeit des Ladezustands (SOC) gewonnen. Innerhalb des zugänglichen SOC-Bereichs ändern sich der Ladungstransferwiderstand sowie die ionische Leitfähigkeit um mehr als eine Größenordnung. Die aus Impedanzspektren abgeleitete chemische Kapazität stimmt mit der differenziellen Kapazität aus Lade-/Entladekurven sehr gut überein und entspricht im verdünnten Gebiet sogar den thermodynamisch berechneten Absolutwerten. Der Verlauf des chemischen Diffusionskoeffizienten entlang der Ladekurve wird in die separaten Beiträge aus ionischer Leitfähigkeit und chemischer Kapazität aufgetrennt. Schließlich wird ein defektchemisches Modell präsentiert, das die beobachteten Veränderungen ausgehend von der Lithiumaktivität und den einzelnen Punktdefektkonzentrationen erklärt. Die Übereinstimmung von Impedanzmessungen, Lade-/Entladekurven und thermodynamischer Theorie unterstreicht die Aussagekraft der chemischen Kapazität als zentrale Materialeigenschaft und die Relevanz defektchemischer Konzepte für alle Lithium-Interkalationselektroden.

Im nächsten Schritt wird eine umfassende Impedanzstudie epitaktisch gesputterter Li_{2-} Mn_2O_4 Dünnschichten als Funktion des Ladezustands für nahezu das gesamte Tetraeder-Gebiet (1 1 9) präsentiert und ein vollständiger Datensatz bestehend aus Ladungstransferwiderstand, ionischer Leitfähigkeit, chemischer Kapazität und chemischem Diffusionskoeffizienten abgeleitet. Die gemessenen Eigenschaften verändern sich um bis zu drei Größenordnungen und geben Aufschluss über die Einflüsse verschiedener Punktdefektkonzentrationen auf das Elektrodenpotential. In weiterer Folge wird ein defektchemisches Modell entwickelt, basierend auf einfachen Konzentrationsabhängigkeiten des chemischen Potentials von Li, unter Berücksichtigung der materialspezifischen tetra- und oktaedrischen Platzbeschränkungen. Die mithilfe des Defektmodells berechnete chemische Kapazität stimmt, bis auf das Zweiphasengebiet um 4.15 V gegen Li^+/Li, mit den experimentellen Daten sowohl qualitativ als auch quantitativ hervorragend überein und kann generell für die defektchemische Analyse aller Spinell-Kathodenmaterialien eingesetzt werden.

Abschließend wird das komplexe Zusammenspiel zwischen Lithium- und Sauerstoff-Nichtstöchiometrie in LIB-Kathodenmaterialien untersucht. Der Sauerstoff-Defizienzgrad in Hochvolt-Spinellen der chemischen Zusammensetzung $LiNi_{0.5}Mn_{1.5}O_{4-}$ (LNMO) beeinflusst maßgeblich die thermodynamischen und kinetischen Eigenschaften des Materials und letztlich auch das elektrochemische Verhalten der entsprechenden LIB. In diesem Teil wird eine umfassende defektchemische Analyse von LNMO-Dünnschichten mit Sauerstoff-Leerstellen-Konzentrationen von 2.4% und 0.53% präsentiert, mit einem besonderen Fokus auf dem Sauerstoff-Leerstellen-Gebiet um 4 V gegen Li^+/Li. Ein Datensatz elektrochemischer Eigenschaften wird aus impedanzspektroskopischen Messungen in Abhängigkeit des Ladezustands für das gesamte Tetraeder-Gebiet (3.8 bis 4.9 V gegen Li^+/Li) gewonnen. Daraus wird ein defektchemisches Modell (Brouwer-Diagramm) abgeleitet, das eine zusammenhängen-

de Erklärung für alle wichtigen Veränderungen der elektrochemischen Eigenschaften und der Ladekurve liefert. Hochaufgelöste Messungen der chemischen Kapazität erlauben zudem eine Verfeinerung des Defektmodells im Sauerstoff-Leerstellen-Gebiet. Dadurch kann gezeigt werden, dass ein hoher Sauerstoff-Defizienzgrad nicht nur die Menge an redoxaktivem $Mn^{3+/4+}$ beeinflusst, sondern darüber hinaus auch Elektronen-Trapping-Reaktionen in unmittelbarer Nähe einer Sauerstoff-Leerstelle begünstigt. Die daraus resultierende Stabilisierung von Mn^{3+} vermindert den Spannungsverlust im Sauerstoff-Leerstellen-Gebiet.

Contents

1 Introduction

1.1 Historical Development and Impact of Lithium-Ion Batteries

Since their first commercialization by Sony in 1991,[1,2] rechargeable lithium-ion batteries (LIBs) have fundamentally changed our lives by providing unprecedented electrical energy storage densities for both mobile and stationary applications. Having enabled the widespread breakthrough of portable consumer electronics such as smartphones and laptops, LIBs are currently out to revolutionize the automotive industry and decarbonize the mobility sector. Furthermore, LIBs have become indispensable for the stationary storage of energy from renewable sources and grid-stabilizing applications.[3,4] It is for this groundbreaking impact on our world and society, that the Nobel Prize in Chemistry was awarded to John B. Goodenough, M. Stanley Whittingham, and Akira Yoshino in 2019.[5]

The development of secondary (rechargeable) LIBs dates back to the 1970s, when Besenhard and coworkers reported the electrochemical intercalation of Li into graphite[6–8] and transition metal oxides,[9,10] although the corresponding lithium-ion cells were lacking a suitable electrolyte and thus exhibited poor cycling stability.[11] The first major breakthrough towards rechargeable LIBs was achieved in 1976 by Whittingham,[12] who demonstrated the highly reversible electrochemical intercalation of Li into layered TiS_2 at a potential of roughly 2 V versus Li^+/Li.[13,14] In 1980, inspired by Whittingham's work, Goodenough and coworkers discovered that the cell voltage versus Li^+/Li could be doubled to about 4 V by using the structurally similar layered oxide $LiCoO_2$ (LCO) as the cathode material.[15] Although the corresponding Li/LCO full cells exhibited energy densities surpassing all other previously known battery cell chemistries, their practical viability was still hampered by the unsolved issue of dendrite formation at the metallic Li anode, shorting the cell upon extended cycling and hence presenting a severe safety threat. In the 1980s, Yoshino accomplished the third major breakthrough that allowed the broad commercialization of LIBs, replacing metallic Li by petroleum coke at the anode and thus allowing safe and reasonably stable cycling.[16] Finally, in 1990, Dahn and coworkers discovered that using electrolytes with ethylene carbonate led to the formation of a stabilizing solid electrolyte interphase (SEI) on the carbon surface in Li/graphite and Li/petroleum coke cells, preventing continuous electrolyte decomposition and thus laying the foundation for modern LIB electrolytes.[17]

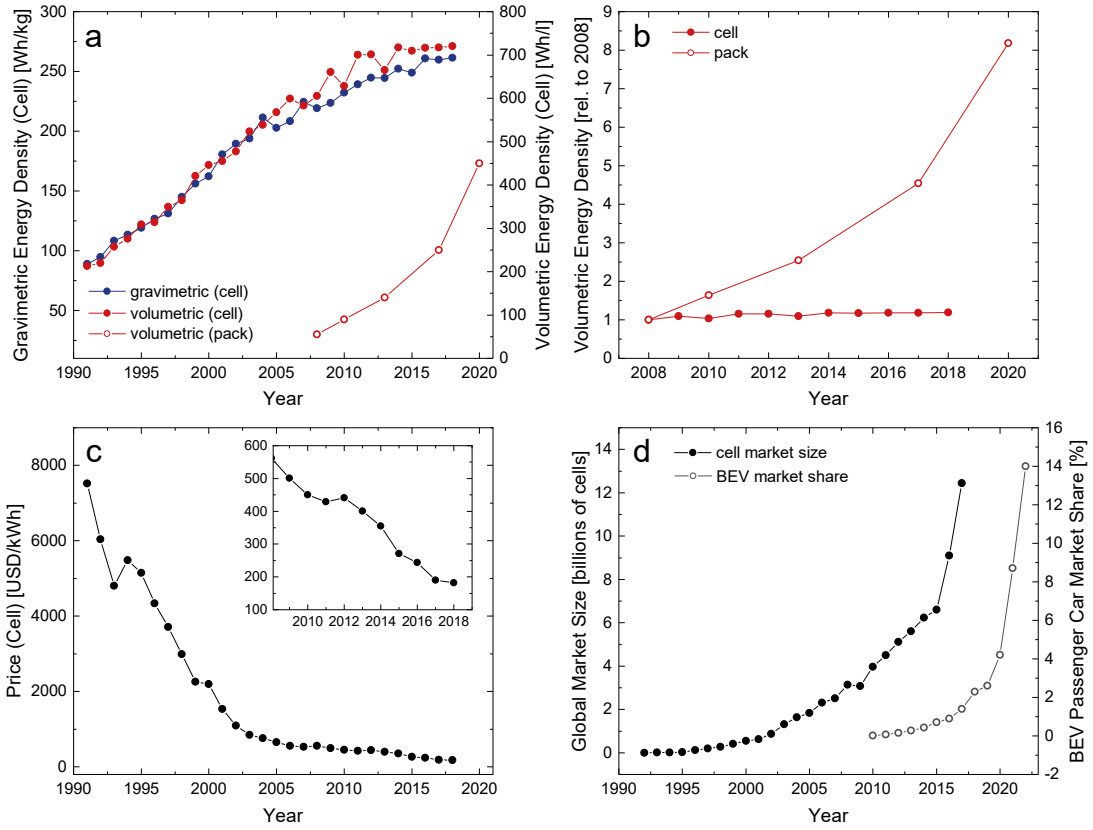

Figure 1.1: (a) Gravimetric and volumetric energy densities of commercial Li-ion cells (all types) and battery packs from 1991 to 2018 and 2020, respectively. For cells, the data refer to 98th percentiles and were taken from refs. 18 and 19. For battery packs, the data were taken from ref. 20. **(b)** Volumetric energy density of commercial Li-ion cells and battery packs from 2008 to 2018 and 2020, respectively, relative to the year 2008. The data shown are taken from subfigure (a). **(c)** Price of commercial Li-ion cells (all types) from 1991 to 2018.[18,19] **(d)** Global market size for Li-ion cells (billions of cells) from 1992 to 2017[18,19] and global passenger car market share of BEVs from 2010 to 2022.[21]

As shown in Figure 1.1a, gravimetric and volumetric energy densities of commercial Li-ion cells have approximately tripled over the past three decades, reaching values around 260 Wh/kg and 720 Wh/l in 2018.[18] On a battery pack level, volumetric energy densities of electric vehicle (EV) batteries have shown an eightfold increase from 55 Wh/l in 2008 to 450 Wh/l in 2020.[20] Within the same time frame, volumetric energy densities on the cell level only increased by about 20%, as shown in Figure 1.1b. This shows that in terms of energy density, the most significant improvements are currently being achieved on the battery pack engineering level, while progress on the cell level is rather slow and tends towards stagnation. Drastic improvements have also been achieved in terms of cost, with the commercial cell price having gone down by approximately a factor three over the past decade (Figure 1.1c). Despite the central importance of LIBs for portable consumer electronics and power tools, the most powerful driver of these rapid developments over the past few years is undoubtedly the automotive industry, with many major manufacturers of combustion engines planning

to complete their transition to battery electric vehicles (BEVs) in the 2030s[22] and relatively new global players such as BYD (China) and Tesla (USA) leading the market with heavy investments in technological development and upscaling of production capacities.[23–25] The total size of the global market for Li-ion cells in billions of cells is plotted in Figure 1.1d for the years 2010 to 2022. A sharp increase in the market growth rate is observed from 2015 onwards. Around the same year, the global market share of BEVs within passenger car sales begins to increase, reaching a record value of about 14% in 2022.[21]

In light of these developments, it is reasonable to state that LIBs will be one of the key technologies of the 21st century and their further improvement in terms of energy and power density, longevity, and cost is of central importance. However, the data presented in Figure 1.1 suggest that LIB technology in its current form is reaching a state of maturity, where most of the optimizing potential for energy density and cost on the cell level has been realized, and only gradual improvements can be expected over next few years. Thus, although production capabilities may realize some remaining cost potential, it stands to reason that alternative cell chemistries would be required to significantly surpass state-of-the-art LIBs, especially in terms of cell-level energy density. Although emerging technologies such as lithium-sulfur or all-solid-state batteries (ASSBs) could offer a possible solution, these are still facing significant hurdles on their way to a potential large-scale commercialization.[26–28] Much more importantly, however, the scarcity of raw materials[29,30] is giving reason to doubt that a full electrification of the global passenger car fleet could even be achieved solely based on LIBs. Thus, it appears likely that post-lithium technologies such as Na-ion batteries, regardless of their innately lower energy density, will have to become involved to meet the rapidly growing demand for BEVs. In fact, CATL (China), currently the world's largest manufacturer of Li-ion batteries,[31] has recently announced their deployment of a Na-ion battery in the upcoming EV models of Chery (China).[32]

Even though such reports point towards a possible future beyond LIBs, the fundamental science presented in this thesis is readily transferable to all other cell chemistries based on ion insertion and will therefore remain relevant for the foreseeable future. Particularly with regard to optimizing charging speed and discharge power density, a detailed understanding of the defect chemistry and state-of-charge-dependent electrochemical properties of ion insertion materials is more important than ever.

1.2 Working Principle of a Lithium-Ion Battery

There are several valid approaches to describing the working principle and thermodynamics of a Li-ion battery. In the following, we will adopt the viewpoint of (electro)chemical potentials, as propagated by Maier,[33,34] which provides the basis of the defect chemical analyses presented in this thesis.

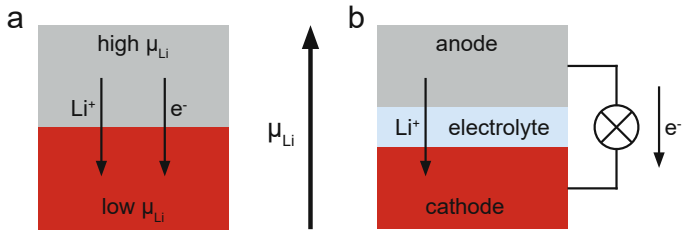

FIGURE 1.2: (a) Schematic representation of a direct reaction between two materials of different Li chemical potential . Electrons and Li ions are directly transferred. **(b)** Schematic representation of an electrochemical discharge reaction between anode (high) and cathode (low). By introducing an ionic conductor (electrolyte) between the two materials and connecting the two electrodes via an external electric circuit, the transfer pathways of electrons and ions are decoupled. Chemical energy is directly converted into electrical energy, which can perform work. This figure was adapted from ref. 33.

In a Li-ion battery, electrical energy is reversibly stored by exploiting a difference in Li chemical potential between two materials.[33] By its definition

— (1.1)

with Gibb's free energy , the amount of substance , temperature , and pressure , the chemical potential of component reflects the amount of chemical energy that can be stored or released upon adding an incremental amount of substance . In qualitative terms, describes the energetic favorability of component in a given phase. For example, the higher a material's , the higher its chemical potential energy per atom of Li. As a consequence, when two materials of different are brought into direct contact, formally neutral Li (i.e., a Li ion Li^+ together with its electron e^-) will be transferred from the high to the low phase, releasing an amount of energy proportional to . This situation is shown schematically in Figure 1.2a. For such a direct chemical reaction, the fraction of the released energy that can perform work is theoretically limited by Carnot's efficiency.

To accurately describe the thermodynamics of electrochemical Li storage, it is essential to explicitly consider the internal dissociation of Li ions and electrons[35] in the mixed conducting insertion material according to

(1.2)

With the electrochemical potential defined as

~ (1.3)

where is the charge number, the elementary charge, and the electrical potential, is related to the electrochemical potential of Li ions and electrons via

~ ~ ~ (1.4)

according to the dissociation equilibrium given in Equation (1.2). Please note that for uncharged species such as neutral Li, the electrochemical and chemical potentials are identical. Based on this dissociation of ions and electrons, the fundamental idea behind a Li-ion cell (and other electrochemical cells) is to separate the flow of ions and electrons by introducing an ionic conductor (electrolyte) between two materials of different and channeling the electron flow through an external circuit, where it can directly perform electrical work, as shown in Figure 1.2b.[33] Such an electrochemical discharge reaction can theoretically reach efficiencies of 100% and above (due to entropy effects). Under open-circuit conditions, a reversible cell voltage corresponding to

(1.5)

is built up between anode (high) and cathode (low). As long as the external wire leads are not connected, the cell is in a restricted equilibrium state, where only the electrochemical potentials of Li^+ are in equilibrium via the electrolyte. Using Equation (1.4), is thus reduced to the electrochemical potential difference of electrons, ~ . When the circuit is closed, the Li chemical potentials of the two electrodes start to equilibrate by transferring Li^+ and electrons from anode to cathode, through the electrolyte and external circuit, respectively. By applying an appropriate voltage (i.e., ~) to the cell, the driving force for the reaction can be reversed and, provided that the individual electrode reactions are reversible, the cell can thus be recharged.

Figure 1.3 schematically shows the structure of a typical Li-ion cell. The cathode commonly consists of a transition metal oxide capable of reversible Li (de)intercalation, with the layered oxide LCO being the archetypal example. Virtually all practically relevant cathode materials are synthesized and processed in the discharged state, that is, at full Li content. On the anode side, graphite usually serves as the active material, being able to intercalate Li ions between its sheets upon reduction. In practical cells, the electrode active materials are processed in the form of powders consisting of primary particles (crystallites) that combine into secondary agglomerates. Together with a polymer binder and conductive carbon additives, the electrode materials are coated onto Al (cathode) or Cu (anode) foil, resulting in a porous network of active particles. To prevent a short circuit, and thus a direct chemical reaction as shown in Figure 1.2a, a separator soaked with liquid electrolyte is sandwiched between anode and cathode. In commercial cells, the separator typically consists of a microporous

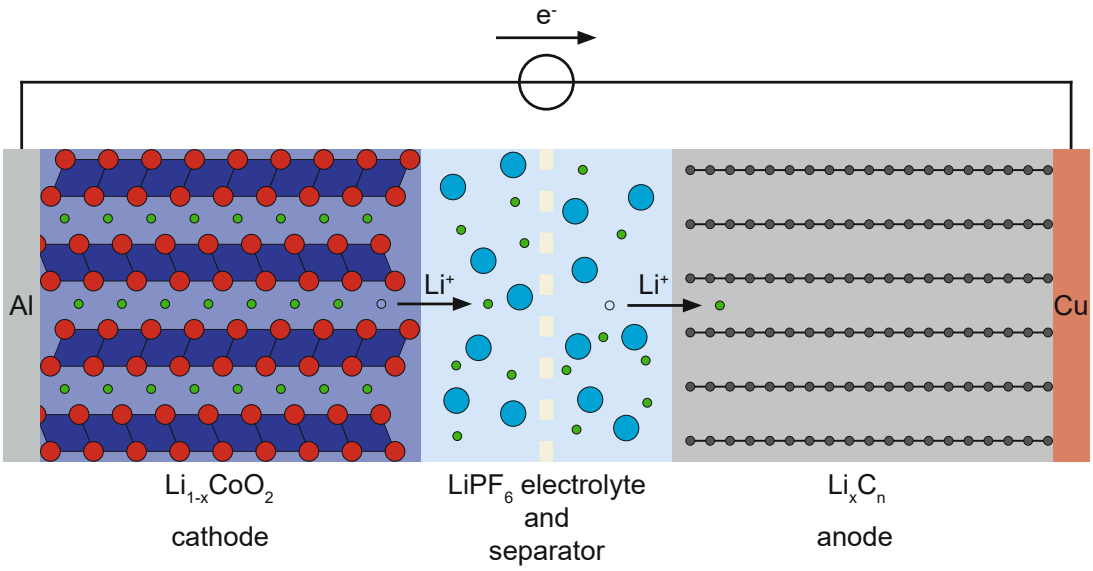

FIGURE 1.3: Schematic representation of a $LiCoO_2$ graphite (C_n) cell with a $LiPF_6$-based electrolyte, showing the direction of ion and electron flow for the charging reaction, driven by an external power supply. Upon discharging, the flow directions are reversed, and electrical energy is supplied to the external circuit.

polymer foil, which melts in the case of a thermal runaway to quench the discharge reaction. The electrolyte usually consists of $LiPF_6$ in a mixture of alkyl carbonate solvents, most often containing ethylene carbonate for stable SEI formation.[17]

After assembly, the Li-ion cell can be charged by applying an external voltage that is larger than the open-circuit voltage given by Equation (1.5). The cathode material is then oxidized and the anode material is reduced by transferring electrons from cathode to anode via the external circuit. Inside the cell, Li^+ is released from the cathode into the electrolyte and intercalated into the anode, such that electroneutrality is maintained. Thus, since Li^+ is being transported back and forth between anode and cathode upon cycling, this is often referred to as a rocking-chair principle. For the charging reaction shown in Figure 1.3, the individual half-cell reactions can be written as

$$LiCoO_2 \quad Li_{1-x}CoO_2 \quad Li^+ \quad e^- \tag{1.6}$$

$$C_n \quad Li^+ \quad e^- \quad Li_xC_n \tag{1.7}$$

where C_n is used to denote graphite.

1.3 LIB Cathode Materials

Although the principles and methods presented in this thesis apply to all battery electrode materials based on ion insertion, the main focus lies on LIB cathode materials. These can be divided into the three practically most relevant structural classes of (i) layered oxides, (ii) spinels, and (iii) phospho-olivines.

$LiCoO_2$ (LCO), the cathode material famously used in the first commercial LIBs,[1,2] represents the archetypal layered oxide. Its layered structure of the space group $\bar{3}$ offers two-dimensional pathways for Li transport, with Li occupying octahedral lattice sites between layers of CoO_2.[36] While LCO/C cells dominated the early LIB market,[2] LCO was eventually replaced by the isostructural compound classes $LiNi_xCo_yAl_zO_2$ (NCAs) and $LiNi_xMn_yCo_zO_2$ (NMCs),[2,37,38] which are used in most modern-day LIBs. The defect chemistry and electrochemical properties of LCO are discussed in detail in Chapter 3.

Spinel compounds represent the second important class of cathode materials, with $LiMn_2O_4$ (LMO) being the most prominent example.[39] In stoichiometric $LiMn_2O_4$ of the space group $\bar{3}$, Li occupies tetrahedral sites within the cubic close packing of O atoms, which offers a three-dimensional network for Li transport. Due to the additional presence of occupiable octahedral sites within the spinel structure, LMO potentially offers two separate storage regimes for tetrahedral and octahedral Li sites, as will be discussed in great detail in Chapter 4. The commercialization of LMO has proven much more difficult than for layered oxides due to its tendency towards Mn dissolution.[2,40] Nonetheless, the excellent rate capability and low cost of LMO have made it attractive for use in blended cathodes or even as a pure material in EVs such as the Mitsubishi i-MiEV and the Nissan Leaf.[41,42] Furthermore, the isostructural high voltage spinel $LiNi_{0.5}Mn_{1.5}O_4$ (LNMO), which will be the main focus of Chapter 5, has been investigated as a promising next-generation cathode material,[43] although its commercialization is still hindered by electrolyte instability.[44]

Finally, phospho-olivines such as $LiFePO_4$ (LFP) of the space group represent the third important class of cathode materials.[45] Although LFP is currently regaining attention for the purpose of low-cost BEVs,[46] it is not considered in this thesis and is therefore not further discussed.

1.4 Defect Chemistry and Electrochemical Properties of LIB Cathode Materials

Equations (1.6) and (1.7) reflect the fact that the anode and cathode active materials undergo changes in their Li concentration in response to an externally applied voltage that differs from the previous open-circuit voltage of the cell. More precisely, formally neutral Li is transferred between anode and cathode to reach a new equilibrium state that is characterized

by a Li chemical potential difference corresponding to the applied voltage (˜). This implies that the electrochemical properties characterizing the thermodynamic and kinetic behavior of LIB electrode materials are expected to vary significantly with the state-of-charge (SOC), since the chemical nature of the material is dynamically evolving throughout the charge and discharge process. Experimentally, these property changes can be effectively studied via electrochemical impedance spectroscopy, as will be discussed in Chapter 2.

In terms of thermodynamics, the transfer of Li in response to an external voltage implies that of both electrodes must be concentration dependent. This concentration dependence of constitutes the equilibrium charge/discharge curve, sometimes referred to as the open-circuit-voltage (OCV) curve, of a cell. In the simplest case of an unrestricted solid solution, of a given phase can be split into a standard term ^{0} and a concentration-dependent term according to

$$^{0} \tag{1.8}$$

with Boltzmann's constant and the temperature . The Li activity is defined as

$$ \tag{1.9}$$

where is the activity coefficient and the Li concentration. As will be explored in the following chapters, it is useful to reference all Li chemical potentials to metallic Li, such that ^{0} . Given the non-linear dependence of on , the amount of Li, and hence the amount of charge, that can be stored within a given electrode potential increment also varies with . This incremental storage capacity, which essentially reflects the shape of the charge curve, is referred to as the chemical capacitance and can be defined as

$$^{2} \quad \frac{}{} \quad ^{1} \tag{1.10}$$

where is the sample volume. The significance of for the electrochemical properties and defect chemical analysis of LIB electrode materials is discussed in depth in Chapter 3.

In terms of kinetics, the strong variation of an electrode material's Li content during charging implies that the relevant charge carrier concentrations for charge-transfer at the electrode/electrolyte interface, as well as for solid-state transport through the bulk material also change significantly. Accordingly, the overall electrode kinetics, and hence the rate capability of the cell, are strongly dependent on the SOC. To understand kinetic limitations of LIB electrodes in different regions of the charge curve, experimentally measured sets of the corresponding electrochemical properties are therefore invaluable. In this thesis, the most relevant electrochemical properties (charge-transfer resistance, ionic conductivity, chemical capacitance and chemical diffusion coefficient) of three different cathode materials ($LiCoO_2$, $LiMn_2O_4$, and $LiNi_{0.5}Mn_{1.5}O_{4-}$) are reported as a function of SOC.

Despite the importance of experimental studies, the electrochemical properties of Li insertion materials are not merely empirical quantities. Rather, they can be related to the variation of the ionic and electronic charge carrier concentrations as a function of the Li chemical potential. To correctly describe these correlations, it is essential to take into account the internal dissociation of Li into Li^+ and e^- (Equation (1.2)), and thus the individual chemical potentials of ions and electrons according to Equation (1.4). However, this leads to a problem when considering cathode materials, which are the main focus of this thesis. Since materials such as LCO and LMO contain a very high concentration of Li (more precisely, Li^+ and e^-) in the discharged state, dilute conditions cannot be assumed, and a description based on Equation (1.8) has to include the corresponding activity coefficients for both ions and electrons. To circumvent this problem, we adopt a defect chemical approach, where the ionic and electronic charge carrier concentrations are described in terms of point defects, that is, Li vacancies and electron holes. It is shown that activity coefficients reflecting only site restrictions of the point defects are already able to describe many important effects measured in LIB cathode materials.

This thesis addresses the topic of SOC-dependent material parameters and their defect chemical interpretation in four original contributions, either published, under review or in preparation for submission to peer-reviewed journals. In Chapter 3, we establish the basic principles and methodology for evaluating the electrochemical properties of LIB cathode materials in terms of defect chemistry at the example of LCO and explore the limitations of the underlying dilute-solution assumptions. In Chapter 4, we demonstrate that a defect chemical model based on dilute-solution thermodynamics adequately describes the electrochemical properties of spinel materials such as LMO over a surprisingly wide stoichiometry region, if lattice site restrictions are taken into account. Finally, in Chapter 5 we showcase the power of chemical capacitance measurements and the corresponding defect chemical analyses for evaluating the complex interplay of lithium and oxygen nonstoichiometry in oxygen-deficient LNMO.

2 Transmission Line Revisited - The Impedance of Mixed Ionic and Electronic Conductors

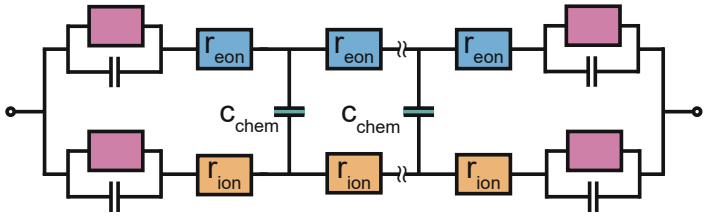

The study presented in this chapter is currently in preparation for publication:
Bumberger, A. E.; Fleig, J. et al. Transmission Line Revisited - The Impedance of Mixed Ionic and Electronic Conductors. **2023**.

2.1 Introduction

Electrochemical impedance spectroscopy (EIS) has become an indispensable tool for studying the thermodynamic and kinetic properties of mixed ionic and electronic conductors (MIECs). In the field of solid-state ionics, the most prominent classes of MIECs include intercalation electrodes for batteries (e.g., LCO), high-temperature mixed-conducting electrodes for solid-oxide cells (e.g., $La_{0.6}Sr_{0.4}CoO_{3-}$ (LSC)), and imperfect electrolytes (e.g., gadolinium-doped ceria (GDC) or $Li_{0.29+}$ $La_{0.57}TiO_3$ (LLTO) under reducing conditions). By applying a low-amplitude voltage or current perturbation onto an electrochemical system, impedance spectroscopy allows the separation of transport processes in the frequency domain according to their characteristic time constants. Generally, the more chemically and morphologically complex a system, the larger the variety of transport processes and time constants that potentially contribute to the overall impedance spectrum. As a result, intricate equivalent circuits with a large number of parameters are required to adequately describe the impedance response of, for example, a porous battery or solid oxide fuel cell (SOFC) electrode.[47–50]

However, even if morphological complexities such as porosity or tortuosity can be excluded and a well-defined, single-crystalline MIEC sample is measured, the analysis of the recorded impedance spectra if often far from trivial, mainly for two reasons. First, despite there only being three independent electrochemical solid-state bulk parameters (see below),

these parameters can vary over orders of magnitude, depending on the chemical potential of the relevant mobile species. For example, the electrochemical properties of LIB electrode materials are strongly dependent on the SOC, i.e., the Li content.[51,52] Analogously, the transport properties of SOFC and solid oxide electrolyzer cell (SOEC) materials vary with the oxygen content.[53] The second reason for the large variety of MIEC impedance spectra is found in the boundary conditions for ionic and electronic transport across the contact interfaces, which necessarily contribute to the measured impedance spectrum. In the simplest case, the contacts are either fully blocking or reversible (non-blocking) for ions and/or electrons. Unfortunately, this qualitative black-and-white distinction is rarely realized in experiments, meaning that the magnitudes of the corresponding interfacial transport resistances and capacitances for both ionic and electronic charge carriers must be taken into account.

The extraction of meaningful solid-state electrochemical properties from an MIEC impedance spectrum requires an equivalent circuit that is based on the underlying differential equations describing the transport of mass and charge in the presence of electrical and chemical potential gradients. In the most general form, the one-dimensional particle flux density of a charged species is described by the Nernst-Planck equation,[54,55] which reads

(2.1)

with the diffusion coefficient , concentration , position along the direction of transport, time , conductivity , charge number , elementary charge , and electrical potential . More descriptively, Equation (2.1) is often referred to as the diffusion-drift equation, as it separately considers the mass and charge transport contributions from diffusion (Fick's law, concentration gradient) and drift (Ohm's law, electrical potential gradient). In principle, Equation (2.1) can be solved for a specific experimental situation by inserting the appropriate boundary conditions defined by the sample and setup. An impedance expression can then be obtained by relating to the electrical current density. However, this approach suffers from two major limitations. First, analytical solutions to Equation (2.1) often rely on simplifying assumptions, such as neglecting the drift term for .[56] For more complicated systems, numerical solutions are required,[57] making the impedance analysis of MIEC devices a tedious task. Moreover, even when an analytical expression can be obtained, it is unclear how to appropriately integrate it into a full equivalent circuit that considers contacts and other contributions to the measured impedance, and equivalent circuits are therefore often constructed intuitively.

As first proposed by Jamnik and Maier,[58–60] these difficulties can be circumvented by mapping Equation (2.1) itself onto an equivalent circuit before applying any simplifying assumptions or boundary conditions. For a one-dimensional current flow across an MIEC slab of area and thickness , this results in a general transmission line circuit, featuring two parallel

resistive rails for ion and electron conduction, which are coupled by chemical capacitors, as shown in Figure 2.1, with , , and . At the rail ends, terminal impedance elements account for the interfacial resistances and capacitances for ions and electrons at the contact/MIEC boundaries. Accordingly, elements are usually inserted for the terminal impedances . The dielectric bulk capacitance of the MIEC is connected in parallel to the entire transmission line. Although an analytical impedance expression was originally only derived for symmetrical contacts,[54] i.e. for , , , and , the circuit can also be solved for the most general case by adapting the derivation in ref. 54 for four distinct terminals,[61] which is essential for inherently non-symmetrical MIEC devices such as battery electrodes. The full impedance expression of the transmission line in Figure 2.1 is given in the Appendix. In contrast to the underlying differential equations, the general transmission line can easily be adapted and simplified for specific experimental situations and allows a physically meaningful integration of the solid-state transport impedance into larger equivalent circuits. Moreover, it provides a highly intuitive approach to understanding the impedance of MIECs and a common root for the impedance responses of different types of MIEC devices.

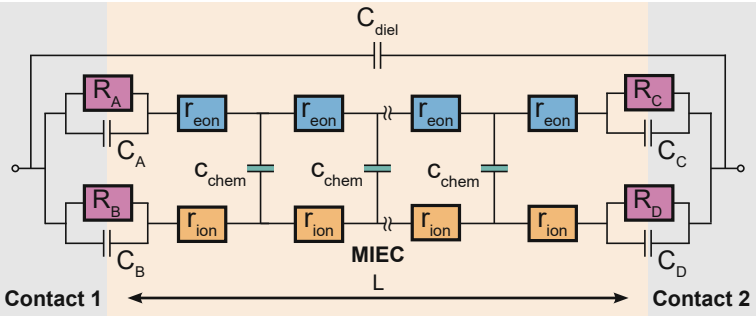

Figure 2.1: General one-dimensional transmission line model for the transport of mass and charge across a mixed ionic and electronic conductor (MIEC) slab of area and thickness . The circuit consists of two parallel resistive rails for electronic and ionic transport, coupled by chemical capacitors. Two different contacts define the terminal impedances for ions and electrons. The bulk dielectric capacitance of the MIEC is connected in parallel to the transmission line.

The general transmission line in Figure 2.1 considers two contact interfaces with each two terminal impedances that can be either partly transmissive (non-blocking, finite) or fully blocking ( ) towards ions and electrons. By considering the resulting symmetry of the transmission line with regard to its terminal elements, three general circuit types can be defined, as shown schematically in Figure 2.2, leaving aside the most general case of four non-blocking terminals. Symmetry considerations only take into account whether the respective rails/contacts are fully blocking or not.

Symmetrical devices (Figure 2.2a) feature two contacts that selectively (fully) block one type of carrier, while being at least partially transmissive for the other (e.g., an MIEC or electrolyte with two metallic, ion-blocking contacts). Asymmetrical devices (Figure 2.2b) exhibit

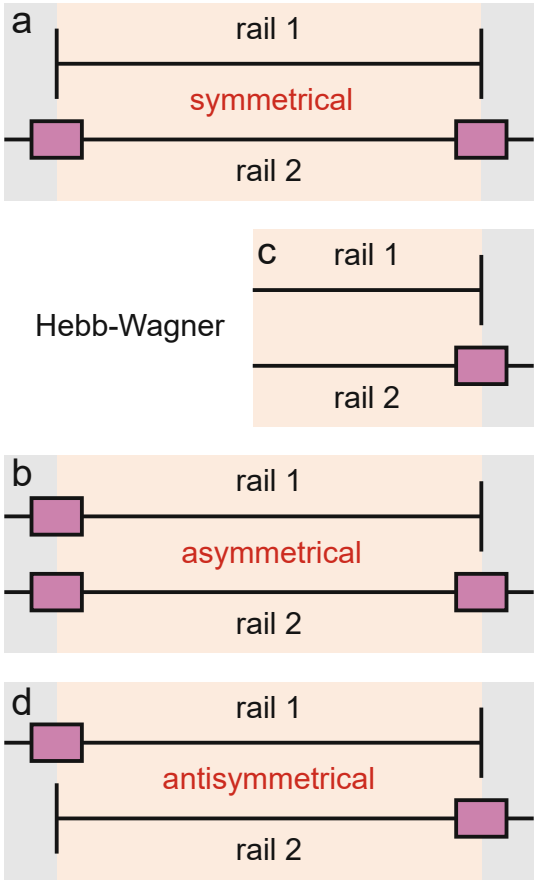

Figure 2.2: Schematic representation of general transmission line types, categorized according to their contact symmetry with respect to ion and electron blocking behavior. Fully blocking and partly transmissive terminals are represented by vertical lines and rectangular boxes, respectively. **(a)** Symmetrical contacts - both contacts are fully blocking towards one and partly transmissive for the other charge carrier. **(b)** Non-ideal Hebb-Wagner geometry, corresponding to half of (a). **(c)** Asymmetrical contacts - One contact is at least partly transmissive for both charge carriers, while the other is fully blocking towards either ions or electrons. **(d)** Antisymmetrical contacts - contacts with opposite blocking behavior. Ions and electrons are blocked at opposite sides of the MIEC sample.

one contact that is at least partially transmissive for both ions and electrons, while the second contact is fully blocking towards either ions or electrons (e.g., non-ideal AC Hebb-Wagner setups or SOFC electrodes).[62–65] In the specific case that the first contact is fully transmissive for both carriers (both 0), the asymmetrical and symmetrical transmission lines are equivalent, which can be rationalized by dividing the symmetrical circuit in Figure 2.2a in half (see Figure 2.2c). Finally, antisymmetrical devices are charaterized by two contacts with opposite blocking behavior, such that ions and electrons are each blocked at opposite sides of the sample (e.g., battery intercalation electrodes).

In this contribution, we provide a practical guide for applying the transmission line model to a wide range of measuring geometries and devices commonly encountered in solid-state electrochemical research, including batteries, solid-oxide cells and symmetrical two-electrode

setups for the characterization of MIECs and solid electrolytes. We provide specific application examples from current research and discuss the limitations of approaches that rely on traditional Warburg elements by relating them back to the transmission line. Furthermore, we emphasize the close relationship between different types of MIEC devices and show how minor experimental adjustments transform the transmission line from one device type to another. Thus, our work is aimed at improving the intuitive understanding of all MIEC impedance spectra and providing a practical approach for the derivation of tailored equivalent circuits for any specific experimental situation.

2.2 Solid-State Diffusion and Warburg Elements

2.2.1 Basic Circuit Elements and Ambipolar Transport

According to the transmission line model, three parameters describe the bulk properties of an MIEC - the chemical capacitance , the ionic conductivity , and the electronic conductivity . The electronic and ionic conductivities can each be quantified by a mobility and a concentration of mobile charge carriers of charge number according to

(2.2)

It is often convenient to consider concentrations and mobilities on a defect level, e.g., vacancies for ions.

The volume-specific chemical capacitance is defined as[58,60]

$$\frac{}{} \quad {}^{2}\,{}^{2}\,\frac{}{} \quad {}^{1} \tag{2.3}$$

where is the chemical potential of the relevant atomic species , is the charge number of the corresponding ion, and denotes the sample volume. For example, in a mixed conducting oxide, where 2, the chemical capacitance is related to the oxygen chemical potential via

$$4\,{}^{2}\,\frac{}{} \quad {}^{1} \tag{2.4}$$

Phenomenologically speaking, the chemical capacitance reflects the material's capacity to store charge by varying its stoichiometry. For example, when oxygen ions are incorporated from the electrolyte into an SOEC anode material, they can either move through the electrode and leave it at the surface as molecular oxygen (with electrons entering the current collector) or stay in the anode and thereby increase the oxygen content of the material.[53,66] Due to charge neutrality, also in the second case electrons have to be transferred to the current collector, and thus an electrical current flows through the external circuit.

For LIB electrode materials, the chemical capacitance

$$^{2}\ \frac{\quad}{\quad}\ ^{1} \tag{2.5}$$

is equivalent to the differential capacity (or •).[51,52] It describes the thermodynamics of Li insertion, consisting of Li^{+} insertion from the electrolyte and the compensating electron transfer from the current collector.

Obviously, on a phenomenological level, neutral atoms (either oxygen or lithium in the examples above) have to move in an MIEC to finally change its composition. This is realized by an electroneutral combined motion of ions and electrons, called ambipolar or chemical transport. This ambipolar transport can be quantified by two ambipolar properties - the ambipolar conductivity ˜ and the ambipolar (or chemical) diffusion coefficient . The ambipolar conductivity

$$\tilde{\ }\ \frac{\quad}{\quad} \tag{2.6}$$

relates the particle flux density of the atoms (and thus also of the corresponding ions) to the chemical potential of atoms (e.g., or) via

$$\frac{\tilde{\ }}{^{2}\ _{2}} \tag{2.7}$$

This property is decisive, for example, for quantifying a steady-state flux across an MIEC.

The chemical diffusion coefficient describes the time dependence of stoichiometry changes according to Fick's law of diffusion

(2.8)

The chemical diffusion coefficient and the ambipolar conductivity are related via the chemical capacitance[67] according to

$$\frac{\tilde{\ }}{\quad} \tag{2.9}$$

Hence, material changes that increase both ˜ and may finally leave unperturbed.

Assuming a one-dimensional geometry, i.e., transport across an MIEC slab of area and thickness , we thus find

$$\frac{^{2}}{\quad}\ \frac{^{2}}{} \tag{2.10}$$

with the time constant of stoichiometry change

(2.11)

or

$$\frac{2}{\tilde{}} \tag{2.12}$$

2.2.2 Warburg Elements

The impedance of diffusion processes has traditionally been accounted for in equivalent circuits by so-called Warburg elements. By definition, these circuit elements consider concentration gradients as the only driving force for mass transport. Thus, electrical potential gradients are neglected and Equation (2.1) is reduced to Fick's first law of diffusion, which can then be solved analytically for the appropriate boundary conditions and expressed as a current density to derive an impedance expression. By variation of the boundary conditions, three different cases result: semi-infinite diffusion, finite-length diffusion and finite-space diffusion. In the following, we briefly summarize the three different Warburg elements, their impedance expressions and their equivalent circuit forms.

Semi-infinite diffusion considers the diffusion of particles from an infinite distance towards a transmissive boundary. In practice, this means that the sample thickness is large enough, or the diffusional resistance is high enough, for spatial limitations not to become relevant within the low-end frequency range of the impedance measurement. The corresponding impedance expression can be derived as[68]

$$\frac{}{=} \quad \frac{}{=} \tag{2.13}$$

with the Warburg coefficient (see below). According to Equation (2.7), the impedance response of semi-infinite diffusion is characterized by a constant -45° phase shift, resulting in a straight line at an angle of 45° in a Nyquist plot, as shown in Figure 2.3a, down to the lowest frequencies. As a result, the Warburg impedance can also be written as a constant phase element (CPE) according to

$$\frac{1}{} \tag{2.14}$$

with = 1/2 and

$$\frac{}{2} \quad 1 \tag{2.15}$$

with containing differential resistive (, real) and capacitive (, imaginary) impedance contributions. More explicitly, such a constant phase element can be expressed as a semi-infinite transmission line of differential resistors and capacitors , as shown in Figure 2.3a, with

$$\frac{}{} \tag{2.16}$$

and thus (cf. telegraph equations)

$$\frac{}{} \tag{2.17}$$

The Warburg impedance is not specific to ion diffusion in a solid, but common to a wide range of diffusion processes, including gaseous diffusion of neutral O_2 towards an absorbing boundary or pore diffusion of Li^+ through a porous LIB electrode. Although the general form of the impedance expressions and transmission line is the same for all cases of semi-infinite diffusion, the physical meaning of the capacitors and resistors depends on the specific context. For example, for the case of concentration-driven ion diffusion through an MIEC (0), we can identify the circuit elements of the transmission line as the incremental ionic resistances and chemical capacitances by comparison to Figure 2.1. Using Equations (2.10), (2.11), (2.16), and (2.17), the Warburg coefficient can then be expressed as

$$\frac{1}{2} \tag{2.18}$$

and the parameter is given by

$$\tag{2.19}$$

Both the resistive and capacitive contributions to are frequency-dependent for the entire frequency range.

When the sample is thin enough, or the diffusional resistance low enough, for spatial limitations to become relevant within the low-end frequency range of the impedance measurement, boundary conditions need to be considered for both sides of the sample. For the case that both boundaries are transmissive for mass transport, the limiting impedance for 0 is real and corresponds to the total diffusional resistance (e.g., for concentration-driven ion diffusion through an MIEC). Thus, in the low-frequency limit, the impedance is independent of frequency. This situation is often referred to as finite-length diffusion (see Figure 2.3b), and its frequency-dependent impedance response is given by

$$\tag{2.20}$$

The corresponding Warburg element is labelled Warburg short ( ) and is equivalent to the transmission line shown in Figure 2.3b.[69]

If only one boundary is transmissive and the other is reflective towards mass transport, the limiting impedance for 0 is purely capacitive with a real offset corresponding to •3, meaning that only the capacitive part of the impedance is frequency dependent in the low-frequency limit.[56] This situation is referred to as finite-space diffusion and results in

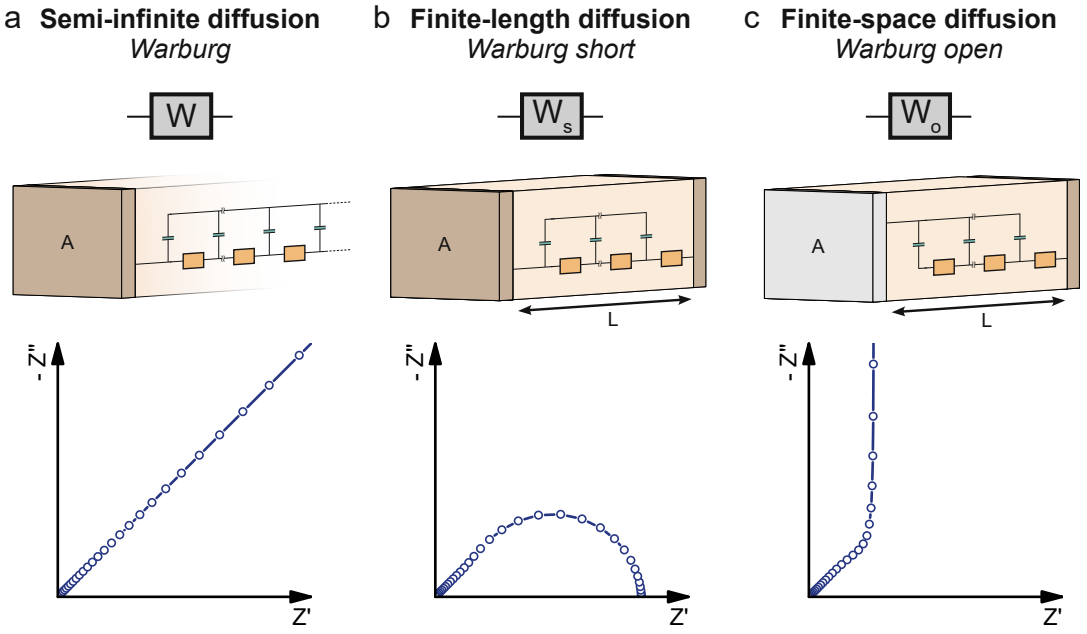

Figure 2.3: Different Warburg elements, their equivalent transmission lines, and their impedance responses, describing the impedance of concentration-driven diffusion for different boundary conditions. **(a)** Semi-infinite diffusion (Warburg). **(b)** Finite-length diffusion (Warburg short). **(c)** Finite-space diffusion (Warburg open).

the impedance expression

(2.21)

The corresponding equivalent circuit element is labelled Warburg open ( ), and its transmission line representation is shown in Figure 2.3c.[69] In contrast to , and allow the simultaneous extraction of the resistive and capacitive transport properties from impedance spectra, due to their different frequency-dependences at low-frequencies.[56]

In the following, the general transmission line from Figure 2.1 will be applied to a variety of different measurement setups involving MIECs and electrolytes. Wherever appropriate, references will be made to the Warburg elements presented above, highlighting their relation to the general MIEC transmission line, but also their limitations.

2.3 Symmetrical Measurements

Symmetrical impedance measurements on electrolytes and MIECs constitute the most simple class of measurements that can be rationalized from a transmission line perspective. For their interpretation, it is usually enough to consider the analytical expression given by Lai and Haile for a symmetrical transmission line with and ,[54] which is less cumbersome than the general expression for four different terminals (see Appendix).

2.3.1 Electrolytes

First, let us consider symmetrical impedance measurements on ideal electrolytes with negligible electronic conductivity and ion-blocking metal electrodes. The main purpose of such measurements is the characterization of an electrolyte's ionic conductivity. Typical experimental setups include in-plane[70–73] and cross-plane[74,75] measurements on thin films, as well as bulk measurements on single crystals and polycrystals.[76–78] In either case, we consider a slab of electrolyte sandwiched between two identical electronically conducting contacts. Due to the negligible electronic conductivity of the electrolyte ( ), the electronic rail can be discarded including its terminal elements (, 0), and is usually also negligibly small. In consequence, the chemical capacitance that couples the ionic and electronic rails can also be neglected. The corresponding adapted transmission

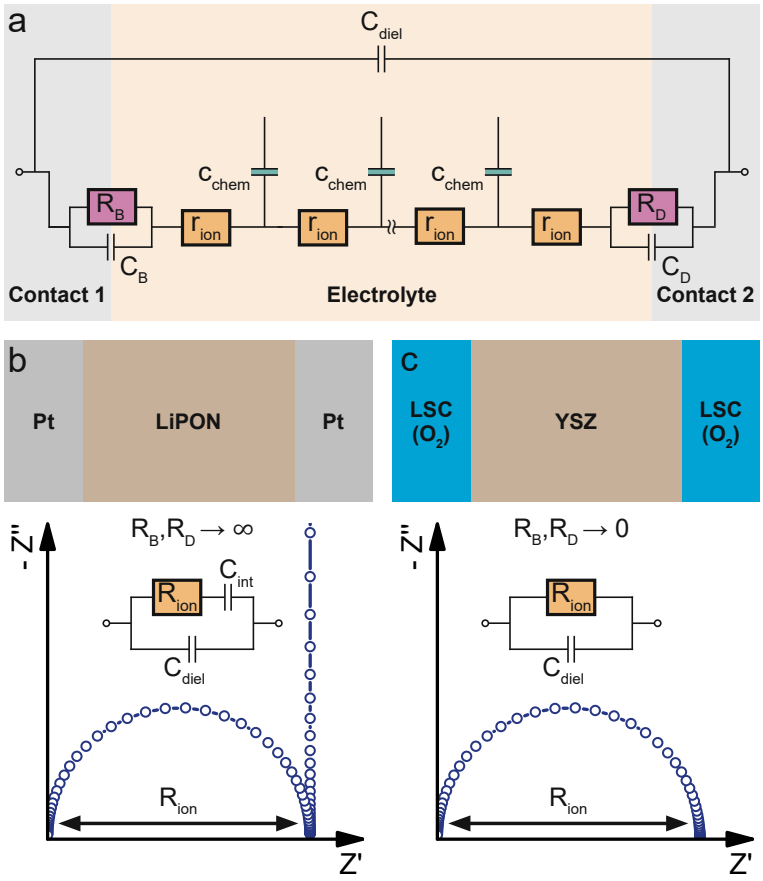

Figure 2.4: (a) Adapted transmission line for an ideal ionic conductor (electrolyte) between two identical contacts. **(b)** Schematic sketch, equivalent circuit and calculated impedance response of lithium phosphorous oxynitride (LiPON) between two ideal (ion-blocking,) Pt contacts. The impedance spectrum consists of a high-frequency semicircle ( ) and a capacitive line at low frequencies. **(c)** Schematic sketch, equivalent circuit and calculated impedance response of yttria-stabilized zirconia (YSZ) between two ideal (fully transmissive, 0) LSC contacts. The impedance spectrum merely consists of a high-frequency semicircle ( ).

line is shown in Figure 2.4a. If the contacts present a blocking boundary to ions from the electrolyte, the interfacial resistances on the ionic rail become infinitely large ( ), leaving only the interfacial capacitances and at the contact interfaces. Experimentally, this could be realized, for example, by contacting a sample of a Li^+ solid electrolyte such as LiPON or LLTO with two Pt electrodes, as shown schematically in Figure 2.4b. Assuming two identical Pt contacts, the transmission line is thus reduced to a simple equivalent circuit consisting only of in parallel to a serial connection of and the total interfacial capacitance ^{1} ^{1} ^{1}.

Since dielectric capacitances are typically much lower than interfacial capacitances ( ), the resulting impedance response ideally consists of a high-frequency semicircle ( ) which transitions into purely capacitive behavior ( ) at lower frequencies. In consequence, the quality of separation between these two regimes depends on the relative magnitudes of and . The former often contains stray capacitances from the experimental setup (for example, from the substrate in in-plane measurements on a thin film) and can therefore deviate from the bulk dielectric capacitance of the electrolyte.[70,72] Further deviations from the ideal impedance spectrum in Figure 2.4b can arise from grain boundaries[70,71] or imperfect ion blockage by the contacts (i.e., finite and).[78]

If the contacts are fully transmissive for ions, the terminal resistances and on the ionic rail in Figure 2.4a become negligible (0), and the capacitances and are bypassed. As a result, the equivalent circuit reduces even further to a simple element, as shown in Figure 2.4c. Experimentally, this situation could occur when a bulk sample of YSZ is sandwiched between two mixed conducting electrodes such as LSC, where the interfacial resistances to the electrolyte are negligible compared to of the electrolyte, and oxygen exchange is reversible at the LSC surface. Additional impedance contributions, such as a finite oxygen exchange resistance at the LSC surface or solid-state transport limitations in LSC, could be considered in series to the equivalent circuit in Figure 2.4c and will be discussed in later sections.

2.3.2 Mixed Ionic and Electronic Conductors

If the electronic and ionic conductivities are both significant, the material classifies as a mixed ionic and electronic conductor (MIEC), and the appropriate impedance model depends on the relative magnitudes of and . In the context of symmetrical devices, we start with the general transmission line in Figure 2.1 for two identical contacts. Assuming metallic contacts that are blocking towards ions and fully transmissive for electrons, the terminal elements on the ionic rail are reduced to an interfacial capacitance (^{1} ^{1} ^{1}), while the elements at the electronic rail ends are replaced by a short circuit, as shown in Figure 2.5a. Since electronic charge carrier mobilities are typically much higher than for ionic carriers, MIECs are often predominantly electronic conductors, such that

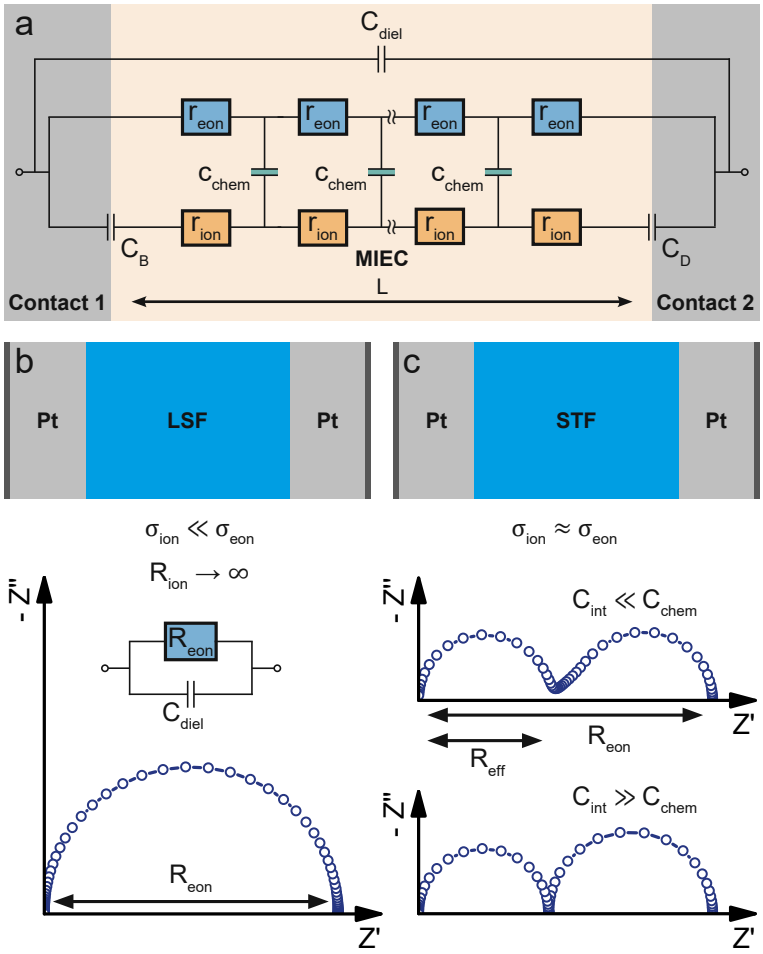

Figure 2.5: (a) Adapted transmission line for a mixed conductor between two ideal (ion-blocking) metal contacts. **(b)** Schematic sketch, equivalent circuit and calculated impedance response of a predominant electronic conductor with , such as LSF, between two ideal Pt contacts. For LSF, the semicircle is beyond the typical measurement range. **(c)** Schematic sketch and calculated impedance response of a mixed conductor with , such as STF at low pO_2, between two ideal Pt contacts.

applies. Examples of such materials include many LIB and SOFC cathode materials such as LCO, LMO, $La_{0.6}Sr_{0.4}FeO_{3-}$ (LSF) or LSC.[51–53,79,80] In some cases, both conductivities are of a similar magnitude ( ), for example, in heavily Tb-doped YSZ,[81] or $Sr(Ti,Fe)O_{3-}$ (STF).[82] Examples of MIECs with predominant ionic conductivity are mostly encountered in the context of non-ideal electrolytes, such as partially reduced LLTO or GDC,[83,84] and often limited to certain stoichiometric regions. An example of an insertion electrode material with predominant ionic conductivity is stoichiometric $Na_3V_2(PO_4)_2F_3$ (NVPF),[85,86] a cathode material for Na-ion batteries.

For symmetrical measurements with electronic contacts on bulk samples, predominant electronic conductivity means that the transmission line can be simplified in analogy to a predominant ionic conductor (electrolyte) by assuming as shown at the example

of LSF between two Pt contacts in Figure 2.5b, resulting in a simple circuit with a corresponding semicircle in the Nyquist plot. This semicircle, however, is often beyond the measured frequency range due to the high electronic conductivity. Hence, four-point DC methods such as van der Pauw measurements are often more suitable for analyzing in thin films of such materials.[87,88] For MIECs with similar ionic and electronic conductivities such as highly Fe-doped STF at low pO_2,[82] the semicircle in the impedance spectrum splits into two separate features that allow a simultaneous extraction of and , as shown in Figure 2.5c. The high frequency semicircle corresponds to the dielectric capacitance coupled to the effective resistance , which is related to the ambipolar (i.e., total) conductivity ˜ according to

$$\frac{1}{} \quad \frac{1}{} \quad \frac{1}{\tilde{}} \qquad (2.22)$$

Depending on the time constant and the frequency range of the measurement, the high-frequency dielectric semicircle may not be fully visible in the impedance spectrum. For example, in the impedance study of STF by Nenning et al.,[82] only its onset can be seen at the highest frequencies. The low-frequency feature either takes the shape of a half-teardrop, similar to a finite-length Warburg element (Warburg short, c.f. Figure 2.3b), or a semicircle, depending on the relative magnitudes of and . In either case, the low frequency axis offset (0) corresponds to , and can then be obtained by comparison with . One example of an MIEC with predominant ionic conductivity is presented by stoichiometric NVPF - a promising cathode material for Na-ion batteries with a low intrinsic electronic (and ionic) conductivity.[85,86] In refs. 85,86, the impedance of stoichiometric NVPF bulk samples are measured with symmetrical metallic contacts. The resulting impedance response resembles that of Figure 2.5c ( ), with a high-frequency dielectric semicircle representing the effective resistance (i.e., the total conductivity) and a low-frequency 45° onset, leading to the conclusion that , and hence .
A more detailed discussion of the characteristics of symmetrical impedance measurements on MIECs with different interfacial blocking selectivities and bulk conductivities can be found in ref. 58 and is beyond the scope of this paper.

Symmetrical impedance measurements with two ionic (i.e., electron blocking) contacts are experimentally much more challenging and therefore less common. Usually such setups consist of a central MIEC sample to be characterized, sandwiched between a double layer of an ion conductor (inner layer = electron blocking layer) and a reservoir electrode (outer layer). The reservoir electrode acts as an elemental source and sink and is therefore required to be a low-impedance electrode with a high chemical capacitance, such as Li metal or a reversible mixed conducting O_2 electrode in the case of Li^+ materials and SOFC materials, respectively. If the ionic contacts to the MIEC are fully blocking towards electrons, the ionic (and ambipolar) conductivity of the MIEC becomes directly accessible by impedance measurements.

Neglecting interfacial resistances, the transmission line from Figure 2.5a can then be adapted by simply moving the interfacial capacitances from the ionic to the electronic rail, as shown in Figure 2.6a.

A possible measurement setup is shown schematically in Figures 2.6b, with the MIEC sandwiched between YSZ and LSC O_2 serving as the reservoir electrode on both sides. If the MIEC is a predominant electronic conductor with , as in the case of LSF, the resistances on the electronic rail can be neglected (0), and the appearance of the

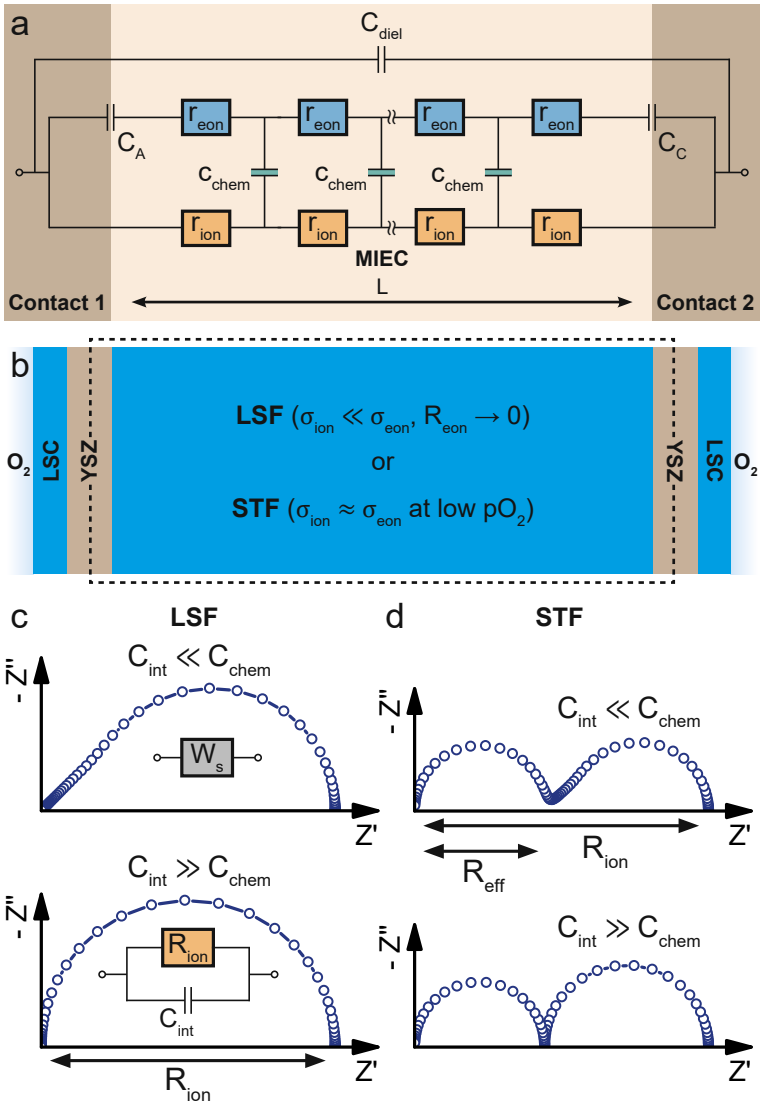

Figure 2.6: **(a)** Adapted transmission line for a mixed conductor between two ideal (electron-blocking) ionic contacts. **(b)** Schematic sketch of a measurement cell consisting of a mixed conductor (LSF or STF) between two YSZ layers and outer LSC O_2 reservoir electrodes. **(c)** Calculated impedance response of the cell (region within dashed line in (b)) for a predominant electronic conductor (LSF,). Depending on the relative magnitudes of ^{1} ^{1} ^{1}, the impedance spectrum corresponds to either a ( ) or a ( ) element. **(d)** Calculated impedance response of the cell for a mixed conductor with (STF at low pO_2).

impedance spectrum depends on the relative magnitudes of and ^{1} ^{1} ^{1}. For large chemical capacitances ( ), the interfacial capacitances can be neglected, and the resulting transmission line and impedance spectrum are identical to the finite-length Warburg element in Figure 2.3b. The impedance expression (2.20) is even obtained analytically from the general transmission line by inserting the appropriate boundary conditions (, 0, 0), which highlights the consistency of the transmission line with the underlying differential transport equations. For small values of ( ), the half-teardrop shape of the element transforms into a semicircle corresponding to a simple circuit.

As already seen for symmetrical measurements with electronic contacts (Figure 2.5), the impedance spectrum splits into two separate features for mixed conductors with , such as STF at low pO_2, with the high-frequency semicircle corresponding to coupled to and the low-frequency axis intercept (0) being the total ionic resistance . Again, the shape of the low-frequency feature (semicircle or half-teardrop) depends on the relative magnitudes of and as indicated in Figure 2.6c. Since the dielectric semicircle is often merely observed as a high-frequency offset ( ) in real impedance spectra, we neglect in the following for better overview.

2.4 Asymmetrical Measurements

When the two contact interfaces can be considered neither symmetrical (e.g., both blocking towards ions and transmissive towards electrons) nor antisymmetrical (oppositely blocking/transmissive towards ions and electrons), the corresponding measurements are classified as asymmetrical. This class of impedance measurements on MIECs is potentially the most complex, as it requires the explicit consideration of finite and in combination with various interfacial resistances and capacitances. Accordingly, such measurements reveal the full potential of the transmission line model, which allows an intuitive description in the form of an equivalent circuit, while still being physically exact in terms of the Nernst-Planck equation (2.1). Furthermore, asymmetrical measurement situations represent the transition region between symmetrical and antisymmetrical devices, as discussed in more detail at the end of this section.

2.4.1 Solid Oxide Fuel and Electrolyzer Cells

SOFC and SOEC electrodes represent perhaps the most prominent class of MIEC devices involving asymmetrical contacts. In an SOFC cathode, for example, the active material is in contact with the current collector and O_2 atmosphere on one side and the O^{2-}-conducting electrolyte (e.g., YSZ) on the other side, as shown in Figure 2.7a. In the corresponding transmission line, the electronic rail ends at the MIEC/electrolyte interface and represents the

only blocking terminal, meaning that , and starting from the general circuit in Figure 2.1, the terminal element can thus be replaced by a simple capacitance . The remaining terminal resistances correspond to the electronic contact resistance ( ), the surface exchange resistance for oxygen incorporation and release ( ) and the interfacial ionic resistance ( ). SOFC and SOEC electrodes may differ strongly in terms of thickness (thin films versus thick layers), porosity (dense thin films versus porous thick layers) and materials (LSF, LSC, $La_{0.8}Sr_{0.2}MnO_{3-}$ (LSM), etc.). Not surprisingly, a large variety of cases is therefore encountered, many requiring an extension of the one-dimensional model due to porosity. In some cases, interfacial resistances are negligible, while in others they dominate and transport resistances can be neglected. For the sake of simplicity, we restrict our considerations to one-dimensional geometries (i.e., dense electrodes) with negligible interfacial ionic resistance. Hence, the impedance is limited by either surface exchange ( ) or bulk transport (,), and we neglect and together with the corresponding interfacial capacitances and replace them by a short circuit. Furthermore, many electrode materials usually exhibit a comparatively large chemical capacitance under common operating conditions, such that can also be neglected in a first approximation. The resulting equivalent circuit is shown in Figure 2.7b.

In the case of a predominant electronic conductor such as LSF, the resistances on the electronic rail can be neglected (0), and the electrode's impedance response falls into one of three categories, as shown in Figure 2.7c. In the case that the bulk transport resistance is significantly higher than the surface exchange resistance (bulk-limited electrode), can be neglected and replaced by a short circuit. In the limit of negligible and , the resulting impedance response corresponds to a finite-length Warburg element (Figure 2.3b). It is worth pointing out, however, that the electronic contact provided by the current collector (i.e., short circuit to the MIEC electronic rail) in Figure 2.7b is not contained in the transmission line representation of (Figure 2.3b), which is a two-terminal circuit element and therefore does not consider separate contact terminals for ionic and electronic transport. Only in the limiting case of 0, the two circuits are identical, since Figure 2.7b is then equivalent to the transmission line in Figure 2.3b divided in half (cf. Figure 2.2c). The crucial difference between the traditional element and a bulk-limited SOFC electrode becomes visible once can no longer be neglected. While the traditional element would imply a simple serial + connection with a corresponding real-axis offset in the Nyquist plot, the physically more accurate transmission line in Figure 2.7b predicts a merging of the surface resistance into the bulk transport feature, as shown in Figure 2.7c (surface + bulk) by the emerging semicircle. An experimental example of such a mixed surface-bulk-limited SOFC electrode can be found in ref. 89, where the partial pressure dependence and rate limiting steps of the oxygen reduction kinetics on LSM thin films is examined. If the surface

exchange resistance dominates and bulk transport resistances can be neglected (0), a simple semicircle results, which is observed, for example, for many SOFC thin film electrodes at high operating temperatures.[65,79,80,90,91]

For balanced mixed conductors with similar and , such as STF at low PO_2,[82] the consideration of electronic bulk resistances requires using the full transmission line shown in Figure 2.7b. As shown in the Nyquist plot in Figure 2.7d, the impedance response is shifted by a real axis offset corresponding to (Equation (2.13)) if the bulk transport resistances cannot be neglected. Only in the surface-limited case, the impedance response is equivalent to that of a predominant electronic conductor, as it transforms into a simple semicircle. Please note that the above discussion only considers the impedance response of the isolated

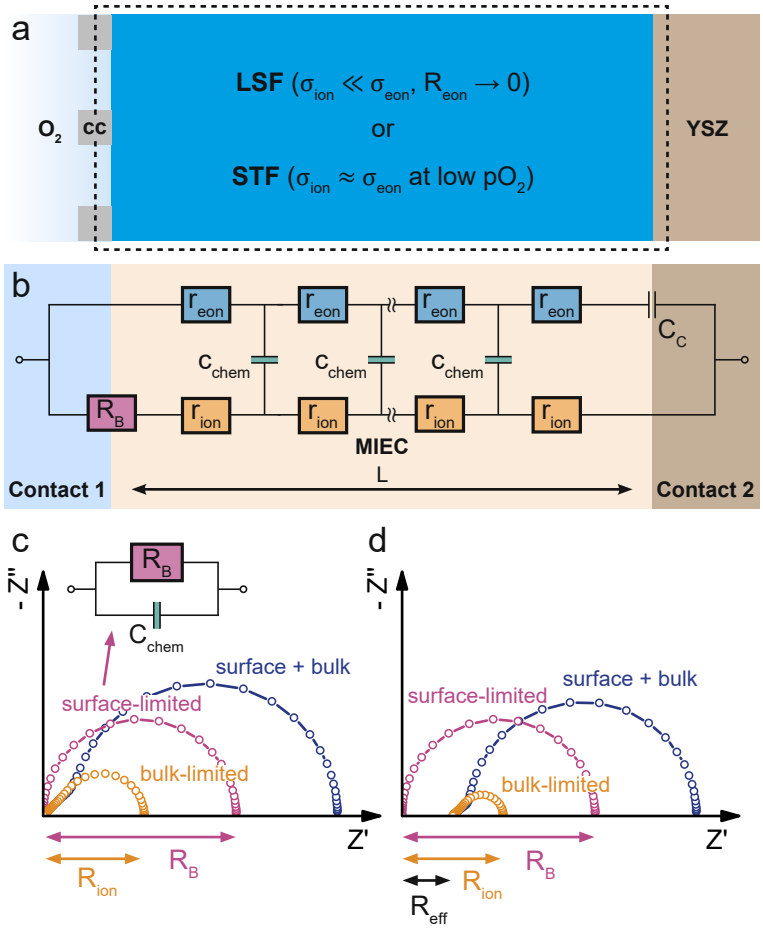

Figure 2.7: (a) Schematic sketch of a dense SOFC electrode consisting of an MIEC on a YSZ electrolyte, with a current collector (cc) contacting the MIEC on the O_2-exposed side. **(b)** Adapted transmission line for the SOFC electrode in (a). The interfacial resistances and (cf. Figure 2.1), together with their corresponding capacitances, as well as have been neglected. **(c)** Calculated impedance response of the SOFC electrode (region within dashed line in (a)) with a predominant electronic conductor (LSF,) for different limiting cases. **(d)** Calculated impedance response of the SOFC electrode with a mixed conductor (STF at low pO_2,) for different limiting cases.

MIEC sample and its interfaces, as marked by the dashed line in 2.7a. In reality, impedance spectra from two-electrode measurements usually contain additional contributions from, for example, the electrolyte and the counter electrode.[79] However, these contributions can simply be considered in series to the MIEC impedance. Especially the electrolyte resistance is often well separated in the Nyquist plot, due to different time constants of the corresponding transport processes. Thus, their inclusion in the equivalent circuit is straightforward.

2.4.2 From SOFC to Battery Electrodes

A highly interesting transition occurs when the oxygen exchange reaction at an SOFC electrode surface is more and more blocked, as shown in Figure 2.8. Starting from a bulk-limited electrode (= 0) of a predominant electronic conductor (0), such as LSF, the

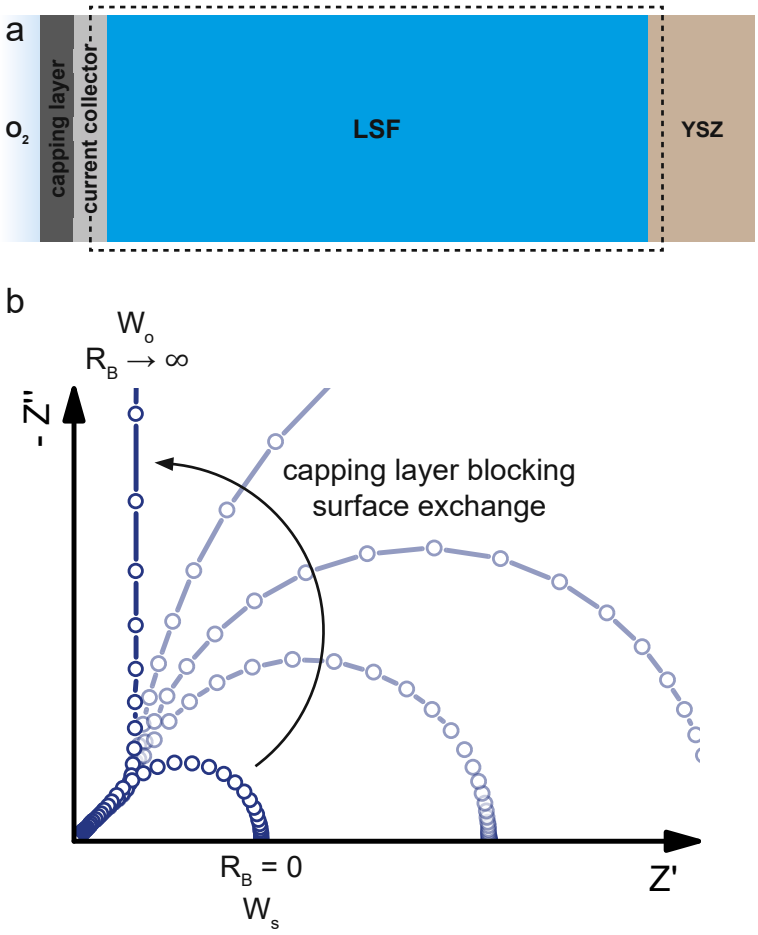

Figure 2.8: (a) Schematic sketch of a dense SOFC electrode consisting of a predominant electronic conductor (LSF,) on a YSZ electrolyte contacted by a current collector on the O_2-exposed side. A capping layer blocks the surface exchange reaction between the O_2 atmosphere and the LSF surface. **(b)** Evolution of the calculated impedance response of the dashed region in (a) for an increasing surface exchange resistance due to the capping layer, showing the gradual transition from a to a type behavior.

impedance spectrum initially corresponds to that of a finite-length Warburg element ( ) characterized by and (c.f. Figure 2.7c). When the surface exchange with the surrounding atmosphere, that constitutes the connection to the ionic (i.e., mass transport) rail of the MIEC transmission line in Figure 2.7b, is partially blocked, increases. This can be achieved, for example, by covering the current collector and MIEC with a dense capping layer of negligible ionic conductivity. As a consequence, the impedance response transitions away from the simple element into a mixed regime, where both and are relevant. While the high frequency 45° part of the spectrum remains nearly unchanged, the low frequency end transforms into a more and more separate semicircle dominated by the growing . If the capping layer is perfectly blocking towards mass transport ( ), the semicircle becomes infinitely large, such that it effectively transforms into a capacitor with a capacitance . For the transmission line in Figure 2.7b, this implies that the connection between the left contact and the ionic rail of the MIEC can be considered as fully disrupted. Thus the resulting circuit is equivalent to the transmission line representation of a finite-space Warburg element (, Figure 2.3c).

In terms of equivalent circuits, blocking the surface exchange reaction of an SOFC electrode corresponds to a transition from (quasi) finite-length ( ) to finite-space ( ) diffusion, with the intermediate region lying beyond the applicability of classical two-terminal Warburg elements. This emphasizes once more the consistency of the general transmission line model with the specific solutions to Fick's first law of diffusion for the respective boundary conditions, and shows that the separate consideration of ionic and electronic transport across the contact interfaces is required to accurately describe realistic measurement setups (e.g., an SOFC electrode with a finite, nonzero). In terms of device functionality, this transition constitutes the transformation of an SOFC electrode into an oxygen-ion battery electrode, which can store charge based on the principle of coulometric titration.[66,92]

2.5 Antisymmetrical Measurements

When an MIEC is contacted by an ideal ionic conductor on one side and by an ideal electronic conductor on the other, neither ions nor electrons can be transferred across both interfaces, leading to a purely capacitive behavior for 0. The most simple case of such a measurement was already discussed above as the limiting case in the transition of a (simplified) SOFC electrode to a battery electrode. Due to the opposite nature of the contact interfaces in terms of their ion and electron blocking behavior, we refer to this class of measurements as antisymmetrical. In such a situation, the only way a direct current through the external circuit can be charge-balanced is by filling or emptying the chemical capacitance of the material, depending on the current direction. Thus, antisymmetrical MIEC devices generally constitute the class of chemical capacitors, i.e., batteries.

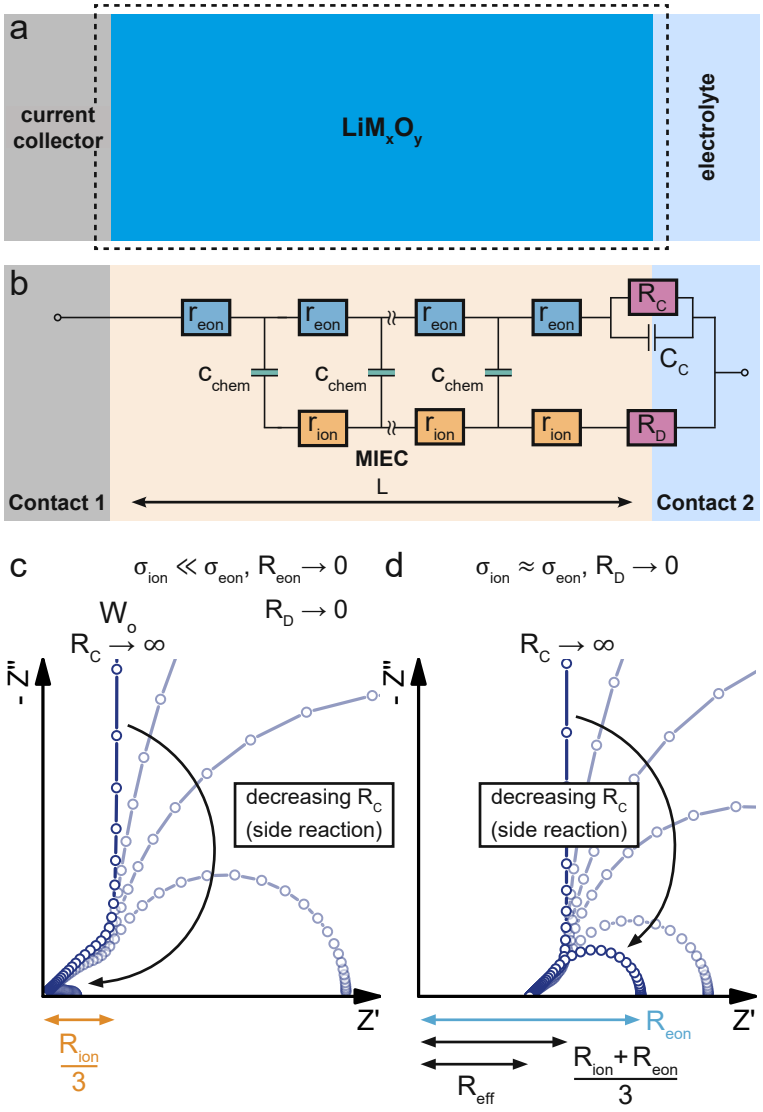

FIGURE 2.9: (a) Schematic sketch of a dense Li insertion electrode consisting of an MIEC of the general composition LiM_xO_y between an ideal (ion-blocking) current collector and an electrolyte. **(b)** Adapted transmission line for the insertion electrode shown in (a). A finite resistance is considered between the MIEC electronic rail and the electrolyte to account for possible side reactions with the electrolyte. **(c)** Impact of a decreasing on the calculated impedance response of a Li insertion electrode for a predominant electronic conductor ( ) with a negligible charge-transfer resistance . **(d)** Impact of a decreasing on the calculated impedance response of a Li insertion electrode for a mixed conductor ( ) with a negligible charge-transfer resistance .

For a specific discussion of insertion electrodes, we consider a mixed conducting LIB cathode material LiM_xO_y contacted by an electronic conductor (current collector) on one side and an ionic conductor (electrolyte) on the other, as shown in Figure 2.9a. The general transmission line in Figure 2.1 can then be simplified by assuming an ideal electronic contact of the current collector to the MIEC (= 0), which is perfectly blocking towards ions ( ), and neglecting the interfacial capacitance . Furthermore, we consider the double-layer

capacitance at the MIEC/electrolyte interface to be located at the electronic rail terminal, such that can also be neglected. To discuss the effect of possible side reactions with the electrolyte, a finite (though large) is kept in the circuit. The resulting simplified transmission line is shown in Figure 2.9b. Since our symmetry considerations only distinguish fully blocking and partially transmissive, this circuit is only strictly within the antisymmetrical category for .

2.5.1 Bulk Transport and Side Reactions

In a first step, we discuss the influence of bulk transport resistances and electrochemical side reactions with the electrolyte on a battery electrode's impedance response. For this purpose, we set the charge-transfer resistance and the double layer capacitance to zero and consider only changes in and . Under common operating conditions, LIB cathode materials are usually predominant electronic conductors with , and the assumption of negligible electronic bulk resistance (= 0) is therefore justified in most cases. If the electron transfer between MIEC and electrolyte is perfectly blocked (i.e., no electrochemical side reactions such as electrolyte oxidation or reactions with impurities,) the resulting transmission line corresponds to that of a finite-space Warburg element (, Figure 2.3c). The Nyquist plot of features a high-frequency semi-infinite (45°) and a low-frequency capacitive (90°) regime, with •3 being the real part and 1• the imaginary part of the impedance in the low-frequency limit, as shown in Figure 2.9c. This exactly corresponds to the limiting impedance of the capped SOFC electrode in Figure 2.8 with .

In reality, all battery electrodes exhibit a finite , and the validity of the assumption often merely depends on the low-frequency limit of the measurement. As demonstrated in Figure 2.9c, a decrease of causes the capacitive low-frequency end of the spectrum to bend downwards into a semicircle that reaches the real axis for 0. In practice, properly assembled battery cells still exhibit a very high , such that only a minor bending can be observed within common frequency ranges.[52] Theoretically, the cell tends towards a short circuit for 0, as we have assumed 0.

For a finite , the transmission line moves beyond the assumptions and applicability of the classical element and transforms into a more general ambipolar diffusion element with reflective boundary conditions. The corresponding impedance response is shown in Figure 2.9d. For , it is closely related to that of , with a real axis offset (Equation (2.22)) and a low-frequency limiting real part •3. Please note that the transition from Figure 2.9c to 2.9d is fully analogous to the transition from Figure 2.6c to 2.6d. In both cases, the transmission line allows a straightforward generalization of the Warburg elements to include the presence of electrical potential gradients (i.e., nonzero electronic resistance). In practice, the bulk transport in battery or solid-oxide electrodes is most often limited by ion conduction, and electronic resistances rarely need to be considered. Even in

phosphate-based Li insertion materials such as LFP, where the isolating PO_4^{3-} groups lead to an intrinsically poor electronic conductivity, ionic conductivities are still significantly lower,[93,94] and no substantial high-frequency offset is observed in impedance spectra.[95–98] Also for NVPF Na-insertion electrodes (near the stoichiometric composition), SOC-dependent impedance measurements do not show a significant variation of the high-frequency offset, despite severe diffusion limitations (45° Warburg feature) at low frequencies.[99] This suggests that NVPF transitions into a predominant electronic conductor upon charging, already at low SOC, such that 0 can again be assumed. In the context of oxygen-ion batteries, STF electrodes may exhibit a bulk impedance response similar to Figure 2.9d ( ) at high oxygen vacancy concentrations, due to its observed mixed conductivity ( ) under reducing conditions.[82]

2.5.2 Charge Transfer and the Validity of Randles' Circuit

Having established the impact of bulk transport resistances and side reactions on the impedance spectrum, we consider the full impedance model of a dense Li insertion electrode. To allow a better comparison with other models found in the literature, we rename the side-reaction ( ) and charge-transfer ( ) resistances appropriately. Furthermore, we add a high-frequency offset resistance in series to the transmission line to account for the sum of ohmic contributions from the electrolyte and other cell components, as shown in Figure 2.10a.

The full circuit in Figure 2.10a results in an additional high-frequency offset corresponding to (Equation (2.22)), a semicircle ( ) followed by a 45° regime in the mid-frequency region, and finally a capacitive line at the lowest frequencies. If can be neglected (0), as in the case of a predominant electronic conductor with , the electronic rail can be replaced by a short circuit. The remaining part of the transmission line (Figure 2.10b) then corresponds to a serial connection of a element (cf. Figure 2.3c) and in parallel to the element, with still in series to everything else. The resulting simplified equivalent circuit (Figure 2.10c) differs from the original Randles' circuit (Figure 2.10d) merely by the presence of a finite side-reaction resistance in parallel to . Thus, for 0 and , the transmission line in Figure 2.10a is identical to Randles' circuit and provides a physical justification for the connectivity of its constituent elements. In particular, the consistency of the transmission line with Randles' circuit requires placing on the electronic rather than the ionic rail terminal. If was placed on the ionic rail, it would end up in parallel to (but in series to) in the simplified circuits (Figure 2.10c-d). Furthermore, these considerations show that a finite can be accounted for by simply adding it in parallel to in Randles' circuit, without needing to use the full transmission line for impedance fits. Such a circuit was successfully applied to Li insertion electrodes, for example, in ref. 52.

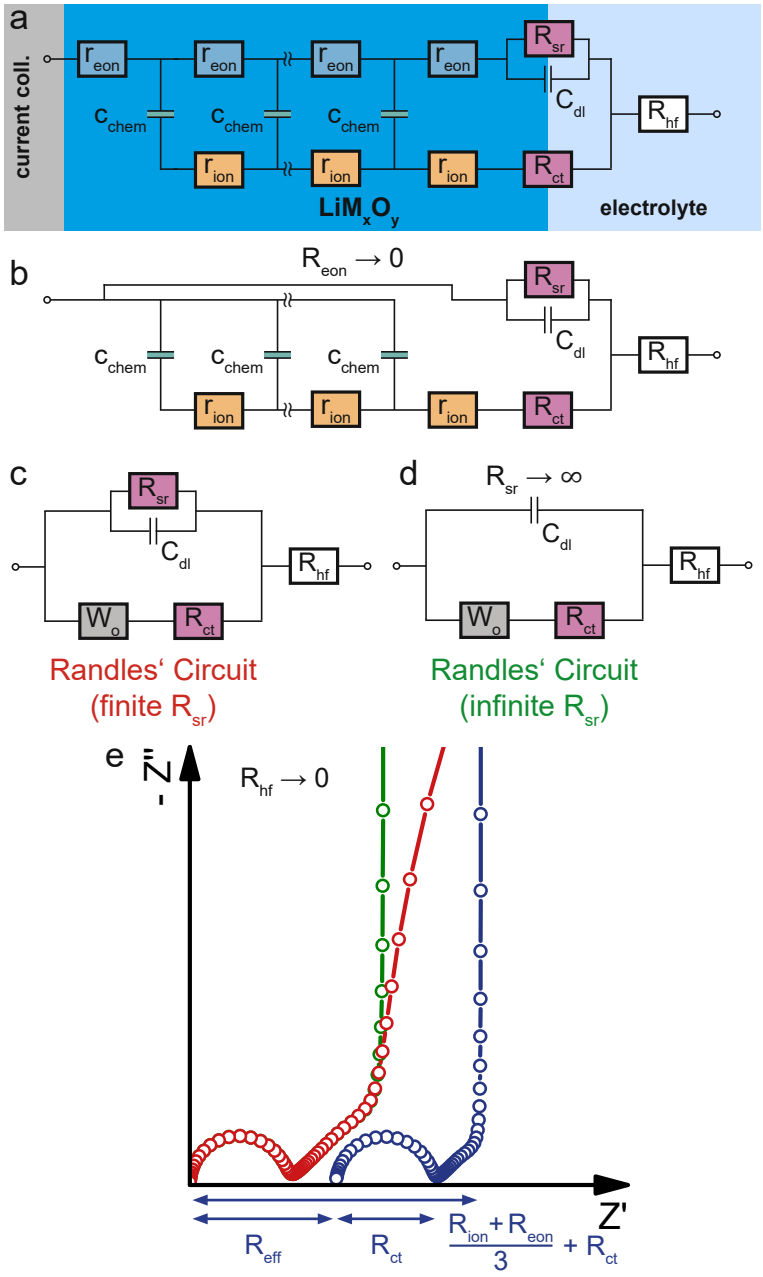

Figure 2.10: (a) Adapted transmission line for a dense Li insertion electrode with , , and . A high-frequency offset resistance has been added in series to account for ohmic impedance contributions from the electrolyte and other cell components. **(b)** Simplified transmission line for a predominant electronic conductor with 0 ( ). The electronic rail is replaced by a short circuit, allowing the replacement of the transmission line by a element. **(c)** Randles' circuit with a finite in parallel to . **(d)** Classical Randles' circuit, assuming an infinite . **(e)** Calculated impedance responses of circuits (a) ( ), (c), and (d), where has been neglected in all cases.

2.6 Conclusion

The impedance of dense mixed ionic and electronic conductors (MIECs) is accurately described by a one-dimensional transmission line consisting of two resistive rails for ion and electron conduction, coupled by chemical capacitors. The resulting circuit is physically exact in terms of the Nernst-Planck equation and provides a highly intuitive and practical approach to understanding and evaluating the impedance responses of various MIEC devices. Four terminal elements at the rail ends allow a tailored adaptation of the general transmission line to specific measurement configurations, which can be classified as symmetrical (e.g., setups for the characterization of bulk properties), asymmetrical (e.g., SOFC electrodes) and antisymmetrical (battery electrodes) with respect to the ion and electron blocking behavior of the two contacts.

Beside providing a universal starting point for the intuitive derivation of tailored, physically exact impedance models, the general transmission line is also consistent with classical Warburg elements (derived from Fick's law of diffusion) and the intuitively constructed Randles' circuit under the corresponding boundary conditions. By moving beyond these boundary conditions, the transmission line model provides several key insights:

1. The general transmission line is consistent with the classical finite Warburg elements and , which are derived from Fick's law of diffusion for negligible electrical potential gradients ( ), under the corresponding boundary conditions.

2. The resistive and capacitive circuit elements in the corresponding transmission lines of the Warburg elements can be identified as the incremental ionic resistance ( ) and the incremental chemical capacitance ( ), respectively.

3. The general transmission line provides an extension of these Warburg elements for MIECs with finite (e.g.,) by considering a resistive rail for electronic transport with .

4. The impedance response of a bulk-limited SOFC electrode with negligible surface resistances corresponds to a finite-length Warburg element ( ), due to the symmetry of the transmission line (cf. Figure 2.2a and 2.2c). For a non-negligble surface exchange resistance, neither nor a serial connection of and the surface exchange resistance appropriately describes the electrode impedance. Only the full transmission line allows a physically meaningful interpretation of the corresponding impedance spectra.

5. The transmission line is consistent with Randles' circuit for , under the condition that is placed on the electronic rather than the ionic rail terminal. Thus, for the given boundary conditions, Randles' circuit can be considered as physically exact in terms of the Nernst-Planck equation.

6. Within Randles' circuit, a finite side-reaction resistance can be placed in parallel to to consider, for example, electrolyte oxidation or reactions with impurities in the electrolyte, while remaining fully consistent with the general transmission line.

7. A finite electronic resistance hinders the application of a simple Randles' circuit and causes a serial high-frequency offset 1 1 1 in the impedance spectrum.

2.7 Appendix

The following equations define the impedance response of the full transmission line shown in Figure 2.1, where refer to the impedances of terminals A to D.

$$\mathbf{A}\ \mathbf{B}\ \mathbf{C} \qquad \mathbf{D}\ \mathbf{E} \tag{2.23}$$

$$\mathbf{A}\ 2 \tag{2.24}$$

$$\mathbf{B}\ ^{2}\ 2 \qquad ^{2}\ 2 \tag{2.25}$$

$$\mathbf{C}\ ^{3}\ ^{3}\ 2\ 2 \qquad 2\ 2\ \mathbf{F}\ 3\ 2 \qquad 2\ 2\ \mathbf{F} \tag{2.26}$$

$$\mathbf{D}\ ^{2} \tag{2.27}$$

$$\mathbf{E}\ ^{3}\ 2\ 2 \tag{2.28}$$

$$\mathbf{F} \tag{2.29}$$

(2.30)

(2.31)

(2.32)

3 Mass and Charge Transport in Li_{1-} CoO_2 Thin Films - A Complete Set of Properties and Its Defect Chemical Interpretation

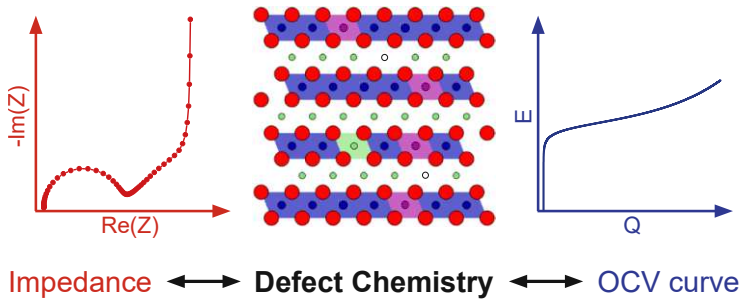

The study presented in this chapter was published in the following article:
Bumberger, A. E.; Steinbach, C.; Ring, J.; Fleig, J. Mass and Charge Transport in Li_{1-} CoO_2 Thin Films - A Complete Set of Properties and Its Defect Chemical Interpretation. *Chemistry of Materials* **2022**, *34*, 10548-10560. DOI: 10.1021/acs.chemmater.2c02614.

3.1 Introduction

With the high demands placed on modern Li-ion batteries with respect to their charging speed and discharge power density, the investigation of Li transport kinetics through the various cell components plays a vital role in optimizing cell performance. However, owing to the morphological and compositional complexities found in porous bulk electrodes, the investigation of their kinetic properties is far from trivial. Measurement approaches range from time-dependent voltage or current measurements, such as the galvanostatic intermittent titration technique,[100–104] to sophisticated transmission line models, taking account of both electrolyte and electrode.[48] However, as pointed out recently by Chueh,[105,106] the transport properties, such as Li diffusion coefficients, deduced from different studies often differ by orders of magnitude.

One of the main reasons for this variance is the fact that several time constants are involved in the time- or frequency-dependent responses of highly porous intercalation electrodes. Moreover, even if extracted from geometrically simple samples such as thin films, the chemical diffusion coefficient of Li ( ) is not the only relevant parameter for the charge and discharge properties of electrode particles. Rather, the kinetics of an individual electrode particle is defined by (i) the interfacial Li exchange reaction with the electrolyte, (ii) the ambipolar conductivity within the mixed conducting electrode material itself, which comprises the ionic and electronic conductivities and , and (iii) the chemical capacitance , as discussed in more detail below. The chemical diffusivity itself is, however, not an elementary property of the electrode material but a composite parameter of ambipolar conductivity and chemical capacitance.[67,107,108] To further complicate things, a battery electrode traverses a broad continuum of operating points or thermodynamic states during every charge/discharge cycle, each being defined by its characteristic Li chemical potential and electrochemical transport parameters. The elucidation of these electrochemical parameters as a function of state-of-charge (SOC) is therefore a notoriously difficult task and has mostly been limited to the evaluation of the chemical diffusion coefficient from the inverse time constant of the observed diffusion processes, without separate consideration of its resistive and capacitive components.[109–115]

It is also frequently overlooked in this context that , which describes the differential variation of Li stoichiometry with the chemical potential, is not only related to the slope of the coulometric titration curve and the energy density but also directly impacts solid-state ambipolar diffusion and hence the power density.[67] Consequently, can be extracted from AC impedance spectra as well as from DC titration curves, and these values should coincide. However, this connection is rarely made, which is mirrored by the context-dependent labels that are used throughout the battery literature to denote the variation of charge with potential. In order to describe the impedance of mixed conducting electrodes, a one-dimensional transmission-line equivalent circuit was suggested by Jamnik and Maier,[54,58–61] giving access not only to but also to the transport properties , , and the interfacial charge-transfer resistance . Applying this model (or simplified versions) to a one-dimensional electrode system, such as a thin-film electrode, should thus enable the analysis of all elementary material parameters and help in understanding the stoichiometry-dependent Li intercalation process into an electrode material. Interestingly, such a transmission-line-based analysis of impedance spectra of mixed conducting thin-film electrodes is quite common in the field of high-temperature solid oxide cells[54,82,87,116] but virtually unknown for thin-film electrodes in Li-ion batteries.

In this contribution, we present a comprehensive impedance study of polycrystalline Li_{1-} CoO_2 (LCO) thin films on Pt for a wide stoichiometry range (0 0 4) that also includes the rarely investigated low-potential region up to 3.9 V versus Li^+/Li, where the

most pronounced changes of the electrochemical properties are observed. Based on these measurements, we discuss three important aspects of Li intercalation into Li_{1-} CoO_2. First, we analyze the variation of , , , and with the Li chemical potential and discuss their relative contributions to the overall electrode kinetics. Second, the role of in AC and DC measurements is discussed and experimentally validated, and its overarching significance for ambipolar transport is considered. Third, we provide a defect chemical perspective on the observed trends of , , , and in terms of Li activity. Special emphasis is thereby put on the rarely investigated SOC region close to full Li stoichiometry,[113] where dilute solution thermodynamics can be applied to describe the electrochemical properties in terms of their dependence on point defect concentrations. All these concepts are herein specified for LCO but are applicable to all battery electrode materials that are based on ion insertion.

3.2 Basic Considerations on C_{chem} and Impedance Models

3.2.1 Chemical Capacitance

There appear to be three separate contexts within which the chemical capacitance[67] is used for describing Li-ion battery electrodes, each using different labels that reflect the purpose at hand. The first and, in studies on porous bulk electrodes, the most widespread use is the monitoring of gradual material changes and phase transitions as a function of cell voltage and cycle number.[117–127] In this context, the chemical capacitance is termed differential capacity, incremental capacity, or • and is almost exclusively obtained via the differentiation of galvanostatic charge curves. Its appearance in impedance spectra is usually not considered, presumably because capacitances in such electrodes are too large to exhibit blocking (finite-space) behavior within reasonable measuring frequencies. This is also reflected in the transmission-line equivalent circuits used to describe porous electrodes. In most cases, they contain no open Warburg element or capacitance in series to the charge-transfer resistance and hence implicitly assume an infinitely large chemical capacitance.[128–131]

The second way chemical capacitances are used in the literature, which is predominant in impedance studies on thin-film electrodes,[109,111,112,132] is as an input parameter for the extraction of diffusion coefficients from the semi-infinite (45°) diffusion regime. These studies still mostly refer to the incremental capacity, although they label it • (or similar) in calculations and recognize it as a parameter that is needed for the calculation of diffusion coefficients from impedance data.[56] However, these reports still treat the chemical capacitance mainly as an empirically derived property of the charge curve rather than an elementary material parameter that relates back to thermodynamics and defect chemistry. This is evidenced by the continued use of the term incremental capacity and the approach of differentiating charge curves adopted from bulk studies. Interestingly, also in the field of Li insertion

thin films, chemical capacitances are barely ever extracted from impedance spectra,[133,134] which is surprising, given that films are typically thin enough to show a finite-space (90°) behavior within the mHz range. Theoretical works on the finite-space diffusion impedance of thin films already refer to a (diffusion- or low-frequency-limiting) *capacitance* rather than a *capacity*,[56,135,136] explicitly recognizing its role as a capacitive element in impedance measurements. However, this perspective does not seem to be adopted by the previously cited studies that apply those theories to battery electrodes.

Finally, the third established context of chemical capacitance is based on an atomistic analysis of the basic relation[58,137]

2 1 (3.1)

which describes the electrochemical Li storage in an electrode with bulk volume (e.g., a dense thin film with thickness , deposited on area) as a function of the equilibrium Li concentration , with the elementary charge . This approach to is particularly helpful if dilute defect chemical considerations are still valid. The Li chemical potential is related to the Li activity via

(3.2)

with and denoting Boltzmann's constant and temperature, respectively, and being the chemical potential of metallic Li. For a given chemical potential difference between Li metal (1) and cathode, the cell voltage can be defined as

(3.3)

For a more detailed analysis of , its separation into electronic and ionic contributions is highly useful. Analogously to the defect chemical considerations of mixed conducting oxides in solid oxide fuel cells, Brouwer diagrams thus come into play, where point defect concentrations and their dependence on Li activity are derived from laws of mass action and chemical potentials. However, as emphasized by Maier,[33,34,138] such concepts have hardly permeated the field of Li electrode materials, despite being very helpful for a more detailed understanding. For this reason, the concept of chemical capacitance and its universal presence in charge/discharge curves, impedance spectra, and ambipolar mass and charge transport has rarely been addressed in Li-ion literature. It is also noted that the interfacial pseudocapacitances of transition-metal oxides include local compositional and oxidation state changes and are thus related to the above definition of chemical capacitances. A detailed discussion of pseudocapacitances can be found, for example, in ref. 139.

In this study, we will investigate the electrochemical behavior of Li_{1-} CoO_2 in the stoichiometry range 0 0 4, where Li is reversibly deintercalated via oxidation of the material, starting at initially full stoichiometry (0). We may consider Li vacancies and electron holes as the relevant defect species, at least as long as defect chemical concepts are applicable to intercalation processes.[138,140] In order to describe the deintercalation in terms of (initially) dilute point defects, it is convenient to reconsider the chemical potential of atomic Li in Li_{1-} CoO_2 (Equation (3.2)) in terms of charged species, that is, as , which, for defects, transforms into[33]

(3.4)

with

$$^{0} \tag{3.5}$$

and

$$^{0} \tag{3.6}$$

The defect activities are related to the corresponding defect concentrations by the activity coefficients , for example, for Li vacancies by

$$\frac{}{^{0}} \tag{3.7}$$

where ^{0} denotes the standard chemical potential of the respective species, and defect concentrations are referred to the concentration of formula units ^{0}. Thus, the nonstoichiometry corresponds to $\bullet$ ^{0}. Under the assumption of dilute conditions and absence of charge trapping, the defect activity coefficients 1, and Equation (3.1) can be evaluated as[107]

$$\frac{^{2}}{} \quad \frac{1}{} \quad \frac{1}{} \quad ^{1} \tag{3.8}$$

This reflects the behavior of as a serial double capacitor with an effective capacitance that is determined by the concentrations of both ionic and electronic charge carriers. The value of is primarily determined by the minority carrier concentration. In general, the interplay of several defect chemical effects determines the minority species, including intrinsic ionic and electronic disorders, doping, or site changes. Assuming , for example, the chemical capacitance becomes

$$\frac{^{2}}{} \tag{3.9}$$

3.2.2 Transmission Line Model, Conductivity, and Chemical Diffusion

In a one-dimensional situation, the electrochemical bulk properties of a mixed ionic electronic conductor at a fixed stoichiometry can be described by a transmission line (Figure 3.1a) consisting of two resistive rails (ions and electrons) and capacitive connections representing the local chemical charge storage, with and .[54,58–61] The corresponding bulk properties are thus fully characterized by the three elementary parameters , , and . By definition, the ionic or electronic conductivity of a material is given as

$$\frac{2\ 2}{} \tag{3.10}$$

with the charge number , carrier mobility , carrier diffusion coefficient , and equilibrium concentration of charge carrier . For mixed conduction, the ambipolar conductivity ˜ can be defined as

$$\tilde{} \quad \frac{}{} \tag{3.11}$$

and is related to the ambipolar (chemical) diffusion coefficient via[67]

$$\frac{\tilde{}}{} \tag{3.12}$$

where is the volume-specific chemical capacitance, with , representing the area, and denoting the thickness. In the case of high electronic conductivity ( ), we have ˜ , and thus

$$\frac{} \quad \frac{2}{} \tag{3.13}$$

where is the total ionic resistance of the thin film in the direction of transport. The ionic conductivity may also be expressed in terms of defects ( ), that is,

$$\frac{2}{} \tag{3.14}$$

and from Equations (3.9), (3.10), and (3.13), we then get for .

3.2.3 Impedance of a Li Intercalation Electrode

The impedance response of a thin film battery electrode is commonly described by Randles' circuit, which is shown in Figure 3.1c.[56,141] This intuitively constructed equivalent circuit can also be derived directly from the general transmission line introduced above (Figure 3.1a) by applying the appropriate boundary conditions and simplifying assumptions.[60] First, we assume that , and therefore the electrical potential gradients within the material can be neglected. This means that electronic resistances in the transmission line can be

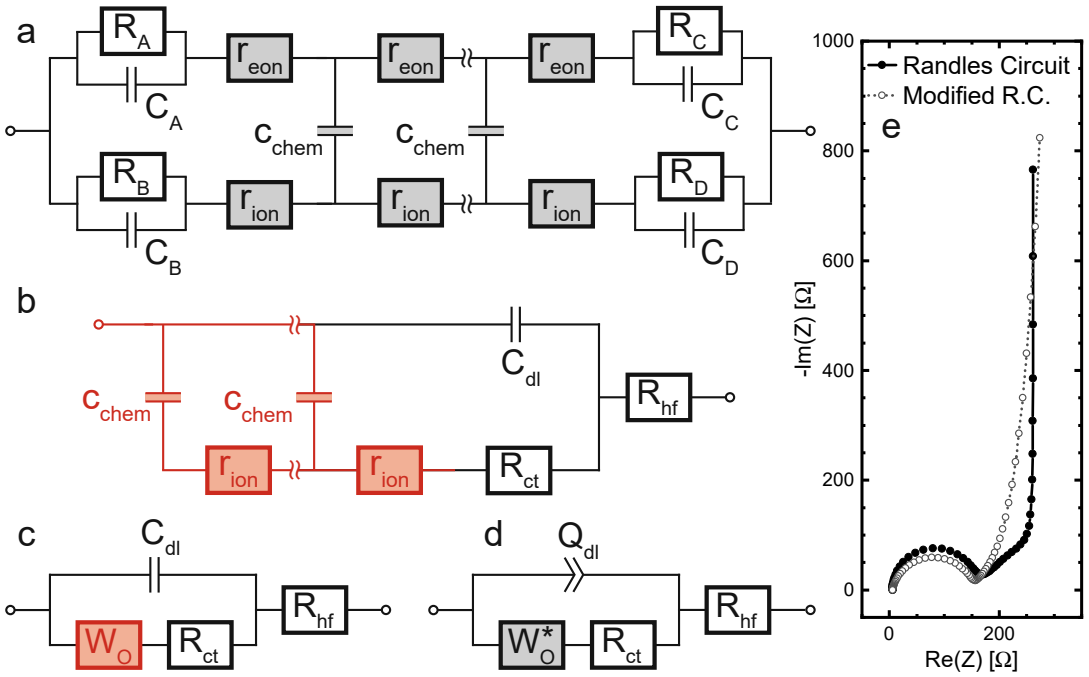

FIGURE 3.1: (a) General one-dimensional transmission line of a mixed conductor consisting of electronic/ionic resistive elements and chemical capacitors, including terminal R/C elements. **(b)** Simplified transmission line for a one-dimensional Li storage electrode extended by a serial high-frequency offset resistance. The obtained circuit is fully equivalent to **(c)** Randles' circuit. **(d)** Modified Randles' circuit with an anomalous diffusion element and nonideal double-layer capacitance. **(e)** Simulated impedance response of circuits (c,d) for 5 66 Ω, 143 6 Ω, 0 12 mF, 327 Ω, and 0 12 mF. For the modified Randles' circuit, the interfacial capacitance was modeled as a constant-phase element, with 0 12 mF s $^{0\ 15}$ and the corresponding constant-phase exponent of 0.85, and the open Warburg element was replaced by an anomalous finite-space diffusion element with a nonideality factor of 0 72 (see Equation (3.19)).

neglected and the corresponding rail replaced by a short circuit. At the bottom of the thin film, the current collector presents an ion-blocking boundary (, 0) that is reversibly transmissive for electrons (0,). The liquid electrolyte in contact with the thin-film surface is electron-blocking with an interfacial double-layer capacitance (,) but allows the reversible transport of Li ions across the corresponding charge-transfer resistance ( ). As the interfacial capacitance is assumed to be located on the electronic rail terminal, the remaining capacitance at the ionic terminal is neglected (0). Upon adding a serial high-frequency resistance to account for an Ohmic offset due to the electrolyte and other cell components, the resulting circuit (Figure 3.1b) is identical to Randles' circuit, with the open Warburg element being equivalent to the reflective transmission line marked in red. The corresponding expression is given by

$$\frac{1 \bullet 2}{1 \bullet 2} \tag{3.15}$$

and describes the impedance of one-dimensional finite-space diffusion, as derived from Fick's laws.[56] As can be seen from Equation (3.15), the impedance of the Fickian diffusion process is composed of a resistance and a time constant . The chemical diffusion coefficient is the inverse time constant normalized by a geometrical factor

$$\frac{^{2}}{—} \tag{3.16}$$

The time constant itself is the product of the characteristic resistance and capacitance of the transport process, and in accordance with Equation (3.13), it reads

(3.17)

3.3 Experimental

3.3.1 Preparation of $LiCoO_2$ Thin Films

One-side-polished sapphire (0001) single-crystal substrates with dimensions 10 × 10 × 0.5 mm^3 (CrysTec, Germany) were sonicated in ethanol (absolute, VWR, Germany) prior to use. A bi-layer of Ti/Pt (5•100 nm) was deposited on both sides of the substrate as a current collector via DC sputtering at room temperature, a current density of 5 mA/cm^2, and Ar pressures of 0.7 and 2.0 Pa, respectively. $LiCoO_2$ thin films were deposited onto the polished side of the substrates via radio-frequency (RF) magnetron sputtering in a custom-built deposition chamber (Huber Scientific, Austria) at room temperature, a total pressure of 2.5 Pa in an Ar/O_2 mixture (25% O_2), power of 60 W, and a substrate-to-target distance of 8.5 cm. The $LiCoO_2$ sputter target (diameter 2") was obtained from Loyaltargets (China) and abraded with fine sandpaper before each deposition to eliminate deviations from bulk stoichiometry at the target surface. The thickness of the $LiCoO_2$ films was approximately 100 nm, as determined by a TEM thickness calibration, and the corresponding deposition rate was 0.5 nm/min. The as-deposited films were annealed in a muffle furnace in air at 700 °C for 5 h at a ramp rate of 10 °C/min. The samples were characterized by grazing-incidence X-ray diffraction (GID, 3), atomic force microscopy (AFM), and elemental analysis via inductively coupled plasma mass spectrometry (ICP-MS).

3.3.2 Electrochemical Characterization

After annealing, the thin film samples were transferred into an argon-filled glovebox (O_2 and H_2O levels 0.1 ppm) and assembled into three-electrode test cells (PAT-Cell by EL-Cell, Germany) using a glass fiber separator (260 µm, EL-Cell), 80 µL of a standard organic electrolyte (1 M $LiPF_6$ in a 1:1 mixture of ethylene carbonate and dimethyl carbonate, Aldrich), and a Li metal anode (0.6 mm, Goodfellow, Germany). All electrochemical measurements were carried

out at room temperature on a BioLogic SP200 potentiostat with a built-in impedance analyzer. Directly after assembly, a cyclic voltammogram of the working electrode was recorded at a scan rate of 0.1 mV/s in the potential range of 3.7–4.0 V versus Li^+/Li, followed by galvanostatic charge and discharge within the same potential range at a current of 7.16 µA (1 C). Subsequently, a series of potentiostatic impedance spectra (1 MHz to 1 mHz, 6 points per decade, and 10 mV amplitude) was recorded in 10 mV steps, ranging from 3.85 to 4.00 V (charge scan) and back to 3.85 V (discharge scan) versus Li^+/Li. Before each measurement, a 15 min constant voltage step was applied to allow the thin film to fully equilibrate at the given potential. To distinguish irreversible degradation from the potential-dependent changes of material parameters, the hysteresis between charge and discharge scans was evaluated. As the hysteresis was substantial for the first set of measurements due to the initial changes of the thin film, the impedance series was repeated, including CV scans before and after, yielding much more stable trends. The spectra obtained after stabilization were then analyzed in detail.

3.4 Results and Discussion

3.4.1 $LiCoO_2$ Thin Films

The GID pattern of a typical $LiCoO_2$ thin-film sample and its corresponding AFM image are displayed in Figure 3.2. The diffraction pattern shows the most characteristic $LiCoO_2$ reflexes around 18.9° (003), 37.5° (101), and 45.3° (104). In addition, signals stemming from the Pt current collector can be clearly identified, as well as some impurity signals, most likely due to small amounts of Co_3O_4 in the sample. The AFM image reveals a reasonably homogeneous and polycrystalline morphology of the thin film, with an RMS roughness of approximately 10 nm. ICP-MS analysis of a thin film dissolved in concentrated hydrochloric acid yielded a Li/Co ratio of 0.95, indicating that the deposition of $LiCoO_2$ was almost stoichiometric.

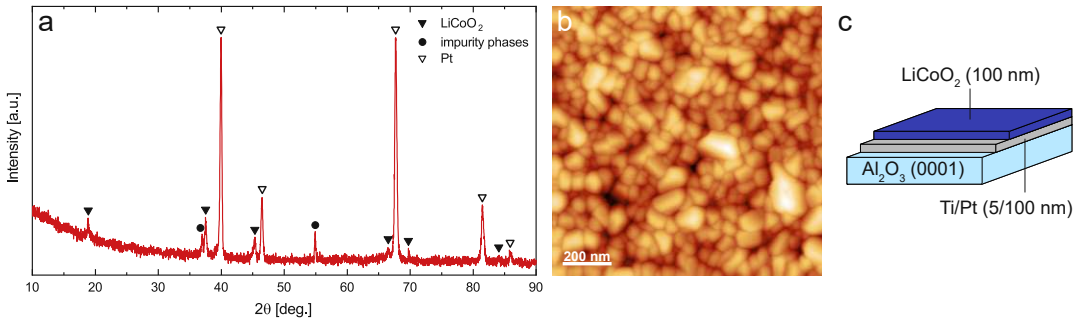

Figure 3.2: **(a)** GID pattern of a $LiCoO_2$ thin film at 3° incident angle. **(b)** AFM image revealing a rather homogeneous but polycrystalline film morphology with an RMS roughness of approximately 10 nm. **(c)** Schematic illustration of a $LiCoO_2$ thin film deposited on a Ti/Pt-coated Al_2O_3 (0001) single-crystal substrate.

3.4.2 DC Cycling

Figure 3.3a shows the initial CV curve of the pristine sample (first charge/discharge) and CV curves after some initial changes and stabilization. More specifically, the latter correspond to the stabilized curves measured before and after the relevant series of impedance measurements discussed in this study. The film shows good electrochemical reversibility, with the initial discharge capacity of 116 mAh/g being in good agreement with the common literature values at this cutoff voltage.[110,115,142,143] To evaluate the thin-film potential as a function of charge and Li stoichiometry, the CV curves are converted into the coulometric titration curves shown in Figure 3.3b. As is characteristic for LCO, the curves exhibit a plateau around 3.9 V, followed by a moderate and roughly constant slope up to 4.0 V. Nominal nonstoichiometry values are also shown in Figure 3.3b, which are deduced by assuming 0 4 at 4.0 V rather than by relating the charge to the theoretical capacity of the film.[144] This is also in accordance with the fact that the plateau region indeed corresponds to that of porous bulk electrodes, with the phase transition between two structurally very similar hexagonal phases in the range of 0 05 0 25, followed by a single-phase (i.e. sloped) region starting at 0 25.[145–149]

Some degradation of the film capacity occurs between the initial cycle and the start of the impedance measurements, with a significant broadening of the CV current peak and the charge curve plateau becoming increasingly inclined. In terms of discharge capacity, the electrode drops to 89 mAh/g or 77% of its initial capacity. A similar broadening of the CV current (or differential capacity) peak accompanying this capacity loss has also been reported for porous bulk electrodes,[150] and the frequently observed irreversible capacity losses of lay-

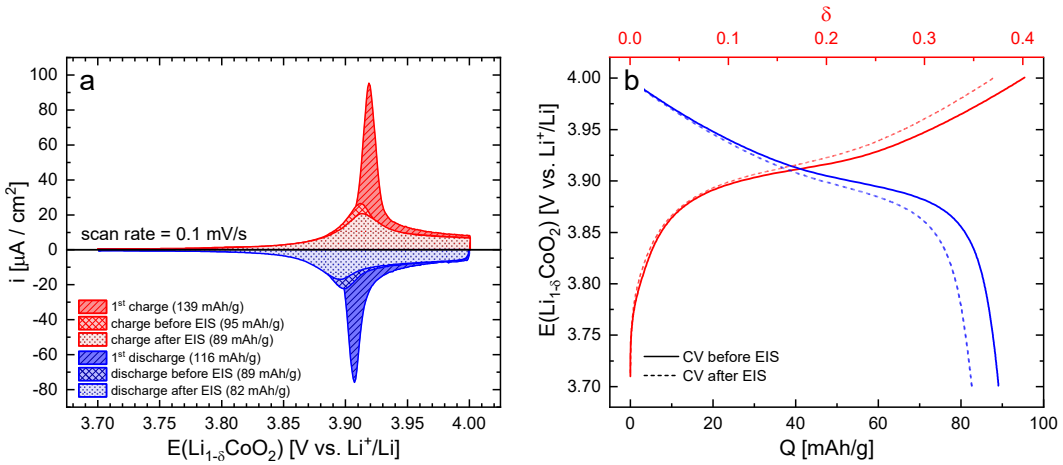

Figure 3.3: (a) CV curves of the $LiCoO_2$ thin film in its pristine state (first charge/discharge) and in its stabilized state before and after EIS measurements. **(b)** Coulometric titration curves derived from stabilized CV curves. Nominal values of are obtained by assuming 0 4 at 4.0 V for the CV scan before EIS. Charge values are normalized to the pristine thin-film mass.

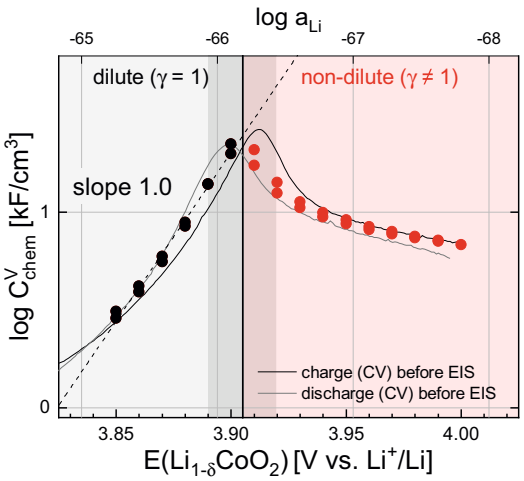

Figure 3.4: Chemical capacitance from CV scans (continuous lines) and impedance fits (discrete points) as a function of electrode potential and Li activity according to Equation (3.2). The dilute to nondilute transition region 3.89 – 3.92 V is marked in dark around a central line at 3.905 V. The peak value of C_{chem} at this transition potential is around 29 kF/cm^3. A linear fit for the dilute region is shown as a dotted line.

ered oxide cathodes are attributed to, among other factors, oxygen release and structural degradation toward denser spinel and rock salt phases, especially in the near-surface region, due to the thermodynamic instability of partially delithiated LCO.[151–155] More importantly, however, there is only minor further degradation throughout the impedance measurements, meaning that the electrochemical properties extracted from the collected impedance spectra can be assumed to vary reversibly with the electrode potential.

The DC data can now be used to determine the chemical capacitance (differential capacity) as a function of electrode potential. In the context of porous bulk electrodes, differential capacity curves are typically obtained via differentiation of galvanostatic charge curves from long cycling experiments, which require galvanostatic conditions to simulate a constant load. However, we perceive CV curves as a more suitable starting point when galvanostatic conditions are not required, as is the case for thin-film studies. This is because the differentiation of galvanostatic data often yields discontinuous and noisy capacitance curves due to the slight potential fluctuations in the original data. As a result, these data require smoothening prior to their conversion into differential capacity values.[117] For CV curves, on the other hand, at a given scan rate v and film thickness L, the measured current density i is directly related to the volume-specific chemical capacitance via

$$C^V_{chem} = \frac{|i|}{v \cdot L} \quad , \tag{3.18}$$

assuming the scan rate is slow enough for the electrode to remain in equilibrium, that is, spatially homogeneous. For 0 1 mV•s and 100 nm, the current density in μA•cm^2 is equivalent to the chemical capacitance in kF/cm^3. Values of 4 to 29 kF/cm^3 result for our films, and these values can then be directly compared to values from impedance fits, as shown in Figure 3.4 and discussed in the following sections.

3.4.3 Impedance Spectra and Their Analysis

Figure 3.5 shows the impedance spectra of the $LiCoO_2$ thin film in the potential range of 3.85 to 4.00 V versus Li^+/Li. It should be noted that only every second spectrum is shown for better visibility. The shape of the spectra generally behaves according to the main features of Randles' circuit (Figure 3.1e), with the semicircle corresponding to the charge-transfer resistance and a double-layer capacitance, followed by a diffusional tail approaching a purely capacitive behavior toward the lowest frequencies. The most notable difference to the 45 – 90° behavior expected from the ideal finite-space diffusion element is that the transition between the semi-infinite and finite-space regimes appears continuous, rather than confined to a specific knee frequency. The charge-transfer resistance and the ionic resistance (as visually

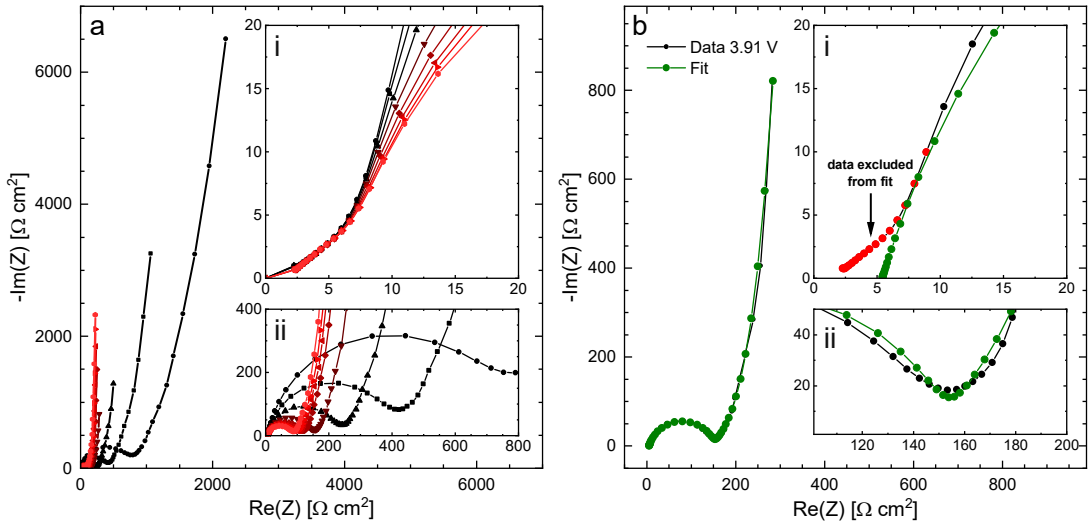

Figure 3.5: Impedance spectra of the Li_{1-} CoO_2 thin film at various electrode potentials. **(a)** Full spectra with decreasing real impedance in the low-frequency region. The sharp increase and subsequent gradual decrease in chemical capacitance toward higher potentials are indicated by the height of the low-frequency tail. Insets show (i) Warburg-like high-frequency tail of the charge-transfer arc and (ii) inverse variation of the charge-transfer resistance with potential. **(b)** Exemplary least-squares fit of an impedance spectrum, acquired at an equilibrium electrode potential of 3.91 V vs Li /Li, using a modified Randles' circuit (Figure 3.1d). The resulting fit corresponds to the simulated spectrum in Figure 3.1e. Insets show magnifications of (i) high-frequency region with the onset of the charge-transfer arc and (ii) mid-frequency region with the transition from charge transfer to the solid-state diffusion regime. Measurement points at or above 389 Hz were excluded from the fit and treated as a high-frequency offset.

estimated by the extrapolated real axis intercept of the diffusional tail) decrease significantly toward higher electrode potentials. A more detailed and quantitative analysis of this part of the spectra is presented below.

At the high-frequency end of the spectrum, a small Warburg-like feature with a real impedance of about $6\,\Omega\,\mathrm{cm}^2$ is observed that appears independent of the electrode's SOC. Although we cannot unambiguously assign this feature, it could possibly originate from the substantial surface roughness of the films and some residual porosity or cracks in the thin film. Due to its invariance, small magnitude, and confinement to the high-frequency region, the corresponding frequency points are excluded from the fit, and thus the feature is simply treated as a real axis offset in the following analysis; cf. inset (i) in Figure 3.5b.

As pointed out in the original literature on finite-space Warburg impedance,[56] the purely capacitive low-frequency region allows the simultaneous extraction of and from the impedance spectrum, as the two parameters are completely separated into the real and imaginary parts of the overall impedance. Another direct consequence of this separation is that for a series of impedance spectra over the same frequency range, the height of the capacitive tail in a Nyquist plot directly indicates the capacitance and thus the steepness of the equilibrium charge/discharge curve at the given electrode potential. Indeed, the height of the diffusional tails in Figure 3.5 clearly reflects the shape of the charge curves in Figure 3.3, with the plateau and hence the highest chemical capacitance around 3.9 V.

In practice, the extraction of and via CNLS fits of Randles' circuit can be rather tricky, as the suggested ideal capacitive behavior at low frequencies does not consider non-idealities such as polycrystallinity of the LCO films on Pt, anisotropy of ion conduction in LCO, surface roughness of the films, cracks or residual porosity of the film, and any type of side reactions. Moreover, the frequency range of the measurement is limited by the rapidly increasing measurement times in the low-frequency region. Deviations from ideality can lead to a flattening of the capacitive line below 90° and a smearing out of the transition between 45° and 90°, making it increasingly difficult to achieve reliable fit results. Presumably, due to this reason, previous thin-film studies mostly derived , or rather • , from coulometric titration curves and then used it as a fixed parameter for the impedance fits to extract or . , and hence information about the equilibrium charge curve (or differential capacity curve), was directly extracted from the impedance spectra of a Li-ion electrode, for example, in refs. 133, 134 and 47.

In our case, we found that reliable fit results can be obtained by using an anomalous finite-space diffusion element implemented in the impedance-analyzing software that is similar to the anomalous finite-space diffusion element reported by Bisquert,[136] yielding the impedance expression

$$\frac{\bullet 2}{1 \quad \bullet 2} \tag{3.19}$$

which allows for a more general power law dependence on time of the mean-squared displacement ^{2} / rather than the standard linear behavior. More specifically, Equation (3.19) leads to a phase shift 45 in the semi-infinite and 90 in the finite-space regime, which correctly describes the practical impedance behavior of virtually all thin-film battery electrodes (see Figure 3.5a).[109,111,112,132] In our case, the nonideality parameter 0 1 turned out to be in the range of 0.6 – 0.7.

As already discussed above, this also means that any conductivity or diffusion coefficient measured in such films must be viewed as an effective rather than a strictly material-intrinsic parameter. Also, normalization of to the nominal surface area , that is, without considering the surface roughness or cracks/pores, may somewhat underestimate the true area-specific resistance. Nonetheless, it is fair to assume that the observed general trends, that is, the essential dependences on the electrode potential, remain valid regardless of the film morphology or grain shape and grain size distribution. The impedance expression, as given by Equation (3.19), is substituted for the classical element into Randles' circuit. Similarly, the interfacial double-layer capacitance is fitted as a constant-phase element to account for the nonideal capacitive behavior. The modified equivalent circuit used for fitting and its simulated impedance response are shown in Figure 3.1d and 3.1e, respectively.

3.4.4 Fit Results of Elementary Material Parameters

As shown by the exemplary least-squares fit in Figure 3.5b, the equivalent circuit in Figure 3.1d adequately describes the recorded impedance spectra and therefore allows the extraction of electrochemical properties as a function of electrode potential. The values of 1• and shown in Figure 3.6a and 3.6b, respectively, are directly obtained from the fit and subsequent normalization by sample geometry (and). results directly from and according to Equation (3.17) and is plotted in Figure (3.4). Finally, either results directly from in Equation (3.16) or from and in Equation (3.13), as shown in Figure 3.7. The parameter values vary by more than 1 order of magnitude and are plotted logarithmically versus the electrode potential and log to facilitate their interpretation. The entire dataset shows a minor hysteresis with respect to the scan direction. In the discharge scan starting at 4.0 V, resistances are slightly higher, and chemical capacitances are lower compared to the charge scan. However, these differences are negligible for the overall trends.

The charge-transfer resistance is the highest (about 1000 cm^2) in the low-potential region and then strongly decreases down to about 100 $\Omega\,cm^2$ at 3.99 V, in good agreement with the literature.[109,111,112,132] At lower potentials, up to ca. 3.9 V, a constant slope of about 0.8 results from the log log plot of 1• versus . Above a threshold potential of around 3.89 – 3.92 V, the log log behavior flattens out. Judging by the values of in Figure 3.3, the corresponding stoichiometry of this transition is approximately $Li_{0.78-0.92}CoO_2$, although

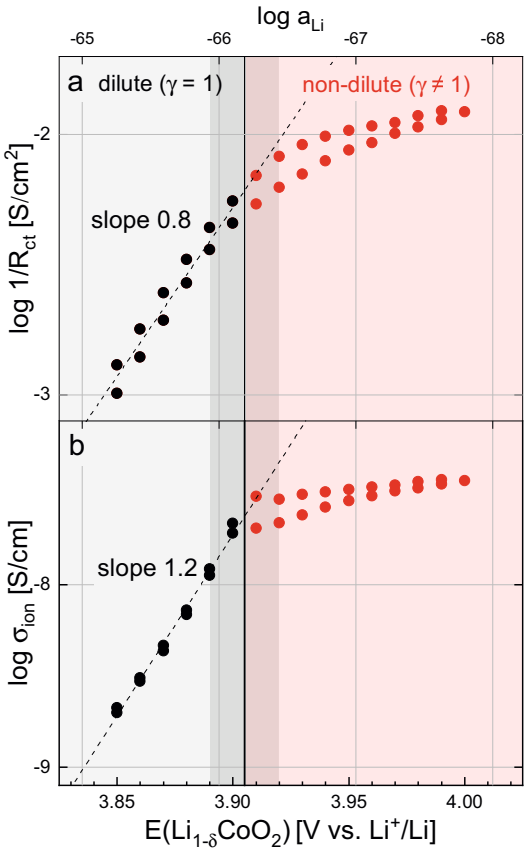

Figure 3.6: Logarithmic plot of **(a)** inverse charge-transfer resistance $1/R_{ct}$ and **(b)** ionic conductivity σ_{ion} versus electrode potential and $\log a_{Li}$. The dilute (activity coefficient $\gamma = 1$) to nondilute transition region 3.89 – 3.92 V is marked in dark around a central line at 3.905 V. Linear fits for the dilute region are shown as dotted lines.

this can only be taken as a rough estimate due to the strong variation of stoichiometry in this potential region. In the following, the low- and high-potential regions separated by this transition will be referred to as dilute and nondilute regimes, respectively.

Effective ionic conductivities strongly increase with the electrode potential, ranging from about $10^{-8.7}$ S/cm at 3.85 V up to $10^{-7.4}$ S/cm at 3.99 V. Literature reports of ionic conductivity as a function of stoichiometry are scarce – the only reported values we could find are around $10^{-7.5}$ to $10^{-6.5}$ S/cm up to $\delta = 0.5$, although the corresponding dataset does not show the expected decrease of conductivity for low δ.[132] In the dilute regime, a slope of 1.2 is observed in the log – log plot of σ_{ion} versus a_{Li} up to the threshold potential region around 3.89 – 3.92 V, above which the slope starts to decrease as already seen for $1/R_{ct}$.

The values of C_{chem} obtained from the impedance fits are plotted in Figure 3.4, together with the CV data. Both sets of data are in very good qualitative and quantitative agreement, starting at very small values at low potentials, sharply increasing toward a marked peak of roughly 30 kF/cm^3 around 3.9 V, and then decreasing to moderate values. The peak abso-

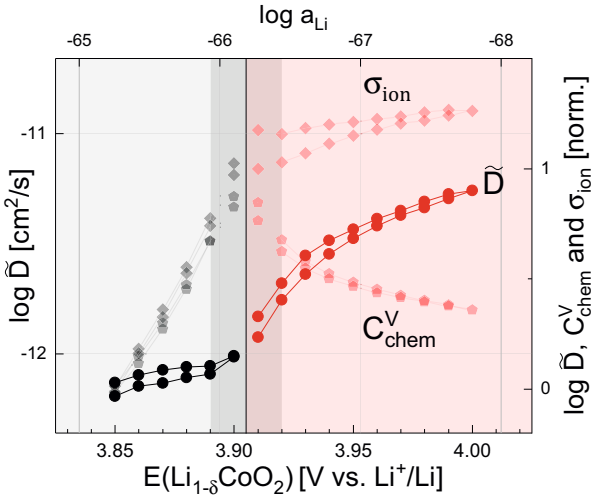

Figure 3.7: Chemical diffusion coefficient compared to its constituent parameters. The absolute value of $\widetilde{D}$ is given on the left. Values of $\widetilde{D}$, C^V_{chem}, and σ_{ion} on the right axis were normalized to their average value at 3.85 V to emphasize their relative trends. The dilute (gray) to nondilute (red) transition region 3.89 – 3.92 V is marked in dark around a central line at 3.905 V.

lute values are in excellent agreement with the typical differential capacities found in the literature,[110,111,114,150] all of the cited values being in the range of 30 – 40 kF/cm^3 when normalized by sample geometry. The close match of values from AC and DC data demonstrates the often-overlooked fact, that the properties of a Li electrode's equilibrium charge curve are fully contained within its potential-dependent impedance response, because both E and C_{chem} relate back to the fundamental thermodynamic relationship between μ_{Li} and a_{Li} in Equation (3.2). Again, a power law dependence between C_{chem} and a_{Li} can be observed in the dilute regime, this time with a slope of 1.0. A more detailed interpretation of the slope of 1 in terms of defect chemistry is given in the next section.

Finally, the chemical diffusion coefficient, as calculated from Equation (3.16), is shown in Figure 3.7. As σ_{ion} and C_{chem}, both of which increase exponentially with E, show a similar increase up to 3.9 V, $\widetilde{D}$ remains nearly constant around 10^{-12} cm^2/s in the dilute regime. Above 3.9 V, $\widetilde{D}$ increases up to almost 10^{-11} cm^2/s, driven by both an increasing σ_{ion} and a decreasing C_{chem}. Values below 3.9 V are rarely reported, but the diffusivities at higher potentials are in good agreement with other studies of LCO thin films.[109–112,114,115]

As both the DC data and C_{chem} from impedance fits clearly show that the dependence of δ on E deviates from a purely exponential behavior in the nondilute regime (i.e., $E \neq E_0 + kT \ln \delta^{\alpha}, \alpha = const$), it is hardly surprising that the corresponding electrochemical properties show a similar deviation. To isolate the concentration dependences from other factors that influence E, it is therefore useful to plot all parameters also in dependence of δ. As shown in Figure 3.8a, the trend of $1/R_{ct}$ straightens, and we get an almost constant slope in the entire range when plotting as a function of nonstoichiometry. In Figure 3.8b, the ionic conductivity

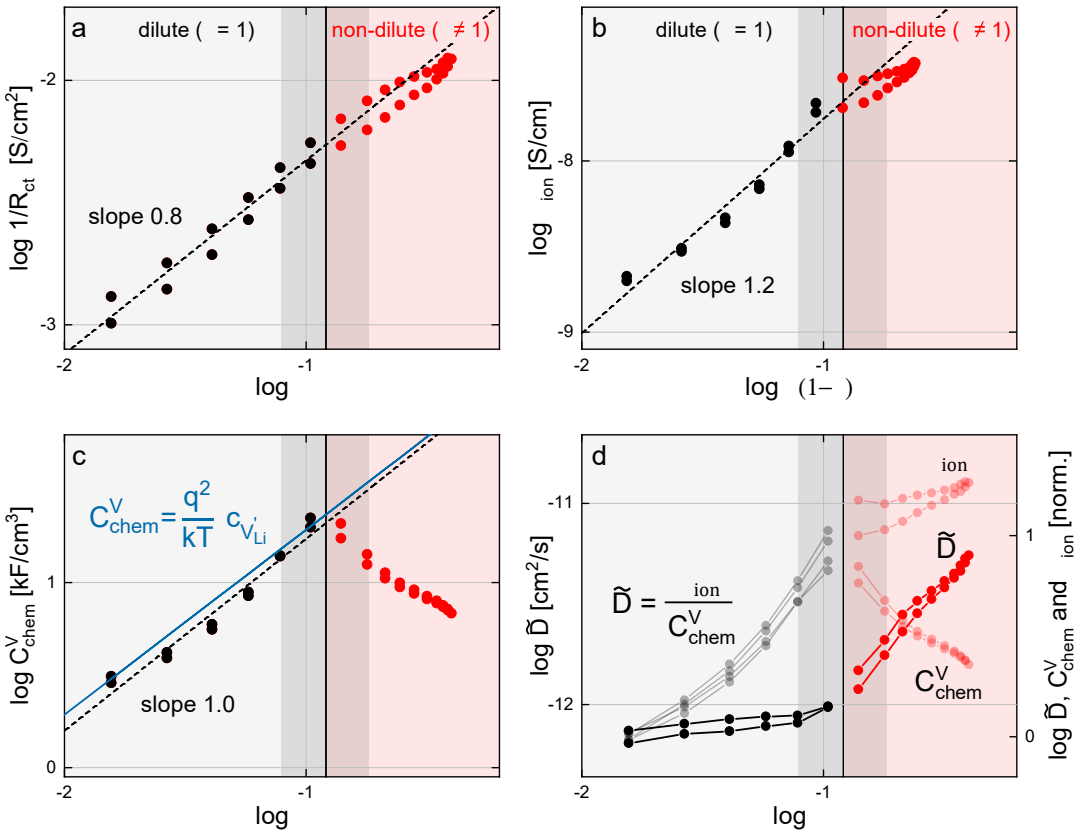

FIGURE 3.8: Electrochemical transport parameters of the $Li_{1-\delta}CoO_2$ thin film extracted from impedance spectra shown as log-log plots versus (a,c,d) or (1 -) (b). Values of were obtained from Figure 3.3b by taking the average of all four coulometric titration curves. **(a)** Inverse charge-transfer resistance, **(b)** ionic conductivity, and **(c)** chemical capacitance from impedance fits. The solid blue line indicates the theoretical values predicted by Equation (3.9). **(d)** Chemical diffusion coefficient compared to its constituent parameters. The absolute value of is given on the left. Values of , , and on the right axis were normalized to their average value at 3.85 V to emphasize their relative trends. The dilute to nondilute transition region 3.89 – 3.92 V is marked in dark around a central line at 3.905 V. Linear fits for the dilute region are shown as a dotted line.

is plotted as a function of 1 rather than to account for the limited number of available lattice sites. This also leads to a straightening of the trend, as compared to Figure 3.6b, with increasing even toward the highest values of 1 , albeit with a smaller slope.

Given the nonidealities of the used impedance model and thus unavoidable uncertainties of the extracted parameters, we consider the slope of in the dilute regime as close to unity. This suggests that for the dilute regime, ion conduction in LCO can be well described by a vacancy-mediated process with almost constant vacancy mobility. At higher vacancy concentrations (nondilute regime), the slope of decreases, meaning that the ionic mobility decreases, probably due to some defect interaction. However, still the total conductivity increases with increasing , even for very high vacancy concentrations. This is very different from the often-observed conductivity decrease of oxide ion conductors with increasing

doping and thus oxygen vacancy concentration (e.g., yttria-stabilized zirconia[78] or doped ceria[156–158]). Since it is mainly the high concentration of the dopants themselves that reduces the defect mobility in those oxide ion conductors, the reason for the different behavior of our LCO thin films might be the absence of a varying dopant concentration.

The observed log log dependence of 1• on (slope 0.8) is in line with a defect chemical picture, where a Li ion from the electrolyte needs a Li vacancy at the LCO surface for a charge transfer into the electrode. The exact dependence of this charge-transfer reaction on the specific defect concentrations, however, also varies with the concentration dependence of the corresponding Galvani potential step,[159] and a more detailed discussion is beyond the scope of this paper.

The chemical capacitance in Figure 3.8c, however, retains its peak in the transition region of the log versus log plot and strongly decreases in the nondilute regime. In the dilute regime, is also proportional to and thus to the vacancy concentration. This is in accordance with the expected defect dependence of Equation (3.9), that is, for . As indicated by the blue solid line in Figure 3.8c, the values of predicted by Equation (3.9) are even in excellent quantitative agreement with the experimental data, strongly suggesting that the therein-contained assumption is in fact valid for low vacancy concentrations, as will be discussed in the next section. Furthermore, this striking agreement of theory and experiment demonstrates that the thermodynamic description based on dilute point defects can offer valuable hints at the underlying defect chemistry of Li-ion battery electrode materials and once more highlights the central importance of the chemical capacitance as a powerful, readily accessible material descriptor.

3.4.5 Defect Chemical Perspective

From all the data presented in Figures 3.4 – 3.8, we conclude that (i) in the dilute regime, log is proportional to log , with a slope close to unity, and (ii) upon transition to the nondilute regime, the electrochemical properties of LCO collectively change in their dependence on Li activity and electrode potential. This dilute to nondilute transition occurs precisely in the region of the highest chemical capacitance – the plateau of the charge curve – where the stoichiometry strongly varies with the electrode potential and particularly affects properties, which themselves include a dependence on the Li activity (,). Charge transport and transfer (and), on the other hand, which primarily depend on the Li vacancy concentration, remain unaffected when plotted versus rather than Li activity.

We first consider the dilute regime and discuss the possible defect chemical reasons behind the slopes of and in their respective log log plots versus , both being reasonably close to 1. We combine Equations (3.4) – (3.6) and, under dilute assumptions,

arrive at

(3.20)

and thus

(3.21)

with

(3.22)

In accordance with Equation (3.2), we may also write

(3.23)

Assuming negligible defect concentrations due to intrinsic ionic or electronic disorder and the absence of any dopant charge, charge neutrality requires ^{0}, and Equation (3.21) reduces to

(3.24)

Similarly, Equation (3.23) leads to

(3.25)

Equation (3.25) predicts a slope of 1•2 in a plot of log versus log , that is, in a Brouwer diagram.

Alternatively, and perhaps more intuitively, the power law dependences of point defect concentrations on activity can also be derived from equilibrium mass action laws.[33] For the case of Li intercalation into a cathode material, the equilibrium reaction and its corresponding mass action law can be formulated as

(3.26)

(3.27)

where is the equilibrium constant of the intercalation reaction. In accordance with Equation (3.25), Equation (3.27) predicts / ^{1} and therefore a slope of 1•2 in a plot of log versus log , again assuming due to charge neutrality.

Instead, we find for a slope of roughly 1 in the log versus log plot. This somewhat surprising result is very consistent with the potential dependence of : assuming only defects due to nonstoichiometry (i.e., Li deintercalation, ^{0}), we would expect a slope of 1•2 according to Equations (3.8), (3.25), and (3.27). However, the measured

slope for is also close to 1. Within the thermodynamic description of presented above, a slope of 1 could be explained if or and assuming the majority carrier concentration as relatively constant on a logarithmic scale. Given the strong variation of and , Li vacancies can be assumed to be the minority carriers, and has to be pinned significantly above to explain the observed slopes. The excellent quantitative agreement of the experimental values of with Equation (3.9) also supports this assumption. If the concentrations of both vacancies and holes were relevant, Equation (3.8) would predict values to be lower by a factor of 2 compared to those found experimentally.

From a defect chemical perspective, pinning of might occur if the hole concentration introduced through nonstoichiometry is negligible compared to the levels of either (i) intrinsic electronic disorder or (ii) extrinsic acceptor doping. The evaluation of the former is far from trivial, as Li_1 CoO_2 is known to undergo a semiconductor-metal transition upon delithiation, accompanied by a significant increase in electronic conductivity and hole mobility as the conduction mechanism transitions from localized polaron hopping toward delocalized metallic conductivity.[145,148,160] Owing to the close entanglement of mobility and conductivity, it is not entirely clear how behaves in this stoichiometry range. Furthermore, the defect chemical description of electronic charge carriers relies on the semiconductor-type behavior with thermally activated, localized polarons and therefore fails to describe metallic conductivity.

A more accessible explanation lies in the presence of an extrinsic acceptor dopant in the material. As reported in the literature, the formation energies of antisite defects such as are relatively low, and the defect chemical composition of nominal $LiCoO_2$ thin films is highly sensitive to synthesis conditions.[140,161–163] It would therefore come as no surprise if the sputter-deposited and post-annealed thin films examined in this work contained a significant amount of defects that act as acceptor dopants in the material, although further experimental investigation would be required to corroborate this hypothesis.

Based on the assumed presence of an acceptor dopant such as , we can also propose a Brouwer diagram. The dopant requires compensation by a formally positively charged defect species to preserve charge neutrality. For high and thus low (see Equation (3.27)), the dopant causes a fixed hole concentration to satisfy the electroneutrality condition 2 . As long as the additional hole concentration introduced through the charging of the electrode is comparatively small, the overall hole concentration will therefore remain nearly constant on a logarithmic scale. If is constant, Equation (3.27) requires / ^{1}. This situation, labeled as the "A" (acceptor) regime, is shown on the left side of Figure 3.9 at high lithium activities. Once the initially fixed hole concentration is surpassed by the additional concentrations introduced through nonstoichiometry, the activity dependences of and behave according to Equations (3.24) and (3.25). The proposed defect model would therefore not only explain the slope of about 1 for at low but would even predict

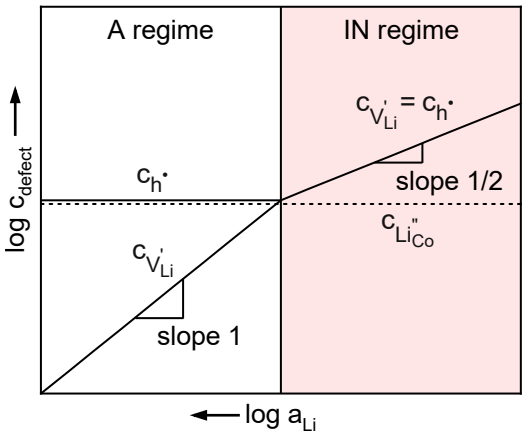

FIGURE 3.9: Proposed Brouwer diagram of inadvertently acceptor-doped Li_{1-} CoO_2, showing logarithmic defect (vacancy and hole) concentrations as a function of log . In the A (acceptor) regime, the electron hole concentration is fixed by the negative acceptor dopant (e.g.,) concentration, and / 1• . In the IN (ideal nonstoichiometry) regime, the hole and vacancy concentrations due to nonstoichiometry start to dominate, and / 1• . In both regimes, defect activity coefficients are assumed to be 1.

a change of slope toward 1•2 at high , where is valid. As a first estimate, as the flattening of the log log slopes in Figures 3.4 and 3.6 occurs around 0 1, we can thus suggest a site fraction of about 5%.

Given the low operating temperature and high defect concentrations, as compared, for example, to high-temperature oxygen-ion conductors, one could also expect additional ionic-electronic defect association of vacancies and holes.[33,138] Although this effect cannot explain the initial slope of 1, it might further enhance the flattening of the slope toward higher and is therefore also consistent with our results. Li interstitials, on the other hand, are not expected to play a significant role. These may come into play for a high level of Frenkel disorder, which would lead to -independent intrinsic vacancy (and interstitial) concentrations, in contrast to the experimental results.

However, under the dilute assumptions implicit in the Brouwer diagram, would be predicted to be $\frac{2}{}$ in the dilute regime and $\frac{2}{2}$ beyond – see Equation (3.8). Hence, it should follow the same slopes as . The decrease of above 3.9 V is therefore beyond the idealized model presented above and can only be explained by considering the varying activity coefficients of holes and vacancies at high concentrations. As both and necessarily scale with the same concentrations within the dilute model, we can also conclude from Equation (3.12) that the strong increase of at high can in fact only result from the nonideal, that is, nondilute, behavior. This highlights the fact that, although it may be in line with intuition to see an increase in diffusivity at higher carrier concentrations, the reasons for this experimentally observed behavior are actually far from obvious, given the parallel

concentration dependences of and . Conversely, a strong variation of diffusivity as a function of SOC can be seen as an indication that the dilute model is no longer sufficient to describe the material's transport properties.

3.5 Conclusion

A full set of electrochemical parameters describing the mass and charge transport properties of Li_1 CoO_2 thin films could be simultaneously extracted from impedance spectra measured in dependence of the state-of-charge (SOC). The relevant elementary material parameters are the ionic conductivity , charge-transfer resistance , and chemical capacitance . It is shown that the chemical capacitance can be deduced alternatively from DC data (coulometric titration curve or cyclic voltammetry), and both approaches lead to very consistent results. For a dilute regime (0 1), the chemical capacitance is even in excellent quantitative agreement with defect chemical predictions. This demonstrates the central importance of the chemical capacitance as a powerful, readily accessible material descriptor. The Li chemical diffusion coefficient, on the other hand, is a composite property, and its dependence on the SOC can only be understood from the underlying ionic conductivity and chemical capacitance. By evaluating the dependence of all elementary material parameters on Li activity and nonstoichiometry, it was shown that at low potentials, that is, low vacancy concentrations, the transport properties of the investigated Li_1 CoO_2 thin film are consistently described by a dilute defect chemical model. However, the analysis of slopes in the log log plots of and versus Li activity, as well as the absolute values of , strongly suggests the presence of an acceptor dopant. antisite defects, inadvertently introduced during sputter deposition, are proposed as a plausible acceptor species. As a result, both and increase exponentially with the electrode potential (up to 0 1) and remains nearly constant. At high potentials, that is, high vacancy concentrations, the dilute model fails, as activity coefficients start to become relevant and begins to decrease. The measured increase of for 0 1 can therefore serve as an indicator of the material moving beyond the ideal dilute behavior. The ionic conductivity, however, increases almost linearly in the corresponding log log plot versus 1 for the entire stoichiometric range, which indicates little concentration dependence of the vacancy mobility.

4 Defect Chemistry of Spinel Cathode Materials - A Case Study of Epitaxial Li_{2-} Mn_2O_4 Thin Films

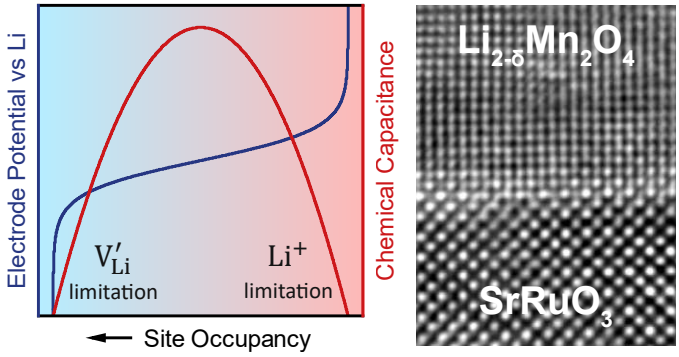

The study presented in this chapter was published in the following article:
Bumberger, A. E.; Boehme, C.; Ring, J.; Raznjevic, S.; Zhang, Z.; Kubicek, M.; Fleig, J. Defect Chemistry of Spinel Cathode Materials - A Case Study of Epitaxial $LiMn_2O_4$ Thin Films. *Chemistry of Materials* **2023**, *35*, 5135-5149. DOI: 10.1021/acs.chemmater.3c00814.

4.1 Introduction

Cathode materials for Li-ion batteries (LIBs) have become one of the most essential classes of modern-day functional materials. Their optimization in terms of capacity, operating voltage, cycling stability, safety, and rate capability is a key part of the collective effort to max out the overall technological potential of LIBs for various applications. Given the rapid improvements of energy densities over the last few years, focus is increasingly put on charging speed and discharge power density. Thus, more than ever, there is a need for a detailed understanding of the individual mass and charge transport processes that determine the overall kinetics. A major challenge in this pursuit is posed by the morphological and compositional complexity of porous electrodes, which makes it difficult to separate the individual contributions of pore diffusion, interfacial charge transfer, and solid-state diffusion. To further complicate things, the active material in porous electrodes is usually processed in the form of secondary

agglomerates, rather than single crystallites, such that boundaries between primary particles may heavily impact the observed solid-state kinetics. Moreover, the active particles in porous electrodes are often (partly) coated, for example, with carbon.

One way to isolate the intrinsic bulk transport properties of a given active material is the fabrication and characterization of thin-film electrodes exhibiting a well-defined geometry and composition. As previously exemplified for Li_{1-} CoO_2,[51] this approach allows the evaluation of ionic conductivity, chemical capacitance, and chemical diffusivity as a function of state-of-charge (SOC) from comparatively simple impedance models that describe solid-state chemical transport as the resistive and capacitive interplay of ions and electrons based on the Nernst-Planck equation. This set of elementary material properties fully describes the transport of mass and charge within a single crystallite and can be related back to defect chemical principles and defect thermodynamics. If these bulk material properties and their continuous variation with the SOC are available, they can be used as input parameters for more complex models considering the behavior of the active material in the intricate network of a porous LIB electrode.

$LiMn_2O_4$ (LMO) of the space group $Fd\bar{3}m$ is the prototypical spinel cathode material. Its crystal structure is commonly described as a cubic close packing of 32 O atoms per unit cell, where Mn occupies half of the 32 octahedral sites (16d sites) and Li occupies one eighth of the 64 tetrahedral sites (8a sites). The unit cell thus consists of 32 O atoms, 16 Mn atoms, and 8 Li atoms, with Mn being in the mixed valence state of +3.5.

Upon oxidation of Mn^{3+} in Li_{2-} Mn_2O_4 to a valence state of +4 (1), Li^+ is released from the occupied tetrahedral 8a sites. The corresponding transition from $LiMn_2O_4$ to -Mn_2O_4 (both of space group $Fd\bar{3}m$) proceeds in two main stages, as evidenced by the characteristic double plateau of the charge curve around 4.00 and 4.15 V versus Li^+/Li. The first plateau is commonly described as a single-phase solid solution of the general composition Li_{2-} Mn_2O_4 (1) up to a nonstoichiometry value of 1 5, accompanied by a gradual decrease of the cubic lattice parameter from 8.24 to 8.19 Å.[164] Depending on synthesis conditions and Li/Mn stoichiometry, this storage regime has also been reported to partially involve the coexistence of two structurally very similar phases, often visible as a sharp peak superimposed on the broader solid-solution peak in differential capacity curves.[165] At 1 5, the remaining Li ions are ordered in a way that minimizes electrostatic repulsion and thus stabilizes the occupied 8a sites with respect to the now emptied 8a sites.[166–169] As a result, further delithiation from the occupied Li sites occurs at a higher electrode potential and leads to a sudden drop of the lattice parameter down to 8.14 Å.[164] In $Li_{0.5}Mn_2O_4$, the formerly equivalent 8a sites are thus split into two nonequivalent tetrahedral sites, one being fully occupied and the other being empty. In addition, it has been proposed that Mn^{3+}/Mn^{4+} ordering according to $Li_{0.5}Mn^{+3}_{0.5}Mn^{+4}_{1.5}O_4$ could occur analogously to the well-established Ni^{2+}/Mn^{4+} ordering observed in the isostructural high-voltage spinel LNMO.[170–174] The second plateau,

spanning from 1 5 to 2 with a significantly flatter potential profile than the first plateau, has been shown to involve a first-order phase transition from a Li-rich (1 65) to a Li-poor (1 9) spinel phase with lattice parameters of approximately 8.14 and 8.04 Å, respectively.[164]

On the other hand, Mn^{4+} in Li_{2-} Mn_2O_4 (1) can also be reduced to a valence state of +3, accompanied by the insertion of Li^+ into the remaining octahedral sites up to a final stoichiometry of $Li_2Mn_2O_4$ (t-$LiMnO_2$). This insertion process is known to proceed as a first-order phase transition from the cubic $Fd\bar{3}m$ to the tetragonal $I4_1/amd$ phase at a potential of approximately 2.89 V versus Li^+/Li, as Mn^{3+}:Mn^{4+} ratios above 1 induce a Jahn-Teller distortion in the cubic host lattice.[39,167,175,176] Since a large part of the analysis presented in this work requires the presence of a single-phase solid solution, this low-potential plateau is not further considered.

In total, electrochemical Li storage in LMO is therefore divided into three separate regimes: (i) storage at octahedral 16d sites (0 1), (ii) disordered storage at tetrahedral 8a sites (1 1 5), and (iii) ordered storage at tetrahedral 8a sites (1 5 2). Due to the effective nonequivalence of the tetrahedral sites, they will be referred to as T1 (1 1 5) and T2 (1 5 2) sites in the following. Leaving aside the possibility of Mn^{3+}/Mn^{4+} ordering, all three storage regimes involve the same redox couple with fully equivalent electronic lattice positions for all three storage regimes (0 2).

In this work, we present a comprehensive impedance study of sputter-deposited epitaxial Li_{2-} Mn_2O_4 thin films on $SrRuO_3$ (SRO) over the entire high-voltage SOC range (3.7 – 4.4 V versus Li metal, approximately corresponding to 1 2) in fine potential increments of 10 mV. We deduce a complete set of bulk electrochemical properties, consisting of the area-specific charge-transfer resistance, ionic conductivity, chemical capacitance, and chemical diffusivity as a function of SOC. Finally, we provide a defect chemical model and Brouwer diagram for LMO that consistently describes the observed trends in terms of Li chemical potential, Li activity, and point defect concentrations. The proposed model can easily be adapted for other transition metal stoichiometries and therefore paves the way toward a more detailed understanding of the defect chemistry of all spinel cathode materials.

4.2 Experimental

4.2.1 Sample Preparation

Epitaxial thin films of $SrRuO_3$ (SRO) and $LiMn_2O_4$ (LMO) were deposited via RF magnetron sputtering onto polished $SrTiO_3$ (STO) (100) single-crystal substrates (10 × 10 × 0.5 mm^3, MaTecK, Germany) in a custom-built deposition chamber (Huber Scientific, Austria). Sputter targets of LMO and SRO with a diameter of 2" were obtained from ALB Materials, USA, and AEM Deposition, China, respectively, and abraded with sandpaper before each use to en-

sure a constant target stoichiometry for successive depositions. Substrates were sonicated in a 3% aqueous solution of Extran (Merck, Germany), bidistilled water and ethanol for 10 min per step prior to use. To provide an electronic contact to the backside for electrochemical measurements, a thin film of Ti/Pt (5/100 nm) was deposited onto the sides and edges of the substrates via DC sputtering at room temperature under an Ar atmosphere of 0.7/2.5 Pa and a current density of 5 mA/cm^2. Ti is used to improve adhesion to the STO substrate, and for the given preparation procedure, we did not observe contact problems of the Ti/Pt layers. Subsequently, SRO and LMO were deposited at a substrate-to-target distance of 6.0 cm, a pressure of 2.5 Pa (25% O2, 75% Ar), a power of 60 W, and nominal substrate temperatures of 650 and 550 °C, respectively. The nominal substrate temperature on the heating stage was determined from a power-temperature calibration on a Y:ZrO_2 (100) single-crystal (9.5 mol % Y_2O_3, CrysTec, Germany) of identical dimensions using an optical pyrometer and assuming a surface emissivity coefficient of 0 9. The SRO thin films reported in this work had a thickness of approximately 170 nm as measured by transmission electron microscopy (TEM), corresponding to a deposition rate of 1.87 nm/min. For the textured LMO thin film, an average of approximately 80 nm was determined by TEM (cf. Figure 4.1g), corresponding to a deposition rate of 0.89 nm/min. Finally, the backside of the samples was covered with another sputter-deposited thin film of Ti/Pt (5/100 nm) to provide a good electrical contact to the steel plunger of the test cell. For the experiments presented in this work, two separate, nominally identical samples were prepared: one for structural characterization and one for electrochemical measurements.

4.2.2 Structural Characterization

The as-prepared samples were characterized by means of X-ray diffraction (XRD), atomic force microscopy (AFM), and TEM. Out-of-plane -2 diffractograms were acquired for 2 angles of 10° to 90° on an Empyrean X-ray diffractometer (Malvern Panalytical, UK) using a hybrid K monochromator of type 2XGe(220) on the incident beam side and a GaliPIX3D area detector in scanning line mode on the diffracted beam side. AFM images of the sample surface were recorded on a Nanoscope V multimode setup (Bruker) and analyzed using Gwyddion.[177]

4.2.3 Electrochemical Characterization

For electrochemical measurements, a thin-film sample was transferred into an argon-filled glovebox (O_2, H_2O 0.1 ppm) and assembled into a three-electrode test cell (PAT-Cell, EL-CELL, Germany) with a concentric Li reference ring electrode (EL-CELL), a Li counter electrode (approximately 10 × 10 × 0.6 mm^3, Goodfellow, Germany), a glass fiber separator (260 µm, EL-CELL), and 80 µL of standard organic electrolyte (1 M $LiPF_6$ in a 1:1 mixture of ethylene carbonate and dimethyl carbonate, Aldrich, USA). All electrochemical measure-

ments were carried out at room temperature on a Biologic SP200 potentiostat with a built-in impedance analyzer. Cyclic voltammetry (CV) was performed at a scan rate of 1 mV/s in the working electrode potential range of 3.7 – 4.4 V versus Li^+/Li. Potential-controlled impedance spectra (200 kHz – 10 mHz, 6 points per decade) were recorded for the same voltage range in intervals of 10 mV using a perturbation amplitude of 10 mV. Before each impedance measurement, the working electrode was left to equilibrate for 5 min at the given potential.

4.3 Results and Discussion

4.3.1 Epitaxial LMO/SRO Thin Films

Figure 4.1 summarizes the structural characterization of a typical RF-sputtered LMO thin film on (100)-oriented SRO/STO. As shown schematically in Figure 4.1a, the sides and backside of the STO single-crystal substrate were sputter-coated with Ti/Pt to provide a good electrical contact between the subsequently deposited SRO thin-film current collector and working-electrode steel plunger of the test cell. The -2 XRD scan in Figure 4.1b clearly shows the (100), (200), and (300) reflexes of STO and SRO, with the SRO reflexes shifted to lower 2 angles with respect to the substrate. More specifically, the (200) reflex is located at 46.49° and 45.19° for STO and SRO, respectively. In addition, the (400) LMO reflex is clearly visible at 43.97°. The corresponding out-of-plane lattice parameters amount to 3.904, 4.010, and 8.230 Å for STO, SRO, and LMO, respectively. For SRO, the elongated out-of-plane lattice parameter implies a significant compressive strain and tetragonal distortion. Reciprocal space mapping of the (103) SRO/STO reflex confirmed that the SRO thin film takes on the in-plane lattice parameter of the STO substrate, as shown in Figure 4.12 of the Appendix. For the LMO thin film, the out-of-plane parameter is virtually identical to that reported for bulk LMO. This, together with the absence of any additional LMO reflexes, suggests that LMO grows epitaxially on the SRO thin film with a significant compressive strain, but immediately relaxes to its bulk lattice parameter within a very short distance from the interface. Due to lack of a suitable reflex with sufficient signal intensity, reciprocal space mapping was not performed for the SRO/LMO films.

Figure 4.1d shows a high-resolution TEM image of the LMO/SRO interface as viewed along the [010] zone axis, confirming the heteroepitaxial growth of LMO on SRO. Despite the heavily strained interface, the film exhibits excellent crystallinity with a clear (200) SRO // (400) LMO epitaxial relationship to the substrate, as shown schematically in Figure 4.1c. Given the large lattice mismatch of 5% between LMO and STO, the observed strain relaxation is hardly surprising. For the present analysis, the absence of strain is highly beneficial, as it means that the sample is representative of bulk LMO, and the extracted electrochemical properties can be understood as intrinsic material properties.

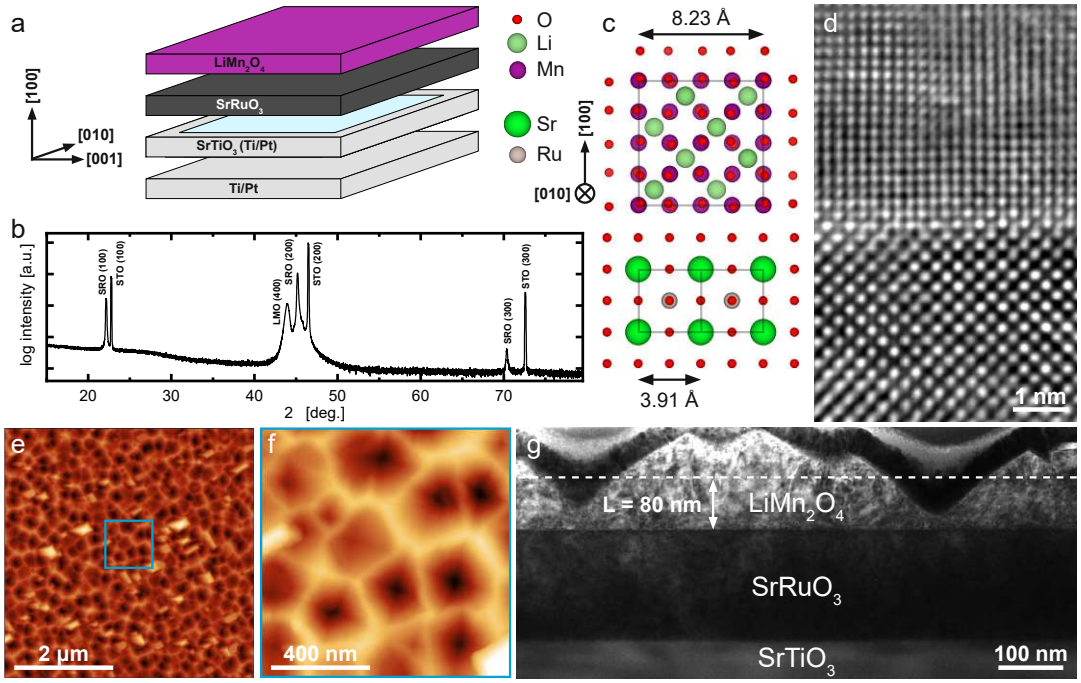

Figure 4.1: **(a)** Schematic representation of a typical sample, consisting of a (100)-oriented polished STO single crystal coated with a bilayer of Ti/Pt on the backside and around the edges, an epitaxial SRO thin-film current collector, and epitaxial LMO thin film. **(b)** -2 X-ray diffractogram showing the (h00) reflexes of LMO and SRO, suggesting the presence of an epitaxial LMO/SRO bilayer on the STO (100) substrate. **(c)** Atomic representation of the (200) SRO // (400) LMO epitaxial relationship, which is confirmed by the high-resolution TEM image of the LMO (top) / SRO (bottom) interface in panel **(d)**. For SRO, the in-plane lattice parameter was confirmed by reciprocal space mapping (Figure 4.12). For LMO, strain relaxation is assumed, resulting in the in- and out-of-plane lattice parameters both being identical to the bulk value of 8.23 Å. **(e,f)** AFM images of the LMO thin-film surface, showing the characteristic pyramidal morphology of a (400)-oriented spinel thin film. **(g)** Bright-field TEM image showing an average LMO film thickness of about 80 nm.

Figure 4.1e,f shows two AFM images of the thin-film surface at different magnifications. The sample exhibits the characteristic surface morphology of a (400)-oriented LMO film, which results from a preferential exposure of the 111 crystal facets.[178] Statistical analysis of the AFM images revealed an RMS roughness of 30 nm and an effective surface area 21% higher than the nominal substrate area.

The bright-field TEM image in Figure 4.1g is in good agreement with these AFM measurements, showing a dense thin film with pyramidal morphology characterized by well-defined angles, with an average thickness of approximately 80 nm. The maximum and minimum thicknesses of the film in the selected sample area were measured as roughly 150 and 30 nm, respectively. This strong variation of thickness leads to a continuous distribution of transport lengths throughout the sample and may cause some frequency dependency of the current distribution. However, owing to the absence of any significant porosity or tortuosity, we still consider the extraction of resistive or capacitive properties as meaningful. Furthermore,

the consistent angles that characterize the film morphology should lead to a homogeneous thickness distribution between the extrema, meaning that the corresponding errors in the calculations of length-normalized properties (ionic conductivity and chemical capacitance) should be minor. For the following analysis, we therefore assume a flat thin film of 80 nm thickness. For the calculations of the charge-transfer resistance, we normalize by the effective surface area measured by AFM, that is, 1.21 cm^2. Current densities in the cyclic voltammetry (CV) scans are normalized by the substrate area (1 cm^2). Although the XRD and TEM measurements indicate a dense, epitaxial thin film, the presence of some grain boundaries cannot be excluded, for example, between the pyramids. Assuming that such grain boundaries, if present, are poorly ion conducting as in other Li-ion conducting materials,[179] this should not significantly impact the measured transport properties, and the extracted properties would still be close to those of the bulk material. Only if the grain boundaries allow fast ion conduction,[180] the extracted properties would have to be regarded as effective rather than strictly bulk-specific transport properties.

4.3.2 DC Electrochemical Characterization

Figure 4.2a shows the CV curve of a typical LMO thin film measured versus Li metal at a scan rate of 1 mV/s from 3.7 to 4.4 V. The sample clearly exhibits two separate storage regimes, with two distinct CV peaks appearing at 4.01 and 4.14 V versus Li^+/Li. These correspond to the emptying and filling of the previously described nonequivalent tetrahedral sites T1 and T2, which effectively differ in lattice site energy due to Li ordering at 1 5. As expected from the different storage modes involved, the T1 peak is significantly broader (solid solution, FWHM = 111 mV) than the T2 peak (biphasic transition, FWHM = 65 mV). In agreement with literature,[165] there appears to be an additional narrow peak superimposed on the T1 peak, suggesting the presence of a small miscibility gap within the T1 storage regime. Nonetheless, the solid-solution behavior remains dominant in this region, with little current added by the superimposed biphasic peak. Despite the relatively high peak current densities of about 90 μA/cm^2, kinetic overpotentials are small, with a charge/discharge hysteresis in the range of 10 mV, judging by the differences between the respective peak positions. The positive current offset at 4.4 V indicates a minor background current in the range of 1 μA/cm^2 that decreases toward lower potentials and is even slightly negative (−0.5 μA/cm^2) at 3.7 V. A charge/discharge curve, obtained by integration of the CV scan in Figure 4.2a, is shown in Figure 4.2b. Absolute values of charge were normalized by the thin-film mass, which was determined via the bulk density of LMO (4.19 g/cm^3) by assuming a flat, singlecrystalline thin film of 80 nm thickness. The LMO thin film exhibits a charge/discharge capacity of 137/132 mAh/g, corresponding to 93/89% of the theoretical capacity (148 mAh/g), in good agreement with commonly reported values,[168,181–183] and a coulombic efficiency of 96%. The close agreement between the measured and theoretical capacities suggests a good

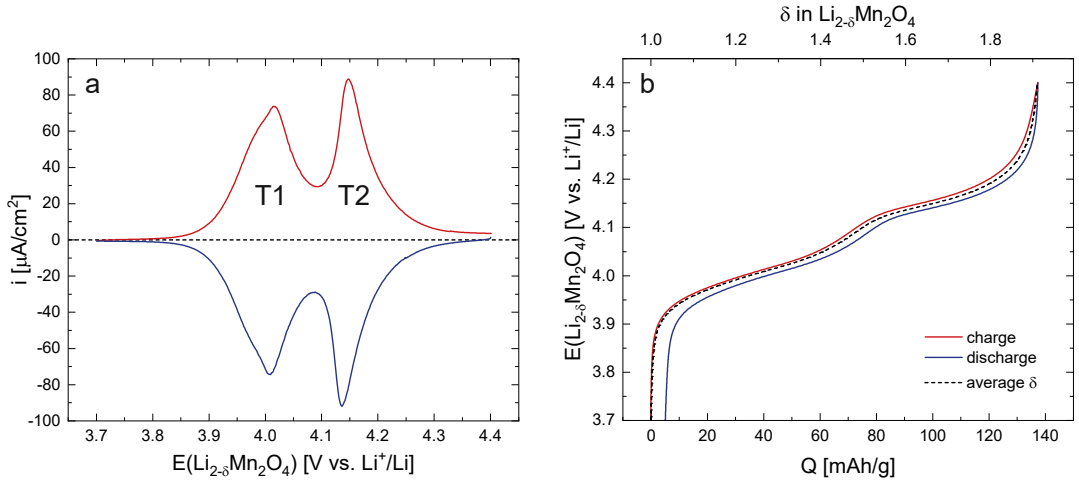

Figure 4.2: (a) Cyclic voltammogram (CV) of a fresh LMO thin-film electrode measured at a scan rate of 1 mV/s from 3.7 to 4.4 V. T1 and T2 denote the two nonequivalent types of tetrahedral sites due to Li ordering and mark the respective storage regimes. **(b)** Coulometric titration curves obtained by integration of the CV curves in panel (a). The values of given at the top axis were obtained from the average charge at a given potential and shifted to = 1 at 3.7 V.

electrical contact to the LMO film. Background currents in DC measurements may play a much larger role for thin-film samples due to the low charge/discharge current densities in the μA/cm^2 range, which could explain the relatively low coulombic efficiency compared to typical bulk electrode measurements. However, a second CV scan (not shown), measured after the extensive series of impedance measurements, was virtually identical to the initial scan. The coulombic inefficiency of 4% between charge and discharge can therefore safely be attributed to the observed background current in the CV scan, rather than any kind of material degradation.

Furthermore, the Li nonstoichiometry extracted from the charge/discharge curve as a function of electrode potential is indicated as a dashed line in Figure 4.2b, with the corresponding axis given at the top. Since the observed background current raises and lowers the effectively measured charge and discharge capacities, respectively, the reported values of were obtained from the average charge at a given potential and shifted to 1 at 3.7 V. The resulting values are in the range of 1 1 9, indicating a final charged state with a stoichiometry of $Li_{0.1}Mn_2O_4$ at 4.4 V. The still incomplete extraction of Li at this cut-off voltage is in good agreement with previous reports.[165,174,184–187]

4.3.3 Electrochemical Impedance Spectroscopy

Given the excellent reversibility of charge and discharge and the stability of the thin film, the electrochemical properties of LMO can be assumed to vary reversibly with electrode potential and hence Li activity, without any significant drift due to material degradation. Impedance spectra were measured for a broad range of stoichiometries to determine the charge-transfer

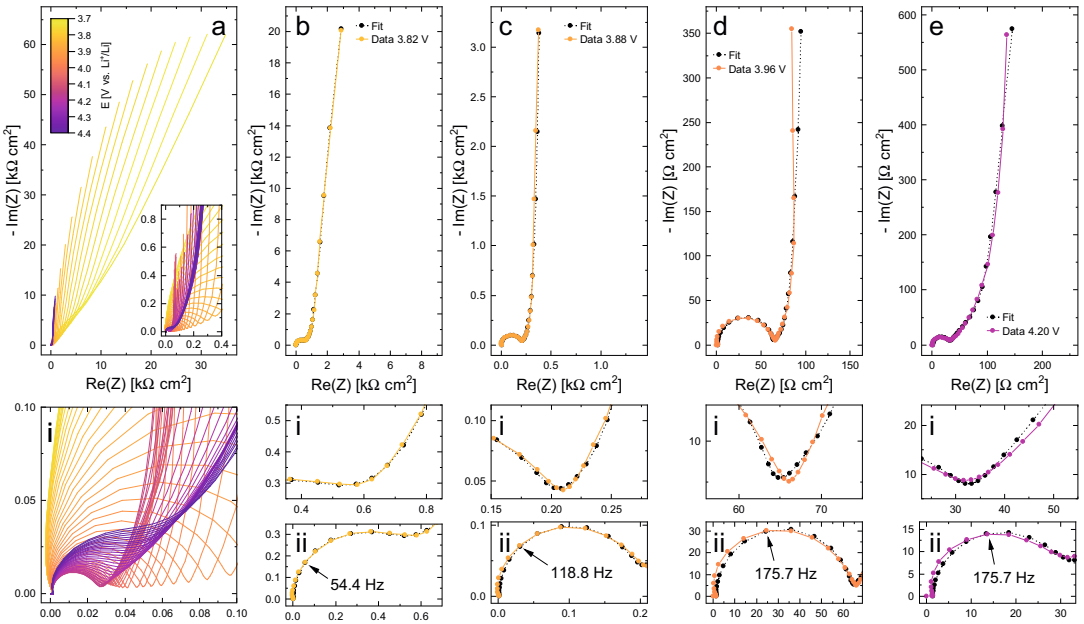

Figure 4.3: Series of impedance spectra at equilibrium electrode potentials of 3.7 to 4.4 V in intervals of 10 mV. Magnifications of the medium-to-high frequency regions are shown in subfigures (i) and (ii). **(a)** Full series of spectra, generally showing a significant decrease of real and imaginary impedance values from low to high electrode potential. The charge-transfer resistance reaches a minimum around 4.15 V. **(b – e)** Exemplary impedance spectra and fits at 3.82, 3.88, 3.96, and 4.20 V. The arrows in subfigures (ii) indicate the upper cut-off frequency used for the fit to exclude the slightly distorted high-frequency region.

resistance R_{ct}, ionic conductivity σ_{ion}, chemical capacitance C_{chem}, and Li chemical diffusivity $\widetilde{D}$ as a function of SOC. A series of measurements, ranging from 3.7 to 4.4 V versus Li^+/Li in potential increments of 10 mV, are shown as a Nyquist plot in Figure 4.3a and the corresponding magnification in Figure 4.3ai. Overall, the impedance spectra exhibit a strong dependence on electrode potential, with both real and imaginary parts varying over orders of magnitude. Starting at 3.7 V, both the real and imaginary parts of the spectra decrease with increasing potential, reaching a minimum around 4.0 – 4.1 V, and then increasing again toward 4.4 V. Qualitatively, this implies a maximum in chemical capacitance as well as minima in the interfacial and bulk transport resistances.

The general transmission line model (Figure 4.4a) first proposed by Jamnik and Maier[54,58–61] describes the impedance of a one-dimensional current flow in a mixed conducting material such as an LMO electrode. This equivalent circuit consists of two resistive rails describing electronic and ionic transport ($R_{eon} = \sum r_{eon}$, $R_{ion} = \sum r_{ion}$) coupled by chemical capacitors ($C_{chem} = \sum c_{chem}$), with the chemical capacitance defined as[58,137]

$$C_{chem} = q^2 V \left(\frac{\partial \mu_{Li}}{\partial c_{Li}} \right)^{-1} \quad , \tag{4.1}$$

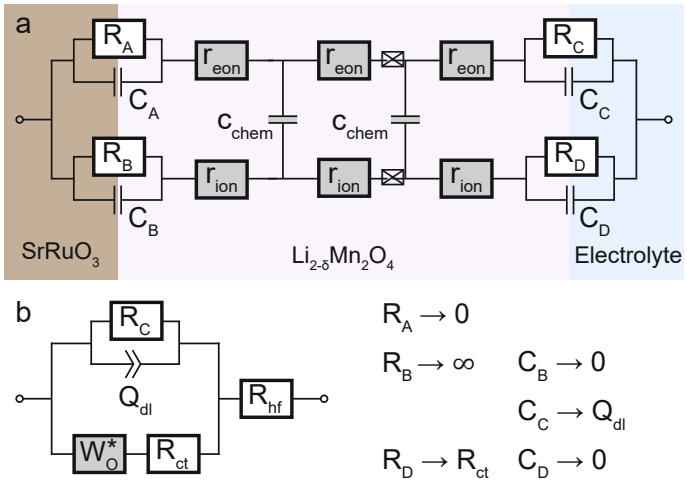

Figure 4.4: (a) General one-dimensional transmission line with four distinct terminals. The resistive and capacitive elements at the SRO/LMO and LMO/electrolyte interfaces can be adapted to account for selective blocking behavior. **(b)** Modified Randles' circuit obtained by simplification of circuit (a) and replacement of the open Warburg element by an anomalous diffusion element .

where is the elementary charge, is the sample volume, is the Li chemical potential, and is the concentration of formally neutral Li, that is, Li^+ together with its electron. The Li chemical potential is defined by the fundamental relationship

(4.2)

with Boltzmann's constant , temperature , the Li chemical potential of metallic Li (reference potential), and the Li activity . The Li activity is related to the electrode potential versus Li metal via

(4.3)

To simplify the equivalent circuit in Figure 4.4a for the case of an LMO electrode, we assume a high electronic conductivity such that 0. If the electronic conductivity was comparable to, or even lower than, the ionic conductivity, one would expect a notable SOC-dependent contribution to the high-frequency offset of the impedance spectra. This is not observed here, and we therefore consider the above assumption as reasonable. The chemical diffusion coefficient can then be expressed as

2 2 (4.4)

where is the volume-specific chemical capacitance, is the film thickness, and is the time constant of the Li storage process.[67] Furthermore, we assume that the SRO current collector presents an electronically ohmic contact and ionically blocking boundary to the mixed conductor and we neglect the corresponding interfacial capacitances, meaning that , 0 and . At the LMO/electrolyte interface, we identify and as the double-layer capacitance and charge-transfer resistance , respectively. Our experiments revealed that, particularly for small values of , side reactions may lead to some background current, that is, a finite DC resistance. This is considered in our impedance model by leaving a finite in the circuit. However, the inclusion of does not interfere with the further simplification of the circuit by replacing the transmission line with an open Warburg element . As in our previous work,[51] we further replace the open Warburg element by an anomalous diffusion element , implemented in the impedance-analyzing software EC-Lab (Biologic, France). This allows for a more general power-law dependence on the frequency, instead of the standard square-root behavior $^{1\bullet 2}$. The corresponding impedance expression can be written as

$$\frac{\bullet 2}{1 \quad \bullet 2} \tag{4.5}$$

with a nonideality parameter 0 1, and is similar to the impedance of the anomalous finite-space diffusion element reported by Bisquert.[136] In the present study, turned out to be in the range of 0.7 – 0.8.

Finally, we replace by a constant-phase element and add a high-frequency offset resistance to account for the sum of resistances due to the electrolyte and other cell components to arrive at the equivalent circuit shown in Figure 4.4b. Please note that the placement of the double-layer capacitance on the electronic (rather than the ionic) rail terminal is required to consider it in parallel to the open Warburg element. Only then, the model is consistent with the commonly used Randles' circuit.[188,189] In Figure 4.13 of the Appendix, the simulated impedance response of this circuit is shown in comparison to Randles' circuit for a typical set of material parameters. Beside the change of the capacitive low-frequency end (Randles' circuit) toward a large semicircle-onset (circuit c in Figure 4.13), the circuit in Figure 4.4b additionally features a steepening of the 45° regime and a flattening of the 90°, which adequately describes the empirical impedance spectra of most thin-film battery electrodes.[109,111,112,132]

Figure 4.3b-e shows selected impedance spectra measured at 3.82, 3.88, 3.96, and 4.20 V with the corresponding fits. At 3.82 and 3.88 V, the quality of fit is excellent for almost the entire frequency range, with a minor deviation at the highest frequencies around the onset of the charge-transfer semicircle, where the spectra appear slightly distorted toward smaller real values. At 3.96 and 4.20 V, there is additionally a deviation in the low-frequency capacitive tail, with the spectra again appearing slightly distorted toward smaller real values at the

lowest frequencies. We attribute these distortions to a minor geometrical misalignment of the square-shaped single-crystal substrate and Li counter electrode with respect to the concentric ring-shaped Li reference electrode. Nonetheless, the essential features of the impedance spectra are captured very well, and the extracted material properties vary continuously with electrode potential (see Figure 4.5). Furthermore, the validity of the extracted parameters is supported by their excellent agreement with DC measurements and thermodynamic theory, as demonstrated by the following analysis.

4.3.4 Analysis of Material Parameters

Figure 4.5 shows the four essential material properties , , , and in a logarithmic plot as a function of electrode potential. The inverse of was plotted to emphasize the parallels and differences between the closely related properties and . Red and blue points indicate the values obtained from the impedance fits for the forward (3.70 – 4.40 V) and the backward (4.39 – 3.70 V) scan, respectively. The solid lines in Figure 4.5c additionally show the values of obtained from the CV scan in Figure 4.2a via the relation

—— (4.6)

with the current density and the scan rate , where red and blue again indicate the forward and backward scan, respectively. On the top axis, log is shown as calculated from the electrode potential via Equation (4.3). All four properties show a strong dependence on the electrode potential, and hence on the SOC and Li activity, with and varying over more than two, and even changing over three orders of magnitude. The smallest variation is seen for , with roughly one order of magnitude.

For the forward scan, starting at 3.70 V, decreases exponentially from an initial value of about 7600 Ω cm^2 (1• 1 3 10 ^{4} S/cm^2) down to only 29 Ω cm^2 at 4.15 V. Above 4.15 V, starts to increase again, reaching a nearly constant value of 70 Ω cm^2 at 4.40 V. The obtained values are in good agreement with literature.[133,190] In the backward scan, starting at 4.39 V, the values of are slightly higher, with a maximum deviation of about +29% around 3.85 V, but otherwise closely match those from the forward scan. Since does not only depend on the electrode's surface concentration of ionic charge carriers, but furthermore varies with the concentration-dependence of the corresponding Galvani potential step across the LMO/electrolyte interface,[51,159] its variation with Li activity can be highly complex and a mechanistic discussion is beyond the scope of this work. At this point, it is sufficient to state that the variation of qualitatively reflects the Li concentration in the material, transitioning from a vacancy-controlled insertion reaction with very few tetrahedral Li vacancies at low potentials to a Li^+-controlled (high potential) insertion reaction. Accordingly, it reflects the two opposite defect regimes that will be further described in the defect chemical analysis.

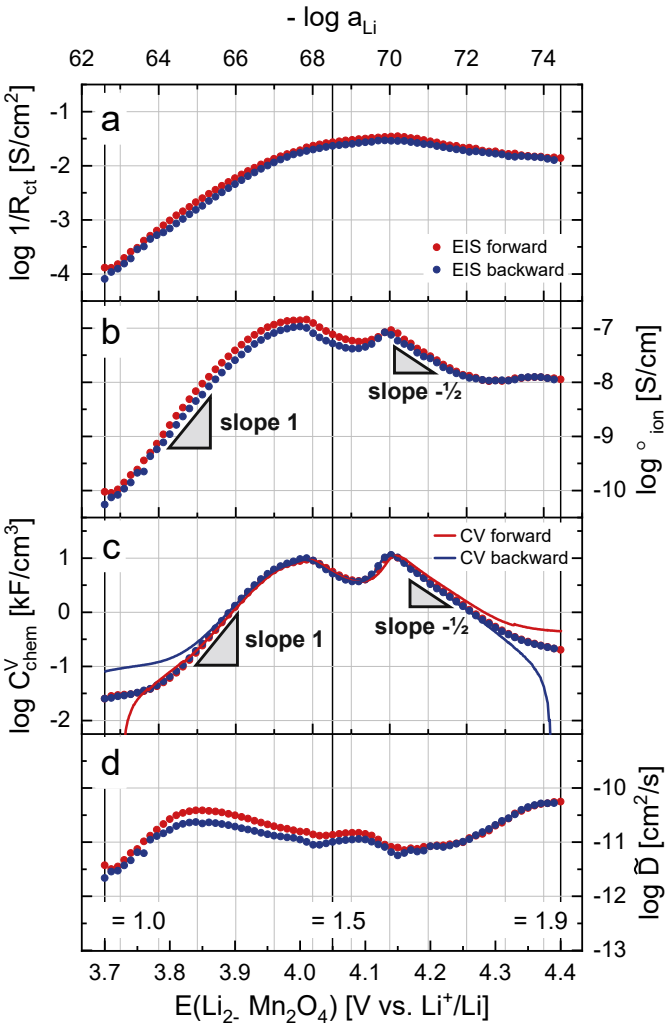

Figure 4.5: Electrochemical properties of the LMO thin film as a function of log and electrode potential, as extracted from the impedance data. Results from the forward and backward scans are shown as red and blue dots, respectively. **(a)** Inverse charge-transfer resistance. **(b)** Ionic conductivity, slopes of 1 and 1•2 are indicated for the dilute regions. **(c)** Volume-specific chemical capacitance, values obtained from the CV scan are shown for comparison. **(d)** Chemical diffusion coefficient.

The ionic conductivity , on the other hand, should be directly proportional to the concentration of the relevant ionic charge carriers, as long as the corresponding carrier mobilities remain relatively constant. Experimentally, was found to vary over three orders of magnitude and roughly follows the double-peak shape of the CV curve in Figure 4.2a. As shown in Figure 4.5b, increases exponentially from 10^{-10} S/cm at 3.70 V to more than 10^{-7} S/cm around 3.95 – 4.00 V. After a slight decrease and minimum around 4.08 V, increases back to 10^{-7} S/cm at 4.14 V and subsequently starts to decrease exponentially until it reaches a near-constant value of 10^{-8} S/cm at 4.26 V and above.

Bulk ionic conductivity values of LMO have rarely been reported in the literature, and even fewer works describe its variation as a function of SOC. Guan and Liu obtained room-temperature ionic conductivities in the order of 10 ^{6} S/cm by means of (nontrivial) electron blocking electrode impedance measurements on sintered pellets of nominally stoichiometric LMO powder,[191] which is four orders of magnitude higher than our values measured at the same stoichiometry. However, the high ionic conductivity measured in ref. 191 might be due to insufficient equilibration times and low-end frequency range in the corresponding DC and impedance measurements, respectively. Although other explicit reports of ionic conductivities are hard to find, various thin-film studies report the SOC-dependent chemical diffusion coefficient together with differential capacities,[188,189,192–194] from which the ionic conductivity can be roughly estimated (via Equation (4.4)) to be in the range of 10 ^{12} to 10 ^{9} S/cm, which is in good agreement with our data. Moreover, the strong variation of with electrode potential at high and low SOC seen in Figure 4.5b is consistent with the strong variation of ionic charge carrier concentrations expected from the defect model (cf. next section), and we therefore consider our experimental values of as meaningful. The two extended linear regions in Figure 4.5b around 3.70 – 3.90 and 4.14 – 4.26 V exhibit slopes versus log of about 1 and 1•2, respectively, and indicate regions where / 10 $^{\log}$ with . The absolute values of the observed slopes and their implication for the underlying defect chemical behavior will be discussed in the next section.

The volume-specific chemical capacitance , plotted in Figure 4.5c, qualitatively follows the same trend as and, for the most part, is in excellent quantitative agreement with the values obtained from the CV scan in Figure 4.2a via Equation (4.6). The additional capacitance seen in the CV data for the forward scan at high potentials and the backward scan at low potentials can be attributed to the previously described background currents in the cell. The diverging values in the forward and backward scan at low and high potentials, respectively, result from a reversal of the current direction in these regions following the reversal of the scan direction. The values of obtained from the impedance fits are almost identical for the forward and backward scans, ranging from 25 F/cm^3 at 3.70 V up to 9.3 kF/cm^3 at 4.01 V and 11 kF/cm^3 at 4.14 V, with a minimum of 3.8 kF/cm^3 between the two maxima. From 4.14 V upward, decreases again down to 200 F/cm^3 at 4.40 V, with the corresponding slope in the log-log plot versus Li activity slightly flattening out above 4.30 V. Values of have rarely been reported as volume-specific capacitances, but the corresponding CV current densities found in literature[133,190,195,196] are similar to those shown in Figure 4.2a. As already seen for , the potential regions 3.80 – 3.95 and 4.14 – 4.30 V exhibit linear slopes of approximately 1 and 1•2, respectively.

The chemical capacitance data from impedance measurements can also be integrated over the electrode potential, as shown in Figure 4.6, to obtain the total charge according to

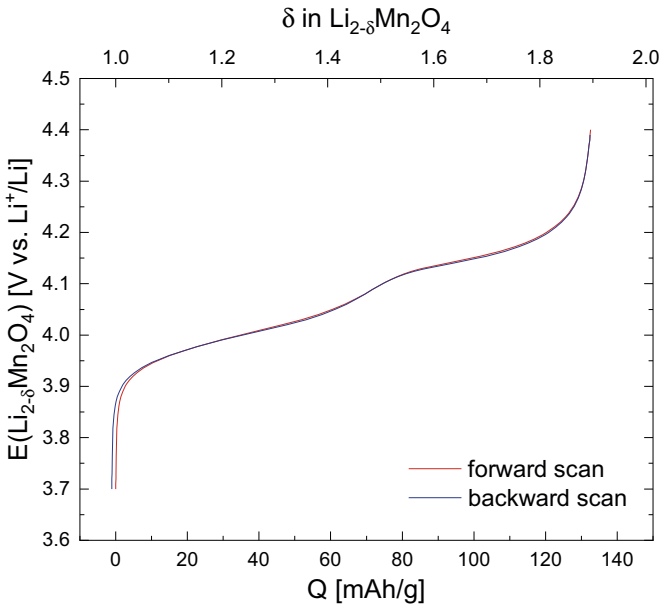

Figure 4.6: Equilibrium charge curve (OCV curve) obtained by integration of the chemical capacitance values from Figure 4.5c via Equation (4.7). The values obtained for the forward (red) and backward (blue) scan are nearly identical. Both the charge and nonstoichiometry values agree very well with the CV data in Figure 4.2.

$$Q = V \int C^{V}_{chem}\, dE \quad . \tag{4.7}$$

The resulting charge/discharge curve should be unaltered by side reactions and truly reflects the relation between the equilibrium open-circuit potential and SOC. In fact, the impedance-based potential profile in Figure 4.6 is not only very similar to that obtained from CV measurements but also nearly identical for the forward and backward scans. This nicely demonstrates the fact that the chemical capacitance, and hence the equilibrium charge curve, is contained in the potential-dependent impedance response of a Li insertion electrode,[47,48,133,134] and, as an equilibrium property, can even be extracted more accurately from impedance spectra than from DC experiments. A direct comparison of the charge/discharge profiles obtained from CV and EIS is shown in Figure 4.14 of the Appendix.

Finally, the logarithmic chemical diffusivity can be calculated from σ_{ion} and C^{V}_{chem} according to Equation (4.4). It is shown in Figure 4.5d as a function of electrode potential and negative logarithmic Li activity. Starting at 3.70 V, $\widetilde{D}$ first increases from about $10^{-11.5}$ to $10^{-10.5}$ cm^2/s at 3.85 V and then gradually decreases again down to 10^{-11} cm^2/s at 4.25 V. Above 4.25 V, $\widetilde{D}$ increases again, up to a final value of about $10^{-10.3}$ cm^2/s at 4.40 V. In agreement with Equation (4.4), $\widetilde{D}$ remains rather constant in regions where σ_{ion} and C^{V}_{chem} vary in concert (3.80 – 4.25 V). Overall, the obtained values of $\widetilde{D}$ are in good agreement with literature.[133,189,193,196,197]

4.3.5 Defect Chemical Model

In terms of atomistic defect chemical considerations, the thermodynamically defined chemical capacitance (cf. Equation (4.1)) is probably the most powerful material descriptor. It is often referred to as differential capacity or • in the battery literature, and experimentally, it can be extracted from both AC impedance spectra and DC coulometric titration curves. To further evaluate and according to Equations (4.1) and (4.2), expressions for the dependence of all charged species on are required.[34] In the following, these expressions will first be derived in generic form to describe Li insertion into (i) a material of the general formula $Li_{1-\delta}MO_2$ with only one type of occupiable Li site, such as a layered oxide, and (ii) a material of the type Li_{2-} Mn_2O_4 with two different Li sites, such as an ideal spinel that has octahedral and tetrahedral sites available for Li insertion. Finally, we will extend our defect chemical description to accurately describe the experimentally observed energetic splitting of tetrahedral sites in the specific case of Li_{2-} Mn_2O_4 and compare the predicted values of to the experimental data to validate our model.

We start by formulating the Li insertion equilibrium of $Li_{1-\delta}MO_2$ in Kröger-Vink notation for the two relevant defects, that is,

(4.8)

Here, neutral Li must not be confused with Li ions in the cathode material. Rather, Li can be regarded as the combination of a Li ion in the electrolyte and an electron in the current collector according to . The activity of this formally neutral Li is then defined by the voltage versus metallic Li (see Equation (4.3)), i.e., the electrochemical potential of the electrons in the current collecting phase, and thus also in the cathode. Only one type of Li site is available (representing a vacant site) and the transition metal M is in the valence state of either +3 or +4, with an electron hole corresponding to ^{4} . The concentration of each species (e.g., holes and vacancies) can be referenced to the total concentration of formula units ^{0} according to

$$\frac{}{0} \tag{4.9}$$

where is the site occupancy of species and is the number of the corresponding sites per formula unit. For example, 1 and 1, since all Li sites are assumed to be filled for $LiMO_2$. We neglect the interactions of all ionic and electronic charged species, as for dilute systems, but consider site restrictions that become relevant when broad variations of Li stoichiometry take place, that is, when a lattice site is almost completely emptied or filled.

The corresponding balance of chemical potentials reads

$$0 \tag{4.10}$$

with the individual site-restricted chemical potentials of vacancies and holes being[33,198]

$$^{0} \quad \frac{}{1} \tag{4.11}$$

and

$$^{0} \quad \frac{}{1} \tag{4.12}$$

where symbols ^{0} denote standard terms, that is, molar Gibbs free energies for noninteracting defects. Equations (4.10), (4.11), and (4.12) can be combined to obtain the corresponding law of mass action

$$\frac{}{1 \quad 1} \quad ^{0} \quad ^{0} \bullet \tag{4.13}$$

In the absence of other charge carriers such as dopants, charge neutrality requires

(4.14)

and from Equation (4.9), we thus obtain

(4.15)

For 1, the concentrations of point defects (vacancies and holes) and their respective occupied sites are related via

$$1 \quad _{4} \quad 1 \quad _{3} \tag{4.16}$$

where indicates the fraction of Li sites occupied by and $_{3}$ / $_{4}$ are the transition metal fractions in the respective valence states. From Equation (4.13) and , we obtain

$$\frac{1}{^{0} \quad ^{0} \bullet 2} \tag{4.17}$$

$$1$$

and thus, the concentration of all four species is given as a function of Li chemical potential. In Equation (4.17), is related to the electrode potential and Li activity according to Equation (4.3). For small defect concentrations, that is, before site restriction becomes relevant, Equation (4.17) reduces to

$$^{0} \quad ^{0} \bullet 2 \tag{4.18}$$

According to Equations (4.1), (4.9), and (4.10), the chemical capacitance can be evaluated as

$$^{2}\ \frac{\quad}{\quad}\ \frac{\quad}{\quad}\ ^{1}\ \frac{^{2}\ ^{0}}{\quad}\ \frac{1}{1}\ \frac{1}{1}\ ^{1} \tag{4.19}$$

which, for and , becomes

$$\frac{^{2}\ ^{0}}{2}\quad 1 \tag{4.20}$$

The concentrations of , , ^{3}, and ^{4} ( ) as calculated by Equations (4.16) and (4.17) and the corresponding chemical capacitance from Equation (4.20) are plotted as a function of log in Figure 4.7a for ^{0} • 3 99 V and ^{0} • 0 00 V. Although the individual values of ^{0} are arbitrary in these generic model calculations, their sum determines the location of chemical capacitance peaks in the defect chemical model. The value of ^{0} is arbitrarily set to zero, and ^{0} is then chosen such that ^{0} ^{0} • corresponds to the experimentally found peak position of the first tetrahedral regime in Li_{2-} Mn_2O_4 (see next section). For the sake of clarity, only is written in Kröger-Vink notation. As expected from Equation (4.18), and ^{4} both vary with a slope of 1•2 at high (low), where ^{3} ^{0}. Conversely, at low (high), and ^{3} vary with a slope of 1•2 while ^{4} ^{0}. The transition point between these two regimes marks the point of the highest chemical capacitance, where the concentration of all four species is the same. In this transition region, where the concentrations of vacant and occupied sites are similar in magnitude, site limitations start to become relevant, and the point defect concentrations are accurately described by Equation (4.17). The sum of ^{0} and ^{0} defines the electrode potential where peaks and the charge curve plateau is the flattest. The individual values of ^{0} and ^{0}, however, are chosen arbitrarily and are assumed to remain constant across the entire stoichiometry range.

It is worth mentioning that our chemical capacitance peak has a different reason than similar peaks found for acceptor-doped mixed conducting oxides used in high-temperature solid oxide fuel cells. There, the peak is caused by a change of the charge compensation mechanism from hole to oxygen vacancy compensation when changing the oxygen chemical potential.[53] In our case, however, site restriction is key and it is always the smaller of the two concentrations and 1 , which dominates .

The above analysis can be extended for the case of two (or more) Li sites that share the same redox-active species. For each Li site , an insertion equilibrium and the corresponding chemical potential balance can be formulated according to

(4.21)

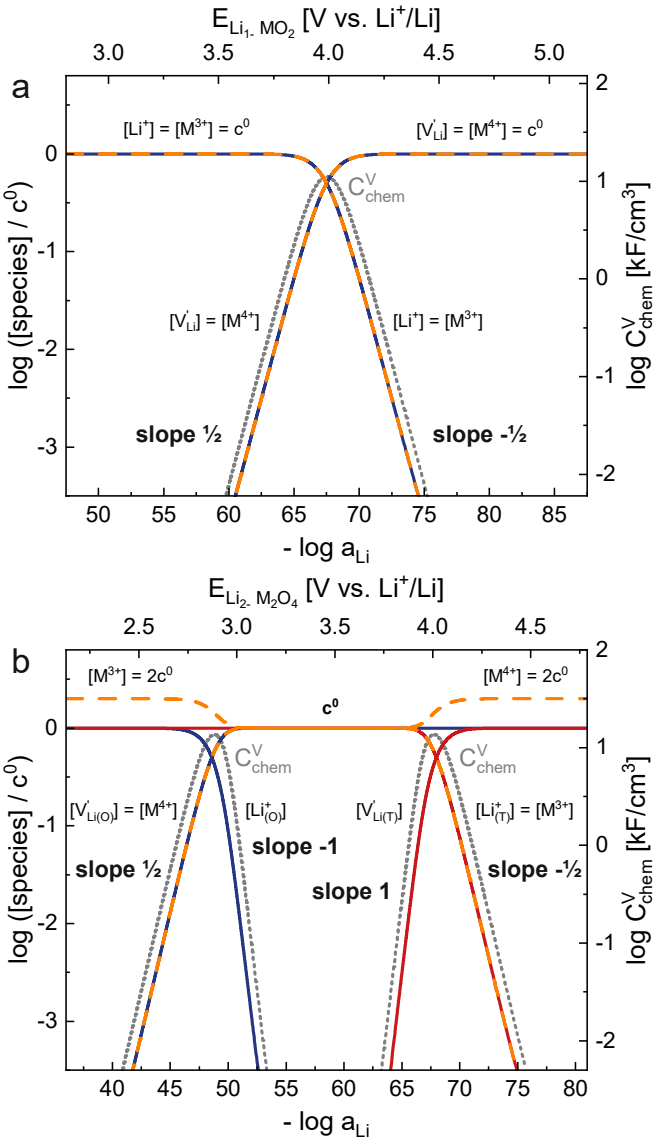

FIGURE 4.7: Calculated Brouwer diagrams for a generic **(a)** layered oxide $Li_{1-}MO_2$ (^{0} • 3 99 V, ^{0} • 0 00 V, 1) and **(b)** spinel $Li_{2-}M_2O_4$ (^{0} • 2 90 V, ^{0} • 3 99 V, ^{0} • 0 00 V, 1, 2). The logarithmic site occupancies of all relevant species are plotted on the left, and the corresponding volume-specific chemical capacitance is plotted on the right y-axis as a function of log (bottom) and electrode potential (top). For each occupiable Li lattice site, there is a corresponding peak in . For the spinel material, the difference of for vacancies (1) and holes (2) leads to asymmetric Brouwer-slopes of the two peaks. The volumes of one formula unit are assumed as 35 and 70 Å^3 for $Li_{1-\delta}MO_2$ and $Li_{2-\delta}M_2O_4$, respectively.

and

0 (4.22)

Because all vacancies on available sites are in equilibrium with the same and , it is immediately clear that the chemical potential of vacancies must also be the same for all sites. Equations (4.11) and (4.12) are still valid for and each Li site individually. However, two laws of mass action result, one for each site (with different ^{0} and 2), which are coupled by a more complicated charge neutrality equation. In principle, the balance of chemical potentials combined with the appropriate charge neutrality condition still defines the relevant point defect concentrations as a function of Li activity. However, the corresponding system of equations can no longer be solved analytically. This can be circumvented, at least partially, by expressing the total vacancy site fraction as

(4.23)

Using Equations (4.9) and (4.11), we can express the dependence of the individual vacancy site fractions on the common vacancy potential according to

$$\frac{}{0} \qquad \frac{}{1} \qquad (4.24)$$

For a hypothetical spinel cathode material $Li_{2-}M_2O_4$ that offers octahedral (O) and tetrahedral (T) lattice sites for Li insertion, 1 and ^{0} ^{0} . The functional inverse of Equation (4.23), , can be obtained numerically and inserted into Equation (4.10) to arrive at the total Li chemical potential . The chemical potential of holes is obtained directly from Equation (4.12) with 2 (•2), since two ^{3} • ^{4} redox centers are available per formula unit. For a better overview, the obtained chemical potential profiles of vacancies and holes are shown in Figure 4.15 of the Appendix, together with an explicit evaluation of Equations (4.23) and (4.24).

The resulting point defect concentrations ("Brouwer diagram") are shown in Figure 4.7b in a log-log plot versus Li activity for ^{0} • 2 90 V, ^{0} • 3 99 V, and ^{0} • 0 00 V. Due to the introduction of a second lattice site, the defect chemical behavior of $Li_{2-}M_2O_4$ now exhibits four distinct subregimes, two for each site. Those shape the dependence of , and hence also , on . Starting at a stoichiometry of $Li_2M_2O_4$ (high , low), Li is extracted from the octahedral sites and and ^{4} increase with a slope of 1•2, while ^{3} 2 2 2 ^{0}. Once most of the octahedral sites are empty, decreases with a slope of -1, while ^{3} ^{4} ^{0}. reaches a maximum close to and the two decreasing sides of the peak are again determined by the smaller of the two concentrations and 1 . The third subregime is entered when the electrode potential is further increased until , which occurs at a stoichiometry of LiM_2O_4. Li is now extracted from the tetrahedral sites and increases with a slope of 1, together with . At the lowest activities and

highest potentials, once most of the tetrahedral sites are empty, and ^{3} decrease with a slope of 1•2, while ^{4} 2 2 2 ^{0}. In the transition region between these last two subregimes, exhibits another peak close to . It is therefore evident that, for every lattice site available for Li insertion and extraction, there is an associated peak in .

4.3.6 Application to the Chemical Capacitance of $Li_{2-}Mn_2O_4$

Finally, this defect chemical description can be adapted to correctly describe the reported experimental behavior of a $Li_{2-}Mn_2O_4$ electrode. The observed Li ordering close to 1 5 leads to an energetic splitting of the tetrahedral 8a sites, which is taken into account by assuming two different tetrahedral sites in the entire 1 2 range, labeled T1 and T2, with ^{0} ^{0} . This leads to two separate peaks in without any stepwise changes. Conversely, if fully equivalent tetrahedral sites were assumed with a sudden split into T1 and T2 at 1 5, would be expected to show a sudden step, contrarily to what is observed experimentally. Furthermore, we exclude all two-phase regions from our analysis, since the defect chemical description above relies on the presence of a solid solution. The Li chemical potential, chemical capacitance, and point defect concentrations are obtained analogously to the previously described general case of $Li_{2-}M_2O_4$, with a third Li site introduced due to the tetrahedral site splitting. The corresponding sites are referred to as O, T1, and T2 with sites per formula unit 1 and 1 2 1•2. The standard potentials ^{0}

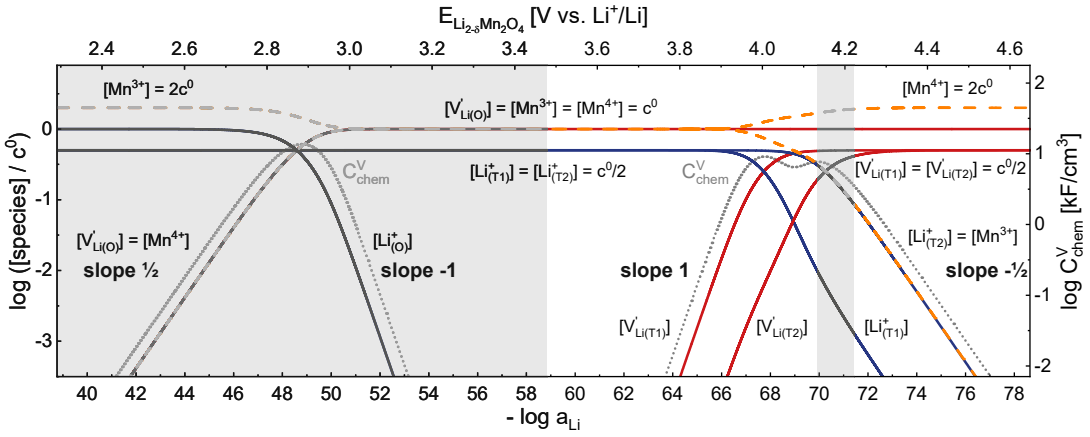

FIGURE 4.8: Calculated Brouwer diagram for $Li_{2-}Mn_2O_4$ (^{0} • 2 90 V, ^{0} $_{1}$ • 3 99 V, ^{0} $_{2}$ • 4 10 V, ^{0} • 0 00 V, 1, $_{1}$ $_{2}$ 1•2). The logarithmic site occupancies of all relevant species are plotted on the left, and the corresponding volume-specific chemical capacitance is plotted on the right y-axis as a function of log (bottom) and electrode potential (top). Approximate regions of reported two-phase regimes (0 1 and 1 65 1 9) of $Li_{2-}Mn_2O_4$ are grayed-out, since the defect chemical model relies on the presence of a single-phase solid solution.

are chosen such that the peaks appear at the same electrode potentials as observed experimentally for $Li_{2-}Mn_2O_4$, that is, ^{0} • 2 90 V, $^{0}_{1}$ • 3 99 V, $^{0}_{2}$ • 4 10 V, and ^{0} • 0 00 V. Please note that these standard values differ slightly from the peak positions due to the additional concentration-dependent contribution of to the total Li chemical potential. This is further illustrated in Figure 4.15 of the Appendix.

The resulting full Brouwer diagram of $Li_{2-}M_2O_4$ is shown in Figure 4.8, where regions are marked in gray that are known experimentally to behave as two-phase regimes rather than solid solutions for M = Mn. The storage regime involving tetrahedral sites, around log 68 (4 versus Li), is now split into two separate regimes with a corresponding double peak in , that is characterized by slopes of 1 and -1•2 at high and low Li activities, respectively. The two peaks differ in their shape and absolute values due to the asymmetric behavior of the electronic charge carriers for 1 2.

To arrive at a more conventional representation of the presented defect model, the calculated chemical potential can also be converted into a charge curve, that is, an electrode potential versus Li as a function of nonstoichiometry , via Equation (4.3). The resulting charge curves for the three presented cases of (i) generic layered oxide, (ii) generic spinel, and (iii) $Li_{2-}Mn_2O_4$ (without two-phase regions) are shown in Figure 4.9a and 4.9b. The generic spinel differs from the generic layered oxide in two essential aspects. First, the spinel structure allows the insertion of a second formula unit of Li by occupying the vacant octahedral sites at a lower electrode potential. Second, due to the availability of two redox active transition metals per formula unit, compared to only one per formula unit for each type of lattice site, the concentration of electronic charge carriers is very high and nearly constant on a logarithmic scale in the region around 3.5 V, where the concentrations of and are very small and vary over orders of magnitude (cf. Figures 4.7 and 4.8). As a result, the logarithmic increase in electrode potential upon removal of Li from the tetrahedral sites is only limited by the concentration of tetrahedral vacancies and the charge curve plateau is therefore flatter than for the layered oxide, as shown in Figure 4.9b.

Finally, the charge curve of $Li_{2-}Mn_2O_4$ differs from the generic spinel due to Li ordering at 1 5, which leads to a splitting of the tetrahedral site plateau into the characteristic double plateau around 4 V. The resulting $Li_{2-}Mn_2O_4$ charge curve exhibits steeper plateau regions than the generic spinel, more similar to the generic layered oxide, with a small potential step around 1 5. Please note that ionic ordering is not strictly specific to spinel cathode materials – Li ordering at half occupancy has also been reported, for example, for layered $Li_{0.5}CoO_2$, where it also causes a visible potential step in the charge curve.[147,199,200]

To verify the proposed defect model for $Li_{2-}Mn_2O_4$, the predicted values of (green continuous line) are plotted in Figure 4.10 together with those obtained from impedance measurements (dots). For a more detailed analysis, the calculated chemical capacitances of the isolated T1 and T2 regimes are plotted in red and blue, respectively, with contributions of

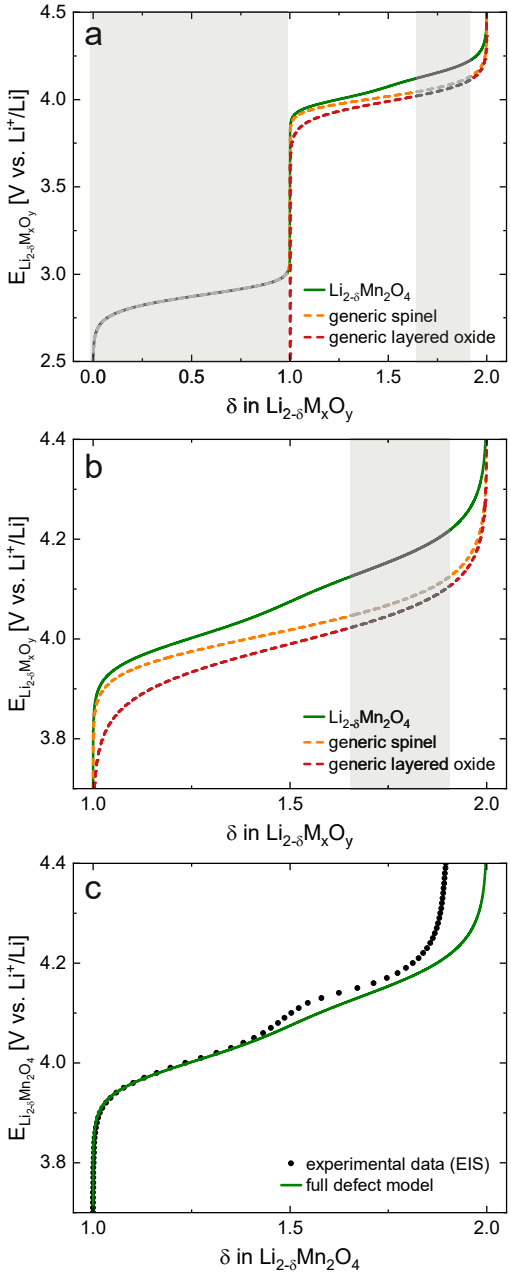

FIGURE 4.9: (a,b) Calculated electrode potential profiles as a function of for (i) a generic layered oxide (red), (ii) a generic spinel (orange), and (iii) Li_{2-} Mn_2O_4 (green), corresponding to the defect models presented in Figure 4.7a, Figure 4.7b, and Figure 4.8, respectively. Approximate regions of reported two-phase regimes (0 1 and 1 65 1 9) of Li_{2-} Mn_2O_4 are grayed-out, since the defect chemical model relies on the presence of a single-phase solid solution. **(a)** Full charge curve for 0 2. **(b)** Magnification of the tetrahedral-site regime with nonstoichiometries 1 2. **(c)** Comparison of the calculated charge curve (full defect model) with the experimental data from EIS, both being in good agreement in the low-voltage region. In the mid- and high-voltage regions, the experimental data deviate from the defect calculations due to the presence of a two-phase regime and incomplete Li extraction.

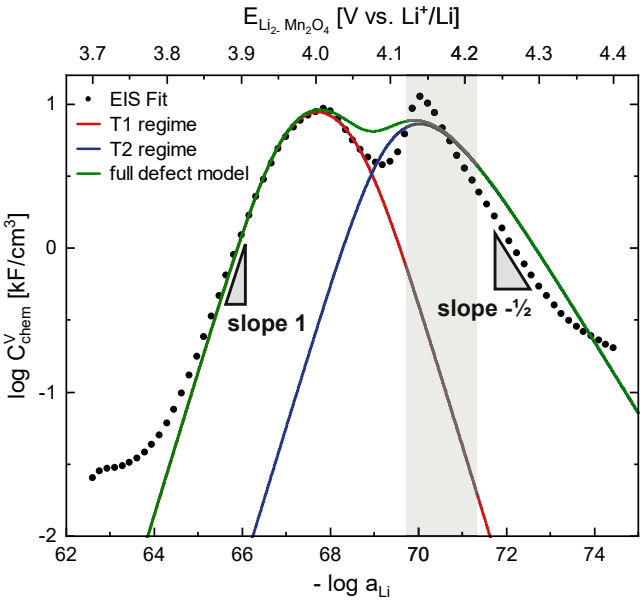

FIGURE 4.10: Calculated and measured (EIS) volume-specific chemical capacitance as a function of log and electrode potential. The approximate region of the reported two-phase regime (1 65 1 9) of $Li_{2-}Mn_2O_4$ is grayed-out, since the defect chemical model relies on the presence of a single-phase solid solution. The green line represents the values of calculated from the full impedance model (Figure 4.8), while the red and blue lines represent the calculated values from the isolated T1 and T2 regimes, respectively.

all other lattice sites to the total chemical potential of vacancies being neglected. In the T1 regime, the values of predicted by the defect model are in excellent qualitative and quantitative agreement, in terms of both absolute values and slopes. In the T2 regime, the general shape of the experimental data is also correctly reproduced, especially the slope of 1•2 at high potentials. However, as expected due to the presence of a two-phase regime in this potential region, the experimental data exhibit a sharper peak in than predicted by the defect chemical single-phase model. Since such a phase transition implies that a certain fraction of the electrode capacity is filled or emptied at a fixed electrode potential, this can also explain why the experimentally observed decrease with a slope of 1•2 is shifted to lower potentials with respect to the model calculations.

The experimental data can also be compared to the charge curve calculated from the proposed $Li_{2-}Mn_2O_4$ defect model, as shown in Figure 4.9c. At low values of , up to 1 4, both curves are in good agreement. Above 1 4, the experimental data deviate from the calculated curve due to the two-phase regime. After the two-phase regime, above 1 8, the experimental charge curve slopes upward to reach a maximum degree of Li extraction of 1 9 at 4.4 V, deviating from the theoretical maximum of 2 0 due to the previously described incomplete Li extraction. Nonetheless, the similar shape of the experimental and calculated charge curves in the high-voltage region suggests that the defect model could in principle also describe the voltage profile of $Li_{2-}Mn_2O_4$ for 1 8, if appropriate cor-

rections for incomplete Li extraction and the two-phase regime were introduced. The good agreement of our dilute defect model with the experimental data over a rather wide stoichiometry range is somewhat surprising, given the high carrier concentrations involved. In a similar electrochemical study on Li_{1-} CoO_2, substantial deviations from the simple model without a defect interaction already appeared at about 10% Li vacancies.[51] In general, defect interactions (or other changes of the materials with varying defect concentrations) seem to be less relevant for the spinel-type electrode compared to layered oxides; this is already visible in the steeper slopes and irregularities of the plateau regions for layered cathodes. Exact reasons for these differences can be manifold and may include the anisotropic volume changes of layered oxides upon cycling, which makes it usually hard to distinguish between ionic defect interactions and interactions with the gradually changing host lattice. Nonetheless, non-idealities due to defect interactions are probably also present in spinel-type materials and might, for example, cause the mismatch between the calculated chemical capacitance minimum around 4.08 V (green curve in Figure 4.10) and the measured minimum.

4.3.7 Analysis of the Ionic Conductivity of Li_{2-} Mn_2O_4

The shape of the potential-dependent ionic conductivity curve (Figure 4.5b) strongly resembles that of , with the characteristic double peak and slopes of 1 and 1•2, for low and high potentials, respectively. This can again be understood from the defect concentrations. The transport of throughout the tetrahedral sublattice takes place via octahedral sites[201–203] and, phenomenologically, can be viewed as a second-order reaction between and a tetrahedral Li vacancy. For independent motion on the T_1 and T_2 sublattices, the ionic conductivity can thus be approximated by

$$ 1 \quad {}_1 \; 1 \quad {}_1 \; 2 \quad {}_2 \; 1 \quad {}_2 \qquad (4.25) $$

The prefactors $_1$ and $_2$ are site-specific proportionality factors and resemble the mobility factors when writing the ionic conductivity in terms of one defect concentration only. For each sublattice, this corresponds to a transition from vacancy-limited (/ , only few vacancies) to -limited (/ 1 , only few ions on the relevant sites) ion conduction, analogously to in Equation (4.20). For constant prefactors and assuming only jumps within a given sublattice (T1, T2), the total ionic conductivity versus log curve predicted by Equation (4.25) therefore shows the same general shape as in Figure 4.10, in accordance with the experimental data (Figure 4.5b). However, while in Equation (4.25) only depends on ionic site fractions, the general term also includes contributions and this may cause some quantitative deviations. Further differences between and may be attributed to the absence of any defect interaction in our model, since the interaction supposedly affects thermodynamics (concentrations) as well as kinetics (-factors).

Given the ionic conductivities in Figure 4.5b and the ionic charge carrier concentrations in Figure 4.8, an effective ionic carrier mobility $_{\text{eff}}$ can be obtained based on the fundamental relationship

$$\text{eff} \quad \text{eff} \tag{4.26}$$

where 1 is the charge number and $_{\text{eff}}$ is a kind of effective concentration of ionic charge carriers on site according to

$$\text{eff} \quad ^{0} \quad _{1} \quad 1 \quad _{1} \tag{4.27}$$

with site concentration ^{0}. Assuming only T1 sites contributing to the ionic conductivity for 1 1 5 and only T2 sites for 1 5 1 9, we can separate Equation (4.25) into its T1 and T2 terms and arrive at expressions for $_{1\,\text{eff}}$ (1 1 5) and $_{2\,\text{eff}}$ (1 5 1 9) according to

$$\text{eff} \quad \frac{}{^{0} \quad _{1} \quad 1 \quad _{1}} \tag{4.28}$$

The effective site mobilities are plotted in Figure 4.11, where the regions of the T1 and T2 regimes are indicated together with the respective limiting ionic charge carriers. The capacity of the tetrahedral regime was scaled down to 1 0 1 9 to correct for the experimentally observed incomplete Li extraction. Starting at 1, the effective ionic mobility initially drops down from approximately 10^{-8} to 10^{-9} cm^2/Vs and then remains relatively constant over most of the compositional range. Close to 1 9, the mobility increases again from $10^{-9\,5}$ to $10^{-8\,2}$ cm^2/Vs. The initial rather sharp drop close to 1 reflects the slope of log being much lower than the slope of 1 predicted by the defect model for log $_{1}$ at electrode potentials close to 3.7 V (see Figure 4.5). The sharp increase close to 1 9 is due to remaining nearly constant above 4.3 V, where the defect model predicts a slope of 1•2 for log $_{2}$. This nominal increase in mobility can be considered an artifact, since the main contribution to in this potential region presumably comes from the remaining (incomplete extraction) in the material, which is only removed at potentials above 4.4 V and is not considered in our model. We therefore consider the ionic mobility of both sites (and thus also the limiting mobilities of the four ionic charge carriers) to be close to 10^{-9} cm^2/Vs for the investigated stoichiometry range.

Finally, we may briefly consider the Li chemical diffusion coefficient in Figure 4.5d, determined from and according to Equation (4.4). In the simplest case of a generic layered oxide (Equation (4.20) and 1), we find even analytically a constant value of . Some variations come into play due to different -factors for different sites, concentration-dependent , -terms in , and the consequences of the defect interactions mentioned above. A more detailed discussion of the rather modest changes, however, is beyond the scope of this paper.

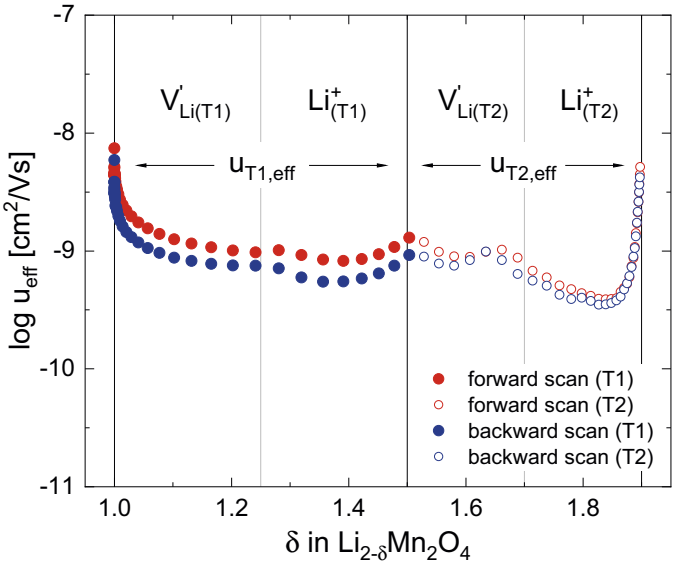

Figure 4.11: Effective ionic mobilities as a function of δ. For the T1 ($1 \leq \delta \leq 1.5$) and T2 ($1.5 \leq \delta \leq 1.9$) regions, values of $u_{i,\text{eff}}$ were calculated via Equation (4.28) by inserting the corresponding vacancy site fractions $x_{V'_{Li(i)}}$ from Figure 4.8.

4.4 Conclusion

Epitaxial thin films of spinel-type $Li_{2-\delta}Mn_2O_4$ were sputter-deposited on (100)-oriented $SrRuO_3/SrTiO_3$ substrates and analyzed electrochemically by means of cyclic voltammetry and impedance spectroscopy. The thin-film electrodes exhibited excellent electrochemical reversibility, thus allowing the reliable extraction of a complete set of electrochemical properties from impedance measurements as a function of state-of-charge (SOC) for a broad potential range of 3.70 – 4.40 V versus Li^+/Li. These properties consist of the charge-transfer resistance R_{ct}, ionic conductivity σ_{ion}, volume-specific chemical capacitance C^V_{chem}, and chemical diffusivity $\widetilde{D}$. The equilibrium open-circuit potential profile could be accurately reconstructed via integration of the C^V_{chem} data from impedance fits, highlighting the central role of the chemical capacitance as a fundamental thermodynamic property of Li insertion materials.

A defect chemical model was deduced, which describes the charge (δ) dependence of the electrode potential of $Li_{2-\delta}Mn_2O_4$ versus Li as the combination of a single-site-restricted electron hole potential $\mu_{h^\bullet}$ and multisite-restricted Li vacancy potential $\mu_{V'_{Li}}$. The model is in excellent qualitative and quantitative agreement with the experimentally obtained values of C^V_{chem}. Characteristic peaks of the chemical capacitance always occur around half occupancy of a certain crystallographic site. A double peak is introduced in $Li_{2-\delta}Mn_2O_4$ by the splitting of tetrahedral sites into two types of sites (vacancy ordering). Significant deviations from the model were only observed in the potential region around 4.1 – 4.2 V, where a phase separation is known to occur. These results demonstrate that the chemical potential and associated electrochemical properties of a solid-solution Li insertion material can be rather accurately

described by simple concentration dependences of the individual point defect chemical potentials of ionic and electronic charge carriers, when taking account of the lattice site restrictions imposed by the material's crystal structure. The presented model can easily be adapted for different transition metal stoichiometries and doping states, and therefore opens the gates toward a better defect chemical understanding of the entire class of spinel cathode materials.

4.5 Appendix

4.5.1 Reciprocal Space Mapping

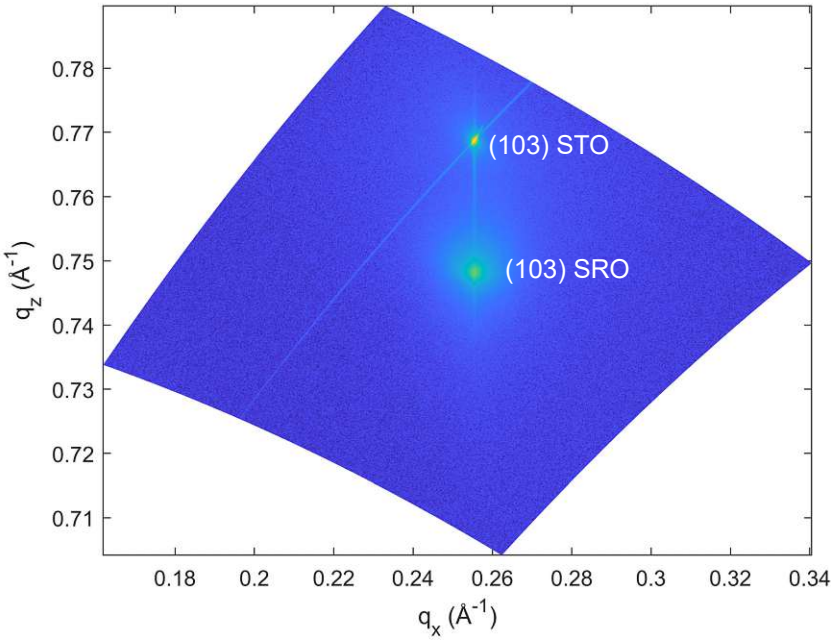

Figure 4.12: Reciprocal space map of the (103) STO/SRO reflex of the sample shown in Figure 4.1. The alignment of the q_x vectors of SRO and STO indicates that both films share the same in-plane lattice parameter.

4.5.2 Impedance Model and Simulated Spectra

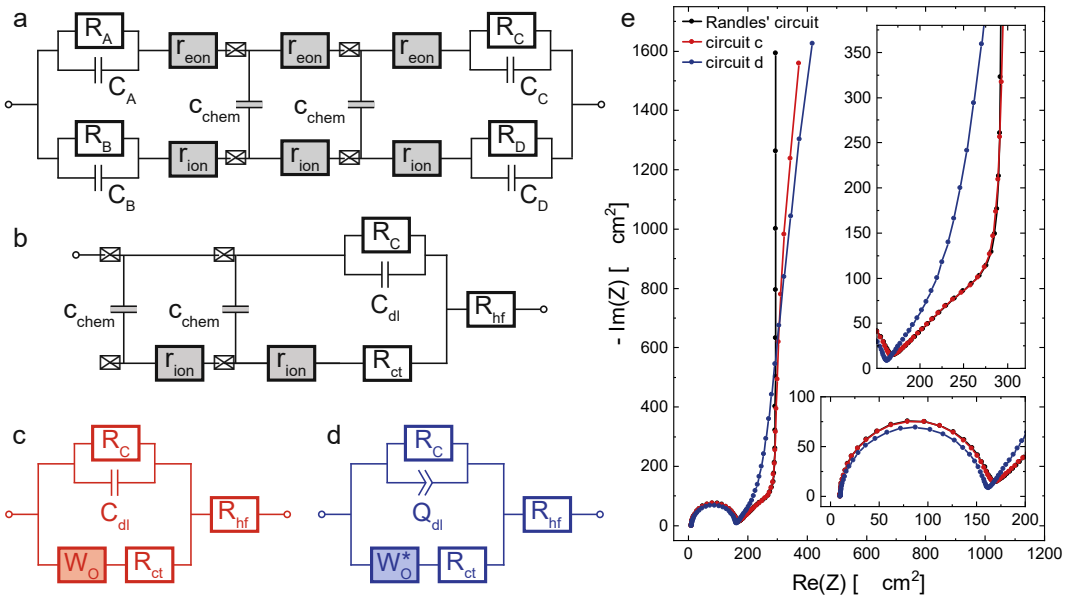

FIGURE 4.13: **(a)** Full one-dimensional transmission line with four distinct interfacial terminals. **(b)** Simplified transmission line model representing a thin-film LMO electrode, taking into account a finite resistance due to side reactions. **(c)** Simplified representation of circuit (b) obtained by replacing the remaining transmission line by an open Warburg element . The resulting circuit is a modified Randles' circuit, with an additional resistance . **(d)** Equivalent circuit used for the fitting of impedance spectra in this work. The open Warburg element was replaced by an anomalous diffusion element , with an impedance response given by Equation (4.5). **(e)** Simulated impedance response of Randles' circuit (10 , 150 , 10 µF, 400 , 100 mF) compared to circuits (c) and (d). For circuit (c) a resistance 300 kΩ was used. For circuit (d) a constant-phase exponent of 0.95 with 10 µF s $^{0\,05}$ was used for the constant-phase element, together with a nonideality factor 0 75 for the anomalous diffusion element.

4.5.3 Comparison of Charge Curves from Cyclic Voltammetry and Impedance Spectroscopy

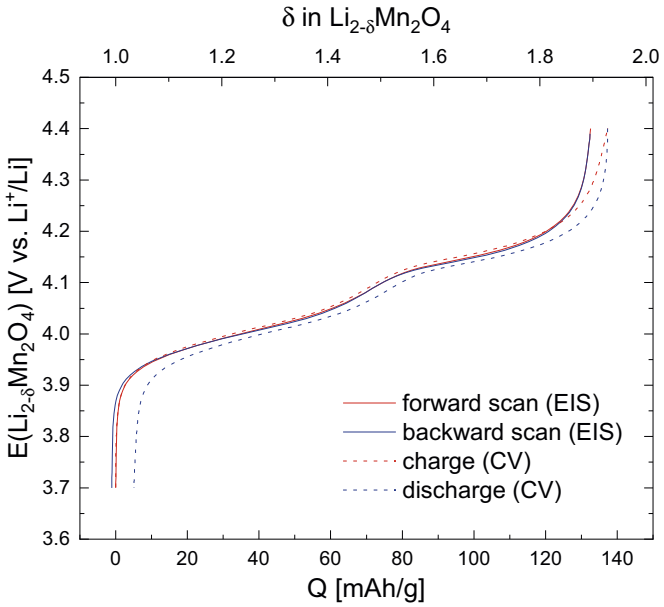

Figure 4.14: Comparison of the charge curves obtained via electrochemical impedance spectroscopy (EIS) and cyclic voltammetry (CV). The CV data show a higher charge capacity and lower coulombic efficiency due to background currents and a slight voltage hysteresis due to overpotentials. The charge/discharge curves from EIS show minimal discrepancy.

4.5.4 Multi-Site-Restricted Chemical Potential

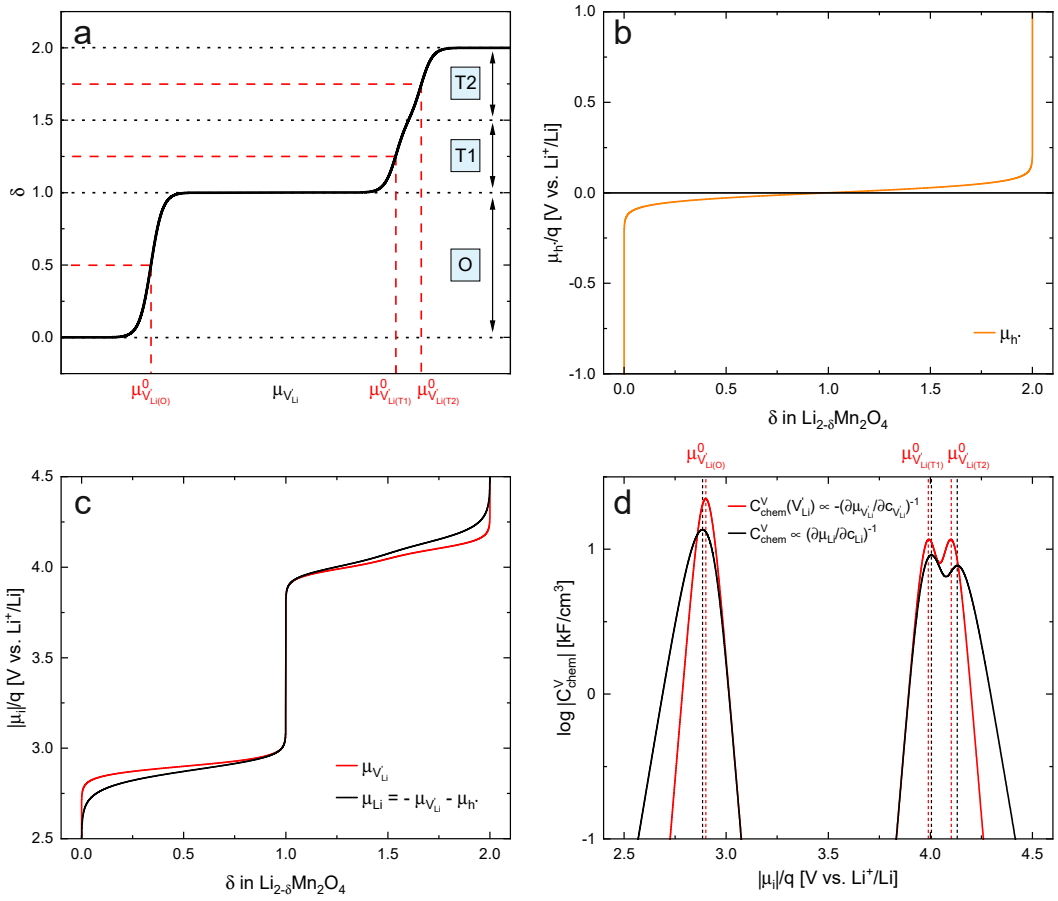

FIGURE 4.15: (a) Total nonstoichiometry in Li_{2-} Mn_2O_4 as a function of the total Li vacancy chemical potential , as calculated from Equation (4.30). The functional inverse can be obtained numerically. **(b)** Chemical potential of electron holes as a function of , as calculated from Equation (4.31). **(c)** Total Li chemical potential (black) as calculated from Equation (4.32), compared to (red) obtained by numerical inversion of in (a). **(d)** Total volume-specific chemical capacitance (black) from Equation (4.33) compared to its isolated vacancy component (red) obtained via Equation (4.34). The peaks of are slightly shifted with respect to the inserted values of ^{0} , due to the concentration-dependent contribution of to .

$$\frac{}{0} \quad \frac{}{0} \qquad 1 \quad \frac{}{} \tag{4.29}$$

$$\frac{1}{0} \quad \frac{0\ 5}{0} \quad \frac{0\ 5}{0} \qquad 1 \quad \frac{}{} \quad 1 \quad \frac{}{1} \quad 1 \quad \frac{}{2} \tag{4.30}$$

$$0 \qquad \frac{\qquad}{1} \qquad 0 \qquad \frac{\overline{2}}{1 \quad \overline{2}} \tag{4.31}$$

(4.32)

$$2 \quad \frac{\qquad}{\qquad} \quad 1 \tag{4.33}$$

$$2 \quad \frac{\qquad}{\qquad} \quad 1 \tag{4.34}$$

5 Chemical Capacitance Measurements Reveal the Impact of Oxygen Vacancies on the Charge Curve of $LiNi_{0.5}Mn_{1.5}O_{4-}$ Thin Films

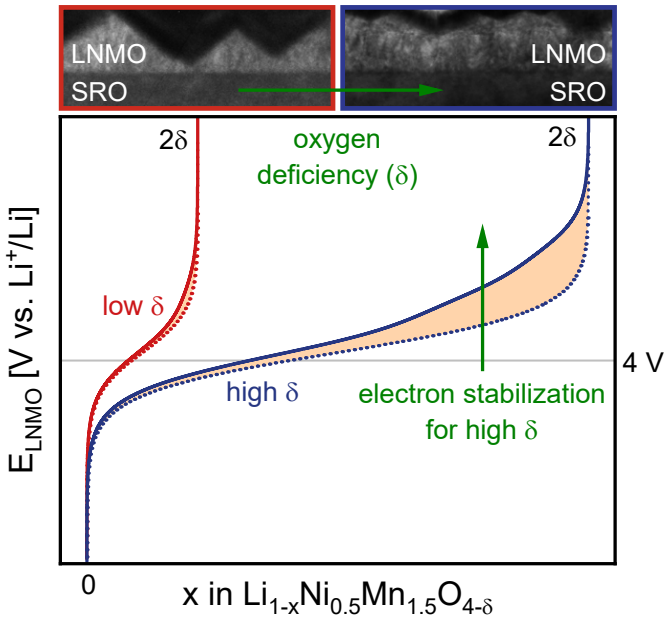

The study presented in this chapter has been submitted for publication:
Bumberger, A. E.; Raznjevic, S.; Zhang, Z,; Kubicek, M.; Friedbacher, G.; Fleig, J. Chemical Capacitance Measurements Reveal the Impact of Oxygen Vacancies on the Charge Curve of $LiNi_{0.5}Mn_{1.5}O_{4-}$ Thin Films. *submitted for publication* **2023**.

5.1 Introduction

The overall power density of a Li-ion cell strongly depends on the specific electrochemical properties of the electrode materials (i.e., charge-transfer resistance , ionic conductivity , volume-specific chemical capacitance , Li chemical diffusion coefficient). However, detailed studies dealing with the dependence of these properties on the state-of-

charge (SOC) are rare. Interestingly, defect chemical models based on dilute-solution thermodynamics can offer valuable insights into the SOC-dependent transport properties of Li storage materials over a surprisingly wide range of charge carrier concentrations.[35,51,52] Nonetheless, defect interactions inevitably come into play when exploiting the full charge/discharge capacity of a given Li storage material.

In the search for new cathode materials, the cobalt-free spinel of the nominal composition $LiNi_{0.5}Mn_{1.5}O_4$ (LNMO) has been investigated as a promising candidate due to its potentially low cost, good rate capability and high voltage versus Li^+/Li.[43,130,170,173,204–209] In contrast to its isostructural parent material $LiMn_2O_4$ (LMO), where Mn is in the mixed valence state of +3.5, Mn in stoichiometric $LiNi_{0.5}Mn_{1.5}O_4$ is fully oxidized to a valence state of +4, while Ni remains in the lower valence state +2. Upon charging, the extraction of Li from the 8a tetrahedral sites is therefore accompanied by the oxidation of Ni to a final valence state of +4 in $Ni_{0.5}Mn_{1.5}O_4$. Thus, the high oxidation potential of $Ni^{2+/3+/4+}$ is exploited to reach a voltage of approximately 4.7 V versus Li, compared to 4.0 V in the $Mn^{3+/4+}$-based LMO.

However, stoichiometric LNMO is difficult to synthesize, due to the material's tendency towards oxygen deficiency, accompanied by partial reduction of Mn^{4+} to Mn^{3+}.[170,173,208,210–216] Due to the exothermal nature of the oxygen incorporation reaction, a high degree of oxidation is favored by low temperatures and high oxygen partial pressures. Thus, the typical synthesis route towards stoichiometric LNMO ends with a slow cooling step under an oxygen-rich atmosphere to allow the material to equilibrate at the lowest possible temperature. It was shown that a high degree of oxidation in LNMO is closely related to Ni ordering on the octahedral sites. While high levels of oxygen deficiency favor the formation of the disordered phase with space group $Fd\bar{3}m$ ("d-LNMO"), samples close to the stoichiometric composition $LiNi_{0.5}Mn_{1.5}O_4$ tend to crystallize in the ordered $P4_332$ phase ("o-LNMO"), although the difference between these two phases is hard to resolve by crystallographic experiments.[170]

From a defect chemical perspective, oxygen deficiency in LNMO can be realized either via oxygen vacancies according to $LiNi_{0.5}Mn_{1.5}O_{4-}$ or via metal interstitials according to $[LiNi_{0.5}Mn_{1.5}]_{1+/(4-)}O_4$. However, these two cases are difficult to distinguish experimentally, because both configurations lead to a donor-doped material of the same chemical composition. Although the metal excess model has been discussed for both LMO and LNMO,[217–219] the larger part of literature seems to adopt the viewpoint of oxygen nonstoichiometry,[170,213,216] and in this paper we therefore also consider oxygen deficiency in terms of oxygen vacancies in $LiNi_{0.5}Mn_{1.5}O_{4-}$. Charge neutrality then requires the reduction of 2 formula units of Mn^{4+} to Mn^{3+}, which can be expressed as $LiNi_{0.5}Mn^{4+}_{1.5-2}\ Mn^{3+}_2O_{4-}$. As a consequence, a fraction corresponding to 2 100% of the total tetrahedral site capacity is moved from the 4.7 V ($Ni^{2+/3+/4+}$) to the 4.0 V ($Mn^{3+/4+}$) regime, resulting in a proportional loss of storable energy due to the lower average voltage.

However, the presence of oxygen vacancies does not simply move part of the total capacity from the high-voltage Ni- to the lower-voltage Mn-regime, but furthermore introduces a variety of possible defect interactions such as defect associates (i.e., electronic and ionic trap states) that influence the material's SOC-dependent electrochemical properties in a nontrivial manner. Although computational studies have suggested a significant impact of such associates (trap states) on the voltage profile of LNMO electrodes,[213,220–222] particularly in the oxygen vacancy regime around 4.0 V, there have been little efforts to quantitatively describe the experimentally observed shape of the LNMO charge curve as a function of oxygen vacancy concentration and defect interaction energies. Furthermore, although the overall cycling performances of ordered (low) and disordered (high) samples have often been compared, the precise variation of their electrochemical transport properties with and the state-of-charge is largely unknown.

In this work, we investigate the impact of oxygen vacancies on the electrochemical properties of epitaxial LNMO thin films by means of impedance measurements as a function of electrode potential. We report a full and detailed set of electrochemical properties (charge-transfer resistance, ionic conductivity, chemical capacitance and chemical diffusion coefficient) as a function of SOC for two different levels of oxygen deficiency. Particularly the chemical capacitance (i.e., differential capacity) turns out to be a highly valuable source of information regarding both ionic and electronic defect interactions in LNMO and their impact on the charge curve. For the first time, we provide a detailed defect chemical analysis of the charge curve in the oxygen vacancy regime around 4 V versus Li^+/Li and show that the level of oxygen deficiency not only determines the amount of redox active $Mn^{3+/4+}$ but furthermore impacts the defect interactions and hence the shape of the charge curve. More generally, the reported results pave the way towards a better understanding of the oxygen-nonstoichiometry in all Li-ion cathode materials and its effect on electrode performance.

5.2 Experimental

5.2.1 Sample Preparation

Thin films of $SrRuO_3$ (SRO) and $LiNi_{0.5}Mn_{1.5}O_{4-}$ (LNMO) were deposited onto the polished side of (100)-oriented $SrTiO_3$ (STO) single crystal substrates of dimensions 10 × 10 × 0.5 mm^3 (MaTecK, Germany) by means of radio-frequency magnetron sputtering in a custom-built deposition chamber (Huber Scientific, Austria), using commercial 2" targets obtained from Advanced Engineering Materials (China) and Loyaltarget (China), respectively. To ensure a good electrical contact around the edges to the backside, the substrate edges were roughened with fine sandpaper and sputter-coated with a 5/200 nm bilayer of Ti/Pt by means of DC sputtering (room temperature, Ar atmosphere, 0.7/2.0 Pa, 5 mA/cm^2) prior to SRO/LNMO deposition. The nominal substrate temperature was determined via a power-temperature cal-

ibration of the heating stage using a polished (100)-oriented Y:ZrO_2 single crystal (9.5 mol% Y_2O_3, CrysTec, Germany) and an optical pyrometer, assuming a surface emissivity of 0 9. SRO was deposited in a gas mixture of Ar:O_2 = 3:1 at a total pressure of 2.5 Pa, a nominal substrate temperature of 650 °C, and a power of 60 W, resulting in a film thickness of approximately 80 nm, as estimated by TEM. LNMO was deposited under oxygen atmosphere at a pressure of 2.5 Pa, a nominal substrate temperature of 550 °C, and a power of 60 W, resulting in a film thickness of approximately 70 nm, as estimated by TEM. For d-LNMO, the sample was cooled down at a rate of 30 °C/min immediately after deposition while maintaining an oxygen partial pressure of 2.5 Pa. For o-LNMO, the nominal substrate temperature was kept at 550 °C after deposition while gradually flooding the deposition chamber with oxygen over the course of 5 h. For this purpose, a separate temperature calibration at atmospheric pressure was used. Finally, the o-LNMO sample was kept at 550 °C under 1 atm of oxygen for 1 h, followed by a cool-down at 15 °C/min. After LNMO deposition, the sample backside was sputter coated with another Ti/Pt bilayer to ensure a good electrical contact to the steel plunger of the electrochemical measuring cell. Due to the characteristic concentric variation of the deposition rate during magnetron sputtering and the large substrate area compared to the target size, a certain degree of thickness variation in the SRO and LNMO thin films across the sample is expected, and the film thicknesses measured by TEM can only be taken as approximate values for the whole sample.

5.2.2 Structural Characterization

Out-of-plane X-ray diffractograms were recorded from 2 = 15° to 80° on an Empyrean X-ray diffractometer (Malvern Panalytical, UK) using a hybrid Kα monochromator of type 2XGe(220) on the incident beam side and a GaliPIX3D area detector in scanning line mode on the diffracted beam side. Atomic force microscopy (AFM) images of the sample surface were acquired on a Nanoscope V multimode setup (Bruker) and analyzed using the open-source software Gwyddion.[177] Electron-transparent lamellae for TEM investigations were prepared by standard lift-out techniques on a Thermo Fisher Scios 2 DualBeam FIB/SEM operating with a Ga-ion beam at 30 kV accelerating voltage. Final thinning and low-voltage polishing steps were carried out at 5 kV and 2 kV to reduce the amount of surface amorphization on the lamellae. All TEM imaging was carried out on a JEOL JEM-2100F field-emission gun microscope equipped with an image-side spherical aberration corrector, operating at an accelerating voltage of 200 kV. TEM images were acquired on a Gatan Orisu SC1000 CCD camera. High-resolution TEM images were further processed using an average background subtraction filter (ABSF).

5.2.3 Electrochemical Characterization

For electrochemical measurements, the thin-film samples were assembled in a two-electrode cell (PAT-Cell, EL-CELL, Germany) using a 260 m glass-fiber separator (EL-CELL), 80 L of a standard organic liquid electrolyte (1 M $LiPF_6$ in a 1:1 mixture of ethylene carbonate and dimethyl carbonate, Aldrich, USA), and a Li metal counter electrode (10 × 10 × 0.6 mm^3, Goodfellow, Germany). All electrochemical measurements were carried out at room temperature on a SP200 Biologic potentiostat with a built-in impedance analyzer. Cyclic voltammetry was carried out with a scan rate of 1 mV/s in the voltage range of 3.7 to 4.9 V versus Li^+/Li for 5 cycles before starting the series of impedance measurements. Potential-controlled impedance spectra were acquired in the frequency range of 200 kHz to 10 mHz (6 points per decade) using a perturbation amplitude of 10 mV. In the voltage range of 3.8 to 4.9 V versus Li^+/Li spectra were recorded in increments of 10 mV with intermittent equilibration (i.e., constant voltage) steps of 5 min.

5.3 Results

5.3.1 Epitaxial SRO/LNMO Thin Films

To analyze the effect of oxygen vacancies on the electrochemical properties of LNMO, two types of thin-film sample were prepared – one with a high and one with a low level of oxygen deficiency, as described in the experimental section. Although the post-oxidized sample is still weakly oxygen deficient (see below), and its space group could not be unambiguously identified as $Fd\bar{3}m$ or $P4_332$, its structural and electrochemical properties are close to what is referred to as ordered LNMO in the literature, and we will therefore refer to the samples with high and low oxygen vacancy concentration as d-LNMO and o-LNMO (d = disordered, o = ordered), respectively.

The structural characterization of typical d-LNMO and o-LNMO samples is summarized in Figure 5.1. As shown in Figure 5.1a, LNMO was deposited onto an epitaxial $SrRuO_3$ (SRO) thin-film current collector on a (100)-oriented $SrTiO_3$ (STO) single crystal substrate coated with Ti/Pt on its sides and backside. The -2 X-ray diffractograms in Figure 5.1b suggest that both o-LNMO and d-LNMO grow epitaxially on the (100)-oriented SRO thin film. For SRO and the STO substrate, only the (100), (200) and (300) reflexes are visible in the measured range of 2 , with the SRO reflexes shifted to lower angles with respect to the substrate. For both samples, the SRO (200) reflex appears around 2 = 45.2°, corresponding to an out-of-plane lattice parameter of approximately 4.01 Å. In a previous study,[52] it was confirmed by reciprocal space mapping that SRO grows on STO as a compressively strained, epitaxial thin film, thereby adopting the in-plane lattice parameter of 3.91 Å from the substrate. As shown in Figure 5.1c, the LNMO (400) reflex appears at 2 = 43.9° and 2 = 44.3° for d-LNMO and

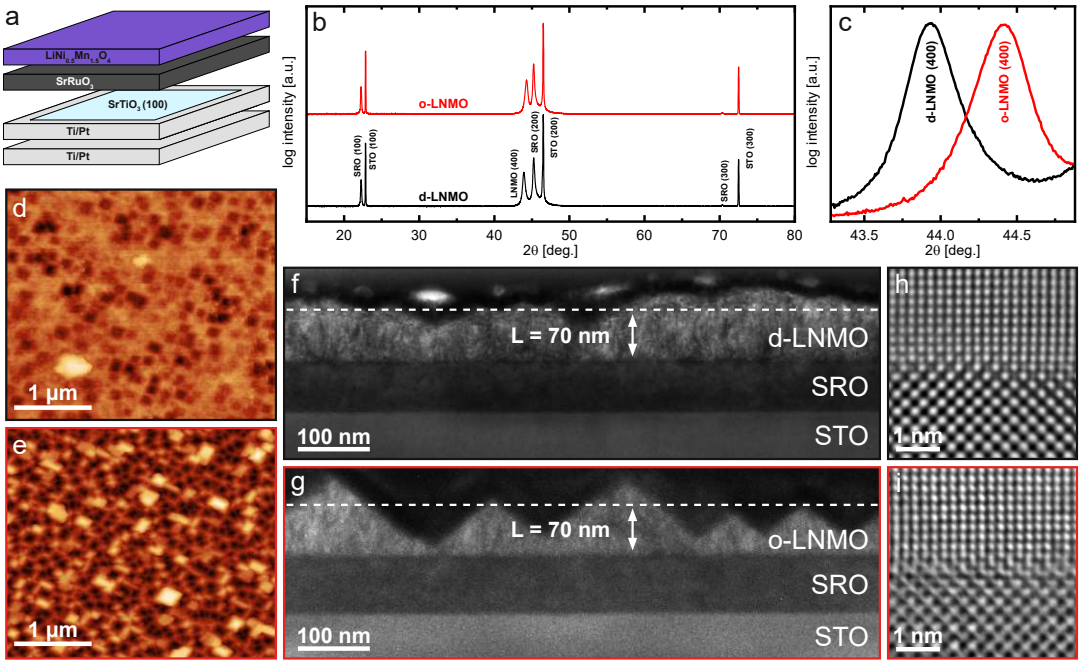

Figure 5.1: Structural characterization of d-LNMO and o-LNMO thin film samples. **(a)** Schematic illustration showing the individual components of the overall sample. SRO and LNMO were deposited onto a (100)-oriented STO single crystal with Ti/Pt-coated edges. An additional layer of Ti/Pt was sputtered onto the backside for a better electrical contact. **(b)** Out-of-plane -2 X-ray diffractogram showing only reflexes of the (h00) family for STO, SRO and LNMO, indicating epitaxial growth of both SRO and LNMO on STO. **(c)** Magnification of the LNMO (400) reflex from the X-ray diffractogram (b) around 2 = 44°, clearly showing a decrease of the cubic lattice parameter from d-LNMO to o-LNMO. **(d-e)** AFM images of the samples surfaces of the d-LNMO and o-LNMO thin films, respectively. **(f-g)** Bright-field TEM images of the d-LNMO and o-LNMO samples, respectively, displaying a more defined pyramidal structure in the o-LNMO film. The estimated average thickness of 70 nm is indicated in both images. **(h-i)** ABS-filtered high-resolution TEM images of the SRO (bottom) / LNMO (top) interface of the d-LNMO and o-LNMO samples, confirming the epitaxial growth of LNMO on SRO.

o-LNMO, corresponding to out-of-plane lattice parameters of 8.25 Å and 8.18 Å, respectively. This is in good agreement with literature, where a larger lattice parameter is reported for d-LNMO due to the larger ionic radius of Mn^{3+} compared to Mn^{4+}.

The epitaxial growth of both d- and o-LNMO on the SRO current collector is confirmed by the high-resolution TEM images in Figure 5.1h and Figure 5.1i, respectively. The close agreement of the measured out-of-plane lattice parameter with the bulk lattice parameters from literature, together with the large lattice mismatch of 5% between LNMO and SRO, suggests that, for both samples, the epitaxial LNMO film relaxes to its bulk in- and out-of-plane lattice parameter within a short distance from the interface, and does not adopt a significant amount of compressive strain from the substrate.

The AFM images of the d- and o-LNMO surfaces are shown in Figure 5.1d and Figure 5.1e, respectively, and show a clear difference in morphology between the disordered and ordered spinel samples. The d-LNMO film exhibits an ill-defined surface morphology with some octa-

hedral imprints that hint at the characteristic morphology of (400)-oriented spinel thin films, an RMS roughness of 15 nm and a surface area that is 12% larger than the projected sample area. The o-LNMO film, on the other hand, exhibits a well-defined morphology with a clear preference for exposure of the ⟨111⟩ facets, resulting in an octahedrally imprinted structure with an RMS roughness of 45 nm and a surface area that is 59% larger than the projected area. The difference in morphology between d-LNMO and o-LNMO is even more evident in the corresponding bright-field TEM images in Figure 5.1f and Figure 5.1g, respectively, with the ordered sample showing clearly defined pyramids, while the disordered sample exhibits a smoother but more irregularly shaped surface.

For the d-LNMO thin film, an average thickness of 70 nm was estimated from the bright-field TEM images. For the o-LNMO film, the estimated average thickness in the cross section shown in Figure 5.1g is only 56 nm. However, due to the strong thickness variation in the o-LNMO film, the comparatively small sample size of the TEM image and the fact that the same deposition rate and time were employed for both samples, we use the same average thickness (70 nm) for the data analysis of both d-LNMO and o-LNMO. Owing to the thickness variations, especially in the o-LNMO film, the geometry normalized properties deduced from the impedance spectra have to be regarded as averaged (effective) values. Although the presence of grain boundaries cannot be ruled out, our TEM investigations indicate a largely single-crystalline, dense thin film for both sample types. Therefore, we consider the extracted electrochemical properties as representative also for the corresponding bulk material.

5.3.2 DC Measurements

After cell assembly, the two different LNMO samples were characterized by cyclic voltammetry (CV) for 5 cycles at a scan rate of 1 mV/s, to ensure sufficient electrochemical stability for the subsequent impedance measurements. The fifth cycle CV scans are plotted in Figure 5.2a. Both samples exhibit the well-known double peak in current density around 4.7 V versus Li^+/Li,[43,170,208] corresponding to the removal/insertion of Li^+ from the tetrahedral sites upon oxidation/reduction of $Ni^{2+/3+/4+}$, with o-LNMO showing higher overall current densities for both the forward and the backward scan. While it may be tempting to assign these two peaks to the separate redox couples $Ni^{2+/3+}$ and $Ni^{3+/4+}$, the potential difference close to 100 mV between the two peaks is very similar to the double peak observed for LMO, where only one redox species ($Mn^{3+/4+}$) is active, and the peak splitting has been reported to originate from Li ordering at the composition $Li_{0.5}Mn_2O_4$.[166–169,223] It is therefore likely, although experimentally not fully established, that a similar ordering occurs in LNMO and may either cause or at least contribute to the observed peak splitting.[208]

A second, broader and much lower current peak is observed around 4.0 V, which is significantly higher for d-LNMO than for o-LNMO. This peak can be assigned to the removal/extraction of Li^+ from the tetrahedral sites upon oxidation/reduction of $Mn^{3+/4+}$, stemming from the

charge compensation of oxygen vacancies. Hence, this peak is the focus of our study. The much lower current densities observed for o-LNMO compared to d-LNMO in the 4.0 V region therefore confirms the successful, although still incomplete, incorporation of additional oxygen into the material in the post-annealing step under oxygen atmosphere.

For both samples, a significant amount of background current is observed, that increases up to approximately 10 µA/cm^2 at 4.9 V. This background current presumably originates from side reactions due to either impurities or residual water content in the electrolyte or the onset of electrolyte oxidation at the highest voltages. Although the observed background currents are negligible compared to typical bulk electrode capacities in the mAh range, they are significant in the context of our thin film electrodes with capacities of only a few µAh. Accordingly, they have a noticeable impact on the coulombic efficiency, as discussed below. Cyclic voltam-

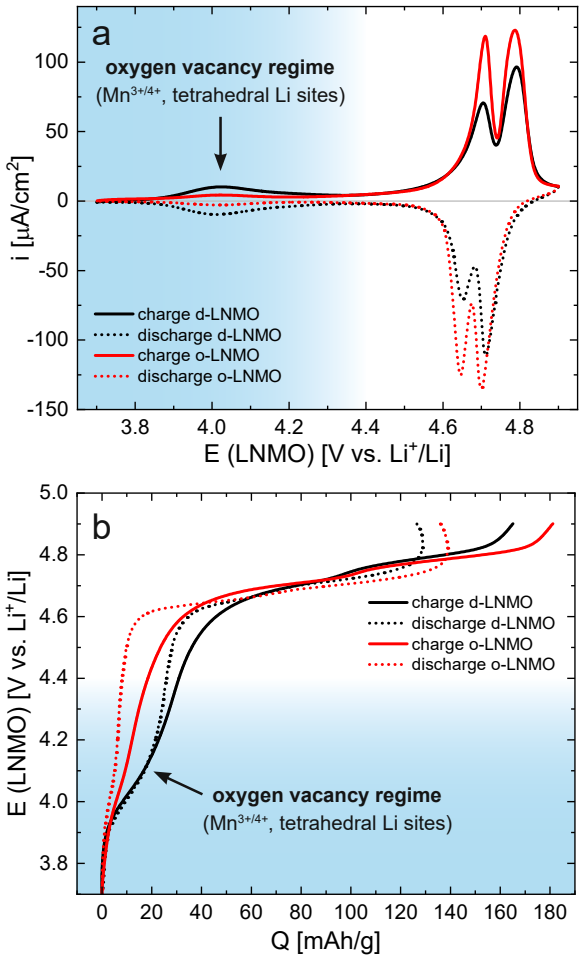

Figure 5.2: DC characterization via cyclic voltammetry of d-LNMO (black) and o-LNMO (red) samples prior to impedance measurements. **(a)** Cyclic voltammograms (fifth cycle, scan rate 1 mV/s) showing clear differences between d-LNMO and o-LNMO in the 4.0 V and 4.7 V regimes. **(b)** Voltage versus charge profiles obtained via integration of the CV curves in (a). In both plots, the voltage range colored in blue corresponds to the oxygen vacancy regime, which is the main focus of this study.

metry was therefore chosen over classical galvanostatic cycling, since the former allows for a better estimation of the background currents contributing to the measured charge/discharge capacities.

By integration, the CV curves in Figure 5.2a can also be converted directly into potential versus charge curves, i.e., voltage profiles, as shown in Figure 5.2b. The integrated charge/discharge capacities amount to 165/127 mAh/g (d-LNMO) and 181/136 mAh/g (o-LNMO), with corresponding coulombic efficiencies of 77% and 75%, respectively. As expected from the oxidative background current observed in the CV scan, the charge/discharge curves are distorted towards higher/lower capacities in the high-voltage region above 4.8 V. More generally, the voltage profiles appear particularly distorted in potential regions outside the main storage regime around 4.7 V, where the currents due to reversible Li intercalation/extraction are low and background currents are comparatively higher. Since these potential regions also correspond to stoichiometries with low charge carrier concentrations, where a dilute defect model could be applied to describe the material's electrochemical properties, the DC measurements shown in Figure 5.2 do not provide sufficiently accurate data for a quantitative comparison with defect chemical calculations. For further investigations, we therefore resort to impedance measurements, as established in our previous studies on $Li_{1-}\ CoO_2$ and $Li_{2-}\ Mn_2O_4$.[51,52] This virtually eliminates the effect of background currents and allows us to extract not only the volume-specific chemical capacitance (i.e., differential capacity), but also the charge-transfer resistance , the ionic conductivity and the Li chemical diffusion coefficient as a function of SOC.

5.3.3 Impedance Measurements

Impedance spectra for LNMO electrode potentials of 3.80 to 4.90 V versus Li^+/Li were measured in increments of 10 mV and are shown in Figure 5.3 for both d-LNMO and o-LNMO in increments of 100 mV. For both samples, the frequency-dependent impedance response exhibits a similar variation with electrode potential, with the highest real and imaginary impedances at 3.80 and 4.90 V. The real impedance only shows a strong variation at low and high voltages and appears to remain relatively constant in the intermediate voltage range. The imaginary part of the impedance reaches a first minimum at 4.00 V and a second, more pronounced minimum around 4.70 V. The high-frequency region of the spectra, which is magnified in Figure 5.3c (d-LNMO) and Figure 5.3g (o-LNMO), consists of two semicircles, one of which exhibits a strong variation with electrode potential, whereas the other remains nearly constant throughout the entire set of measurements. At intermediate voltages, the two semicircles appear to be of similar magnitude and blend into each other, signifying a similar capacitance of the corresponding transport processes. The most notable difference between the d-LNMO and o-LNMO samples can be seen in the low and intermediate voltage region, up to approximately 4.40 V. For d-LNMO, the previously described variation of real

and imaginary impedance around 4.00 V is more pronounced than for o-LNMO. For example, the impedance spectrum of o-LNMO at 3.90 V is very similar to the spectrum at 4.90 V, while for d-LNMO, the real and imaginary impedances are significantly lower at 3.90 V. Since both the real and imaginary parts of the electrode impedance are related to charge carrier concentrations in the material (see next section), this hints at a higher capacity of d-LNMO in the Mn-regime, as could already be estimated from the CV curves in Figure 5.2a.

5.3.4 Fitting of Impedance Spectra

Impedance spectra of Li storage thin films have conventionally been fitted to Randles' circuit,[188,189] which is based on an intuitive combination of an open Warburg element with a charge-transfer resistance , a double-layer capacitance and a high-frequency offset resistance . More generally, the impedance response of a Li storage electrode can be described by the general transmission line model proposed by Jamnik and Maier, shown in Fig-

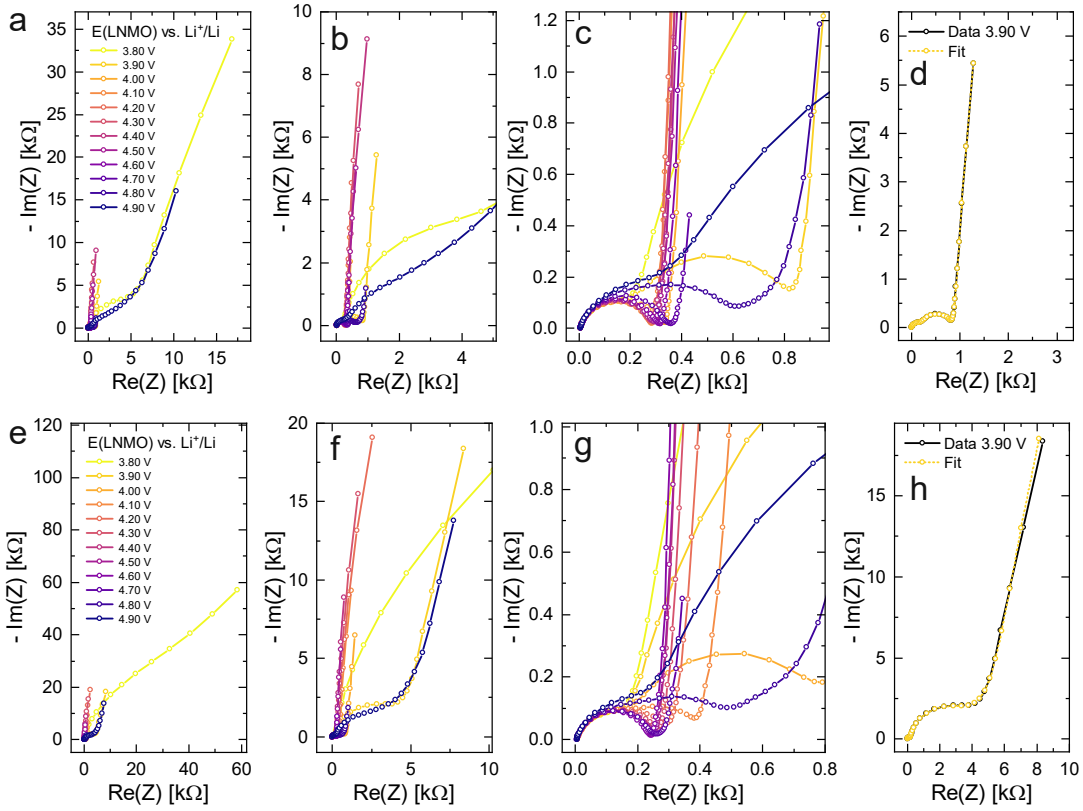

Figure 5.3: Impedance spectra of d-LNMO (a-d) and o-LNMO (e-h) as a function of electrode potential in the range of 3.80 V to 4.90 V versus Li^+/Li in increments of 100 mV. For better overview, the remaining spectra in 10 mV increments are not shown. **(a-c)** Impedance spectra of d-LNMO at different magnifications. **(d)** Exemplary impedance fit for the d-LNMO spectrum at 3.90 V. **(e-g)** Impedance spectra of o-LNMO at different magnifications. **(h)** Exemplary impedance fit for the o-LNMO spectrum at 3.90 V.

ure 5.4a. This physically derived impedance model considers the one-dimensional transport of mass and charge across a mixed ionic and electronic conductor (MIEC) slab of thickness by two parallel resistive rails for ions and electrons, coupled by chemical capacitors, with , , and .[54,58–61] For a Li storage electrode, the volume-specific chemical capacitance can be defined as[137]

$$^{2}\ \frac{}{}\ ^{1} \tag{5.1}$$

where is the elementary charge, is the concentration of formally neutral Li. The Li chemical potential of the MIEC versus Li metal is related to the Li activity in the MIEC via

(5.2)

with Boltzmann's constant and the temperature . The Li chemical potential and activity are both related to the electrode potential versus Li metal via

$$\frac{}{} \tag{5.3}$$

As in most other thin film impedance studies of LIB cathodes, we assume a comparatively high electronic conductivity of the material such that and 0. Please note that if and were of similar magnitude, an SOC-dependent shift of the high-frequency offset would be expected, which is not observed experimentally. With negligible electronic resistance, the chemical diffusion coefficient can be expressed as

$$\frac{}{}\ \frac{^{2}}{}\ \frac{^{2}}{} \tag{5.4}$$

where is the time constant of chemical diffusion, that is, the Li storage process.[67]

For the present study, we further assume a current collector that presents an ohmic electronic contact to the mixed ionic and electronic conductor (LNMO), i.e., a negligible contact resistance, and an LNMO/electrolyte interface that allows for both charge transfer (transport of Li^+ across the interface) and side reactions (i.e., electron transfer to or from the electrolyte, for example due to electrolyte oxidation at high voltages). The charge-transfer and side-reaction resistances are denoted as and , respectively. The electrochemical double-layer capacitance at the LNMO/electrolyte interface is placed on the electronic rail terminal to remain consistent with the commonly used Randles' circuit after replacement of the transmission line with an open Warburg element (see below). The resulting equivalent circuit is shown in Figure 5.4b.

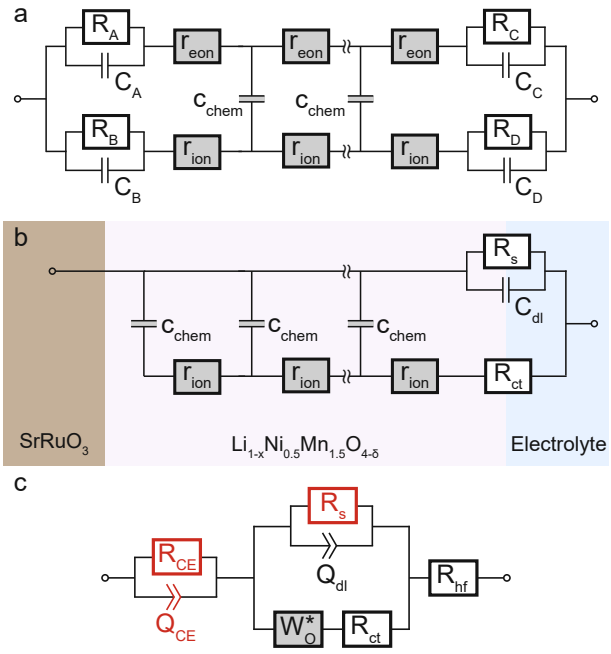

FIGURE 5.4: Stepwise derivation of the equivalent circuit used for impedance fitting. **(a)** general transmission line with four distinct R/C terminals. **(b)** Simplified transmission line obtained by (i) neglecting electronic resistances, (ii) assuming an ohmic electronic contact at the SRO/LNMO interface, and (iii) assuming an LNMO/electrolyte interface that allows for both Li^+ and electron transfer. **(c)** Final equivalent circuit used for fitting, obtained by accounting for anomalous diffusion as well as for the contributions of the Li metal counter electrode (CE) and the electrolyte. Circuit elements with fixed parameters are marked in red, and their respective values are summarized in Table 5.1.

The remaining portion of the transmission line is identical to an ideal open Warburg element , which describes the impedance transition from semi-infinite to finite-space diffusion with characteristic phase angles of 45° and 90°, respectively. In our previous studies on Li_{1-} CoO_2 and Li_{2-} Mn_2O_4,[51,52] we have shown that the diffusional impedance of real intercalation electrodes can be fitted with an anomalous finite-space diffusion element embedded in the impedance analysing software EC-Lab (Biologic, France), which is closely related to the anomalous open Warburg element proposed by Bisquert.[136] The corresponding impedance expression reads

$$\frac{\bullet 2}{1 \quad \bullet 2} \tag{5.5}$$

with a nonideality parameter 0 1. Thus, also in the present study, we replace the transmission line in Figure 5.4b with the anomalous diffusion element . The nonideality parameter was found to be in the range of 0.4 to 1. Furthermore, we replace the ideal double-layer capacitance by a constant-phase element and add a serial high-frequency offset resistance to account for the ohmic resistance contributions of the electrolyte and other cell components. A two-electrode cell setup is used in this study to avoid distortions of the

impedance spectra that are potentially encountered in a three-electrode setup due to slight misalignments of the square-shaped working and counter electrodes. Hence, also the Li metal counter electrode must be included in the equivalent circuit. Its impedance is observed as a nearly invariant high-frequency semicircle, as shown in Figure (5.3), and can therefore be accounted for by a / element in series to the remaining equivalent circuit with fixed values of , , and the corresponding constant-phase exponent . The side-reaction resistance was also found to be nearly constant throughout the series of measurements and was therefore fixed to ensure a meaningful fit in the potential regions of high chemical capacitance, where the low-frequency diffusional tail is too short to allow an unambiguous identification of . The final equivalent circuit used for fitting is shown in Figure 5.4c, with the fixed circuit elements marked in red. The corresponding fixed fit parameters for d-LNMO and o-LNMO, which were extracted from the impedance spectra at 3.90 V and 4.50 V, respectively, are summarized in Table 5.1. Exemplary impedance fits at 3.90 V are shown in Figure 5.3d and Figure 5.3h for d-LNMO and o-LNMO, respectively. A more extensive overview of the impedance fits is shown in Figure 5.11 of the Appendix.

Table 5.1: Summary of fixed parameters for d-LNMO and o-LNMO impedance fits. The corresponding equivalent circuit elements are marked in red in Figure 5.4c.

Sample type	(k)	( )	(µF s^{n-1})	
d-LNMO	195	206	6.48	0.836
o-LNMO	245	192	8.18	0.818

5.3.5 Analysis of Electrochemical Properties

The electrochemical properties obtained by fitting the impedance spectra in Figure 5.3 to the equivalent circuit from Figure 5.4c are shown in Figure 5.5 as a function of Li activity and electrode potential versus Li^+/Li. The data sets of d-LNMO and o-LNMO are marked in red and black, respectively. For o-LNMO, impedance spectra at electrode potentials below 3.83 V versus Li^+/Li could not be evaluated due to the high values of and , which blend into each other in the low-frequency region and can no longer be distinguished by the fit (see, for example, the impedance spectrum at 3.80 V in Figure 5.3e). The entire data set was therefore limited to an electrode potential range of 3.83 V to 4.90 V for both d-LNMO and o-LNMO.

The charge-transfer resistance, normalized to the electrode surface area (1.59 cm^2), is plotted as the inverse 1/ in Figure 5.5a to emphasize the similar concentration dependences of and 1/ . For d-LNMO, decreases from 3.7 k cm^2 at 3.83 V to a minimum value of about 80 cm^2 at 4.14 V. From 4.05 V to 4.60 V, remains relatively constant around 100 cm^2. Above 4.60 V, starts to increase again and reaches a final value of 3.7 k cm^2 at 4.90 V. For o-LNMO, decreases from 23 k cm^2 at 3.83 V to about 100 cm^2 at around

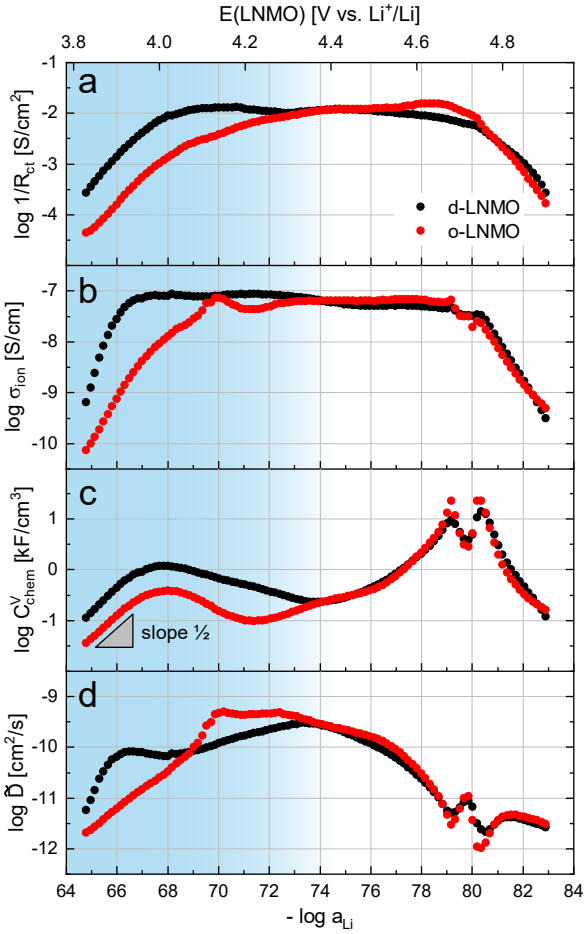

Figure 5.5: Logarithmic electrochemical properties of the d-LNMO (black) and o-LNMO (red) samples plotted as a function of negative logarithmic Li activity and electrode potential versus Li^+/Li. The voltage range colored in blue corresponds to the oxygen vacancy regime, which is the main focus of this study, and where the most relevant differences between d-LNMO and o-LNMO are observed. **(a)** Inverse charge-transfer resistance, **(b)** ionic conductivity, **(c)** volume-specific chemical capacitance, **(d)** chemical diffusion coefficient.

4.33 V and then remains relatively constant up to 4.67 V, where it shows a slight further decrease down to a minimum of 70 cm^2, before increasing again up to 6.0 k cm^2 at 4.90 V. In the low potential region around 3.83 V to 4.15 V, is almost one order of magnitude higher for o-LNMO than for d-LNMO. From 4.15 V to 4.90 V, however, is very similar for o-LNMO and d-LNMO, with little variation between approximately 4.20 and 4.70 V. Overall, measured values of are in good agreement with literature.[224,225]

The SOC-dependent ionic conductivity is plotted in Figure 5.5b and shows a very similar variation with Li activity and electrode potential as for both d-LNMO and o-LNMO. In the range up to roughly 4.15 V, is about one order of magnitude lower for o-LNMO than for d-LNMO. For d-LNMO, increases by two orders of magnitude from 10^{-9} S/cm at 3.83 V to approximately 10^{-7} S/cm at 3.95 V. For o-LNMO, even increases

by three orders of magnitude from 10^{-10} S/cm to 10^{-7} S/cm at about 4.15 V. Above 4.15 V the ionic conductivity of both samples is nearly identical, remaining surprisingly constant up to 4.70 V and then decreasing again down to around $10^{-9.5}$ S/cm at 4.90 V. The broad plateau can be attributed to the presence of oxygen vacancies, as described in the defect chemical discussion. Literature reports of the SOC-dependent ionic conductivity are hard to find, but the value of about 10^{-9} S/cm measured by Amin and Belharouk for a nominally stoichiometric LNMO pellet[216] is in good agreement with our results at the lowest electrode potentials (i.e., close to full lithiation of the tetrahedral sites).

The volume-specific chemical capacitance of d-LNMO and o-LNMO is shown in Figure 5.5c. Up to around 4.30 V versus Li^+/Li, values of are about half an order of magnitude higher for d-LNMO than for o-LNMO. For both samples, exhibits a broad peak at 4.02 V, reaching a maximum value of 1185 F/cm^3 and 382 F/cm^3 for d-LNMO and o-LNMO, respectively. Above 4.30 V the data sets of both samples closely match each other, with the only difference being the sharper and higher double peaks of for o-LNMO at 4.68 V and 4.74 V. The double peaks around 4.7 V strongly resemble the peaks found in LMO, presumably due to ordering of Li ions on the tetrahedral sites at half occupancy. A detailed analysis of these peaks is beyond the scope of this paper, which focusses on the broad peak around 4.0 V caused by oxygen vacancies. The general appearance and magnitude of our measurements are in good agreement with CV curves and differential capacity plots found in the literature.[224–226]

The chemical capacitance from impedance fits can be compared to the values obtained from cyclic voltammetry via

—— (5.6)

where is the current density, the scan rate and the film thickness. The values from CV and impedance measurements are shown in a combined plot in Figure 5.6a and Figure 5.6b for d-LNMO and o-LNMO, respectively. Overall, the two data sets are in good agreement with each other for both samples, with the values from CV scans being slightly higher than those from impedance measurements due to the presence of side reactions and corresponding background currents. Notably, for from impedance data, the double peak around 4.7 V is confined to a smaller electrode potential range and appears in between the charge and discharge peaks of the CV scans. Both the broadening and shifting of the CV peaks with respect to the impedance data can be attributed to overpotentials encountered in the CV scans that increase with increasing current density and therefore are especially evident in regions of high chemical capacitance. These results again highlight the fact that the chemical capacitance of a Li storage thin film electrode, and hence also the equilibrium charge curve unaltered by kinetic overpotentials or side reactions, can be extracted from SOC-dependent impedance spectra.

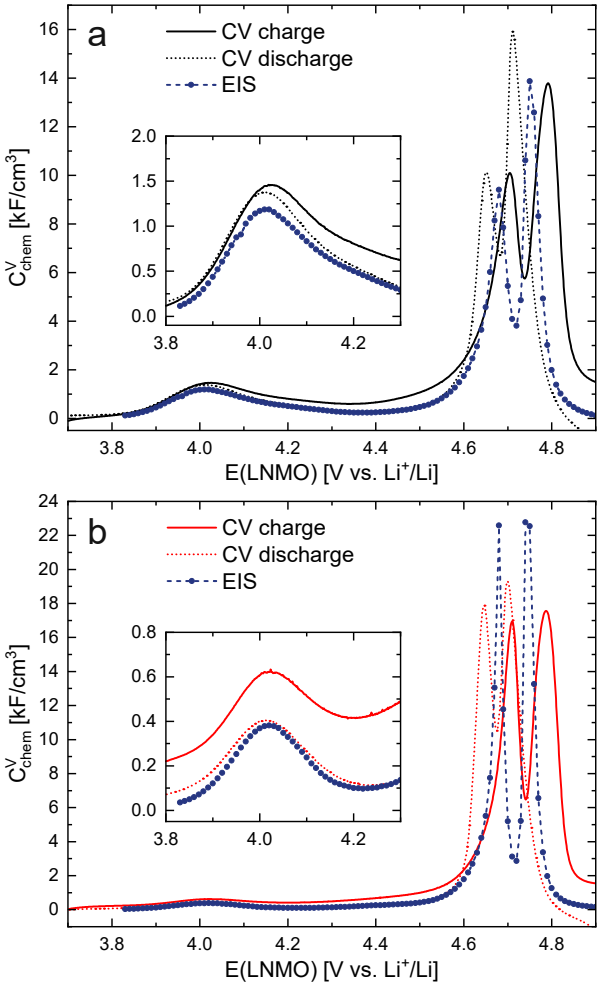

Figure 5.6: Comparison of the volume-specific chemical capacitance obtained from impedance fits (EIS) and from cyclic voltammetry (CV) scans for **(a)** d-LNMO and **(b)** o-LNMO.

The variation of the chemical diffusion coefficient with Li activity and electrode potential (Figure 5.5d) is more complex than the trends of , , and , and needs to be understood as the ratio between and according to Equation (5.5). Without going into details of the differences between d-LNMO and o-LNMO, we can state that the values are very similar above 4.4 V and significantly different for lower voltages. The latter is not surprising, considering the differences in and in the same potential region. The two sharp minima at 4.68 V and 4.74 V reflect the corresponding maxima of at the same electrode potentials. As expected from the curve, these minima are sharper and deeper for o-LNMO than for d-LNMO. The shape and magnitude of the variation of with SOC agree excellently with other literature reports, although values below 4.3 V are rarely reported.[224,226,227]

Overall, the d-LNMO and o-LNMO samples behave similarly in the high-voltage region above approximately 4.30 V, where reversible Li^+ release/insertion occurs at the tetrahedral Li sites upon oxidation/reduction of $Ni^{2+/3+/4+}$. At potentials below 4.30 V, on the other hand, the strongly deviating electrochemical properties of the two samples clearly reflect the higher charge carrier concentrations of d-LNMO in the $Mn^{3+/4+}$ regime due to a higher level of oxygen deficiency, which was already evident from the CV curves in Figure 5.2a. We define the oxygen vacancy regime as the electrode potential region below 4.37 and 4.21 V for d-LNMO and o-LNMO, respectively, which corresponds to the position of the respective minima in Figure 5.6. By integrating the chemical capacitance (from EIS) according to

(5.7)

for the corresponding potential limits, the fraction of the total reversible capacity located in the Mn-regime can be evaluated as 19% and 4.2% for d-LNMO and o-LNMO, respectively. By reconsidering the explicit chemical formula $LiNi_{0.5}Mn^{4+}_{1.5-2}\ Mn^{3+}_{2}O_{4-}$, the corresponding oxygen nonstoichiometries can then be estimated as = 0.095 and = 0.021, which amounts to oxygen vacancy concentrations of 2.4% and 0.53% with respect to oxygen sites, respectively. Beside the differences in total capacity, the curves of d-LNMO and o-LNMO in the oxygen vacancy regime also differ in their slope above 4.02 V, which will be analyzed in more detail in the next section. As already discussed in the introduction, the cation/anion imbalance may also be due to cation interstitials, even though in literature mostly oxygen vacancies are assumed. The following defect chemical analysis of the electrochemical properties would then have to be adapted without changing its basic concepts and conclusions.

5.4 Discussion

5.4.1 Defect Chemical Model for Oxygen-Deficient LNMO

The material parameters deduced so far describe the kinetics of Li insertion (, ,) and its thermodynamics ( ). For and , a more or less straightforward relation to defect chemical properties and considerations can be expected. Particularly a defect chemical analysis of may be a powerful tool for understanding and interpreting the impact of oxygen vacancies on the charge/discharge behavior of LNMO. This is shown in the remaining part of the paper. First, we introduce the basic defect chemical model of stoichiometric and oxygen-deficient LNMO, which already qualitatively explains many features of the measured (and) dependences on voltage. In a second step, we specify the defect model for the additional storage regime introduced by oxygen vacancies (oxygen vacancy regime). Finally, we compare the measured chemical capacitance with the model and refine the model such that all essential features (absolute value of and slope shapes at both sides of

the peak) can be explained. This refined consideration leads to important conclusions with respect to the local chemical environment of oxygen vacancies and defect interactions between oxygen vacancies, lithium vacancies and electrons. Thus, it substantially improves the understanding of LNMO voltage profiles.

In a recent study on LMO thin films,[52] it was shown that the defect chemistry of spinel cathode materials, i.e., the ionic and electronic point defect concentrations and chemical capacitance as a function of electrode potential, can be described by dilute-solution thermodynamics over a surprisingly wide Li stoichiometry range when taking site restriction effects into account. By solving the set of mass action laws defined by the available octahedral and tetrahedral lattice sites, together with the appropriate charge neutrality expression, the corresponding point defect concentrations as a function of Li activity (i.e., a Brouwer diagram) can be obtained. As long as only one type of Li site and one type of redox couple need to be considered, an analytical expression for can be derived, which depends only on the relevant defect concentrations. As soon as two or more lattice sites become relevant, such as the octahedral and tetrahedral sites in a typical spinel material, can only be calculated via Equation (5.1) and therefore requires detailed knowledge of the Li chemical potential and its defect concentration dependences. For oxygen-deficient LNMO, this defect chemical description is further complicated by (i) the presence of a second type of transition metal redox couple ^{2} $^{\bullet 3}$ $^{\bullet 4}$ in addition to ^{3} $^{\bullet 4}$ (ii) the presence of oxygen vacancies that act as donor dopants and (iii) the potential of these oxygen vacancies to engage in charge trapping (i.e., defect association) reactions. The general formalism for calculating (i) the total Li chemical potential, and thus also , for multiple Li sites, multiple redox couples and variable doping states, as well as (ii) the relevant defect concentrations as a function of electrode potential is detailed in Section 5.6.2 of the Appendix. Herein, we restrict ourselves to a qualitative discussion of the resulting Brouwer diagrams under certain assumptions.

To simplify our brief discussion of the Ni regime around 4.7 V, we consider neither separate ^{2} $^{\bullet 3}$ and ^{3} $^{\bullet 4}$ redox regimes nor Li ordering. We treat Ni as a single type of redox couple contributing to the total capacity with one electron per formula unit, instead of considering it as two different redox couples, each contributing 0.5 electrons per formula unit. In the following analysis, an electron on Mn corresponds to ^{3} and an electron on Ni corresponds to 1/2 ^{2} , with ^{4} ^{0} and ^{0} being the concentration of formula units. In a first step, we discuss the defect concentrations as a function of Li activity (i.e., the Brouwer diagram), assuming a single tetrahedral site regime without ordering effects. For the sake of illustration, we also include a continuous octahedral site regime without any two-phase regions, even though this is not observed in experiments. The resulting Brouwer diagram is shown in Figure 5.7a.

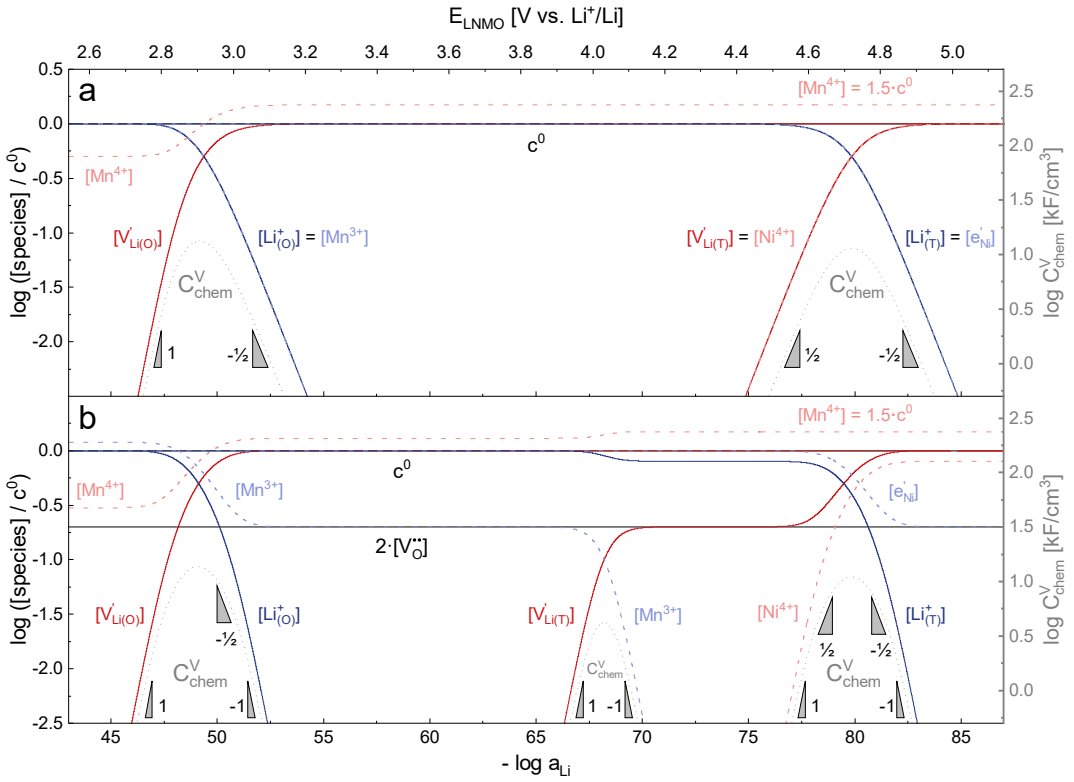

FIGURE 5.7: Calculated Brouwer diagrams of **(a)** stoichiometric and **(b)** oxygen-deficient LNMO, neglecting Li ordering on tetrahedral sites and thus the characteristic double peak at 4.7 V. For both diagrams, charge carrier concentrations were calculated via Equations (5.26), (5.27), (5.30), and (5.31) in the Appendix. was calculated from Equation (5.1) by inserting as derived in the Appendix (Equations (5.23)-(5.29)). The values ^{0} • = 2.90 V, ^{0} • = 4.02 V, ^{0} • = 0.00 V, and ^{0} • = 0.70 V were chosen such that the chemical capacitance peaks of the defect model occur around the same electrode potentials as observed experimentally. For the defect model of oxygen-deficient LNMO, an oxygen deficiency of = 0.1 was inserted into Equation (5.32). Please note that the continuous octahedral regime around 2.9 V is not observed experimentally due to the presence of a two-phase region.

As also shown for LMO,[52] the Brouwer diagram of stoichiometric LNMO features two main storage regimes that correspond to the octahedral and tetrahedral sites. However, in LNMO there are two different transition metals (Mn and Ni) with redox capacities of 1.5 and 1 electron per formula unit, respectively, rather than a single transition metal (Mn) that covers the total storage capacity of two formula units in LMO. As a consequence, the voltage-dependent concentrations of electrons show a similar site-restricted behavior as the ionic charge carriers, that is, Li vacancies and on the Li sites. In the tetrahedral site regime without ordering (around 4.7 V), the Brouwer diagram of stoichiometric LNMO resembles that of a generic layered oxide (see ref. 52, Figure 7a). At high and low tetrahedral site occupancy, ^{4} and vary with slopes of 1•2 and 1•2, respectively, with a corresponding peak in the transition region around half site occupancy, where

^{4} . Hence, the chemical capacitance peak originates from the site restriction of both Li on the tetrahedral sites and electrons on Ni. In the hypothetical octahedral site regime around 2.9 V, increases with a slope of 1 at high site occupancy with ^{4} 0 5 ^{0}, while ^{3} varies with a slope of 1•2 at low site occupancy. These slopes are again reflected in the corresponding peak. It is also straightforward to include Li ordering in the tetrahedral regime by considering two energetically different tetrahedral sites. This was extensively discussed for pure LMO and can explain the experimentally observed characteristic double peak around 4.7 V.[52] In this study, however, we focus on the effects introduced by oxygen vacancies, i.e., donor doping.

Figure 5.7b displays the Brouwer diagram for such an oxygen-deficient material, again without Li ordering on the tetrahedral sites. Assuming that oxygen vacancies are electronically compensated by ^{3} according to 2 ^{3} for $LiNi_{0.5}Mn^{4+}_{1.5-2}$ $Mn^{3+}_{2}O_{4-}$, the tetrahedral site regime is split into a low-voltage Mn (4.0 V) and a high-voltage Ni (4.7 V) subregime, as shown in Figure 5.7b. Interestingly, the peaks now are no longer caused solely by Li and/or electron site restriction, but reflect transitions from ionically to electronically dominated charge compensation of the oxygen vacancies. More specifically, in the oxygen vacancy regime around 4.0 V, charge compensation switches from ^{3} to , with slopes of 1 and -1, respectively, and a corresponding peak in . The total storage capacity of this regime is defined by the oxygen vacancy concentration. Please note that this situation is fully analogous to the chemical capacitance peak observed in acceptor-doped mixed conducting oxides, where charge compensation switches from oxygen vacancies to electron holes when increasing the oxygen chemical potential.[53]

In the tetrahedral-site Ni regime around 4.7 V, the oxygen vacancies remain compensated by Li vacancies, resulting in slopes of 1 and -1 for ^{4} and , being the minority charge carriers at high and low site occupancy, respectively. At intermediate site occupancies, where ^{4} 2 and 2 , the slopes flatten from 1 and -1 to 1•2 and 1•2 for ^{0} and , respectively. For the entire hypothetical octahedral site regime, oxygen vacancies remain compensated by ^{3} , resulting in a steepening of the slope of from 1•2 to -1 for 2 . Since a total of 1.5 ^{4} are available per formula unit compared to only 1 octahedral Li site, the total capacity of the octahedral regime is not affected for realistic levels of oxygen deficiency.

Qualitatively, the tetrahedral regime (approximately 3.7 V to 5.0 V) of the Brouwer diagram for oxygen-deficient LNMO in Figure 5.7b can explain several key features of the experimental data presented in Figure 5.5. The inverse charge-transfer resistance and the ionic conductivity both increase and decrease at low and high electrode potentials, respectively, but remain nearly constant at intermediate potentials from about 4.1 V to 4.6 V. This constancy of 1• and is remarkably consistent with the almost constant concentration of the relevant ionic charge carrier between the 4.0 V and 4.7 V regimes. Both 1•

and are lower for o-LNMO than for d-LNMO in the low-voltage region due to the lower oxygen vacancy and hence lower Li vacancy concentrations in this potential region. The fact that this difference almost vanishes at intermediate electrode potentials suggests a difference in the concentration-dependence of the respective ionic mobilities of d-LNMO and o-LNMO.

As predicted by Figure 5.7b, exhibits two main peaks corresponding to the tetrahedral-site Mn and Ni regimes around 4.0 V and 4.7 V, respectively, the former being lower for o-LNMO due to the lower oxygen vacancy concentration. As already discussed above, the pronounced double peak measured at 4.68/4.74 V is attributed to Li ordering on tetrahedral sites, as for pure LMO.[52] This effect is not included in the calculations of Figure 5.7b and beyond the scope of this paper. However, at the onset of the Ni regime, around 4.6 V, both samples show a slope of 1•2, in agreement with Figure 5.7b for high charge carrier concentrations. The region of low ^{4} , where a slope of 1 would be expected, is not visible in the experimental data due to an overlap with the smeared out low-voltage oxygen vacancy regime (see below). In the following, we analyze the impact of oxygen deficiency on the defect chemistry of LNMO in more detail and therefore focus on the oxygen vacancy regime (Mn regime) below 4.5 V.

5.4.2 Defect Chemical Model for the Oxygen Vacancy Regime

We start by isolating the oxygen vacancy regime (i.e., the tetrahedral-site Mn regime introduced through charge compensation of oxygen vacancies) from the full defect chemical model in Figure 5.7b. Since only one Li site (tetrahedral site) and one redox couple (^{3} •^{4}) are relevant in this regime, an explicit expression for the Li chemical potential can easily be derived, without resorting to the more complicated multi-site formalism in Section 5.6.2 of the Appendix. For this purpose, we consider the Li insertion equilibrium

(5.8)

for the relevant defects, that is, tetrahedral Li vacancies and electrons, in Kröger-Vink notation, with corresponding to ^{3} . To account for different capacities, and thus also different site restrictions, of lattice sites and redox species, we write the site occupancy of species as

$$\frac{}{0} \tag{5.9}$$

with and being the concentration of species and the number of corresponding sites per formula unit, respectively. For example, $_{3}$ 1 5 and $_{4}$ 0 5. The balance of chemical potentials can then be written as

(5.10)

where and are the individual site-restricted chemical potentials of tetrahedral vacancies and electrons (or ^{3}), which are related to the respective site occupancies according to

$$^{0} \quad \frac{}{1} \tag{5.11}$$

and

$$^{0} \quad \frac{}{1} \tag{5.12}$$

with ^{0} being the standard chemical potential of species . By combining Equations (5.2), (5.10), (5.11), and (5.12), the corresponding law of mass action can then be formulated as

$$\frac{1}{1} \quad \frac{^{\text{metal}\ 0} \quad ^{0}}{} \tag{5.13}$$

with being the equilibrium constant of Li insertion according to Equation (5.10). In the case of oxygen-deficient LNMO, the charge neutrality expression reads

$$2 \tag{5.14}$$

The concentrations of ^{3} , ^{4} , and are related via

$$1 \tag{5.15}$$

and

$$_{3} \quad 1 \quad _{4} \tag{5.16}$$

with 1 and $_{3}$ $_{4}$ 1 5. The system of equations defined by Equations (5.13), (5.14), (5.15), and (5.16) can then be solved for the four individual point defect concentrations as a function of Li activity if or the corresponding standard chemical potentials ^{0} are known.

Furthermore, the chemical capacitance can be obtained by inserting Equations (5.9), (5.10), (5.11), (5.12), and (5.14) into Equation (5.1). For realistic oxygen vacancy concentrations, i.e., for 1, site restriction of and can be neglected and Equations (5.11) and (5.12) can be simplified by assuming • 1 and • 1 . In this case, the chemical capacitance can be expressed as[59]

$$\frac{^{2}}{} \quad \frac{1}{} \quad \frac{1}{} \tag{5.17}$$

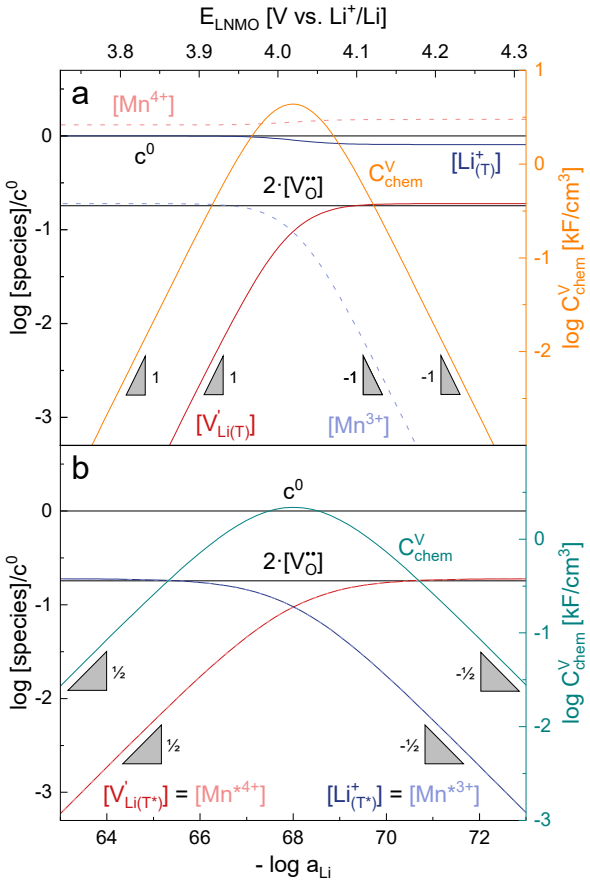

FIGURE 5.8: (a) Brouwer diagram and chemical capacitance of the oxygen vacancy regime extracted from Figure 5.7b for 0 095 ^{0} and 10 $^{67\,8}$. **(b)** Brouwer diagram and chemical capacitance of the oxygen vacancy regime, assuming energetically non-equivalent and sites, for 0 095 ^{0} and 10 ^{68}.

The resulting point defect concentrations and chemical capacitance are shown in a log-log plot versus (i.e., a Brouwer diagram) in Figure 5.8a for 0 095 ^{0} and 10 $^{67\,8}$. The value of is taken from the integration of the d-LNMO data of impedance fits below 4.37 V (see Equation (5.7) and following paragraph). is chosen such that the peak of the defect model appears at the same electrode potential versus Li^+/Li as in the experimental results. Due to the clear separation of the octahedral (2.9 V), oxygen vacancy (4.0 V) and Ni tetrahedral (4.7 V) regimes in Figure 5.7b, the isolated defect model of the oxygen vacancy regime (Figure 5.8a) is virtually identical to the full defect model (Figure 5.7b) of oxygen-deficient LNMO in the selected potential region. The Brouwer slopes of 1 and -1 in the chemical capacitance result from the corresponding variation of and ^{3} ( ]), respectively, while and ^{4} remain nearly constant on a logarithmic scale.

A direct comparison of the chemical capacitance from impedance fits (black dots) and from the defect model in Figure 5.8a (orange line) is shown in Figure 5.9a and Figure 5.9b for d-LNMO (0 095 ^{0}) and o-LNMO (0 021 ^{0}), respectively. For both o-LNMO and d-LNMO, the defect model from Figure 5.8a predicts a peak, the position of which reflects the value of . The total charge contained within the peak corresponds to 2 , and enters the defect chemical calculation as a fixed parameter derived via integration of the experimental curve up to the minimum between the oxygen vacancy and Ni regimes via Equation (5.7). Although the calculated curve appears to be in the same order of magnitude as the experimental data in terms of total charge (i.e., area under the peak), the calculated curve exhibits steeper slopes and significantly higher peak values for both d-LNMO and o-LNMO. Furthermore, the model fails to describe the particularly flat slope of the experimental data between 4.0 and 4.3 V. In the following, we refine the defect model by including different Li site energies close to oxygen vacancies.

5.4.3 Chemical Capacitance Indicating Modified Tetrahedral Li Sites in the Oxygen Vacancy Regime

The defect model in Figure 5.8a assumes that the tetrahedral Li sites and ^{3} $^{\bullet 4}$ redox centers being active in the oxygen vacancy regime around 4.0 V are indistinguishable from the tetrahedral Li sites involved in the tetrahedral-site Ni regime around 4.7 V and the remaining Mn sites, respectively. In other words, it is assumed that the local chemical environments surrounding each point defect are unaffected by the oxygen vacancies. However, owing to electrostatic considerations, it is reasonable to assume that Li vacancies and ^{3} are significantly stabilized in vicinity to an oxygen vacancy. This leads us to conclude that a suitable defect chemical model for d-LNMO has to consider not only the presence of ^{3} due to charge compensation of the oxygen vacancies, but also the different local chemical environments of the ionic and electronic point defects involved in the corresponding oxygen vacancy regime.

As a first step to include defect interactions, we adapt our defect model to treat the tetrahedral Li sites and ^{3} $^{\bullet 4}$ species involved in the oxygen vacancy regime as energetically non-equivalent to the remaining Li sites and Mn redox centers. Accordingly, we assume that Li storage in the oxygen vacancy regime is locally restricted to the lattice sites in immediate proximity to the oxygen vacancies. In a first approximation, this can simply be done by relating the number of available tetrahedral lattice sites T* or electronic sites Mn* per formula unit to the oxygen nonstoichiometry according to 2 , where the asterisk denotes the non-equivalence of ^{3} (=), ^{4} , , and the corresponding defect species in Figure 5.8a. Equations (5.8)-(5.16) are then still valid for species j*, and can again

be solved for the individual point defect concentrations , with the additional condition

$$1 \quad 3 \quad 1 \quad 4 \tag{5.18}$$

However, then site restriction can no longer be neglected, meaning that the full site-restricted chemical potentials in Equations (5.11) and (5.12) have to be inserted into Equation (5.1), together with the balance of chemical potentials (Equation (5.10)) to obtain the correct expression for , which reads

$$\frac{2}{\frac{2\ 0}{}} \frac{1}{\frac{1}{1}} \frac{1}{\frac{1}{1}} \tag{5.19}$$

For $_3$ 2 , Equation (5.19) simplifies into

$$\frac{2}{2} \quad \frac{1}{} \quad \frac{1}{} \tag{5.20}$$

The resulting point defect concentrations are plotted together with from Equation (5.20) as a Brouwer diagram in Figure 5.8b for 0 095 ^{0} and 10 ^{68}. While in the original defect model in Figure 5.8a, only and ^{3} vary significantly and cause a relatively sharp peak with slopes of 1 and -1, the concentrations ^{4} and ^{3} vary in concert in the adapted defect model in Figure 5.8b, resulting in a relatively broad peak with slopes of 1•2 and 1•2. The total storage capacity, i.e., the total area under the curves, is the same for both models and is defined by the oxygen vacancy concentration in the material. Please note that due to the asymmetry of the defect model in Figure 8a, the peak of appears at , while in the adapted (now symmetric) defect model the peak position is defined by . We therefore chose a slightly lower value for the defect model in Figure 5.8a so that for both models the peak is located at approximately 68 (E_{LNMO} 4.02 V versus Li^+/Li), where it is observed experimentally.

The comparison of the two different defect models with the experimental data is shown in Figure 5.9a and Figure 5.9b for d-LNMO and o-LNMO, respectively. The adapted defect model clearly fits the experimental data better, in terms of both slopes and absolute values. In the low-potential region below 4.0 V versus Li^+/Li, the adapted model comes remarkably close to the experimental data, although the absolute values predicted by the model are slightly higher.

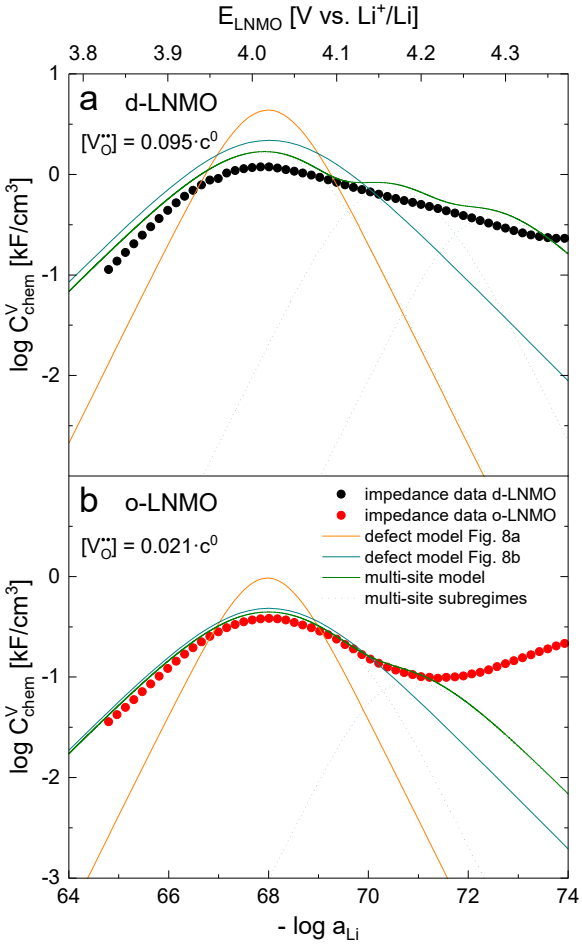

Figure 5.9: Calculated chemical capacitance of three different defect models (continuous lines) compared to the data from impedance fits (black dots). **(a)** d-LNMO: experimental data and calculated chemical capacitances from Figure 5.8a, Figure 5.8b and from the multi-site model for 0 095 ^{0}, $_{1}$ 0 66, $_{2}$ 0 21, $_{3}$ 0 13, $^{0}_{1}$ • 0 00 V, $^{0}_{2}$ • 0 12 V, $^{0}_{3}$ • 0 21 V, and ^{0} • 4 02 V. **(b)** o-LNMO: experimental data and calculated chemical capacitances from Figure 5.8a, Figure 5.8b and from the multi-site model for 0 021 ^{0}, $_{1}$ 0 86, $_{2}$ 0 14, $^{0}_{1}$ • 0 00 V, $^{0}_{2}$ • 0 12 V, and ^{0} • 4 02 V.

Interestingly, the ^{3} •^{4} transition and thus the peak of the oxygen vacancy regime in LNMO is very close, in terms of electrode potential, to the main ^{3} •^{4} transition in LMO. This requires very similar values. However, we already discussed that significant stabilization of Li vacancies and electrons in the vicinity of oxygen vacancies are required to explain our measured data. According to Equation (5.13), a similar of LNMO and LMO despite very different ^{0} and ^{0} is only possible if changes of the two standard chemical potentials are very similar.

However, in the high-potential region above 4.0 V, there are still substantial deviations of the model from the measured values, with the calculated peak value being significantly higher and the slope being steeper than the experimental data. Especially for d-LNMO, the measured peak appears smeared-out towards high potentials, with a slope that is significantly flatter than predicted by both defect models in Figure 5.8. It is worth mentioning that this smeared-out peak of d-LNMO is also seen in various other studies in the literature,[43,173,228–230] but has received relatively little attention so far. In the following, we explain these deviations by leaving the assumption of only one ^{0} level.

5.4.4 Chemical Capacitance as a Fingerprint of Stabilized Mn^{3+}

So far, our defect model explains the absolute values of the peak as well as its flattened slope close to 1●2 for voltages below 4.0 V. We still have to understand the even smaller slope above 4.0 V and the very broad decrease for the d-LNMO sample with a high concentration of oxygen vacancies.

In principle, we face a complex situation with multiple-defect interaction including (at least) oxygen vacancies , lithium vacancies or occupied Li sites , and electrons ^{3} . Different concepts may be employed for dealing with defect interactions, for example, activity coefficients or defect association equilibria. Owing to the complex situation with three relevant particles/defects, we choose a third approach to extend the given model with modified site energies around an oxygen vacancy. We simply introduce a finite number of different standard defect energies and thus different ^{0} terms.

In this manner, we consider the existence of multiple energetically different lattice sites in proximity to oxygen vacancies, where Li storage is assumed to be located for the oxygen vacancy regime. The variations in the local chemical environments of these sites can modulate the stabilizing effect of the oxygen vacancy on both Li vacancies and electrons (^{3}). Additional stabilization of Li vacancies would move part of the chemical capacitance to lower electrode potentials, as the corresponding is more easily removed from the lattice. For electrons, on the other hand, additional stabilization would shift part of the chemical capacitance to higher electrode potentials, as the stabilized ^{3} is less easily oxidized. Since the defect model in Figure 5.8b is already in good agreement with the measured data below 4 V, but still shows significant deviations above 4 V, especially for d-LNMO (c.f. Figure 5.9a), we refine the defect model only for electrons to account for different local chemical environments in vicinity to an oxygen vacancy.

For this purpose, we resort to the multi-site formalism described in Section 5.6.2 of the Appendix. More specifically, we consider the presence of three (d-LNMO) or two (o-LNMO) types of sites, each site having a different value of ^{0} , and derive the corresponding multi-site-restricted electron chemical potential from Equation (5.27) and (5.29). Since the total number of available and sites is the same and no additional doping ef-

fects need to be considered within the oxygen vacancy regime itself, the correction term c in Equation (5.29) can be set to zero. To assign each of the sites a fraction of the total oxygen vacancy regime capacity 2 , the number of available lattice sites per formula unit can be defined as 2 , with 0 1, 1, and 2 . The resulting can then be inserted into Equation (5.10), together with the unchanged from Equation (5.11), to obtain the total Li chemical potential and finally the chemical capacitance via Equation (5.1).

The resulting chemical capacitance curves (green line) are shown in comparison to the experimental data and the previous defect models in Figure 5.9a and Figure 5.9b for d-LNMO (0 095) and o-LNMO (0 021), respectively. The corresponding subregimes for each site are indicated as dotted lines. For both plots, the values of ^{0} and were chosen manually to approximate the experimental data, as indicated in the figure caption. Please note that, although a mathematical fitting algorithm could in principle be applied to obtain the closest approximation, the conclusions of our qualitative discussion would remain the same. For both d-LNMO and o-LNMO, the calculated curves are in good agreement with the experimental data for the entire relevant voltage range (up to 4.37 and 4.21 V versus Li^+/Li for d-LNMO and o-LNMO, respectively).

As expected for a multi-site model, the peaks are now split into three/two sub-peaks for d-/o-LNMO. For both samples, the model features sub-peaks at 4.02 V and 4.17 V, with d-LNMO having an additional sub-peak at 4.28 V. Each sub-peak corresponds to a different , with the total capacity remaining the same as for defect models from Figure 5.8a and Figure 5.8b. The relative capacities of the peaks were set to $_1$ 0 66, $_2$ 0 21, $_3$ 0 13 for d-LNMO, and $_1$ 0 86, $_2$ 0 14 for o-LNMO.

For d-LNMO, the multi-site model correctly describes the smeared-out chemical capacitance curve towards higher electrode potentials, although the calculated curve still exhibits a wavier profile than the experimental data. In principle, this could be corrected by assuming a larger number of sites with slightly different values of ^{0} . Given the large variety of possible local chemical environments of oxygen vacancies in disordered LNMO,[213] this would be a plausible assumption.

For o-LNMO, the multi-site model also gives a good fit of the experimental data, with the peak at 4.17 V being significantly diminished compared to d-LNMO and the third peak at 4.28 V being completely obsolete. Thus, while the curve of d-LNMO in the oxygen vacancy regime is stretched out towards higher electrode potentials due to additional stabilization of ^{3} , the o-LNMO sample largely follows the single-site behavior from Figure 5.8b. This suggests that the two samples differ not only in their oxygen vacancy concentrations, but also in the variety of local chemical environments surrounding each oxygen vacancy, which excellently agrees with the well-established correlation of Ni-disorder and oxygen-deficiency.[213]

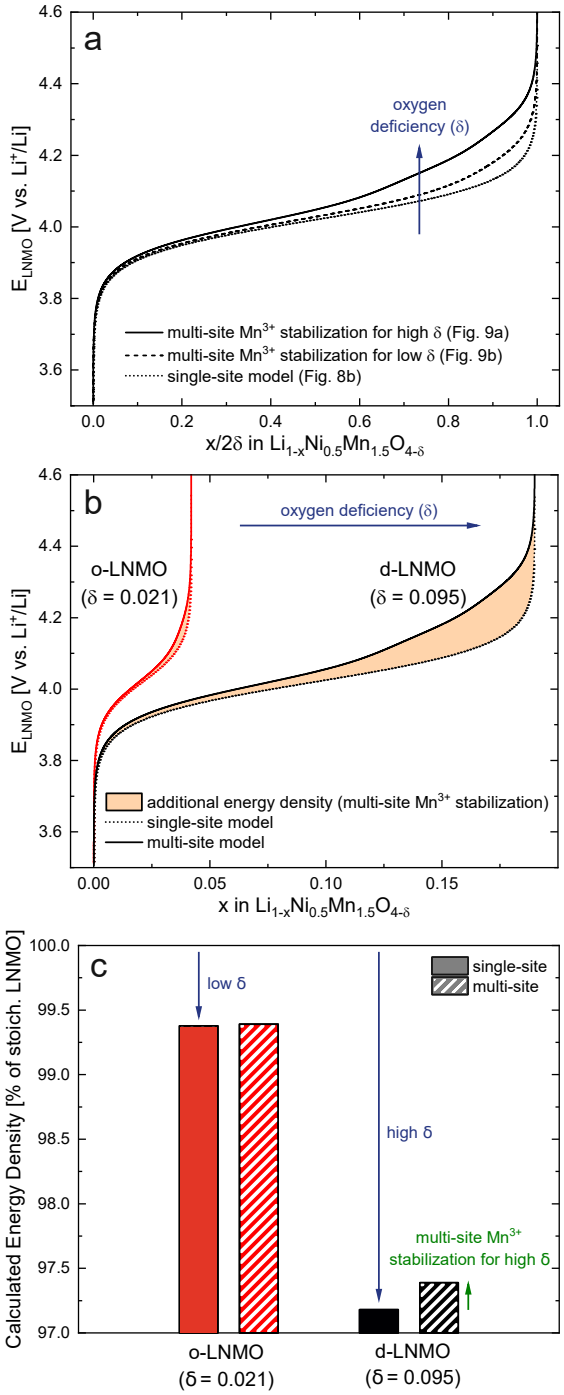

Figure 5.10: (a) Charge curves of the oxygen vacancy regime calculated by integration of via Equation (5.7) for the single-site model in Figure 5.8b and the multi-site models in Figure 5.9. Capacities were normalized by 2 to allow a direct comparison between d-LNMO and o-LNMO. **(b)** Calculated charge curves of d-LNMO and o-LNMO showing the impact of oxygen deficiency and additional ^{3} stabilization in the multi-site model. **(c)** Impact of oxygen deficiency and defect interactions on the calculated energy density of LNMO compared to stoichiometric LNMO for 0 1. For the Ni regime (2 1), an average electrode potential of 4.72 V vs Li^+/Li was assumed.

Finally, we can illustrate the impact of oxygen vacancies on the shape of charge curves, which are obtained by integration of according to Equation (5.7). First, we compare the capacity-normalized charge curves of the oxygen vacancy regime for d-LNMO, o-LNMO and the ideal defect model in Figure 5.8b. As shown in Figure 5.10a, the additional stabilizing defect interactions of oxygen vacancies and ^{3} in the multi-site model lead to an upwards shift of the charge curve towards higher electrode potentials, thereby raising the average voltage in the oxygen vacancy regime. As expected from the respective distributions of in Figure 5.9, this effect is more pronounced for d-LNMO than for o-LNMO. The corresponding increase in energy density is marked in Figure 5.10b as the area between the calculated charge curves with and without multi-site electron (^{3}) stabilisation. Not only is the additional stabilization of ^{3} stronger for d-LNMO than for o-LNMO, but the total impact on the average voltage, and hence energy density, is further scaled up by the higher level of oxygen deficiency ( ) in d-LNMO.

On the other hand, an increase in also reduces the average voltage of the overall tetrahedral-site regime by moving part of its capacity from the high-voltage Ni to the lower-voltage Mn (oxygen vacancy) region. This leads to a trade-off between charge compensation by ^{3}, which lowers the average voltage, and the additional multi-site stabilization of ^{3} by oxygen vacancies, which again compensates at least part of the voltage loss. As shown in Figure 5.10c, the lower energy density of the o-LNMO sample compared to ideal stoichiometric LNMO is still dominated by the level of charge compensation due to oxygen deficiency, and only a very small fraction of this loss is regained by multi-site electron stabilization. For d-LNMO, on the other hand, a significant fraction of the energy density loss is compensated, thus mitigating the negative impact of oxygen vacancies on the average voltage.

These considerations raise the question whether oxygen vacancies and the accompanying electron (^{3}) stabilization might also increase the average voltage and energy density in $LiMn_2O_{4-}$ cathodes. In fact, Wang et al. recently reported differential capacity curves of oxygen-deficient LMO samples, which appear shifted by more than +50 mV with respect to nearly stoichiometric LMO,[231] and are therefore consistent with our results for oxygen-deficient LNMO.

5.5 Conclusion

The electrochemical properties (charge-transfer resistance , ionic conductivity , specific chemical capacitance and chemical diffusion coefficient) of $LiNi_{0.5}Mn_{1.5}O_{4-}$ thin films were investigated by cyclic voltammetry and impedance spectroscopy as a function of SOC for high (d-LNMO) and low (o-LNMO) levels of oxygen deficiency . The extracted properties vary by up to three orders of magnitude, with the most notable differences between d-LNMO and o-LNMO being observed in the oxygen vacancy regime below approx-

imately 4.3 V versus Li^+/Li, where d-LNMO exhibits significantly higher values of 1/ , , , and (up to 4.15 V) than o-LNMO. Overall, the measured electrochemical properties are in excellent agreement with a defect chemical model based on ionic and electronic lattice site restrictions, with oxygen vacancies acting as a donor dopant. Closer analysis of the oxygen vacancy regime revealed that oxygen vacancies are not merely charge-compensated by Mn^{3+} or Li vacancies, but are involved in defect interactions that significantly impact the charge curve. For both d-LNMO and o-LNMO, the charge curve below 4.0 V is accurately described by a single-site defect model that treats the tetrahedral Li sites T* and Mn sites (Mn*) as locally restricted to the proximity of an oxygen vacancy due to stabilization (i.e., trapping) of electrons and Li vacancies. For a high level of oxygen deficiency (d-LNMO), the charge curve in the oxygen vacancy regime bends upwards towards higher electrode potentials, thus mitigating the voltage suppression introduced through to the presence of Mn ^{3} . This characteristic feature of the charge curve suggests that the oxygen vacancy concentration not only affects the amount of redox active Mn ^{3} $^{\bullet 4}$, but also causes multiple energetically different electron sites in the vicinity of an oxygen vacancy. Overall, these results reveal the complexity of effects introduced by oxygen vacancies in oxide-based Li insertion materials, but also the power of chemical capacitance measurements to understand and interpret the corresponding phenomena. Moreover, this study once more highlights the relevance of defect chemical concepts for understanding the complex interplay of ionic and electronic charge carriers in all battery materials.

5.6 Appendix

5.6.1 Fitting of Impedance Spectra

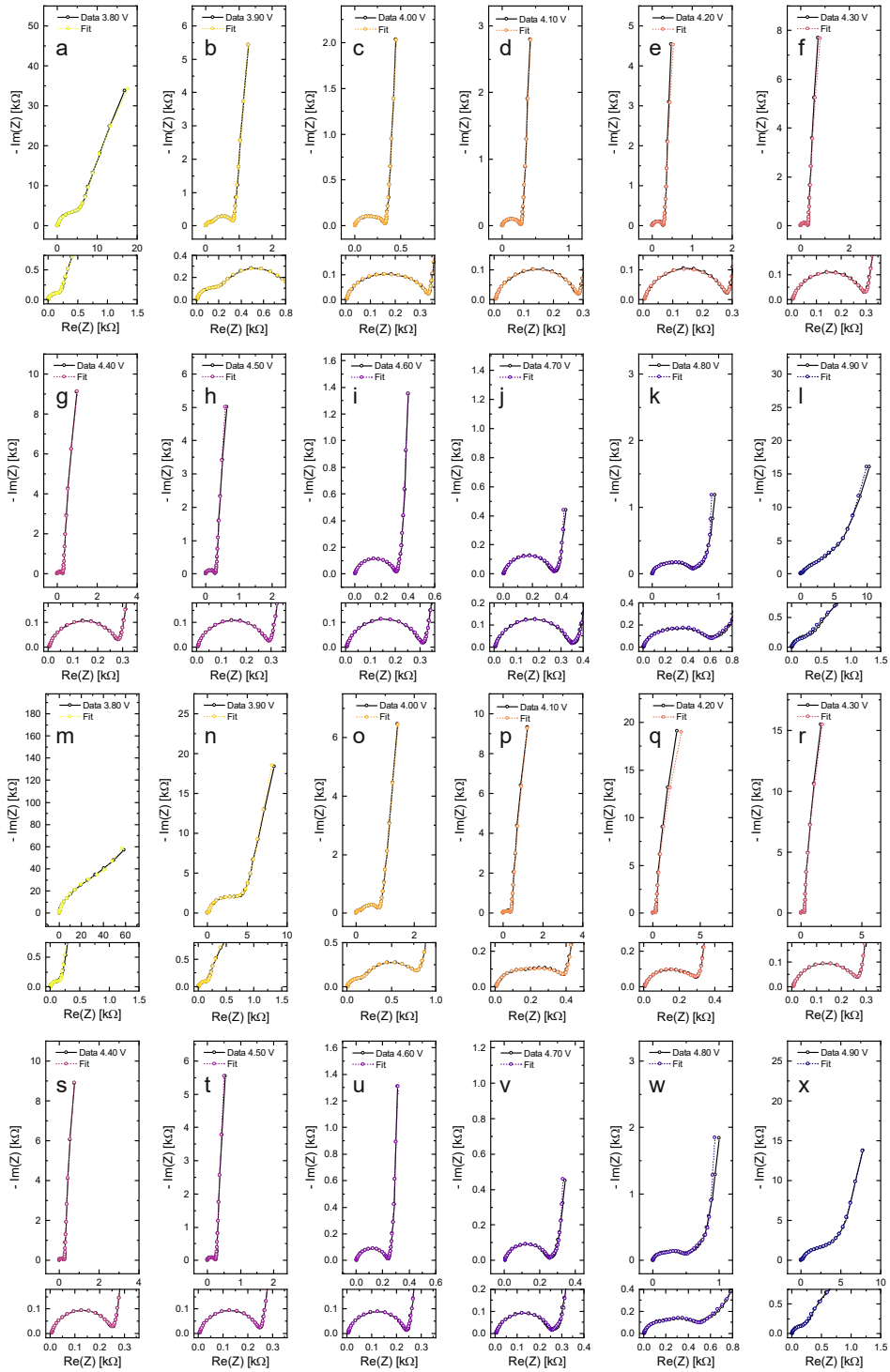

Figure 5.11: Fits of all impedance spectra shown in Figure 5.3. **(a-l)** d-LNMO (Figure 5.3a). **(m-x)** o-LNMO (Figure 5.3e).

5.6.2 Multi-Site Defect Chemical Models

Stoichiometric LNMO

Here we derive the general form of the Li chemical potential, and hence the chemical capacitance, for the case of multiple Li sites with different vacancy formation energies (e.g., octahedral and tetrahedral Li sites in a spinel structure) and multiple redox couples with different redox potentials (e.g., Mn and Ni in $LiNi_{0.5}Mn_{1.5}O_{4-}$). We start by considering the general insertion equilibrium of Li into an arbitrary material according to

(5.21)

where Li corresponds to formally neutral lithium in the external phase (i.e., a Li ion from the electrolyte together with an electron from the current collector according to) that defines the Li chemical potential with which the material is in equilibrium. and , in Kröger-Vink notation, correspond to a Li vacancy at lattice site i and an electron at transition metal site k. For example, in LNMO, corresponds to ^{3} and corresponds to either ^{3} or 1•2 ^{2} . As discussed in Section 5.4.1, we treat Ni as a single type of redox couple with a capacity of one electron per formula unit, hence we stick to the label without specifying its atomistic meaning. For further calculations, it is useful to reference the concentration of species to the total concentration of formula units ^{0} according to

$$\frac{}{^{0}} \tag{5.22}$$

with being the site occupancy of species j and the corresponding number of sites per formula unit. For example, 1 for the tetrahedral (T) and octahedral (O) Li sites in a typical spinel material. In the case of LNMO, two different transition metals (Mn and Ni) act as active redox couples in the insertion reaction with corresponding capacities of 1 5 and 1. The goal is now to obtain (i) an expression for the total Li chemical potential and (ii) the concentration of all electronic and ionic species as a function of , i.e., a Brouwer diagram. Although the latter could be obtained by solving the corresponding system of mass action laws combined with the appropriate charge neutrality equations, it is not straightforward to obtain an expression for , and hence the chemical capacitance, via this approach. As in our previous study on on LMO,[52] we therefore approach the defect chemical calculation via the separate chemical potentials of ionic and electronic charge carriers, as shown in the following.

For the insertion equilibrium in Equation (5.21) we can formulate the corresponding balance of chemical potentials as

(5.23)

with being the total Li chemical potential. We note that equilibrium conditions require that all Li sites share a common Li vacancy chemical potential and all electrons share a common electron chemical potential , which can be written as

0 (5.24)

1

and

0 (5.25)

1

As described in our previous study on $LiMn_2O_4$,[52] it is convenient to rearrange Equations (5.24) and (5.25) to obtain the individual site fractions and according to

(5.26)

0 0

1

and

(5.27)

0 0

1

The total vacancy and electron site fractions can then be expressed as

(5.28)

and

(5.29)

An additional correction term c was introduced in Equation (5.29) to describe a possible shift of with respect to , as discussed below. The value of c can be derived by comparing the values of and at the compositional boundaries of the material. For example, for stoichiometric LNMO with 1, 1 5, and 1, the total site fractions and should vary from 0 to 2 and 2 to 0, respectively, as the material is oxidized from $Li_2Ni^{2+}_{0.5}Mn^{+4}_{0.5}Mn^{+3}_{1.0}O_4$ to $Ni^{4+}_{0.5}Mn^{+4}_{1.5}O_4$. This requires a value of c = 0.5 to account for the fact that in the fully reduced state of the material, i.e., at full occupancy of the octahedral sites, 0.5 formula units of ^{3} remain. The correction term c can also be conveniently used to describe the effect of dopants, as shown in the next section.

Finally, the total chemical potentials and of Li vacancies and electrons, respectively, can be obtained by numerical inversion of Equations (5.28) and (5.29) and inserted into Equation (5.23) to obtain the total Li chemical potential, and hence the chemical capacitance via Equation (5.1). To obtain the concentration of all relevant species as a function of Li chemical potential, and can simply be inserted into Equa-

tions (5.26) and (5.27). The concentrations of species that are not explicitly considered in the above calculation, i.e., ^{4} , and can be obtained via

$$^{4} \quad 1 \quad ^{3} \tag{5.30}$$

and

$$1 \tag{5.31}$$

The resulting Brouwer diagram for stoichiometric LNMO, including the corresponding chemical capacitance, is shown in Figure 5.7a. The values ^{0} • = 2.90 V, ^{0} • = 4.02 V, ^{0} • = 0.00 V, and ^{0} • = 0.70 V (= elementary charge) were chosen such that the chemical capacitance peaks (i.e., charge curve plateaus) of the defect model occur around the same electrode potentials as observed experimentally.

Oxygen-deficient LNMO

The defect chemical calculation of stoichiometric LNMO can easily be adapted for the presence of an electronically compensated donor dopant, such as oxygen vacancies, by subtracting the donor site fraction from the correction term c according to

$$0\ 5 \qquad 0\ 5 \quad \frac{2}{^{0}} \tag{5.32}$$

where z is the charge number of the corresponding donor species. For oxygen vacancies ,

2. The adapted Brouwer diagram for oxygen-deficient LNMO is shown in Figure 5.7b for 0 1, with all other parameters remaining the same.

6 Summary

In this thesis, the defect chemistry and electrochemical properties of lithium-ion battery cathode materials were investigated by a combined theoretical and experimental approach. Using a physically derived transmission-line model, the impedance behavior of various MIEC devices was explored and tailored equivalent circuits for thin-film battery electrodes were derived. These allow the extraction of the relevant electrochemical material parameters, consisting of the charge-transfer resistance, the ionic conductivity, the chemical capacitance and the chemical diffusion coefficient as a function of SOC. Based on the experimentally measured variation of these parameters with the electrode potential, defect chemical models (Brouwer diagrams) were derived, which predict the individual concentrations of ionic and electronic point defects in dependence of the total Li chemical potential. By considering separate site restrictions of electronic and ionic defects under otherwise dilute assumptions, these models still lead to comparatively simple mass action laws and concentration dependences of the Li chemical potential. The validity of this approach, its limitations and the insights gained from its application to real materials was explored at the examples of $LiCoO_2$, $LiMn_2O_4$, and $LiNi_{0.5}Mn_{1.5}O_{4-}$ thin films.

For each of these three materials, a complete set of electrochemical material parameters was obtained as a function of SOC. For $LiNi_{0.5}Mn_{1.5}O_{4-}$, even the impact of oxygen deficiency on the SOC-dependence of the material's electrochemical properties was quantified. Given the scarcity of such comprehensive data sets and their crucial importance for the evaluation of electrode kinetics and rate capabilities, these results alone represent a significant contribution to the further development of lithium-ion batteries and other post-lithium cell chemistries based on ion insertion. For all materials investigated, the obtained parameters vary over orders of magnitude throughout a charge/discharge cycle, such that assuming a fixed set of electrochemical properties inevitably leads to major errors in estimating, for example, the impact of solid-state transport on the overall electrode resistance. Importantly, the most significant changes are observed close to full lithiation and delithiation, where the relevant point defect concentrations show the strongest relative variations. This implies that values obtained from the characterization of stoichiometric cathode materials at full Li content must be approached with particular caution, as they are likely not representative of the full SOC range.

Based on the extracted sets of electrochemical properties, a viable thermodynamic approach to evaluating the defect chemistry of LIB cathode materials on an atomistic level was developed in three steps, corresponding to the three investigated materials. In the first step, the methodology and principles of our approach were established at the example of $LiCoO_2$, discussing the meaning and significance of the chemical capacitance as a material descriptor as well as the relationships between electrode potential, Li chemical potential, Li activity, electrochemical properties (, ,), and their dependence on point defect (,) concentrations. It was shown that in the dilute regime, up to a composition of approximately $Li_{0.9}CoO_2$, the chemical capacitance of our LCO thin films is accurately described by a single-site defect model without site restrictions, in the presence of an acceptor dopant, possibly Li on Co sites. At higher SOC, the experimental data deviate from the model due to an increasing relevance of the corresponding activity coefficients.

As a second step, our defect chemical analysis was extended to include multiple nonequivalent types of Li lattice sites together with the corresponding site restriction phenomena. This was accomplished by using the spinel $LiMn_2O_4$ as a model material, which exhibits octahedral and tetrahedral Li sites and reversibly tolerates almost complete delithiation. It was shown that the Brouwer diagram calculated from our defect model of Li_{2-} Mn_2O_4 for 1 1 9 closely matches the experimentally measured values of over a surprisingly wide stoichiometry range. In particular, site restriction straightforwardly explains the observed chemical capacitance peaks. Furthermore, the ionic conductivity and charge-transfer resistance also reflect the tetrahedral site restrictions imposed by the spinel crystal structure, and are therefore in excellent agreement with our defect model. Thus, we have established an effective and accurate method to describe the thermodynamics of full-range intercalation in LIB electrodes, including all relevant point defect concentrations as a function of SOC.

Finally, our defect chemical approach was applied to the practically highly relevant issue of oxygen deficiency in the high-voltage spinel $LiNi_{0.5}Mn_{1.5}O_{4-}$, which combines the effects of lithium and oxygen nonstoichiometry in a complex interplay of the corresponding point defects. By comparing the SOC-dependent electrochemical properties for oxygen vacancy concentrations of 2.4% and 0.53%, a defect model for the full tetrahedral-site regime (3.8 to 4.9 V) was introduced based on the presence of a donor dopant (oxygen vacancies), which correctly describes all important trends of the material parameters. Using highly resolved chemical capacitance measurements, a refined defect model could be derived for the oxygen vacancy regime, suggesting that the level of oxygen deficiency not only impacts the amount of redox active $Mn^{3+/4+}$, but also causes multiple energetically different electron sites in proximity of an oxygen vacancy. The resulting stabilizing effect on Mn^{3+} mitigates the voltage reduction in the oxygen vacancy regime and thus positively impacts the overall energy density of oxygen-deficient LNMO.

Overall, these results highlight the power of defect chemical concepts for all battery materials based on ion insertion and provide a concrete, actionable method to evaluate the electrochemical properties of such materials in terms of point defect concentrations as a function of SOC. Highly resolved SOC-dependent chemical capacitance measurements represent the most important experimental tool for developing and testing the corresponding defect models. Furthermore, the atomistic defect models presented in this thesis allow the surprisingly accurate calculation of equilibrium voltage profiles (charge curves) based on simple solid-solution thermodynamics. In sum, these findings shed light on the electrochemical properties of ion insertion materials, their dependence on the SOC, and their relevance for the overall kinetics and thermodynamics of lithium-ion batteries.

List of Publications

1. **Bumberger, A. E.**; Steinbach, C.; Ring, J.; Fleig, J. Mass and Charge Transport in Li_{1-} CoO_2 – A Complete Set of Properties and Its Defect Chemical Interpretation. *Chemistry of Materials* **2022**, *34*, 10548-10560.

2. **Bumberger, A. E.**; Böhme, C.; Ring, J.; Raznjevic, S.; Zhang, Z.; Kubicek, M.; Fleig, J.; Defect Chemistry of Spinel Cathode Materials – A Case Study of Epitaxial $LiMn_2O_4$ Thin Films. *Chemistry of Materials* **2023**, *35*, 5135-5149.

3. **Bumberger, A. E.**; Raznjevic, S.; Zhang, Z,; Kubicek, M.; Friedbacher, G.; Fleig, J. Chemical Capacitance Measurements Reveal the Impact of Oxygen Vacancies on the Charge Curve of $LiNi_{0.5}Mn_{1.5}O_{4-}$ Thin Films. *submitted for publication* **2023**.

4. **Bumberger, A. E.**; Fleig, J. et al. Transmission Line Revisited - The Impedance of Mixed Ionic and Electronic Conductors *in preparation* **2023**.

5. Krammer, M.; Schmid, A.; Siebenhofer, M.; **Bumberger, A. E.**; Herzig, C.; Limbeck, A.; Kubicek, M.; Fleig, J. Formation and detection of high pressure oxygen in closed pores of $La_{0.6}Sr_{0.4}CoO_{3-}$ solid oxide electrolysis anodes. *ACS Applied Energy Materials* **2022**, *5*, 8324-8335.

6. Herzig, C.; Frank, J.; Nenning, A.; Gerstl, M.; **Bumberger, A. E.**; Fleig, J.; Opitz, A. K.; Limbeck, A. Combining electrochemical and quantitative elemental analysis to investigate the sulfur poisoning process of ceria thin film fuel electrodes. *Journal of Materials Chemistry A* **2022**, *10*, 1840-1851.

7. Siebenhofer, M.; Haselmann, U.; Nenning, A.; Friedbacher, G.; **Bumberger, A. E.**; Wurster, S.; Artner, W., Hutter, H.; Zhang, Z.; Fleig, J. Surface Chemistry and Degradation Processes of Dense $La_{0.6}Sr_{0.4}CoO_{3-}$ Thin Film Electrodes. *Journal of The Electrochemical Society* **2023**, *170*, 014501.

8. Krammer, M.; Schmid, A.; Nenning, A.; **Bumberger, A. E.**; Siebenhofer, M.; Herzig, C.; Limbeck, A.; Rameshan, C.; Kubicek, M.; Fleig, J. Closed Pore Formation in Oxygen Electrodes for Solid Oxide Electrolysis Cells Investigated by Impedance Spectroscopy. *ACS Applied Materials & Interfaces* **2023**, *15*, 8076-8092.

9. Raznjevic, S.; Siebenhofer, M.; **Bumberger, A. E.**; Böhme, C.; Riedl, C.; Chen, Z.; Kubicek, M., Zhang, Z. Electron beam-induced brownmillerite–perovskite phase transition in $La_{0.6}Sr_{0.4}CoO_{3-}$. *Applied Physics Letters* **2023**, *122*, 211903.

10. Riedl, C.; Siebenhofer, M.; Raznjevic, S.; **Bumberger, A. E.**; Zhang, Z.; Limbeck, A.; Opitz, A. K.; Kubicek, M.; Fleig, J. In situ electrochemical observation of anisotropic lattice contraction of $La_{0.6}Sr_{0.4}FeO_{3-}$ electrodes during pulsed laser deposition. *Physical Chemistry Chemical Physics* **2023**, *25*, 142-153.

Bibliography

[1] Nagaura, T.; Tozawa, K. Lithium ion rechargeable battery. *Progress in Batteries & Solar Cells* **1990**, *9*, 209.

[2] Tarascon, J. M. The Li-Ion Battery: 25 Years of Exciting and Enriching Experiences. *The Electrochemical Society Interface* **2016**, *25*, 79.

[3] Kebede, A. A.; Kalogiannis, T.; Van Mierlo, J.; Berecibar, M. A comprehensive review of stationary energy storage devices for large scale renewable energy sources grid integration. *Renewable & Sustainable Energy Reviews* **2022**, *159*, 112213.

[4] Müller, M.; Viernstein, L.; Truong, C. N.; Eiting, A.; Hesse, H. C.; Witzmann, R.; Jossen, A. Evaluation of grid-level adaptability for stationary battery energy storage system applications in Europe. *Journal of Energy Storage* **2017**, *9*, 1–11.

[5] Nobel Foundation, The Nobel Prize in Chemistry 2019, https://www.nobelprize.org/prizes/chemistry/2019/summary/ (Accessed: September 6, 2023).

[6] Besenhard, J. O.; Fritz, H. P. Cathodic Reduction of Graphite in Organic Solutions of Alkali and NR^{4+} Salts. *Journal of Electroanalytical Chemistry* **1974**, *53*, 329–333.

[7] Besenhard, J. O. Electrochemical Preparation and Properties of Ionic Alkali Metal- and NR_4-Graphite Intercalation Compounds in Organic Electrolytes. *Carbon* **1976**, *14*, 111–115.

[8] Besenhard, J. O.; Eichinger, G. High-Energy Density Lithium Cells, Part I. Electrolytes and Anodes. *Journal of Electroanalytical Chemistry* **1976**, *68*, 1–18.

[9] Schöllhorn, R.; Kuhlmann, R.; Besenhard, J. O. Topotactic Redox Reactions and Ion-Exchange of Layered MoO_3 Bronzes. *Materials Research Bulletin* **1976**, *11*, 83–90.

[10] Besenhard, J. O.; Schöllhorn, R. Discharge Reaction-Mechanism of MoO_3 Electrode in Organic Electrolytes. *Journal of Power Sources* **1977**, *1*, 267–276.

[11] Eichinger, G.; Besenhard, J. O. High-Energy Density Lithium Cells, Part II. Cathodes and Complete Cells. *Journal of Electroanalytical Chemistry* **1976**, *72*, 1–31.

[12] Whittingham, M. S. Electrical Energy-Storage and Intercalation Chemistry. *Science* **1976**, *192*, 1126–1127.

[13] Whittingham, M. S. Chemistry of Intercalation Compounds - Metal Guests in Chalcogenide Hosts. *Progress in Solid State Chemistry* **1978**, *12*, 41–99.

[14] Whittingham, M. S. Intercalation Chemistry and Energy-Storage. *Journal of Solid State Chemistry* **1979**, *29*, 303–310.

[15] Mizushima, K.; Jones, P. C.; Wiseman, P. J.; Goodenough, J. B. Li_xCoO_2 (0 < x 1) - A New Cathode Material for Batteries of High-Energy Density. *Materials Research Bulletin* **1980**, *15*, 783–789.

[16] Yoshino, A.; Sanechika, K.; Nakajima, T. Secondary Battery, US Patent US4668595A. 1987.

[17] Fong, R.; Vonsacken, U.; Dahn, J. R. Studies of Lithium Intercalation into Carbons Using Nonaqueous Electrochemical-Cells. *Journal of the Electrochemical Society* **1990**, *137*, 2009–2013.

[18] Ziegler, M. S.; Trancik, J. E. Re-examining rates of lithium-ion battery technology improvement and cost decline. *Energy & Environmental Science* **2021**, *14*, 1635–1651.

[19] Ziegler, M. S.; Trancik, J. E. 2021, "Data series for lithium-ion battery technologies" (respresentative series), https://doi.org/10.7910/DVN/9FEJ7C , Trancik Lab Dataverse, V1, UNF:6:sVT2vBwWolbQL4BxsTSDUg== [fileUNF] (Accessed: September 6, 2023).

[20] Muralidharan, N.; Self, E. C.; Dixit, M.; Du, Z. J.; Essehli, R.; Amin, R.; Nanda, J.; Belharouak, I. Next-Generation Cobalt-Free Cathodes - A Prospective Solution to the Battery Industry's Cobalt Problem. *Advanced Energy Materials* **2022**, *12*, 2103050.

[21] International Energy Agency, Global EV Outlook 2023, https://www.iea.org/reports/global-ev-outlook-2023 (Accessed: August 29, 2023).

[22] New York Times, 6 Automakers and 30 Countries Say They'll Phase Out Gasoline Car Sales, https://www.nytimes.com/2021/11/09/climate/cars-zero-emissions-cop26.html#:~:text=GLASGOW%20%E2%80%94%20At%20least%20six%20major,2035%20in%20%E2%80%9Cleading%20markets.%E2%80%9D (Accessed: September 6, 2023).

[23] CNN, Tesla wants to turn its Berlin factory into Europe's biggest car plant, https://edition.cnn.com/2023/07/20/cars/tesla-germany-biggest-car-plant-europe/index.html (Accessed: September 6, 2023).

[24] Power Technology, China's BYD to open EV plant in former Ford factory, https://www.power-technology.com/news/byd-opens-ev-hub-brazil/ (Accessed: September 6, 2023).

[25] Forbes Middle East, Chinese Automaker BYD's FinDreams EV Subsidiary To Build $1.2B Battery Plant In China, https://www.forbesmiddleeast.com/industry/transport/ev-maker-byd-to-build-%2412b-battery-factory-in-china (Accessed: September 6, 2023).

[26] Huang, Y. Z.; Lin, L.; Zhang, C. K.; Liu, L.; Li, Y. K.; Qiao, Z. S.; Lin, J.; Wei, Q. L.; Wang, L. S.; Xie, Q. S.; Peng, D. L. Recent Advances and Strategies toward Polysulfides Shuttle Inhibition for High-Performance Li-S Batteries. *Advanced Science* **2022**, *9*, 2106004.

[27] Du, M. J.; Liao, K. M.; Lu, Q.; Shao, Z. P. Recent advances in the interface engineering of solid-state Li-ion batteries with artificial buffer layers: challenges, materials, construction, and characterization. *Energy & Environmental Science* **2019**, *12*, 1780–1804.

[28] Lou, S. F.; Zhang, F.; Fu, C. K.; Chen, M.; Ma, Y. L.; Yin, G. P.; Wang, J. J. Interface Issues and Challenges in All-Solid-State Batteries: Lithium, Sodium, and Beyond. *Advanced Materials* **2021**, *33*, 2000721.

[29] Vaalma, C.; Buchholz, D.; Weil, M.; Passerini, S. A cost and resource analysis of sodium-ion batteries. *Nature Reviews Materials* **2018**, *3*, 18013.

[30] Ghadbeigi, L.; Harada, J. K.; Lettiere, B. R.; Sparks, T. D. Performance and resource considerations of Li-ion battery electrode materials. *Energy & Environmental Science* **2015**, *8*, 1640–1650.

[31] CnEVPost, CATL remains world's largest EV battery maker, https://cnevpost.com/2022/05/02/catl-remains-worlds-largest-ev-battery-maker-with-35-share-in-q1/ (Accessed: August 29, 2023).

[32] CATL, CATL's First Sodium-ion Battery to Power Chery EV Models, https://www.catl.com/en/news/6013.html (Accessed: August 29, 2023).

[33] Maier, J. Thermodynamics of Electrochemical Lithium Storage. *Angewandte Chemie-International Edition* **2013**, *52*, 4998–5026.

[34] Maier, J. Review - Battery Materials: Why Defect Chemistry? *Journal of the Electrochemical Society* **2015**, *162*, A2380–A2386.

[35] Zhu, Y.; Maier, J. How to Adequately Describe Full Range Intercalation - A Two-Sided Approach. *Advanced Materials* **2023**, 2304666.

[36] Park, J.-K. *Principles and Applications of Lithium Secondary Batteries*; Wiley-VCH Verlag & Co. KGaA: Weinheim, Germany, 2012; p 29.

[37] Ohzuku, T.; Ueda, A.; Kouguchi, M. Synthesis and characterization of $LiAl_{1/4}Ni_{3/4}O_2$ ($R\bar{3}m$) for lithium-ion (shuttlecock) batteries. *Journal of the Electrochemical Society* **1995**, *142*, 4033–4039.

[38] Yabuuchi, N.; Ohzuku, T. Novel lithium insertion material of $LiCo_{1/3}Ni_{1/3}Mn_{1/3}O_2$ for advanced lithium-ion batteries. *Journal of Power Sources* **2003**, *119*, 171–174.

[39] Ohzuku, T.; Kitagawa, M.; Hirai, T. Electrochemistry of Manganese-Dioxide in Lithium Nonaqueous Cell 3. X-Ray Diffractional Study on the Reduction of Spinel-Related Manganese-Dioxide. *Journal of the Electrochemical Society* **1990**, *137*, 769–775.

[40] Amatucci, G.; Tarascon, J. M. Optimization of insertion compounds such as $LiMn_2O_4$ for Li-ion batteries. *Journal of the Electrochemical Society* **2003**, *150*, K31–K46.

[41] Schmuch, R.; Wagner, R.; Horpel, G.; Placke, T.; Winter, M. Performance and cost of materials for lithium-based rechargeable automotive batteries. *Nature Energy* **2018**, *3*, 267–278.

[42] Andre, D.; Kim, S. J.; Lamp, P.; Lux, S. F.; Maglia, F.; Paschos, O.; Stiaszny, B. Future generations of cathode materials: an automotive industry perspective. *Journal of Materials Chemistry A* **2015**, *3*, 6709–6732.

[43] Zhong, Q. M.; Bonakdarpour, A.; Zhang, M. J.; Gao, Y.; Dahn, J. R. Synthesis and electrochemistry of $LiNi_xMn_{2-x}O_4$. *Journal of the Electrochemical Society* **1997**, *144*, 205–213.

[44] Kim, J. H.; Pieczonka, N. P. W.; Yang, L. Challenges and Approaches for High-Voltage Spinel Lithium-Ion Batteries. *ChemPhysChem* **2014**, *15*, 1940–1954.

[45] Padhi, A. K.; Nanjundaswamy, K. S.; Goodenough, J. B. Phospho-olivines as positive-electrode materials for rechargeable lithium batteries. *Journal of the Electrochemical Society* **1997**, *144*, 1188–1194.

[46] Reuters, For EV batteries, lithium iron phosphate narrows the gap with nickel, cobalt, https://www.reuters.com/business/autos-transportation/ev-batteries-lithium-iron-phosphate-narrows-gap-with-nickel-cobalt-2023-06-22/ (Accessed: September 7, 2023).

[47] Moskon, J.; Zuntar, J.; Talian, S. D.; Dominko, R.; Gaberscek, M. A Powerful Transmission Line Model for Analysis of Impedance of Insertion Battery Cells: A Case Study on the NMC-Li System. *Journal of the Electrochemical Society* **2020**, *167*, 140539.

[48] Moskon, J.; Gaberscek, M. Transmission line models for evaluation of impedance response of insertion battery electrodes and cells. *Journal of Power Sources Advances* **2021**, *7*, 100047.

[49] Nenning, A.; Bischof, C.; Fleig, J.; Bram, M.; Opitz, A. K. The Relation of Microstructure, Materials Properties and Impedance of SOFC Electrodes: A Case Study of Ni/GDC Anodes. *Energies* **2020**, *13*, 987.

[50] Flura, A.; Nicollet, C.; Fourcade, S.; Vibhu, V.; Rougier, A.; Bassat, J. M.; Grenier, J. C. Identification and modelling of the oxygen gas diffusion impedance in SOFC porous electrodes: application to Pr_2NiO_{4+} . *Electrochimica Acta* **2015**, *174*, 1030–1040.

[51] Bumberger, A. E.; Steinbach, C.; Ring, J.; Fleig, J. Mass and Charge Transport in Li_{1-} CoO_2 Thin Films - A Complete Set of Properties and Its Defect Chemical Interpretation. *Chemistry of Materials* **2022**, *34*, 10548–10560.

[52] Bumberger, A. E.; Boehme, C.; Ring, J. S.; Raznjevic, S.; Zhang, Z.; Kubicek, M.; Fleig, J. Defect Chemistry of Spinel Cathode Materials - A Case Study of Epitaxial $LiMn_2O_4$ Thin Films. *Chemistry of Materials* **2023**, *35*, 5135–5149.

[53] Schmid, A.; Rupp, G. M.; Fleig, J. Voltage and partial pressure dependent defect chemistry in $(La,Sr)FeO_{3-}$ thin films investigated by chemical capacitance measurements. *Physical Chemistry Chemical Physics* **2018**, *20*, 12016–12026.

[54] Lai, W.; Haile, S. M. Impedance spectroscopy as a tool for chemical and electrochemical analysis of mixed conductors: A case study of ceria. *Journal of the American Ceramic Society* **2005**, *88*, 2979–2997.

[55] Rickert, H. *Electrochemistry of Solids*, 1st ed.; Inorganic Chemistry Concepts; Springer Berlin: Heidelberg, 1982; pp 79–87.

[56] Ho, C.; Raistrick, I. D.; Huggins, R. A. Application of AC Techniques to the Study of Lithium Diffusion in Tungsten Trioxide Thin-Films. *Journal of the Electrochemical Society* **1980**, *127*, 343–350.

[57] Yokota, I. On the Theory of Mixed Conduction with Special Reference to Conduction in Silver Sulfide Group Semiconductors. *Journal of the Physical Society of Japan* **1961**, *16*, 2213–2223.

[58] Jamnik, J.; Maier, J. Treatment of the impedance of mixed conductors - Equivalent circuit model and explicit approximate solutions. *Journal of the Electrochemical Society* **1999**, *146*, 4183–4188.

[59] Jamnik, J.; Maier, J.; Pejovnik, S. A powerful electrical network model for the impedance of mixed conductors. *Electrochimica Acta* **1999**, *44*, 4139–4145.

[60] Jamnik, J.; Maier, J. Generalised equivalent circuits for mass and charge transport: chemical capacitance and its implications. *Physical Chemistry Chemical Physics* **2001**, *3*, 1668–1678.

[61] Adamic, M.; Talian, S. D.; Sinigoj, A. R.; Humar, I.; Moskon, J.; Gaberscek, M. A Transmission Line Model of Electrochemical Cell's Impedance: Case Study on a Li-S System. *Journal of the Electrochemical Society* **2019**, *166*, A5045–A5053.

[62] Ahn, P. A.; Shin, E. C.; Jo, J. M.; Yu, J. H.; Woo, S. K.; Lee, J. S. Mixed Conduction in Ceramic Hydrogen/Steam Electrodes by Hebb-Wagner Polarization in the Frequency Domain. *Fuel Cells* **2012**, *12*, 1070–1084.

[63] Litzelman, S. J.; Tuller, H. L. Measurement of mixed conductivity in thin films with microstructured Hebb-Wagner blocking electrodes. *Solid State Ionics* **2009**, *180*, 1190–1197.

[64] Nam, G. D.; Ahn, J. H.; Joo, J. H. Using an in-plane geometry in Hebb-Wagner measurements to avoid errors from electrode overpotential. *Electrochimica Acta* **2018**, *260*, 855–860.

[65] Riedl, C.; Siebenhofer, M.; Nenning, A.; Schmid, A.; Weiss, M.; Rameshan, C.; Limbeck, A.; Kubicek, M.; Opitz, A. K.; Fleig, J. In situ techniques reveal the true capabilities of SOFC cathode materials and their sudden degradation due to omnipresent sulfur trace impurities. *Journal of Materials Chemistry A* **2022**, *10*, 14838–14848.

[66] Schmid, A.; Krammer, M.; Fleig, J. Rechargeable Oxide Ion Batteries Based on Mixed Conducting Oxide Electrodes. *Advanced Energy Materials* **2023**, *13*, 2203789.

[67] Maier, J. Chemical resistance and chemical capacitance. *Zeitschrift für Naturforschung B* **2020**, *75*, 15–22.

[68] Lvovich, V. F. *Impedance Spectroscopy Applications to Electrochemical and Dielectric Phenomena*; John Wiley & Sons, Ltd: New Jersey, 2012; p 80.

[69] Lvovich, V. F. *Impedance Spectroscopy Applications to Electrochemical and Dielectric Phenomena*; John Wiley & Sons, Ltd: New Jersey, 2012; pp 82–83.

[70] Gerstl, M.; Friedbacher, G.; Kubel, F.; Hutter, H.; Fleig, J. The relevance of interfaces for oxide ion transport in yttria stabilized zirconia (YSZ) thin films. *Physical Chemistry Chemical Physics* **2013**, *15*, 1097–1107.

[71] Jiang, J.; Shen, W.; Hertz, J. L. Structure and ionic conductivity of nanoscale gadolinia-doped ceria thin films. *Solid State Ionics* **2013**, *249*, 139–143.

[72] Peters, C.; Weber, A.; Butz, B.; Gerthsen, D.; Ivers-Tiffee, E. Grain-Size Effects in YSZ Thin-Film Electrolytes. *Journal of the American Ceramic Society* **2009**, *92*, 2017–2024.

[73] Kosacki, I.; Rouleau, C. M.; Becher, P. F.; Bentley, J.; Lowndes, D. H. Nanoscale effects on the ionic conductivity in highly textured YSZ thin films. *Solid State Ionics* **2005**, *176*, 1319–1326.

[74] Hamon, Y.; Douard, A.; Sabary, F.; Marcel, C.; Vinatier, P.; Pecquenard, B.; Levasseur, A. Influence of sputtering conditions on ionic conductivity of LiPON thin films. *Solid State Ionics* **2006**, *177*, 257–261.

[75] Navickas, E.; Gerstl, M.; Friedbacher, G.; Kubel, F.; Fleig, J. Measurement of the across-plane conductivity of YSZ thin films on silicon. *Solid State Ionics* **2012**, *211*, 58–64.

[76] Smetaczek, S.; Limbeck, A.; Zeller, V.; Ring, J.; Ganschow, S.; Rettenwander, D.; Fleig, J. Li^+/H^+ exchange of $Li_7La_3Zr_2O_{12}$ single and polycrystals investigated by quantitative LIBS depth profiling. *Materials Advances* **2022**, *3*, 8760–8770.

[77] Vendrell, X.; West, A. R. Electrical Properties of Yttria-Stabilized Zirconia, YSZ Single Crystal: Local AC and Long Range DC Conduction. *Journal of the Electrochemical Society* **2018**, *165*, F966–F975.

[78] Ahamer, C.; Opitz, A. K.; Rupp, G. M.; Fleig, J. Revisiting the Temperature Dependent Ionic Conductivity of Yttria Stabilized Zirconia (YSZ). *Journal of the Electrochemical Society* **2017**, *164*, F790–F803.

[79] Siebenhofer, M.; Huber, T. M.; Friedbacher, G.; Artner, W.; Fleig, J.; Kubicek, M. Oxygen exchange kinetics and nonstoichiometry of pristine $La_{0.6}Sr_{0.4}CoO_{3-\delta}$ thin films unaltered by degradation. *Journal of Materials Chemistry A* **2020**, *8*, 7968–7979.

[80] Siebenhofer, M.; Haselmann, U.; Nenning, A.; Friedbacher, G.; Bumberger, A. E.; Wurster, S.; Artner, W.; Hutter, H.; Zhang, Z. L.; Fleig, J.; Kubicek, M. Surface Chemistry and Degradation Processes of Dense $La_{0.6}Sr_{0.4}CoO_{3-\delta}$ Thin Film Electrodes. *Journal of the Electrochemical Society* **2023**, *170*, 014501.

[81] Boukamp, B. A.; Bouwmeester, H. J. M. Interpretation of the Gerischer impedance in solid state ionics. *Solid State Ionics* **2003**, *157*, 29–33.

[82] Nenning, A.; Volgger, L.; Miller, E.; Mogni, L. V.; Barnett, S.; Fleig, J. The Electrochemical Properties of $Sr(Ti,Fe)O_{3-\delta}$ for Anodes in Solid Oxide Fuel Cells. *Journal of the Electrochemical Society* **2017**, *164*, F364–F371.

[83] Ring, J.; Nenning, A.; Fleig, J. Defect Chemistry and Mixed Conduction in Lithium Lanthanum Titanate During the Transition from Electrolyte to Anode Material. *Journal of the Electrochemical Society* **2023**, *170*, 050530.

[84] Shimonosono, T.; Hirata, Y.; Ehira, Y.; Sameshima, S.; Horita, T.; Yokokawa, H. Electronic conductivity measurement of Sm- and La-doped ceria ceramics by Hebb-Wagner method. *Solid State Ionics* **2004**, *174*, 27–33.

[85] Broux, T.; Fleutot, B.; David, R.; Brull, A.; Veber, P.; Fauth, F.; Courty, M.; Croguennec, L.; Masquelier, C. Temperature Dependence of Structural and Transport Properties for $Na_3V_2(PO_4)_2F_3$ and $Na_3V_2(PO_4)_2F_{2.5}O_{0.5}$. *Chemistry of Materials* **2018**, *30*, 358–365.

[86] Zhu, C. B.; Wu, C.; Chen, C. C.; Kopold, P.; van Aken, P. A.; Maier, J.; Yu, Y. A High Power-High Energy , $Na_3V_2(PO_4)_2F_3$ Sodium Cathode: Investigation of Transport Parameters, Rational Design and Realization. *Chemistry of Materials* **2017**, *29*, 5207–5215.

[87] Rupp, G. M.; Glowacki, M.; Fleig, J. Electronic and Ionic Conductivity of $La_{0.95}Sr_{0.05}Ga_{0.95}Mg_{0.05}O_{3-}$ (LSGM) Single Crystals. *Journal of the Electrochemical Society* **2016**, *163*, F1189–F1197.

[88] Rupp, G. M.; Kubicek, M.; Opitz, A. K.; Fleig, J. In Situ Impedance Analysis of Oxygen Exchange on Growing $La_{0.6}Sr_{0.4}CoO_{3-}$ Thin Films. *ACS Applied Energy Materials* **2018**, *1*, 4522–4535.

[89] Fleig, J.; Kim, H. R.; Jamnik, J.; Maier, J. Oxygen Reduction Kinetics of Lanthanum Manganite (LSM) Model Cathodes: Partial Pressure Dependence and Rate-Limiting Steps. *Fuel Cells* **2008**, *8*, 330–337.

[90] Krammer, M.; Schmid, A.; Siebenhofer, M.; Bumberger, A. E.; Herzig, C.; Limbeck, A.; Kubicek, M.; Fleig, J. Formation and Detection of High-Pressure Oxygen in Closed Pores of $La_{0.6}Sr_{0.4}CoO_{3-}$ Solid Oxide Electrolysis Anodes. *ACS Applied Energy Materials* **2022**, 8324-8335.

[91] Krammer, M.; Schmid, A.; Nenning, A.; Bumberger, A. E.; Siebenhofer, M.; Herzig, C.; Limbeck, A.; Rameshan, C.; Kubicek, M.; Fleig, J. Closed-Pore Formation in Oxygen Electrodes for Solid Oxide Electrolysis Cells Investigated by Impedance Spectroscopy. *ACS Applied Materials & Interfaces* **2023**, 8076-8092.

[92] Krammer, M.; Schmid, A.; Kubicek, M.; Fleig, J. Utilizing oxygen gas storage in rechargeable oxygen ion batteries. *Journal of Power Sources* **2023**, *577*, 233167.

[93] Amin, R.; Balaya, P.; Maier, J. Anisotropy of electronic and ionic transport in $LiFePO_4$ single crystals. *Electrochemical and Solid State Letters* **2007**, *10*, A13–A16.

[94] Amin, R.; Maier, J.; Balaya, P.; Chen, D. P.; Lin, C. T. Ionic and electronic transport in single crystalline $LiFePO_4$ grown by optical floating zone technique. *Solid State Ionics* **2008**, *179*, 1683–1687.

[95] Illig, J.; Ender, M.; Chrobak, T.; Schmidt, J. P.; Klotz, D.; Ivers-Tiffee, E. Separation of Charge Transfer and Contact Resistance in $LiFePO_4$-Cathodes by Impedance Modeling. *Journal of the Electrochemical Society* **2012**, *159*, A952–A960.

[96] Jiang, J. C.; Shi, W.; Zheng, J. M.; Zuo, P. J.; Xiao, J.; Chen, X. L.; Xu, W.; Zhang, J. G. Optimized Operating Range for Large-Format $LiFePO_4$/Graphite Batteries. *Journal of the Electrochemical Society* **2014**, *161*, A336–A341.

[97] Liu, Y. D.; Xie, J. Failure Study of Commercial $LiFePO_4$ Cells in Overcharge Conditions Using Electrochemical Impedance Spectroscopy. *Journal of the Electrochemical Society* **2015**, *162*, A2208–A2217.

[98] Tang, K.; Yu, X. Q.; Sun, J. P.; Li, H.; Huang, X. J. Kinetic analysis on $LiFePO_4$ thin films by CV, GITT, and EIS. *Electrochimica Acta* **2011**, *56*, 4869–4875.

[99] Li, L.; Xu, Y. L.; Chang, R.; Wang, C.; He, S. N.; Ding, X. D. Unraveling the mechanism of optimal concentration for Fe substitution in $Na_3V_2(PO_4)_2F_3$/C for Sodium-Ion batteries. *Energy Storage Materials* **2021**, *37*, 325–335.

[100] Choi, Y. M.; Pyun, S. I.; Bae, J. S.; Moon, S. I. Effects of Lithium Content on the Electrochemical Lithium Intercalation Reaction into $LiNiO_2$ and $LiCoO_2$ Electrodes. *Journal of Power Sources* **1995**, *56*, 25–30.

[101] Hess, A.; Roode-Gutzmer, Q.; Heubner, C.; Schneider, M.; Michaelis, A.; Bobeth, M.; Cuniberti, G. Determination of state of charge-dependent asymmetric Butler-Volmer kinetics for Li_xCoO_2 electrode using GITT measurements. *Journal of Power Sources* **2015**, *299*, 156–161.

[102] Tang, S. Q.; Wang, Z. X.; Guo, H. J.; Wang, J. X.; Li, X. H.; Yan, G. C. Systematic parameter acquisition method for electrochemical model of 4.35 V $LiCoO_2$ batteries. *Solid State Ionics* **2019**, *343*, 115083.

[103] Weppner, W.; Huggins, R. A. Electrochemical Investigation of Chemical Diffusion, Partial Ionic Conductivities, and Other Kinetic-Parameters in Li_3Sb and Li_3Bi. *Journal of Solid State Chemistry* **1977**, *22*, 297–308.

[104] Weppner, W.; Huggins, R. A. Determination of Kinetic and Thermodynamic Parameters of Mixed-Conducting Electrodes, and Application to System Li-Sb. *Journal of the Electrochemical Society* **1977**, *124*, C135–C135.

[105] Kang, S. D.; Chueh, W. C. Galvanostatic Intermittent Titration Technique Reinvented: Part I. A Critical Review. *Journal of the Electrochemical Society* **2021**, *168*, 120504.

[106] Kang, S. D.; Kuo, J. J.; Kapate, N.; Hong, J.; Park, J.; Chueh, W. C. Galvanostatic Intermittent Titration Technique Reinvented: Part II. Experiments. *Journal of the Electrochemical Society* **2021**, *168*, 120503.

[107] Maier, J. Mass-Transport in the Presence of Internal Defect Reactions - Concept of Conservative Ensembles: III, Trapping Effect of Dopants on Chemical Diffusion. *Journal of the American Ceramic Society* **1993**, *76*, 1223–1227.

[108] Chen, C. C.; Navickas, E.; Fleig, J.; Maier, J. Kinetics of Space Charge Storage in Composites. *Advanced Functional Materials* **2018**, *28*, 1705999.

[109] Tang, S. B.; Lai, M. O.; Lu, L. Li-ion diffusion in highly (003) oriented $LiCoO_2$ thin film cathode prepared by pulsed laser deposition. *Journal of Alloys and Compounds* **2008**, *449*, 300–303.

[110] Xia, H.; Lu, L.; Meng, Y. S.; Ceder, G. Phase transitions and high-voltage electrochemical behavior of $LiCoO_2$ thin films grown by pulsed laser deposition. *Journal of the Electrochemical Society* **2007**, *154*, A337–A342.

[111] Xia, H.; Lu, L.; Ceder, G. Li diffusion in $LiCoO_2$ thin films prepared by pulsed laser deposition. *Journal of Power Sources* **2006**, *159*, 1422–1427.

[112] Xie, J.; Imanishi, N.; Hirano, A.; Matsumura, M.; Takeda, Y.; Yamamoto, O. Kinetics investigation of a preferential (104) plane oriented $LiCoO_2$ thin film prepared by RF magnetron sputtering. *Solid State Ionics* **2007**, *178*, 1218–1224.

[113] McGraw, J. M.; Bahn, C. S.; Parilla, P. A.; Perkins, J. D.; Readey, D. W.; Ginley, D. S. Li ion diffusion measurements in V_2O_5 and $Li(Co_{1-x}Al_x)O_2$ thin-film battery cathodes. *Electrochimica Acta* **1999**, *45*, 187–196.

[114] Jang, Y. I.; Neudecker, B. J.; Dudney, N. J. Lithium diffusion in Li_xCoO_2 ($0.45 < x < 0.7$) intercalation cathodes. *Electrochemical and Solid State Letters* **2001**, *4*, A74–A77.

[115] Xia, H.; Lu, L. Texture effect on the electrochemical properties of $LiCoO_2$ thin films prepared by PLD. *Electrochimica Acta* **2007**, *52*, 7014–7021.

[116] Fleig, J.; Schmid, A.; Rupp, G. M.; Slouka, C.; Navickas, E.; Andrejs, L.; Hutter, H.; Volgger, L.; Nenning, A. The Chemical Capacitance as a Fingerprint of Defect Chemistry in Mixed Conducting Oxides. *Acta Chimica Slovenica* **2016**, *63*, 509–518.

[117] Croguennec, L.; Deniard, P.; Brec, R.; Biensan, P.; Broussely, M. Electrochemical behavior of orthorhombic $LiMnO_2$: Influence of the grain size and cationic disorder. *Solid State Ionics* **1996**, *89*, 127–137.

[118] Robertson, A. D.; Armstrong, A. R.; Bruce, P. G. Layered $Li_xMn_{1-y}Co_yO_2$ intercalation electrodes-influence of ion exchange on capacity and structure upon cycling. *Chemistry of Materials* **2001**, *13*, 2380–2386.

[119] Jung, R.; Metzger, M.; Maglia, F.; Stinner, C.; Gasteiger, H. A. Oxygen Release and Its Effect on the Cycling Stability of $LiNi_xMn_yCo_zO_2$ (NMC) Cathode Materials for Li-Ion Batteries. *Journal of the Electrochemical Society* **2017**, *164*, A1361–A1377.

[120] Smith, A. J.; Dahn, J. R. Delta Differential Capacity Analysis. *Journal of the Electrochemical Society* **2012**, *159*, A290–A293.

[121] Smith, A. J.; Burns, J. C.; Dahn, J. R. High-Precision Differential Capacity Analysis of $LiMn_2O_4$/graphite Cells. *Electrochemical and Solid State Letters* **2011**, *14*, A39–A41.

[122] Dubarry, M.; Liaw, B. Y.; Chen, M. S.; Chyan, S. S.; Han, K. C.; Sie, W. T.; Wu, S. H. Identifying battery aging mechanisms in large format Li ion cells. *Journal of Power Sources* **2011**, *196*, 3420–3425.

[123] Dubarry, M.; Svoboda, V.; Hwu, R.; Liaw, B. Y. Incremental capacity analysis and close-to-equilibrium OCV measurements to quantify capacity fade in commercial rechargeable lithium batteries. *Electrochemical and Solid State Letters* **2006**, *9*, A454–A457.

[124] Armstrong, G.; Armstrong, A. R.; Canales, J.; Bruce, P. G. TiO2 (B) nanotubes as negative electrodes for rechargeable lithium batteries. *Electrochemical and Solid State Letters* **2006**, *9*, A139–A143.

[125] Armstrong, A. R.; Paterson, A. J.; Robertson, A. D.; Bruce, P. G. Nonstoichiometric layered $Li_xMn_yO_2$ with a high capacity for lithium intercalation/deintercalation. *Chemistry of Materials* **2002**, *14*, 710–719.

[126] Sinha, N. N.; Smith, A. J.; Burns, J. C.; Jain, G.; Eberman, K. W.; Scott, E.; Gardner, J. P.; Dahn, J. R. The Use of Elevated Temperature Storage Experiments to Learn about Parasitic Reactions in Wound $LiCoO_2$/Graphite Cells. *Journal of the Electrochemical Society* **2011**, *158*, A1194–A1201.

[127] Dubarry, M.; Liaw, B. Y. Identify capacity fading mechanism in a commercial $LiFePO_4$ cell. *Journal of Power Sources* **2009**, *194*, 541–549.

[128] Landesfeind, J.; Pritzl, D.; Gasteiger, H. A. An Analysis Protocol for Three-Electrode Li-Ion Battery Impedance Spectra: Part I. Analysis of a High-Voltage Positive Electrode. *Journal of the Electrochemical Society* **2017**, *164*, A1773–A1783.

[129] Pritzl, D.; Landesfeind, J.; Solchenbach, S.; Gasteiger, H. A. An Analysis Protocol for Three-Electrode Li-Ion Battery Impedance Spectra: Part II. Analysis of a Graphite Anode Cycled vs. LNMO. *Journal of the Electrochemical Society* **2018**, *165*, A2145–A2153.

[130] Pritzl, D.; Bumberger, A. E.; Wetjen, M.; Landesfeind, J.; Solchenbach, S.; Gasteiger, H. A. Identifying Contact Resistances in High-Voltage Cathodes by Impedance Spectroscopy. *Journal of the Electrochemical Society* **2019**, *166*, A582–A590.

[131] Linsenmann, F.; Pritzl, D.; Gasteiger, H. A. A Reference Electrode for In Situ Impedance Measurements in Sodium-Ion Batteries. *Journal of the Electrochemical Society* **2019**, *166*, A3668–A3674.

[132] Xie, J.; Imanishi, N.; Matsumura, T.; Hirano, A.; Takeda, Y.; Yamamoto, O. Orientation dependence of Li-ion diffusion kinetics in $LiCoO_2$ thin films prepared by RF magnetron sputtering. *Solid State Ionics* **2008**, *179*, 362–370.

[133] Mohamedi, M.; Takahashi, D.; Uchiyama, T.; Itoh, T.; Nishizawa, M.; Uchida, I. Explicit analysis of impedance spectra related to thin films of spinel $LiMn_2O_4$. *Journal of Power Sources* **2001**, *93*, 93–103.

[134] Schönleber, M.; Ivers-Tiffee, E. The Distribution Function of Differential Capacity as a new tool for analyzing the capacitive properties of Lithium-Ion batteries. *Electrochemistry Communications* **2015**, *61*, 45–48.

[135] Fabregat-Santiago, F.; Garcia-Belmonte, G.; Bisquert, J.; Ferriols, N. S.; Bueno, P. R.; Longo, E.; Anton, J. S.; Castro-Garcia, S. Dynamic processes in the coloration of WO_3 by lithium insertion. *Journal of the Electrochemical Society* **2001**, *148*, E302–E309.

[136] Bisquert, J.; Compte, A. Theory of the electrochemical impedance of anomalous diffusion. *Journal of Electroanalytical Chemistry* **2001**, *499*, 112–120.

[137] Maier, J. Electrochemical Investigation Methods of Ionic Transport Properties in Solids. *Solid State Phenomena* **1994**, *39-40*, 35–60.

[138] Maier, J.; Amin, R. Defect chemistry of $LiFePO_4$. *Journal of the Electrochemical Society* **2008**, *155*, A339–A344.

[139] Fleischmann, S.; Mitchell, J. B.; Wang, R. C.; Zhan, C.; Jiang, D. E.; Presser, V.; Augustyn, V. Pseudocapacitance: From Fundamental Understanding to High Power Energy Storage Materials. *Chemical Reviews* **2020**, *120*, 6738–6782.

[140] Hoang, K.; Johannes, M. D. Defect chemistry in layered transition-metal oxides from screened hybrid density functional calculations. *Journal of Materials Chemistry A* **2014**, *2*, 5224–5235.

[141] Randles, J. E. B. Kinetics of Rapid Electrode Reactions. *Discussions of the Faraday Society* **1947**, *1*, 11–19.

[142] Ohzuku, T.; Ueda, A. Solid-State Redox Reactions of $LiCoO_2$ ($R\bar{3}m$) for 4 Volt Secondary Lithium Cells. *Journal of the Electrochemical Society* **1994**, *141*, 2972–2977.

[143] Striebel, K. A.; Deng, C. Z.; Wen, S. J.; Cairns, E. J. Electrochemical behavior of $LiMn_2O_4$ and $LiCoO_2$ thin films produced with pulsed laser deposition. *Journal of the Electrochemical Society* **1996**, *143*, 1821–1827.

[144] Ozawa, K. Lithium-Ion Rechargeable Batteries with $LiCoO_2$ and Carbon Electrodes - the $LiCoO_2$/C System. *Solid State Ionics* **1994**, *69*, 212–221.

[145] Milewska, A.; Swierczek, K.; Tobola, J.; Boudoire, F.; Hu, Y.; Bora, D. K.; Mun, B. S.; Braun, A.; Molenda, J. The nature of the nonmetal-metal transition in Li_xCoO_2 oxide. *Solid State Ionics* **2014**, *263*, 110–118.

[146] Marianetti, C. A.; Kotliar, G.; Ceder, G. A first-order Mott transition in Li_xCoO_2. *Nature Materials* **2004**, *3*, 627–631.

[147] Reimers, J. N.; Dahn, J. R. Electrochemical and Insitu X-Ray-Diffraction Studies of Lithium Intercalation in Li_xCoO_2. *Journal of the Electrochemical Society* **1992**, *139*, 2091–2097.

[148] Menetrier, M.; Saadoune, I.; Levasseur, S.; Delmas, C. The insulator-metal transition upon lithium deintercalation from $LiCoO_2$: electronic properties and ^7Li NMR study. *Journal of Materials Chemistry* **1999**, *9*, 1135–1140.

[149] Cho, W.; Myeong, S.; Kim, N.; Lee, S.; Kim, Y.; Kim, M.; Kang, S. J.; Park, N.; Oh, P.; Cho, J. Critical Role of Cations in Lithium Sites on Extended Electrochemical Reversibility of Co-Rich Layered Oxide. *Advanced Materials* **2017**, *29*, 1605578.

[150] Chen, Z. H.; Dahn, J. R. Methods to obtain excellent capacity retention in $LiCoO_2$ cycled to 4.5 V. *Electrochimica Acta* **2004**, *49*, 1079–1090.

[151] Ceder, G.; Van der Ven, A. Phase diagrams of lithium transition metal oxides: investigations from first principles. *Electrochimica Acta* **1999**, *45*, 131–150.

[152] Wolverton, C.; Zunger, A. Prediction of Li intercalation and battery voltages in layered vs. cubic Li_xCoO_2. *Journal of the Electrochemical Society* **1998**, *145*, 2424–2431.

[153] Wang, L.; Maxisch, T.; Ceder, G. A first-principles approach to studying the thermal stability of oxide cathode materials. *Chemistry of Materials* **2007**, *19*, 543–552.

[154] Sharifi-Asl, S.; Lu, J.; Amine, K.; Shahbazian-Yassar, R. Oxygen Release Degradation in Li-Ion Battery Cathode Materials: Mechanisms and Mitigating Approaches. *Advanced Energy Materials* **2019**, *9*, 1900551.

[155] Radin, M. D.; Hy, S.; Sina, M.; Fang, C. C.; Liu, H. D.; Vinckeviciute, J.; Zhang, M. H.; Whittingham, M. S.; Meng, Y. S.; Van der Ven, A. Narrowing the Gap between Theoretical and Practical Capacities in Li-Ion Layered Oxide Cathode Materials. *Advanced Energy Materials* **2017**, *7*, 1602888.

[156] Meyer, M.; Nicoloso, N.; Jaenisch, V. Percolation model for the anomalous conductivity of fluorite-related oxides. *Physical Review B* **1997**, *56*, 5961–5966.

[157] Inaba, H.; Tagawa, H. Ceria-based solid electrolytes - Review. *Solid State Ionics* **1996**, *83*, 1–16.

[158] Wang, D. Y.; Park, D. S.; Griffith, J.; Nowick, A. S. Oxygen-Ion Conductivity and Defect Interactions in Yttria-Doped Ceria. *Solid State Ionics* **1981**, *2*, 95–105.

[159] Hamann, C. H.; Hamnett, A.; Vielstich, W. *Electrochemistry*, 2nd ed.; Wiley-VCH: Weinheim, 2007; p 165.

[160] Molenda, J.; Stoklosa, A.; Bak, T. Modification in the Electronic-Structure of Cobalt Bronze Li_xCoO_2 and the Resulting Electrochemical Properties. *Solid State Ionics* **1989**, *36*, 53–58.

[161] Fisher, C. A. J.; Zheng, S.; Kuwabara, A.; Moriwake, H.; Ikuhara, Y. H.; Oki, H.; Ikuhara, Y. Atomic-Level Characterization of Interfaces in $LiCoO_2$. *ECS Transactions* **2014**, *58*, 1–11.

[162] Fisher, C. A. J.; Islam, M. S.; Moriwake, H. Atomic Level Investigations of Lithium Ion Battery Cathode Materials. *Journal of the Physical Society of Japan* **2010**, *79*, 59–64.

[163] Ong, P. V.; Yang, Z. Z.; Sushko, P. V.; Du, Y. G. Formation, Structural Variety, and Impact of Antiphase Boundaries on Li Diffusion in $LiCoO_2$ Thin-Film Cathodes. *Journal of Physical Chemistry Letters* **2018**, *9*, 5515–5520.

[164] Liu, W.; Kowal, K.; Farrington, G. C. Mechanism of the electrochemical insertion of lithium into $LiMn_2O_4$ spinels. *Journal of the Electrochemical Society* **1998**, *145*, 459–465.

[165] Bianchini, M.; Suard, E.; Croguennec, L.; Masquelier, C. Li-Rich $Li_{1+x}Mn_{2-x}O_4$ Spinel Electrode Materials: An Operando Neutron Diffraction Study during Li^+ Extraction/Insertion. *Journal of Physical Chemistry C* **2014**, *118*, 25947–25955.

[166] Ammundsen, B.; Roziere, J.; Islam, M. S. Atomistic simulation studies of lithium and proton insertion in spinel lithium manganates. *Journal of Physical Chemistry B* **1997**, *101*, 8156–8163.

[167] Barker, J.; Koksbang, R.; Saidi, M. Y. Lithium insertion in manganese oxides: A model lithium ion system. *Solid State Ionics* **1995**, *82*, 143–151.

[168] Gummow, R. J.; Thackeray, M. M. An Investigation of Spinel-Related and Orthorhombic $LiMnO_2$ Cathodes for Rechargeable Lithium Batteries. *Journal of the Electrochemical Society* **1994**, *141*, 1178–1182.

[169] Ooi, K.; Miyai, Y.; Katoh, S.; Maeda, H.; Abe, M. Topotactic Li^+ Insertion to $-MnO_2$ in the Aqueous Phase. *Langmuir* **1989**, *5*, 150–157.

[170] Kim, J. H.; Myung, S. T.; Yoon, C. S.; Kang, S. G.; Sun, Y. K. Comparative study of $LiNi_{0.5}Mn_{1.5}O_{4-}$ and $LiNi_{0.5}Mn_{1.5}O_4$ cathodes having two crystallographic structures: $Fd\bar{3}m$ and $P4_332$. *Chemistry of Materials* **2004**, *16*, 906–914.

[171] Li, D. C.; Ito, A.; Kobayakawa, K.; Noguchi, H.; Sato, Y. Electrochemical characteristics of $LiNi_{0.5}Mn_{1.5}O_4$ prepared by spray drying and post-annealing. *Electrochimica Acta* **2007**, *52*, 1919–1924.

[172] Takahashi, K.; Saitoh, M.; Sano, M.; Fujita, M.; Kifune, K. Electrochemical and structural properties of a 4.7 V-class $LiNi_{0.5}Mn_{1.5}O_4$ positive electrode material prepared with a self-reaction method. *Journal of the Electrochemical Society* **2004**, *151*, A173–A177.

[173] Wang, L. P.; Li, H.; Huang, X. J.; Baudrin, E. A comparative study of $Fd\bar{3}m$ and $P4_332$ "$LiNi_{0.5}Mn_{1.5}O_4$". *Solid State Ionics* **2011**, *193*, 32–38.

[174] Bianchini, M.; Fauth, F.; Suard, E.; Leriche, J. B.; Masquelier, C.; Croguennec, L. Spinel materials for Li-ion batteries: new insights obtained by operando neutron and synchrotron X-ray diffraction. *Acta Crystallographica* **2015**, *71*, 688–701.

[175] Thackeray, M. M.; David, W. I. F.; Bruce, P. G.; Goodenough, J. B. Lithium Insertion into Manganese Spinels. *Materials Research Bulletin* **1983**, *18*, 461–472.

[176] Thackeray, M. M.; Dekock, A.; Rossouw, M. H.; Liles, D.; Bittihn, R.; Hoge, D. Spinel Electrodes from the Li-Mn-O System for Rechargeable Lithium Battery Applications. *Journal of the Electrochemical Society* **1992**, *139*, 363–366.

[177] Necas, D.; Klapetek, P. Gwyddion: an open-source software for SPM data analysis. *Central European Journal of Physics* **2012**, *10*, 181–188.

[178] Hendriks, R.; Cunha, D. M.; Singh, D. P.; Huijben, M. Enhanced Lithium Transport by Control of Crystal Orientation in Spinel $LiMn_2O_4$ Thin Film Cathodes. *ACS Applied Energy Materials* **2018**, *1*, 7046–7051.

[179] Yu, S.; Siegel, D. J. Grain Boundary Contributions to Li-Ion Transport in the Solid Electrolyte $Li_7La_3Zr_2O_{12}$ (LLZO). *Chemistry of Materials* **2017**, *29*, 9639–9647.

[180] Schwab, C.; Howeling, A.; Windmuller, A.; Gonzalez-Julian, J.; Moller, S.; Binder, J. R.; Uhlenbruck, S.; Guillon, O.; Martin, M. Bulk and grain boundary Li-diffusion in dense $LiMn_2O_4$ pellets by means of isotope exchange and ToF-SIMS analysis. *Physical Chemistry Chemical Physics* **2019**, *21*, 26066–26076.

[181] Guyomard, D.; Tarascon, J. M. Li Metal-Free Rechargeable $LiMn_2O_4$/Carbon Cells - Their Understanding and Optimization. *Journal of the Electrochemical Society* **1992**, *139*, 937–948.

[182] Liu, W.; Farrington, G. C.; Chaput, F.; Dunn, B. Synthesis and electrochemical studies of spinel phase LiMn2O4 cathode materials prepared by the Pechini process. *Journal of the Electrochemical Society* **1996**, *143*, 879–884.

[183] Manev, V.; Momchilov, A.; Nassalevska, A.; Kozawa, A. Rechargeable Lithium Battery with Spinel-Related -MnO_2, I. Synthesis of -MnO_2 for Battery Applications. *Journal of Power Sources* **1993**, *44*, 551–559.

[184] Baehtz, C.; Buhrmester, T.; Bramnik, N. N.; Nikolowski, K.; Ehrenberg, H. Design and performance of an electrochemical in-situ cell for high resolution full-pattern X-ray powder diffraction. *Solid State Ionics* **2005**, *176*, 1647–1652.

[185] Berg, H.; Rundlov, H.; Thomas, J. O. The $LiMn_2O_4$ to -MnO_2 phase transition studied by in situ neutron diffraction. *Solid State Ionics* **2001**, *144*, 65–69.

[186] Berg, H.; Thomas, J. O. Neutron diffraction study of electrochemically delithiated $LiMn_2O_4$ spinel. *Solid State Ionics* **1999**, *126*, 227–234.

[187] Dupont, L.; Hervieu, M.; Rousse, G.; Masquelier, C.; Palacin, M. R.; Chabre, Y.; Tarascon, J. M. TEM studies: The key for understanding the origin of the 3.3 V and 4.5 V steps observed in $LiMn_2O_4$-based spinels. *Journal of Solid State Chemistry* **2000**, *155*, 394–408.

[188] Rho, Y. H.; Dokko, K.; Kanamura, K. Li^+ ion diffusion in $LiMn_2O_4$ thin film prepared by PVP sol-gel method. *Journal of Power Sources* **2006**, *157*, 471–476.

[189] Xie, J.; Kohno, K.; Matsumura, T.; Imanishi, N.; Hirano, A.; Takeda, Y.; Yamamoto, O. Li-ion diffusion kinetics in $LiMn_2O_4$ thin films prepared by pulsed laser deposition. *Electrochimica Acta* **2008**, *54*, 376–381.

[190] Yamada, I.; Abe, T.; Iriyama, Y.; Ogumi, Z. Lithium-ion transfer at $LiMn_2O_4$ thin film electrode prepared by pulsed laser deposition. *Electrochemistry Communications* **2003**, *5*, 502–505.

[191] Guan, J.; Liu, M. L. Transport properties of $LiMn_2O_4$ electrode materials for lithium-ion batteries. *Solid State Ionics* **1998**, *110*, 21–28.

[192] Shu, D.; Chung, K. Y.; Cho, W. I.; Kim, K. B. Electrochemical investigations on electrostatic spray deposited $LiMn_2O_4$ films. *Journal of Power Sources* **2003**, *114*, 253–263.

[193] Tang, S. B.; Lai, M. O.; Lu, L. Study on Li^+-ion diffusion in nano-crystalline $LiMn_2O_4$ thin film cathode grown by pulsed laser deposition using CV, EIS and PITT techniques. *Materials Chemistry and Physics* **2008**, *111*, 149–153.

[194] Xie, J.; Tanaka, T.; Imanishi, N.; Matsumura, T.; Hirano, A.; Takeda, Y.; Yamamoto, O. Li-ion transport kinetics in $LiMn_2O_4$ thin films prepared by radio frequency magnetron sputtering. *Journal of Power Sources* **2008**, *180*, 576–581.

[195] Inaba, M.; Doi, T.; Iriyama, Y.; Abe, T.; Ogumi, Z. Electrochemical STM observation of $LiMn_2O_4$ thin films prepared by pulsed laser deposition. *Journal of Power Sources* **1999**, *81*, 554–557.

[196] Julien, C.; Haro-Poniatowski, E.; Camacho-Lopez, M. A.; Escobar-Alarcon, L.; Jimenez-Jarquin, J. Growth of $LiMn_2O_4$ thin films by pulsed-laser deposition and their electrochemical properties in lithium microbatteries. *Materials Science and Engineering B* **2000**, *72*, 36–46.

[197] Kuwata, N.; Nakane, M.; Miyazaki, T.; Mitsuishi, K.; Kawamura, J. Lithium diffusion coefficient in $LiMn_2O_4$ thin films measured by secondary ion mass spectrometry with ion-exchange method. *Solid State Ionics* **2018**, *320*, 266–271.

[198] Julien, C.; Mauger, A.; Vijh, A.; Zaghib, K. *Lithium Batteries*, 1st ed.; Springer International Publishing Switzerland, 2016; pp 74–75.

[199] Shao-Horn, Y.; Levasseur, S.; Weill, F.; Delmas, C. Probing lithium and vacancy ordering in O3 layered Li_xCoO_2 (x approximate to 0.5) - An electron diffraction study. *Journal of the Electrochemical Society* **2003**, *150*, A366–A373.

[200] Takahashi, Y.; Kijima, N.; Tokiwa, K.; Watanabe, T.; Akimoto, J. Single-crystal synthesis, structure refinement and electrical properties of $Li_{0.5}CoO_2$. *Journal of Physics-Condensed Matter* **2007**, *19*, 436202.

[201] Nakayama, M.; Kanekoa, M.; Wakihara, M. First-principles study of lithium ion migration in lithium transition metal oxides with spinel structure. *Physical Chemistry Chemical Physics* **2012**, *14*, 13963–13970.

[202] Verhoeven, V. W. J.; de Schepper, I. M.; Nachtegaal, G.; Kentgens, A. P. M.; Kelder, E. M.; Schoonman, J.; Mulder, F. M. Lithium dynamics in $LiMn_2O_4$ probed directly by two-dimensional ^{7}Li NMR. *Physical Review Letters* **2001**, *86*, 4314–4317.

[203] Xu, B.; Meng, S. Factors affecting Li mobility in spinel $LiMn_2O_4$ - A first-principles study by GGA and GGA plus U methods. *Journal of Power Sources* **2010**, *195*, 4971–4976.

[204] Gao, Y.; Myrtle, K.; Zhang, M. J.; Reimers, J. N.; Dahn, J. R. Valence band of $LiNi_xMn_{2-x}O_4$ and its effects an the voltage profiles of $LiNi_xMn_{2-x}O_4$/Li electrochemical cells. *Physical Review B* **1996**, *54*, 16670–16675.

[205] Hu, M.; Pang, X. L.; Zhou, Z. Recent progress in high-voltage lithium ion batteries. *Journal of Power Sources* **2013**, *237*, 229–242.

[206] Kraytsberg, A.; Ein-Eli, Y. Higher, Stronger, Better ... A Review of 5 Volt Cathode Materials for Advanced Lithium-Ion Batteries. *Advanced Energy Materials* **2012**, *2*, 922–939.

[207] Li, J. C.; Ma, C.; Chi, M. F.; Liang, C. D.; Dudney, N. J. Solid Electrolyte: the Key for High-Voltage Lithium Batteries. *Advanced Energy Materials* **2015**, *5*, 1401408.

[208] Santhanam, R.; Rambabu, B. Research progress in high voltage spinel $LiNi_{0.5}Mn_{1.5}O_4$ material. *Journal of Power Sources* **2010**, *195*, 5442–5451.

[209] Yi, T. F.; Xie, Y.; Ye, M. F.; Jiang, L. J.; Zhu, R. S.; Zhu, Y. R. Recent developments in the doping of $LiNi_{0.5}Mn_{1.5}O_4$ cathode material for 5 V lithium-ion batteries. *Ionics* **2011**, *17*, 383–389.

[210] Cabana, J.; Casas-Cabanas, M.; Omenya, F. O.; Chernova, N. A.; Zeng, D. L.; Whittingham, M. S.; Grey, C. P. Composition-Structure Relationships in the Li-Ion Battery Electrode Material $LiNi_{0.5}Mn_{1.5}O_4$. *Chemistry of Materials* **2012**, *24*, 2952–2964.

[211] Xiao, J.; Chen, X. L.; Sushko, P. V.; Sushko, M. L.; Kovarik, L.; Feng, J. J.; Deng, Z. Q.; Zheng, J. M.; Graff, G. L.; Nie, Z. M.; Choi, D. W.; Liu, J.; Zhang, J. G.; Whittingham, M. S. High-Performance $LiNi_{0.5}Mn_{1.5}O_4$ Spinel Controlled by Mn^{3+} Concentration and Site Disorder. *Advanced Materials* **2012**, *24*, 2109–2116.

[212] Zheng, J. M.; Xiao, J.; Yu, X. Q.; Kovarik, L.; Gu, M.; Omenya, F.; Chen, X. L.; Yang, X. Q.; Liu, J.; Graff, G. L.; Whittingham, M. S.; Zhang, J. G. Enhanced Li^+ ion transport in $LiNi_{0.5}Mn_{1.5}O_4$ through control of site disorder. *Physical Chemistry Chemical Physics* **2012**, *14*, 13515–13521.

[213] Sushko, P. V.; Rosso, K. M.; Zhang, J. G.; Liu, J.; Sushko, M. L. Oxygen Vacancies and Ordering of d-levels Control Voltage Suppression in Oxide Cathodes: the Case of Spinel $LiNi_{0.5}Mn_{1.5}O_{4-}$. *Advanced Functional Materials* **2013**, *23*, 5530–5535.

[214] Hu, E. Y.; Bak, S. M.; Liu, J.; Yu, X. Q.; Zhou, Y. N.; Ehrlich, S. N.; Yang, X. Q.; Nam, K. W. Oxygen-Release-Related Thermal Stability and Decomposition Pathways of $Li_xNi_{0.5}Mn_{1.5}O_4$ Cathode Materials. *Chemistry of Materials* **2014**, *26*, 1108–1118.

[215] Kim, J. H.; Huq, A.; Chi, M. F.; Pieczonka, N. P. W.; Lee, E.; Bridges, C. A.; Tessema, M. M.; Manthiram, A.; Persson, K. A.; Powell, B. R. Integrated Nano-Domains of Disordered and Ordered Spinel Phases in $LiNi_{0.5}Mn_{1.5}O_4$ for Li-Ion Batteries. *Chemistry of Materials* **2014**, *26*, 4377–4386.

[216] Amin, R.; Belharouk, I. Part I: Electronic and ionic transport properties of the ordered and disordered $LiNi_{0.5}Mn_{1.5}O_4$ spinel cathode. *Journal of Power Sources* **2017**, *348*, 311–317.

[217] Hosoya, M.; Ikuta, H.; Uchida, T.; Wakihara, M. The defect structure model in nonstoichiometric $LiMn_2O_{4-}$. *Journal of the Electrochemical Society* **1997**, *144*, L52–L53.

[218] Koyama, Y.; Tanaka, I.; Adachi, H.; Uchimoto, Y.; Wakihara, M. First principles calculations of formation energies and electronic structures of defects in oxygen-deficient $LiMn_2O_4$. *Journal of the Electrochemical Society* **2003**, *150*, A63–A67.

[219] Shiiba, H.; Zettsu, N.; Nakayama, M.; Oishi, S.; Teshima, K. Defect Formation Energy in Spinel $LiNi_{0.5}Mn_{1.5}O_{4-}$ Using Ab Initio DFT Calculations. *Journal of Physical Chemistry C* **2015**, *119*, 9117–9124.

[220] Tang, Z. K.; Xue, Y. F.; Teobaldi, G.; Liu, L. M. The oxygen vacancy in Li-ion battery cathode materials. *Nanoscale Horizons* **2020**, *5*, 1453–1466.

[221] Kim, J. H.; Jung, J. W.; Cho, S. H.; Kim, I. D.; Park, Y. C.; Seo, D. H.; Kim, H. S. Investigation of Ordering on Oxygen-Deficient $LiNi_{0.5}Mn_{1.5}O_{4-}$ Thin Films for Boosting Electrochemical Performance in All-Solid-State Thin-Film Batteries. *Small* **2022**, *18*, 2201134.

[222] Cen, J. Y.; Zhu, B. A.; Kavanagh, S. R.; Squires, A. G.; Scanlon, D. O. Cation disorder dominates the defect chemistry of high-voltage $LiMn_{1.5}Ni_{0.5}O_4$ (LMNO) spinel cathodes. *Journal of Materials Chemistry A* **2023**, 13353–13370.

[223] Gao, Y.; Reimers, J. N.; Dahn, J. R. Changes in the voltage profile of Li/$Li_{1+x}Mn_{2-x}O_4$ cells as a function of x. *Physical Review B* **1996**, *54*, 3878–3883.

[224] Mohamedi, M.; Makino, A.; Dokko, K.; Itoh, T.; Uchida, I. Electrochemical investigation of $LiNi_{0.5}Mn_{1.5}O_4$ thin film intercalation electrodes. *Electrochimica Acta* **2002**, *48*, 79–84.

[225] Gellert, M.; Gries, K. I.; Zakel, J.; Ott, A.; Spannenberger, S.; Yada, C.; Rosciano, F.; Volz, K.; Roling, B. $LiNi_{0.5}Mn_{1.5}O_4$Thin-Film Cathodes on Gold-Coated Stainless Steel Substrates: Formation of Interlayers and Electrochemical Properties. *Electrochimica Acta* **2014**, *133*, 146–152.

[226] Xia, H.; Meng, Y. S.; Lu, L.; Ceder, G. Electrochemical properties of nonstoichiometric $LiNi_{0.5}Mn_{1.5}O_{4-}$ thin-film electrodes prepared by pulsed laser deposition. *Journal of the Electrochemical Society* **2007**, *154*, A737–A743.

[227] Ito, A.; Li, D.; Lee, Y.; Kobayakawa, K.; Sato, Y. Influence of Co substitution for Ni and Mn on the structural and electrochemical characteristics of $LiNi_{0.5}Mn_{1.5}O_4$. *Journal of Power Sources* **2008**, *185*, 1429–1433.

[228] Park, S. H.; Oh, S. W.; Kang, S. H.; Belharouak, I.; Amine, K.; Sun, Y. K. Comparative study of different crystallographic structure of $LiNi_{0.5}Mn_{1.5}O_{4-}$ cathodes with wide operation voltage (2.0 - 5.0 V). *Electrochimica Acta* **2007**, *52*, 7226–7230.

[229] Wang, Y.; Peng, Q.; Yang, G.; Yang, Z.; Zhang, L. C.; Long, H.; Huang, Y. H.; Lu, P. X. High-stability 5 V spinel $LiNi_{0.5}Mn_{1.5}O_4$ sputtered thin film electrodes by modifying with aluminium oxide. *Electrochimica Acta* **2014**, *136*, 450–456.

[230] Lin, C. L.; Yin, J. X.; Cui, S. R.; Huang, X.; Liu, W.; Jin, Y. C. Improved Electrochemical Performance of Spinel $LiNi_{0.5}Mn_{1.5}O_4$ Cathode Materials with a Dual Structure Triggered by LiF at Low Calcination. *ACS Applied Materials & Interfaces* **2023**, *15*, 16778–16793.

[231] Wang, J.; Xing, H. Y.; Hou, W. Q.; Xu, Y. L. The role of oxygen vacancies in the performance of $LiMn_2O_4$ spinel cathodes for lithium-ion batteries. *Physical Chemistry Chemical Physics* **2023**, *25*, 18903–18914.

List of Figures

List of Abbreviations

AFM atomic force microscopy

BEV battery electric vehicle

CPE constant phase element

CV cyclic voltammetry

EIS electrochemical impedance spectroscopy

EV electric vehicle

GDC gadolinium-doped ceria

LSC $La_{0.6}Sr_{0.4}CoO_{3-}$

LSF $La_{0.6}Sr_{0.4}FeO_{3-}$

LSM $La_{0.8}Sr_{0.2}MnO_{3-}$

LIB lithium-ion battery

LiPON lithium phosphorous oxynitride

LCO $LiCoO_2$

LFP $LiFePO_4$

LLTO $Li_{0.29+}\ La_{0.57}TiO_3$

LMO $LiMn_2O_4$

LNMO $LiNi_{0.5}Mn_{1.5}O_4$

MIEC mixed ionic and electronic conductor

NVPF $Na_3V_2(PO_4)_2F_3$

RF radio-frequency

SOC state-of-charge

SOEC solid oxide electrolyzer cell

SOFC solid oxide fuel cell

STF $Sr(Ti,Fe)O_{3-}$

STO $SrTiO_3$

SRO $SrRuO_3$

TEM transmission electron microscopy

XRD X-ray diffraction

YSZ yttria-stabilized zirconia

Danksagung

Als ich mich vor vier Jahren an diesen Schreibtisch setzte, konnte ich mir nicht im Entferntesten vorstellen, wie es sich anfühlen würde, die letzten Zeilen meiner Dissertation zu verfassen. Es war ein Losgehen ohne klares Ziel, im Vertrauen, dass sich dieses entlang des Weges herauskristallisieren würde. Zwei Jahre später, mitten in der berüchtigten „mid-PhD crisis“, schien das Ziel schließlich in unerreichbare Ferne zu rücken. Umso größer ist nun meine Erleichterung und Freude, diese Abschlussarbeit vorlegen zu können, die ohne die fachliche und persönliche Unterstützung vieler Menschen nicht möglich gewesen wäre.

Zunächst möchte ich mich bei dir, Jürgen, für den großen Vertrauensvorschuss bedanken, den du mir entgegengebracht hast. Du hast mir damals, ohne mich oder meine Arbeitsweise zu kennen, diese Stelle angeboten, und mir in meiner Forschung jede Freiheit gelassen. Außerdem hast du neben deiner fachlichen Expertise auch immer wieder ein gewisses menschliches Fingerspitzengefühl bewiesen, das, glaube ich, in der gesamten Arbeitsgruppe sehr wertgeschätzt wird.

Zusätzlich möchte ich mich beim gesamten Fachbereich Technische Elektrochemie dafür bedanken, dass ihr diesen Arbeitsplatz mit Leben erfüllt habt, und mit euren Ideen und fachlichen Inputs meine Arbeit bereichert habt. Joseph, vielen Dank für die abwechslungsreiche Zeit mit dir im Lithium-Büro, angefangen von meinem Schnupperpraktikum 2019 bis hin zu unseren abenteuerlichen Besuchen bei Billy’s Sub Shop am Rande der SSI-Konferenz 2022 in Boston. Martin, unser gemeinsamer 12-Stunden-Feiertag am USTEM und unsere philosophischen Gespräche über die chemische Kapazität werden mir lange in Erinnerung bleiben. Christin, danke für deine Hilfsbereitschaft und die viele Zeit, die du dir für meine Probleme an der PLD oder am Empyrean genommen hast. Claudia, du hast in deiner Zeit als Diplomandin wesentlich zum Voranschreiten meiner Arbeit beigetragen und hast mich seither immer wieder durch Elementaranalysen und AFM-Messungen unterstützt - vielen Dank dafür. Ein besonderer Dank gilt auch Alex S. für unsere erhellenden Diskussionen zu den Parallelen und Unterschieden zwischen Batterien und Brennstoffzellen, Tobias für die vielseitige technische Unterstützung und Andreas N. für die ausgiebige Beratung in allen möglichen physikalischen Belangen.

Mein allergrößter Dank gilt meinen Eltern und meinen beiden Brüdern, Armin und Alex, die immer an mich geglaubt haben und mir in der schwersten Zeit meines Doktorats dabei geholfen haben, die richtige Perspektive auf das Leben zu bewahren.